# AN INVESTIGATION ON MAGNETIC APPLICATORS FOR HYPERTHERMIA APPLICATIONS

By

**CHAI SIEW KEY**

A dissertation submitted to the Department of Electrical and Electronic Engineering,

Faculty of Engineering and Science,

Universiti Tunku Abdul Rahman,

in partial fulfilment of the requirements for the degree of

Master of Engineering Science

November 2013

**ABSTRACT**

**AN INVESTIGATION ON MAGNETIC APPLICATORS FOR HYPERTHERMIA APPLICATIONS**

**CHAI SIEW KEY**

Hyperthermia is one of the latest techniques to fight cancer. It works by heating cancer cells to about 42°C ~ 45°C. One promising way of doing this is by depositing nanoparticles in between cancer cells and subjecting them to an AC magnetic field.

However, to be effective, the magnetic field must be able to reach the nanoparticles deep inside the body and be confined or focused in order to limit patient discomfort. Current commercial applicators suffer from these drawbacks by subjecting patients to a uniform field with little discrimination.

Based on the discovery that curved distributed coils have better field focusing and field penetration than that of solenoids and loop coils, a novel magnetic field applicator was invented to address these drawbacks. In the design process, 2D analytical field synthesis models of the applicator were developed to assist in the optimisation procedure. This process yielded an optimised paired convex distributed applicator design.

In order to improve upon this 2D applicator design, 3D simulation models were developed and solved using the CST MWS® solver. It was discovered that adding deflector plates at the coil poles can improve the field penetration. The result is a 1 : 2 scaled design of a paired spherical convex coils with these deflector plates added. This design employs a constant coil current density with air return media.

A prototype of this applicator design including the speciality electronics were constructed to verify the magnetic flux values at both 50Hz and 50kHz. In both cases, the readings from the prototype agree well with its simulation output.

For comparison with the state of the art magnetic hyperthermia applicator, the new applicator design was scaled to life-size. This novel applicator design has demonstrated better magnetic field focus and energy efficiency, thus improving heating efficacy significantly but at a lower cost.

## ACKNOWLEDGEMENT

I would like to place on record my sincere appreciation and gratitude to my supervisors, Prof. Dr. Ewe Hong Tat and Prof Dr. Chung Boon Kuan for their valuable advices and guidances.

I would also like to express my utmost gratitude to Prof. Dr. Tan Hong Siang whose influence has shaped much of the thoughts, ideas and indeed, the person in me.

A special word of thanks goes to Mr. Fong See Ni whose camaraderie and unwavering support was the lifeline of this project.

Many thanks go to Pn. Roziyana Md. Said, Mr. Albert Tee and Mr. Tan Lee Haw for their expertise and resource support in the prototype realisation.

Last but not least, I would like to thank my friends, UTAR staff members and my family members who have supported me, one way or another in this project.

## APPROVAL SHEET

This dissertation entitled "**<u>AN INVESTIGATION ON MAGNETIC APPLICATORS FOR HYPERTHERMIA APPLICATIONS</u>**" was prepared by CHAI SIEW KEY and submitted as partial fulfilment of the requirements for the degree of Master of Engineering Science at Universiti Tunku Abdul Rahman.

Approved by:

________________________________

(Prof Dr Ewe Hong Tat) Date: …..........................

Professor / Supervisor

Department of Internet Engineering and Computer Science

Faculty of Engineering and Science

Universiti Tunku Abdul Rahman

________________________________

(Prof Dr Chung Boon Kuan) Date: …..........................

Professor / Co-supervisor

Department of Electrical and Electronic Engineering

Faculty of Engineering and Science

Universiti Tunku Abdul Rahman

**FACULTY OF ENGINEERING AND SCIENCE**

**UNIVERSITI TUNKU ABDUL RAHMAN**

Date: 1st November 2013

**SUBMISSION SHEET**

It is hereby certified that **CHAI SIEW KEY** (ID No: **09UEM09183**) has completed this dissertation entitled "**AN INVESTIGATION ON MAGNETIC APPLICATORS FOR HYPERTHERMIA APPLICATIONS**" under the supervision of PROF. DR. EWE HONG TAT (Supervisor) from the Department of Internet Engineering and Computer Science, Faculty of Engineering and Science, and PROF. DR. CHUNG BOON KUAN (Co-Supervisor) from the Department of Electrical and Electronic Engineering, Faculty of Engineering and Science.

I understand that the University will upload the softcopy of the dissertation in pdf format into the UTAR Institutional Repository which may be accessible to the UTAR community and the public.

Name: CHAI SIEW KEY

## DECLARATION

I hereby declare that the dissertation is based on my original work except for quotations and citations which have been duly acknowledged. I also declare that it has not been previously or concurrently submitted for any other degree at UTAR or other institutions.

Name: CHAI SIEW KEY

Date: 1st November 2013

## TABLE OF CONTENT

## LIST OF TABLES

## LIST OF FIGURES

## LIST OF ABBREVIATIONS

| | |
|---|---|
| AC | Alternating Current |
| AWG | American Wire Gage |
| CST | Computer Simulation Technology |
| DC | Direct Current |
| e.m.f. | electromotive force |
| EI | Interleaving E and I shaped core plates |
| EU | European Union |
| FEMM© | Finite Element Method Magnetics |
| HPBW | Half Power Beam Width |
| IFAC-CNR | Italian National Research Council |
| MFH | Magnetic Fluid Hyperthermia |
| MWS® | Microwave Studio |
| ***pk*** | peak |
| ***rms*** | root mean square |
| RF | Radio Frequency |
| SAR | Specific Absorption Rate |
| TMS | Transcranial Magnetic Stimulation |
| VA | Volt Ampere |
| VBA | Visual Basic |
| WHO | World Health Organisation |
| 0.9FBW | 90 % Field Beam Width |
| 2D | 2-Dimension |
| 3D | 3-Dimension |

## CHAPTER 1

## INTRODUCTION

### 1.1 Background

Heating as a means for treating cancer has been known for decades (Jordan *et al.* 2006). In particular, cancerous cells heated modestly to between 42ºC to 46ºC - a condition known as hyperthermia - tend to degenerate, thus leading to apoptosis or programmed cell death. Coupled with its ability to enhance radiosensitivity (Duguet *et al.* 2009), it has shown promise as a complementary therapy for narrowing the therapeutic gap of conventional oncology as shown in Fig 1.1 (Szasz *et al.* 2006).

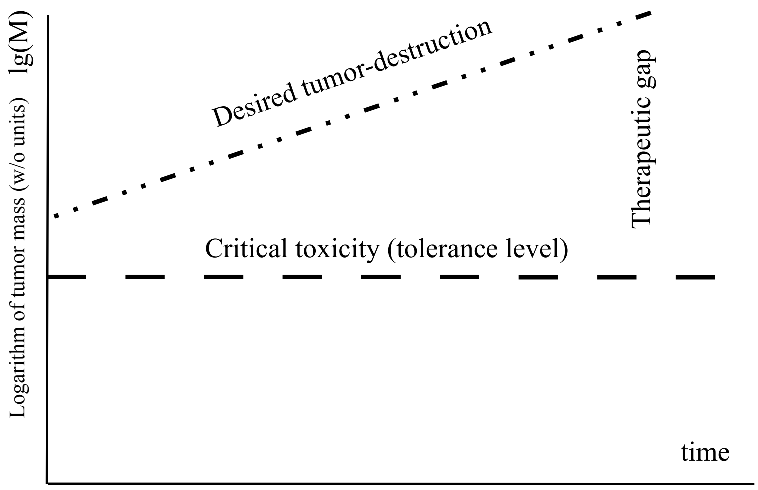


Fig 1.1 Logarithm of tumour mass/destruction requirement vs time. The difference between the desired destruction toxicity and critical tolerance toxicity is the therapeutic gap (Szasz *et al.* 2009).

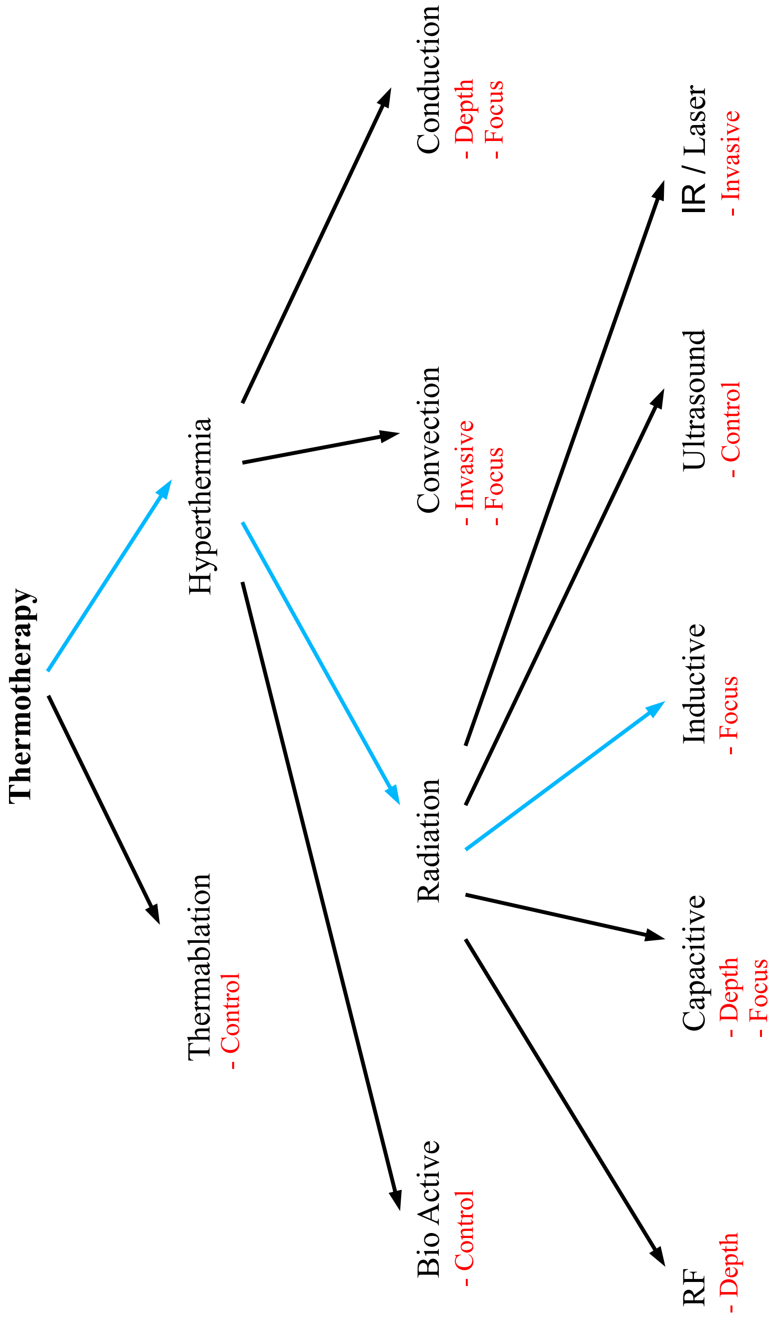


Fig 1.2 Tree diagram illustrating the perspective modes of thermotherapy leading to inductive hyperthermia. The corresponding main drawbacks are also highlighted below each mode. Adapted from Szasz *et al.* (2009).

The means for delivering heat to these cells can broadly be categorised into (a) conduction, (b) convection, (c) radiation and (d) bioactive methods (Szasz *et al*. 2006). Specifically, within the radiation category, the various functional modes are (a) infra red, (b) ultrasound, (c) RF, (d) capacitive field and (e) inductive field (Plewako *et al.* 2003, Hager 2006) as shown in Fig 1.2. Each category and mode, to varying degrees, carries practical drawbacks, some of which are highlighted in Fig 1.2 as generalised by Szasz (2006). Jordan (2006) has further narrowed them down to (a) uneven distribution of heat across the area of treatment and (b) access to deep tumours.

Due to the largely non-magnetic nature of biological tissues, magnetic field has been able to reach deep into the human body (Szasz *et al*. 2006). By concentrating ferromagnetic material that produces heat in response to an AC magnetic field around the target cells, heating can thus be localised, leaving the surrounding healthy cells without ferromagnetic material largely unaffected (Rand *et al.* 1983, Hergt *et al.* 2004).

### 1.1.1 Heating Material and Methods of Administration

Ferromagnetic material for magnetic hyperthermia can broadly be categorised into (a) bulk material and (b) nanoparticles. Nanoparticles are further sub-categorised into (a) ferroparticles and (b) superparamagnetic fluid (Bahadur & Giri 2003).

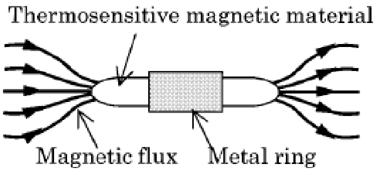


(a)

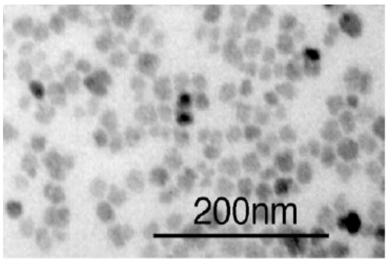


(b)

Fig 1.3 Illustrations of (a) thermo circuits (Jojo et al. 2001) and (b) ferromagnetic particles (Hergt *et al*. 2004).

The bulk material is ferromagnetic rods or seeds, up to the order of 20 mm that may optionally be strapped with a lossy metal ring (Jojo *et al*. 2001, Eggers & Ridihalgh 2009) as illustrated in Fig 1.3(a). This material is surgically implanted into the tumour (Sievert *et at*. 1993, Bahadur & Giri 2003), hence the need for another post-treatment surgery to remove the material. Apart from this invasive nature, its heat distribution on the tumour is not uniform, although the heating capability is very high.

On the other hand, nanoparticles are sub-micron ferromagnetic material typically in the order of 1 to 100 nm as illustrated in Fig 1.3(b). These particles are at least an order smaller than biological cells as illustrated in Fig 1.4 and therefore lend themselves to intratumoural hyperthermia (Jordan *et al*. 2006, Trahms 2009).

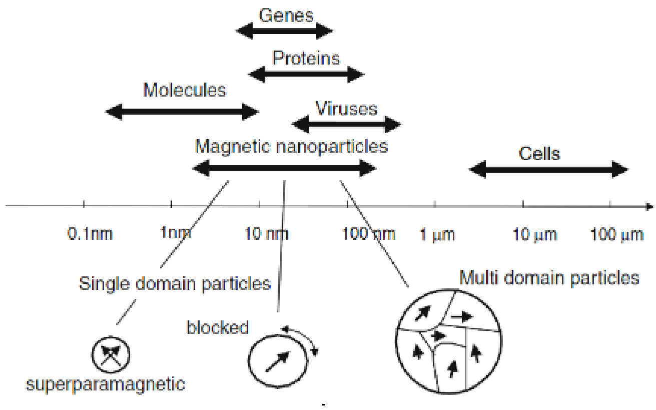


Fig 1.4 Size of magnetic particles relative to common biological entities and the corresponding magnetisation modes (Trahm 2009).

Larger multi-domain particles, generally referred to as ferroparticles, are usually injected directly into the tumour (Wust *et al.* 2006) since they are prone to extravasation by the body's reticuloendothelial system. On the other hand, sub-domain particles, being smaller, have a longer vascular half-life against extravasation, especially when coated with a hydrophilic barrier and thus can be administered intravenously as a stable colloidal suspension, also known as a superparamagnetic fluid. These particles can be attached to the target tumour cells either by (a) molecular binding between the particle coating and the cell receptors, (b) ferroembolism when the superparamagnetic fluid is injected into the hepatic arterial system (Duguet e*t al.* 2009) or (c) magnetic targeting where a static magnetic field is applied over the target cells to guide the nanoparticles to the tumour (Zechbauer 2007, Trahm 2009). Although minimally invasive, its heating dependence on the magnetic field strength is weaker (second power) compared to that of multi-domain ferroparticles (third power) ( Trahms 2009).

### 1.1.2 Heating Mechanism

Apart from the properties of the material, the heating mechanism of ferromagnetic material in biological tissues also depends on the particle size. It determines whether the dominant heating mechanism is through (a) hysteresis loss or (b) superparamagnetic loss.

In multi-domain particles, typically above tens of nm as illustrated in Fig 1.4, and in thermo rods, the dominant heating effect comes from hysteresis loss due to the movement of Bloch walls under the influence of the applied magnetic field and it is characterised by (Trahm 2009):

$$W_{hys}=\frac{\mu_0}{\rho}\oint M_H(H)\,dH \tag{1.1}$$

where $W_{hys}$ is the specific hysteresis loss per cycle, $\mu_0$ the permeability constant, ρ the material density, $M_H(H)$ the magnetisation strength and $H$ the magnetising field strength. This power loss is dependent on the third power of $H$ according to Rayleigh's law (Hergt & Dutz 2007) and given its larger volume, its heating capacity tends to be high.

For smaller single domain particles, the dominant heating effect comes from superparamagnetic loss due to Néel relaxation, the magnetic anisotropy energy released when the magnetising field is relaxed. Its time constant is characterised by (Duguet *et al.* 2009):

$$\tau_n=\tau_0\exp\frac{KV}{k_B T} \tag{1.2}$$

where $\tau_n$ is the Néel relaxation time, $\tau_0$ the characteristic attempt time, typically $10^{-9}$ s, $k_B$ the Boltzmann constant, $T$ the absolute temperature, $V$ the volume of the particle and $K$ the characteristic anisotropy energy density. This time constant yields an equivalent complex susceptibility, $\chi''(\upsilon)$ given by (Trahm 2009):

$$\chi''(\upsilon) = \frac{M_s^2 V}{k_B T} \frac{\upsilon \tau_n}{1+(\upsilon \tau_n)^2} \tag{1.3}$$

where $\upsilon$ is the excitation frequency and $M_s$ the saturation magnetisation. Fig 1.5 shows the theoretical and measured $\chi''$ against the excitation frequency for $Fe_2O_3$ particles of mean diameter 15.3 nm. Note that $\chi''$ peaks at ~100 kHz.

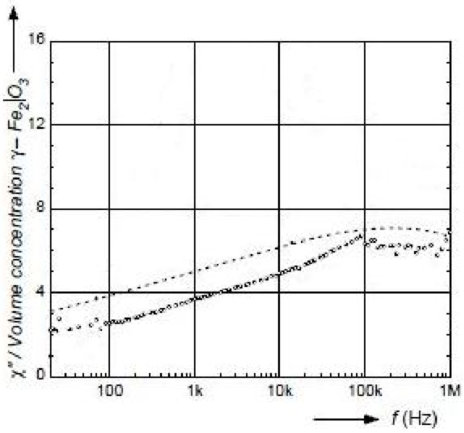


Fig 1.5 Measured $\chi''$ of $Fe_2O_3$ particles with mean diameter 15.3 nm versus the excitation frequency as compared with the corresponding calculated $\chi''$ (dashed line) (Hergt *et al*. 2004).

The corresponding specific power dissipation, $P$ is given by (Hergt *et al*. 2004):

$$P = \frac{\mu_0 \pi \chi''(\upsilon) H^2 \upsilon}{\rho} \tag{1.4}$$

Eq 1.4 is a non-linear function of frequency but it can be simplified to (Chen *et al.* 2010):

$$SAR = k\, H^2 \upsilon^n \tag{1.5}$$

where $SAR$ is the specific absorption rate, $k$ a constant depending on the particle properties and $n$ an exponent between 1 and 2, typically 1.6.

For the same smaller particles, there's another heating effect coming from Brownian relaxation, the rotation frictional energy released when the magnetising field is relaxed. However, due to their limited motion when attached to cells, Brownian relaxation is considered ineffective on biological tissues (Hergt *et al.* 1998) and is usually ignored.

Superparamagnetic loss is dependent on the second power of $H$ as expressed by Eq 1.5 (Hergt & Dutz 2007) and given its small volume, a higher $H$ is generally required to achieve sufficient heating.

**1.2 Prior Art**

Over the years, numerous studies have been done on the particle types & sizes, magnetic field strength and excitation frequency (Duguet *et al.* 2009, Xu *et al.* 2009, Hergt *et al.* 2004, Chen *et al.* 2010, Pollert *et al.* 2009). However, one commercial solution stands out in the forefront with growing acceptance (von Landeghem *et al.* 2009, Johannsen *et al.* 2007) and it is already approved by the EU regulatory body. The Nanotherapy® solution, developed by MagForce AG, uses the patented 15 nm nanoparticles coated with aminosilane, suspended in an aqueous solution at 112 mg $cm^{-3}$ (Johannsen et al. 2007) that can be administered intravenously or through intratumoural injection (Jordan 2006).

As shown in Fig 1.5, $\chi''$ peaks at around 100 kHz, yielding the optimum *SAR*. Therefore, it is natural for its applicator, MFH®-300F as illustrated in Fig 1.6 to work at 100 kHz. MFH®-300F generates up to 18 kA $m^{-1}$ (Feucht 2003, Duguet *et al*. 2009) at 90 % field uniformity within a 20 cm diameter (Di Barba *et al*. 2010). For the reason of its leadership in this field, the present investigation will benchmark this applicator's performance.


Fig 1.6 MagForce's MFH®-300F AC magnetic field applicator (Johannsen *et al*. 2007).

### 1.2.1 Drawbacks

An AC magnetic field induces e.m.f. inside the body's conductive fluid environment and this e.m.f. generates eddy current which in turn generates heat, causing patient discomfort. This induction heating power, $P_{eddy}$ is given by (Hergt & Dutz 2007):

$$P_{eddy} \propto |H \cdot f \cdot D|^2 \qquad (1.6)$$

where $H$ is the magnetising field strength, $f$ the excitation frequency and $D$ the diameter of the area exposed to the applied field. This places a practical limit on the applied field strength, depending on the excitation frequency and the exposure area. Although heat tolerance varies from patient to patient, a widely accepted empirical limit up to an hour's exposure without major discomfort at $D$ = 30 cm is given by (Duguet *et al.* 2009):

$$| H \ . \ f \ | < 4.85 \, x \, 10^8 \ A \ m^{-1} \ s^{-1} \quad (1.7)$$

In clinical studies using MFH®-300F, Wust (2006) has reported patient tolerance of magnetising field strength between 3 kA $m^{-1}$ and 10 kA $m^{-1}$ depending on the area of treatment. Eqs 1.6 and 1.7 give the *H* limit at 7.27 kA $m^{-1}$ adjusted for *D* = 20 cm, consistent with the above result. Unfortunately, the trial only achieved a 30 % efficacy in reaching above the 42°C necessary for hyperthermia. Nonetheless, on an optimistic note, Wust (2006) claimed that a moderate increase of 2 kA $m^{-1}$ would increase the efficacy up to 98 %, implying that even a modest field strength improvement is enough to produce substantial results.

As illustrated in Fig 1.6, the MFH®-300F applicator is rather bulky. Feucht (2003) has disclosed its construction of a closed-loop magnetic circuit, air-gapped at 30 cm (MagForce 2009) to maintain a minimal field decay for reaching deep tumours. Notably, its power consumption has been reported to be between 18 kW to 80 kW when the required heating is typically in the order of Watts (Feucht 2003), implying a very low power conversion factor (Tai & Chen 2008).

### 1.2.2 Mitigations

To improve the efficacy of reaching the hyperthermia temperature within tolerable eddy current heating, Hergt *et al*. (2004) has suggested lowering the excitation frequency and increasing the applied field strength. Provided the (*H . f)* product in Eq 1.7 is maintained, the *SAR* in Eq 1.5 can be increased since the order of *f* is weaker than that of *H*.

However, in order to avoid neuromuscular electrostimulation, the lower bound of the excitation frequency is limited to 50 kHz (Duguet *et al.* 2009, Pollert *et al.* 2009, Rand *et al.* 1983). Indeed, Bahadur & Giri (2003) has reported an encouraging study done at 55 kHz, 40 kA $m^{-1}$ to prove the feasibility of using a lower excitation frequency. Although this is done at the expense of a sub-optimum χ", upon inspection of Fig 1.5, the deterioration of χ" at 3 % (χ" drops from 6.3 to 6.1) did not hamper its success. Indeed, Magforce (2008) has been working on the development of a 50 kHz applicator since 2007. A higher *SAR* also allows smaller tumours to be treated as shown in Fig 1.7 (Trahms 2009).

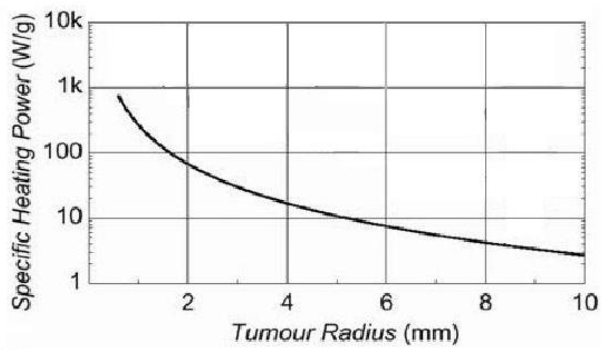


Fig 1.7 Power requirement versus various tumour sizes to achieve 15ºC temperature rise with solution concentration of 100 mg $cm^{-3}$. Adapted from Trahms (2009).

Another option is the reduction of *D*. Duguet *et al.* (2009) has indirectly suggested this by advocating the use of smaller coil diameters. Evident from Eq 1.6, when *D* is reduced, the (*H* . *f*) product can be increased while maintaining the $P_{eddy}$, therefore allowing the (*H* . *f* ) limit set forth in Eq 1.7 and thus, tumour heating to be increased (Hergt & Dutz 2007). Additionally, a local device with a smaller *D* also allows better heating control (Duguet *et al.* 2009) and possibly consumes less power.

### 1.3 Objectives

The objective of this research is to improve the performance of magnetic hyperthermia from the applicator standpoint against the prior art as outlined in section 1.2. It seeks out a novel applicator with a smaller $D$ or better focus balanced with a comparable field decay or field penetration, thus offering the promise of portability and better power efficiency. It does this by seeking out the following goals:

(a) design an improved applicator configuration and simulate the field output of the design.

(b) build a concept prototype and verify the field measurements against the simulation output.

On the premise that a lower excitation frequency can increase the heating efficacy, the improved applicator will be based on a 50 kHz excitation frequency.

This research does not seek to confirm the performance of the applicator through *in-vivo* or *in-vitro* experiments as the performance of magnetic hyperthermia and its relationship with field parameters are well documented and understood as outlined in Sections 1.1 and 1.2.

## 1.4 Methodology

In order to achieve the objectives set forth in Section 1.3, the research was carried out according to the following steps:

(a) review literature to draw upon applicable ideas or concepts

(b) formulate possible design configurations from the ideas and concepts drawn from the literature review

(c) calculate or simulate the performance of the possible design options.

(d) from the simulations, choose the optimum design and realise a prototype model based on this design.

(e) measure the field parameters of the prototype and verify against the simulation output at 2 different excitation frequencies.

(f) analyse the result and conclude the project with solutions & recommendations.

# CHAPTER 2

# LITERATURE REVIEW

## 2.1 Background

In this chapter, the prior art magnetic field applicators will be reviewed. These applicators will be categorised according to their construction and working principles. A brief description of their merits and drawbacks will be discussed and some of these principles will be selected to formulate the design configurations for performance simulation and improvement.

Magnetic applicators can be generalised into 3 basic classes based on the principles of generating and shaping the magnetic field in the target space where biological tissues are located. They are (a) direct field applicators, (b) local field concentrator & attractors and (c) field saturation applicators.

## 2.2 Direct Field Applicators

The direct field method works by injecting current into either singular or multiple coils and applying the field induced directly by this current flow, with or without a magnetic core. Broadly, this direct field method can further be classified into 3 broad coil geometries, i.e. (a) loop coils, (b) distributed planar coils & (c) solenoids and 3 broad core geometries, i.e. (d) non-circular core, (e) convex / concave pole & (f) air-gapped core.

(a) The simplest coil geometry is the current loop. In US Patent US7,567,843 B2, Eggers & Ridihalgh (2009) used a singular loop applicator as illustrated in Fig 2.1(a) in conjunction with thermo circuit implants to effect hyperthermia.

Multiple coils may be combined to shape and enhance the field at the target space. Fig 2.1(b) illustrates an example used in the Transcranial Magnetic Stimulation (TMS) application (Tsuyama *et al*. 2009).

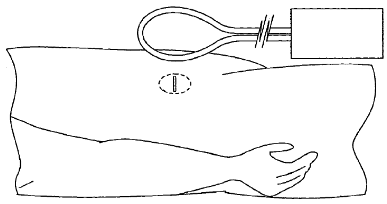

(a)

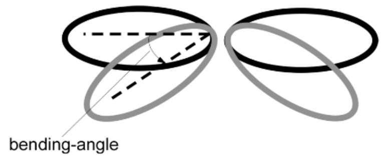


(b)

Fig 2.1 (a) Singular loop (Eggers & Ridihalgh 2009) and (b) multiple loop (Tsuyama *et al*. 2009) applicators.

Despite being constructively simple, the current loop has limited field penetration (Huang *et al*. 2009) and it is usually employed on targets with limited depth such as the head or targets implanted with thermo circuits where the required field strength is relatively low. Moreover, due to its geometrical limitation, the injected current is high (in the order of kA) and usually pulsed (Talebinejad *et al*. 2011).

(b) Distributed planar coils are popular in applications where a wide area of magnetic coupling is desired such as in dermal hyperthermia (Bartusek & Geschiedtova 2005). However, as small distributed planar coils have shallow field penetration (Hanak *et al*. 2006), large distributed planar coils are required in order to achieve deep penetration and they tend to take up space.

(c) Early applications of the solenoid in hyperthermia entail positioning the target in-core, i.e. inside the air core of a singular solenoid. In one implementation (Storm *et al.* 1982), a loop sheet is used to form the air core solenoid as illustrated in Fig 2.2(a). Despite its simplicity, its power loss is high as the current is concentrated on its periphery due to the skin effect.

In order to reduce this loss, a helical wire coil is used instead so that the skin effect can be distributed over a larger conductor area. To cool the coil, copper tubes are used instead of wires for circulating coolants in the coil (Rand 1991) as illustrated in Fig 2.2(b).

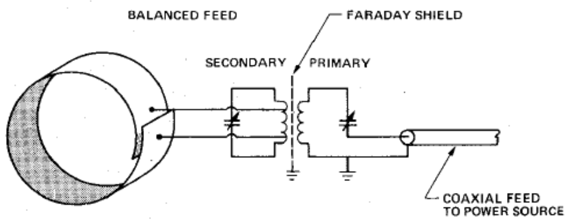


(a)

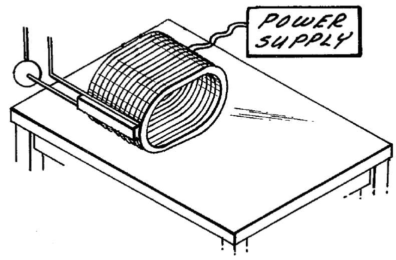


(b)

Fig 2.2 In-core solenoid applicators in the (a) singular loop sheet form (Storm *et al.* 1982) and (b) singular helical coil form (Rand 1991).

Unfortunately, positioning the target inside the air core imposes practical constraints on the types and sizes of targets. To overcome this problem, the target can be placed ex-core, i.e. outside the solenoid's air core despite its limited field penetration. However, the target can be placed right outside the air core (Sievert *et al.* 1993) as illustrated in Fig 2.3 in order to mitigate against this limitation.

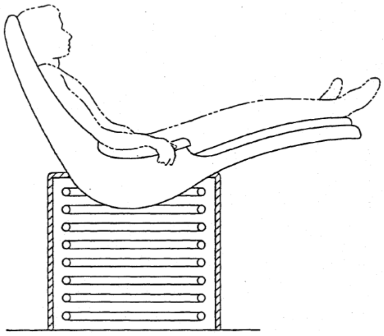

Fig 2.3 Ex-core solenoid applicators using a singular coil (Sievert *et al*. 1993).

Positioning the target outside the solenoid also allows a ferromagnetic core to be used instead of an air core in order to boost the magnetising field strength on the target. However, as with air core solenoids, its field penetration is also limited.

(d) By varying the cross section geometry of the core, the magnetic field can be made directional or focused in specific directions. For example, Kong (2009) has claimed that the focusing effect in elliptical and triangular shaped cores are useful in hyperthermia applications. Unfortunately, he did not demonstrate any field penetration effect in his studies.

(e) When the core is convexed or concaved at its pole, the magnetic field can be converged or diverged around its poles. Siemens' magnetic targeting applicator (Zechbauer 2007) as illustrated in Fig 2.4(a) has employed the conical pole to create field focus or field gradient. However, its field penetration is limited, evident from the proximity of the pole to the target.

In contrast, Ho (2012a) has used convex poles to diverge magnetic field away from around the target in order to create the field focus in his hyperthermia applicator as illustrated in Fig 2.4(b). Unfortunately, this applicator also has limited penetration.

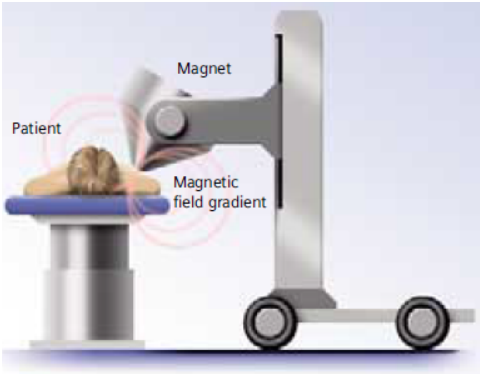


(a)

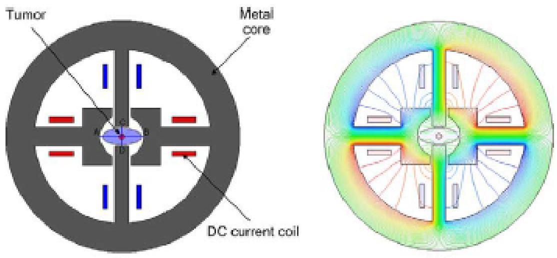


(b)

Fig 2.4 Core (a) convexed at its pole to concentrate field at the target (Zechbauer 2007) and (b) concaved at its poles to create a near null region around the target (Ho *et al.* 2012a).

(f) One of the most common applicator configurations for magnetic hyperthermia is the air-gapped core (Mornet *et al.* 2004). In order to achieve field penetration, the target is placed in the air gap between 2 opposing magnetic poles. The magnetic field at the poles can be induced by (a) the magnetisation of the ferromagnetic media excited by a singular coil and/or (b) current elements in individual coils local to each pole.

In the case of a singular coil excitation as shown in Fig 2.5, the ferromagnetic media usually takes the form of a magnetic yoke, forming a closed-loop circuit. The coil can be placed at one end of the yoke (Xu *et al*. 2009) as illustrated in Fig 2.5(a). Alternatively, the coil can also be positioned remote from both poles (Handy *et al*. 2006) as illustrated in Fig 2.5(b). Positioning the coil remote from the poles shields the patient from heat and electrical hazards. On the other hand, having the coil at one pole allows the field in the target space to be shaped locally by the current elements to enhance the field strength and field penetration. This is particularly useful when asymmetrical field penetration is desired.

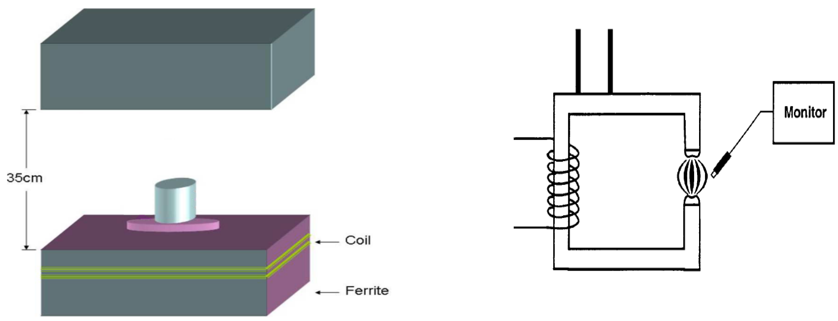


(a) (b)

Fig 2.5 Scheme of singular coil air-gapped applicators with a coil (a) at the pole (ferrite limbs joining the top and bottom poles not shown) (Xu *et al*. 2009) and (b) remote from the poles (adapted from Handy *et al*. 2006).

For pair coil excitation, the coils are mounted on both poles facing the target space. By having its own excitation coil, the poles do not necessarily need a ferromagnetic media to close the magnetic circuit. With more coils facing the target space, more modes of field modulation are possible. The poles can face each other (i) directly or (ii) skewed and additional pairs of coils can act on the same target space either by (iii) sharing poles as auxiliary coils or (iv) acting from multiple separate poles, directly or skewed.

(i) A case in point for direct pair coils is the Helmholtz coil for hyperthermia application, producing a uniform field in the target space (Miers *et al*. 2002). Being air cored, it has no magnetisation loss but its magnetising field strength is limited and there is no field focus. Improving on Miers' Helmholtz coil, two distributed coils are supported vertically by a yoke & limb structure in Feucht's (2003) MFH®-300F applicator as illustrated in Fig 2.6. This air-gapped core applicator emphasises more importance on a uniform field over a focused field. The distributed coil and the magnetic yoke & limb structure allow a higher field strength to be produced with lower copper loss but at the expense of ferromagnetic core loss.

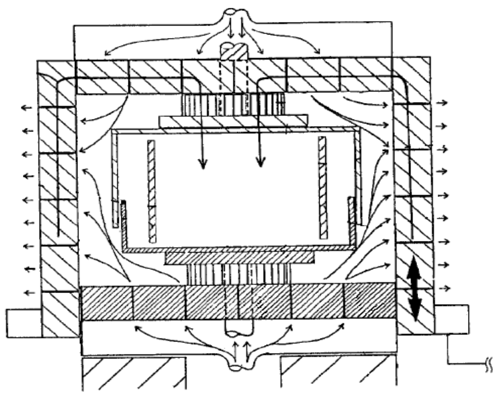

Fig 2.6 Direct pair coil applicators in the MFH®-300F applicator (Feucht 2003).

(ii) By varying the pair coils spatially, a wide range of field patterns can be produced. Pair coils may be skewed to accommodate the anatomical contour of the body. The poles straddled over 2 sides of an organ at a skew angle can vary from near anti-parallel poles (Kotsuka *et al*. 2000) as illustrated in Fig 2.7(a) to near diametric poles (Gronmeyer *et al*. 2009) as illustrated in Fig 2.7(b) in order to shape the field pattern at the target space.

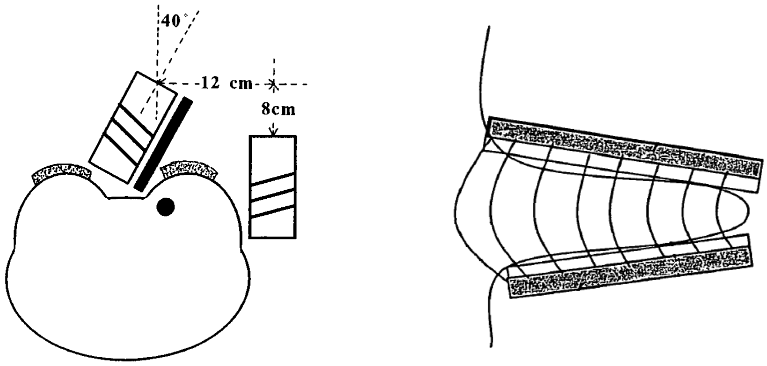


(a) (b)

Fig 2.7 Single pair skewed air-gapped core applicators with a (a) near anti-parallel skew angle (Kotsuka *et al*. 2000) and (b) near diametric skew angle (Gronmeyer *et al*. 2009).

However, if the poles are nearby, conductive shield plates are usually inserted between the coils to minimise field leakages, hence the additional losses. In addition, due to its low field penetration, the coils must be positioned close to the organ and the applicator is usually only suitable for protruded organs like the human breast.

(iii) Auxiliary coils may be positioned around the primary poles (Handy *et al.* 2006) as shown in Fig 2.8 in order to shape the field distribution in the target space. However, their secondary field is short-ranged, confined to the regions near the poles, hence its limited use.

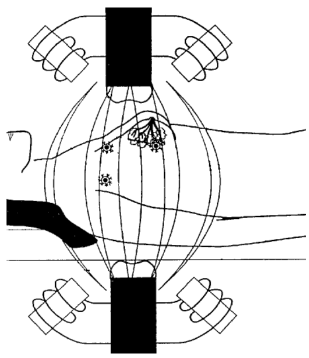

Fig 2.8 Direct pair coil air-gapped applicator with auxiliary coils at each main pole (Handy *et al.* 2006).

(iv) In order to accentuate the field in the target space, multiple pair coils may be assembled such that they share the same target space. The pair coils excited by synchronised current sources may be displaced orthogonally (Huang *et al*. 2010) as illustrated in Fig 2.9(a). Although they can increase the magnetising field strength, especially if they are held by a magnetic yoke, their field penetration is limited, complicated by stray reluctance paths.

If the orthogonal pair coils are excited by current sources displaced by a quadrant, the effect is a rotating field around the centre of the target space (Gray & Jones 2000) as illustrated in Fig 2.9(b). This sustains the field strength at the centre but its peripheral field maxima manifests only once per electrical revolution, hence the pseudo-focus effect. However, this effect is overstated as the field pattern of each pair coil is not spatially uniform throughout the target space, complicated by the varying loop magnetic reluctance as the field rotates.

In an attempt to overcome this problem, the field is rotated by sequentially coupling the field of circularly spaced pair coils using an alternating ring (Ho *et al*. 2012a) as illustrated in Fig 2.9(c). However, having a rotating structure, this applicator may be bulky, subject to noise and vibration.

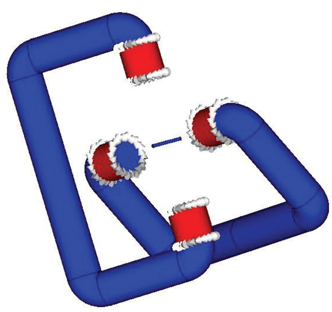

(a)

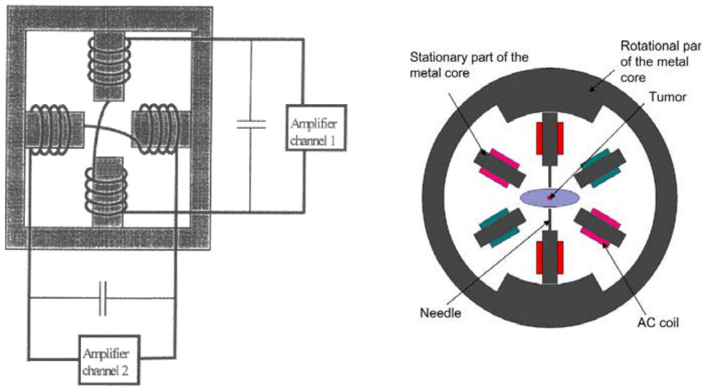


(b) (c)

Fig 2.9 Multiple direct pair coils, excited by (a) synchronised current sources (Huang *et al*. 2010), (b) current sources displaced by a quadrant (Gray & Jones 2000) and (c) switched reluctance of a rotating ring (Ho *et al*. 2012a).

For adapting to the body's anatomy, the skewed coils may be broken up into several coils, hence the multiple skewed pair coils (Gronmeyer *et al*. 2009) with near diametric skew angle as shown in Fig 2.10. However, as with the singular skewed pair coils, they are only suitable for protruded, short-ranged, local targets.

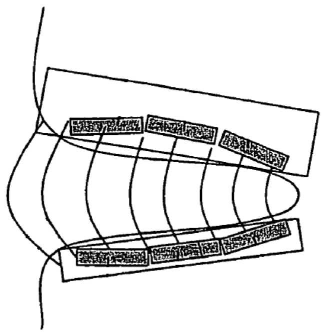

Fig 2.10 Multiple skewed pair coils with near diametric skew angle (Gronmeyer *et al*. 2009).

**2.3 Local Field Concentrator and Attractors**

Magnetic field acting on ferromagnetic material can influence magnetic dipoles to produce nett magnetisation which then augments the surrounding magnetic field. Therefore, by placing ferromagnetic material in proximity to the target space, its local surrounding magnetic field can be increased (Feucht *et al*. 2011) as illustrated in Fig 2.11(a). By selecting the appropriate sized ferromagnetic concentrator, the area exposed to high magnetic field can be confined. However, due to its short-ranged effect, this method cannot work well if the target and the ferromagnetic concentrator are spaced too far apart. Therefore, the ferromagnetic concentrator has to be implanted into the body near the target or inserted into accessible cavities or ducts such as the rectum for treating prostate cancer, thus limiting treatment flexibility. After the treatment is over, the concentrator has to be removed and in the case of implants, invasive surgery is required for both pre- and post-treatments.

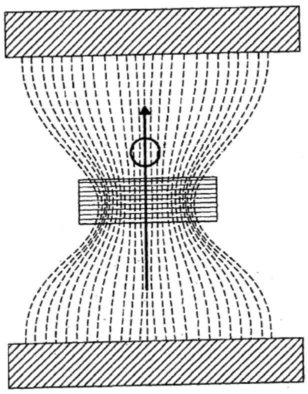

(a)

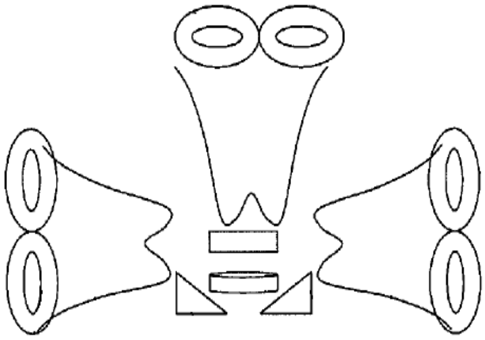

(b)

Fig 2.11 Local field (a) concentrators (Feucht *et al*. 2011) and (b) attractors (Mishelevich & Schneider 2009).

The ferromagnetic material can also act as an attractor, resulting in a higher magnetic flux density at the target space, provided the target lies along the magnetic flux path from the pole to the attractor (Mishelevich & Schneider 2009) as illustrated in Fig 2.11(b). In this application, the attractors are placed in the patient's oral cavity to direct the field pattern from the loop coils on the skull cap. Similar to the case of concentrators, its effect is short-ranged and therefore, the field convergence effect diminishes when the target and the attractors are spaced too far apart. Thus, its application is confined to organs with a limited span such as the brain.

## 2.4 Field Saturation Applicators

When a ferromagnetic material is subjected to a low power AC magnetic field, superimposed by a comparatively stronger constant magnetic field of sufficient level to saturate its magnetic flux, the heating effect diminishes as the loop integral of Eq 1.1 becomes small when $B$ is saturated even as $H$ varies. Therefore, in the presence of an AC magnetic field, a strong constant magnetic field can be superimposed in selected regions of the ferromagnetic material where heating is not desired.

By modulating the excitation current of 3 pairs of coils arranged orthogonally to each other, such regions can be created (Gleich 2008) as illustrated in Fig 2.12(a). In this design, another adjacent pair of coils superimposes an AC magnetic field for heating the desired region in the ferromagnetic material. In another design illustrated in Fig 2.12(b), 6 pairs of coils are arranged in a circular ring to create the same effect (Ho *et al*. 2012b).

While the orthogonal coils are simpler to use than the ring coils, this advantage is lost if the ferromagnetic material is concentrated on the tumour, with little ferromagnetic material in the non-treated regions. Above all, the eddy current heating drawback is not mitigated, thus limiting its heating efficacy.

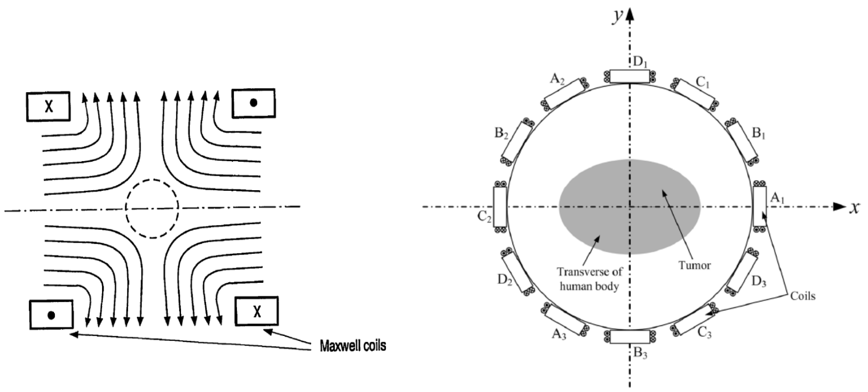


(a) (b)

Fig 2.12 Field saturation applicators where the coils are arranged (a) orthogonally (Gleich 2008) and (b) in a circle (Ho *et al*. 2012b).

**2.5 Research Trajectory**

At the current state of the art, the most promising method is the direct applicator method, judging from the myriad of applicators arising from it. Within the direct applicator method, all 3 coil geometries have shown their potential use. In order to simplify further analyses, only the singular coil configuration will be considered. In-core coils will not be considered as they do not meet the objective of focusing the magnetic field on the target.

In order to achieve field penetration, the gapped core offers the best option and this is evident in the applicators under this option. Again, in order to simplify further analyses, only the direct pair method will be considered.

Fig 2.13 shows a tree diagram, summarising the state of the art in applicator design. It also highlights the selected methods for further investigation.

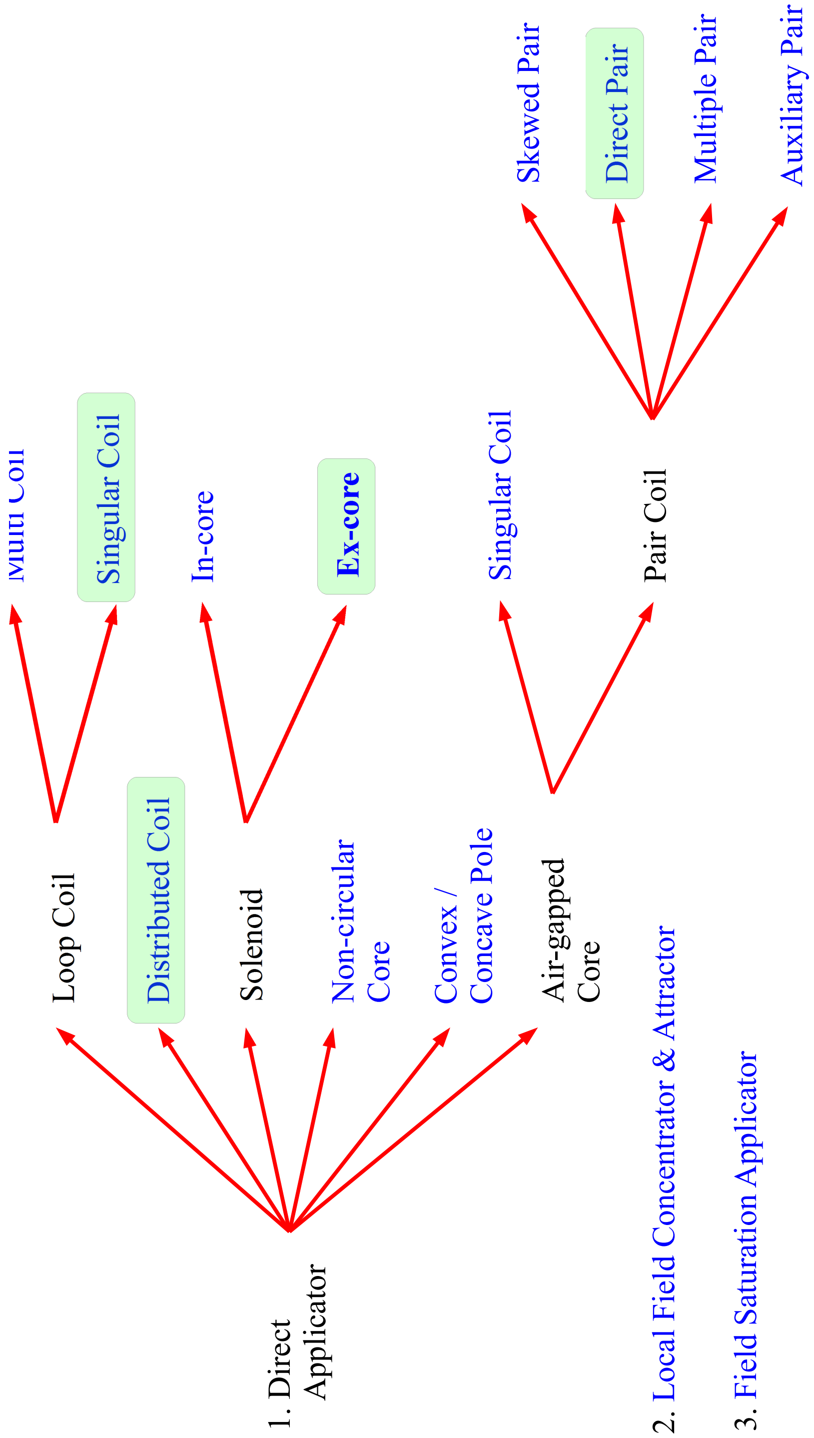


Fig 2.13 Summary of state of the art in applicator design. The selected areas for further analyses are highlighted.

# CHAPTER 3

# ANALYSIS OF 2D MODELS

## 3.1 Background

The 3 main coil geometries identified in the literature review: loop coil, distributed coil and the solenoid will be modelled mathematically in order to provide insight into their characteristics pertaining to field penetration and focusing. The performance of coils combined as a gapped core applicator will then be explored. From this analysis, design decisions in regard to the configuration and parameters will be made.

For this exploratory purpose, 2D analytical models will be developed where current sheets and paths of infinite depth with current flowing into and out of the page will be used to represent the actual coils.

Throughout this chapter, the $\boldsymbol{y}$ axis is taken as the upwards vertical axis and the $\boldsymbol{x}$ axis the horizontal axis towards the right of the page. Also, the point where the current sheet profile intersects the $\boldsymbol{y}$ axis is taken to be the origin $(\boldsymbol{x},\boldsymbol{y}) = (0,0)$. In a related definition, the normalised field strength is the field strength normalised with respect to that at the origin. For dimension normalisations, the distance $\boldsymbol{b}$ is used as the base dimension.

## 3.2 Field Penetration of Different Coil Geometries

In representing the solenoid, 2 parallel current sheets of equal but opposing current density $\boldsymbol{J}$ with breadth $\boldsymbol{l}$, spaced by a distance of $\boldsymbol{2b}$ as shown in Fig 3.1 are considered.

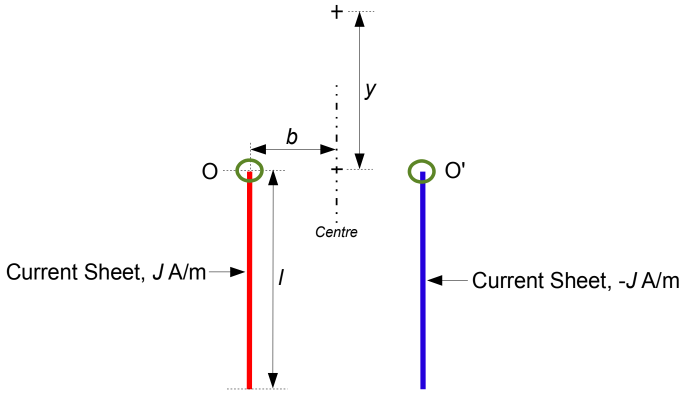


Fig 3.1 Parallel current sheets representing a solenoid.

The magnetising field strength at the field point of distance ***y*** from the origin along the ***y*** axis due to these parallel current sheets is derived in Appendix A.2 using Ampere's law and shown to be:

$$H = \frac{J}{\pi}\left(\tan^{-1}\frac{y+l}{b} - \tan^{-1}\frac{y}{b}\right) \quad (3.1)$$

Supposing the current sheets are now rotated 90º clockwise and anti-clockwise around the **O** and **O'** ends of the respective current sheets in order to represent a distributed planar coil. The resultant geometry is thus the distributed planar current sheets as shown in Fig 3.2.

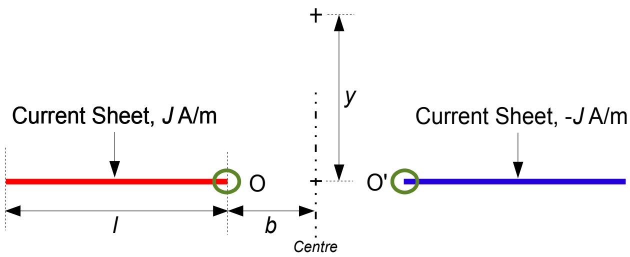


Fig 3.2 Distributed planar current sheets representing a distributed planar coil.

The magnetising field strength at the field point of distance ***y*** from the origin along the ***y*** axis due to these planar current sheets is derived in Appendix A.3 and shown to be:

$$H = \frac{J}{\pi}\ln\frac{y^2+(b+l)^2}{y^2+b^2} \quad (3.2)$$

The normalised field strength values of Eqs 3.1 and 3.2 are plotted as shown in Fig 3.3 for $l/b = 1$ in order to compare their field penetration effect.

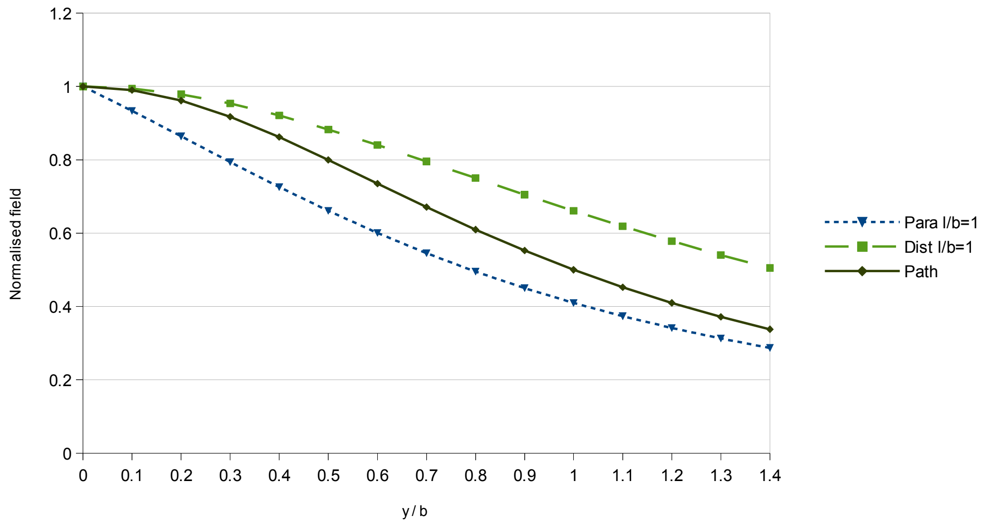


Fig 3.3 Field penetration along the $y$ axis of various current flow geometries at $l / b = 1$.

Fig 3.3 shows that the field penetration of distributed planar current sheets is better than that of parallel current sheets. Contributing to this is the fact that the separation distance between the field points and the current source of distributed planar current sheets is shorter than that of parallel current sheets. In an attempt to produce even better field penetration, this separation distance is further shortened by concentrating the total current of each current sheet to points $O$ and $O'$ respectively, forming parallel current paths. This representation of a loop coil is shown in Fig 3.4.

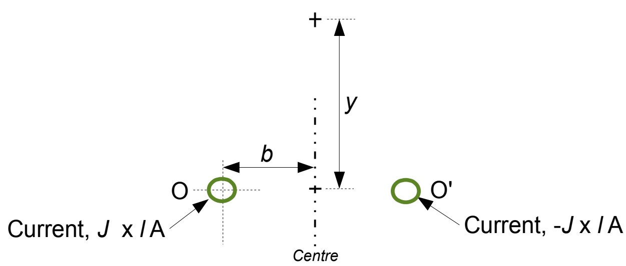


Fig 3.4 Parallel current paths representing a loop coil.

The magnetising field strength at the field point of distance $\boldsymbol{y}$ from the origin along the $\boldsymbol{y}$ axis, due to these parallel current paths is derived in Appendix A.4 and shown to be:

$$H=\frac{J}{\pi}\frac{lb}{(y^2+b^2)} \tag{3.3}$$

The normalised field strength in Eq 3.3 is plotted as shown in Fig 3.3 for comparison with that of the other current sheets. Although the separation distance between the field points and its current source is lesser, the field penetration of parallel current paths is only better than that of parallel current sheets but inferior to that of distributed planar current sheets. This is because in distributed planar current sheets, the magnetic field due to the spatially distributed current source mutually reinforce vectorially such that its field penetration is the farthest.

Interpreted in coil geometry equivalents, the normalised field strength values of Eqs 3.1, 3.2 and 3.3 are compared in Fig 3.5 at normalised breadths of $\boldsymbol{l/b}$ = 0.6, $\boldsymbol{l/b}$ = 1.0 and $\boldsymbol{l/b}$ = 1.4 where applicable.

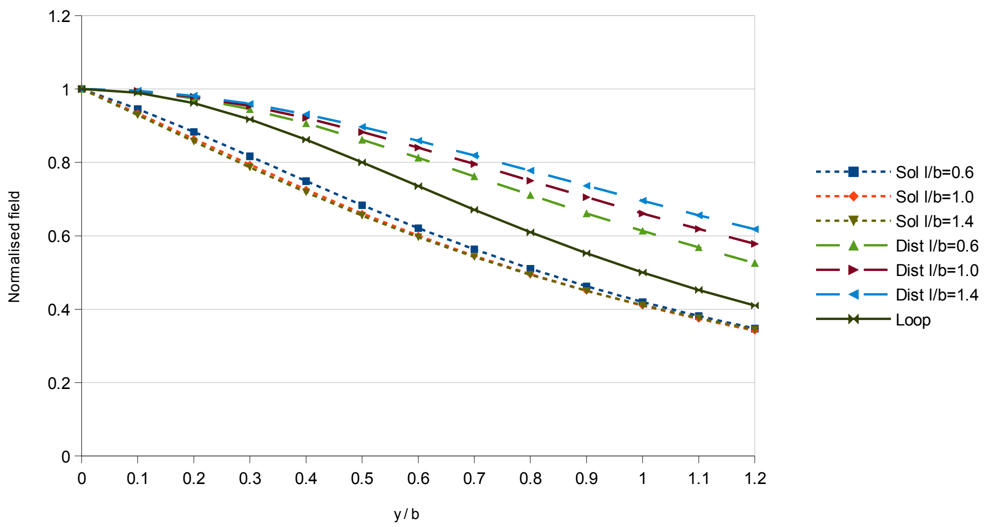


Fig 3.5 Field penetration along the $\boldsymbol{y}$ axis of various coil geometries at various normalised breadths.

It can be seen that the distributed planar coil yields the farthest field penetration across different coil breadths. In addition, the broader the coil, the farther is the field penetration and this is markedly so for the distributed planar coil. For this reason, the distributed planar coil is selected for further investigation.

The equivalent models with a finite current sheet thickness of 0.05$\boldsymbol{b}$ were simulated with FEMM© using the block scripts described in Appendices C.1 to C.3 and the simulated magnetising field along the $\boldsymbol{y}$ axis is compared with that calculated by Eqs 3.1, 3.2 and 3.3 as shown in Fig 3.6.

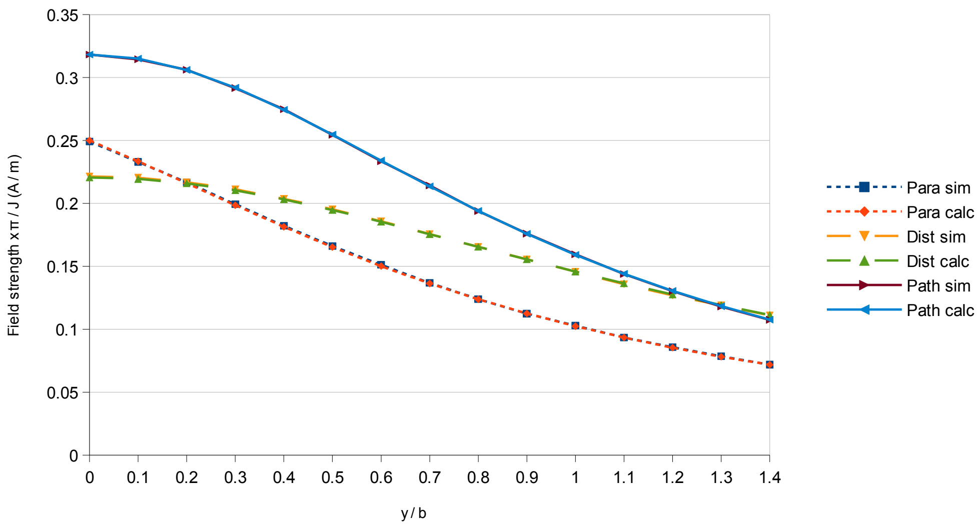


Fig 3.6 Field penetration along the $\boldsymbol{y}$ axis comparison between the calculated and simulated values for various current flow geometries.

The close agreement between the simulated and calculated values lends credibility to the analytical models as a tool to study field penetration along the $\boldsymbol{y}$ axis.

### 3.3 Focusing Effect of the Distributed Planar Sheets

In order to get an insight of the focusing effect of the distributed planar current sheets, the field point **on** the current sheet along the ***x*** axis of the distributed planar sheet at a distance ***m*** from the ***y*** axis as shown in Fig 3.7 is considered.

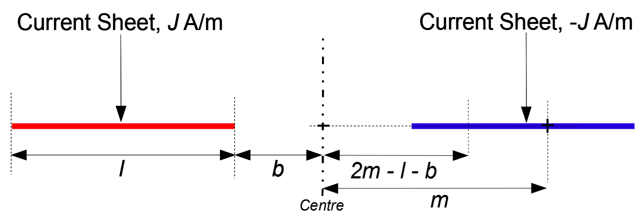


Fig 3.7 Field point **on** the distributed planar current sheets.

The magnetising field strength at this point (***m***,0) is derived in Appendix A.5 and shown to be:

$$H = \frac{J}{2\pi} \ln\left[\frac{(b+l)^2 - m^2}{(m^2 - b^2)}\right], \qquad b < m < b+l \tag{3.4}$$

Fig 3.8 shows the magnetising field strength along the ***x*** axis given by Eq 3.4 for ***l*** / ***b*** = 1.

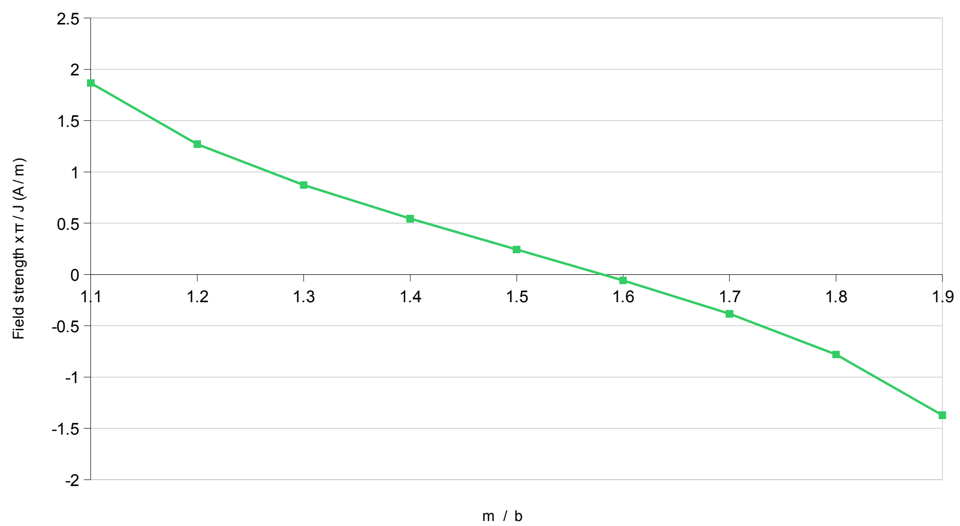


Fig 3.8 Magnetising field strength **on** the distributed planar current sheets at ***l*** / ***b*** = 1.

As shown in Fig 3.8, the magnetic field drops to a null point within the breadth of the current sheet before reaching the far edge of the current sheet at $\boldsymbol{x} = \boldsymbol{l} + \boldsymbol{b}$. This null point at $\boldsymbol{x} = \boldsymbol{m}_0$ as derived in Appendix A.5 is shown to be:

$$m_0 = \sqrt{\frac{b^2 + (b+l)^2}{2}} \tag{3.5}$$

This is a consequence of the Biot-Savart law where the field due to the current element of one limb at $\boldsymbol{x} \in (\boldsymbol{m}_0, \boldsymbol{l}+\boldsymbol{b})$ is cancelled out by the field due to the current element of the same limb at $\boldsymbol{x} \in (2\boldsymbol{m}_0-\boldsymbol{l}-\boldsymbol{b}, \boldsymbol{m}_0)$. The field due to the current element in the remaining section of the limb at $\boldsymbol{x} \in (\boldsymbol{b}, 2\boldsymbol{m}_0-\boldsymbol{l}-\boldsymbol{b})$ is cancelled by the field due to the current element at the other limb at $\boldsymbol{x} \in (-\boldsymbol{b}, -\boldsymbol{l}-\boldsymbol{b})$. Such an effect tends to vanish in the parallel current sheets and parallel current paths where $\boldsymbol{b} >> \boldsymbol{l}$. This phenomena suggests that field focusing is possible on distributed planar current sheets. It also suggests that by curving the distributed current sheets, thus bringing the null field points of both limbs closer, it is possible to improve upon the field focusing property.

### 3.4 Curved Distributed Coils

To investigate the characteristics of curved distributed coils, both concave and convex distributed coils are considered. These coils will be analysed for both their field penetration and field focusing properties using the distributed current sheet representations.

#### 3.4.1 Field Penetration of Curved Distributed Coils

The distributed planar current sheets as shown in Fig 3.2 are curved upwards at both its limbs to become concave distributed current sheets as shown in Fig 3.9(a).

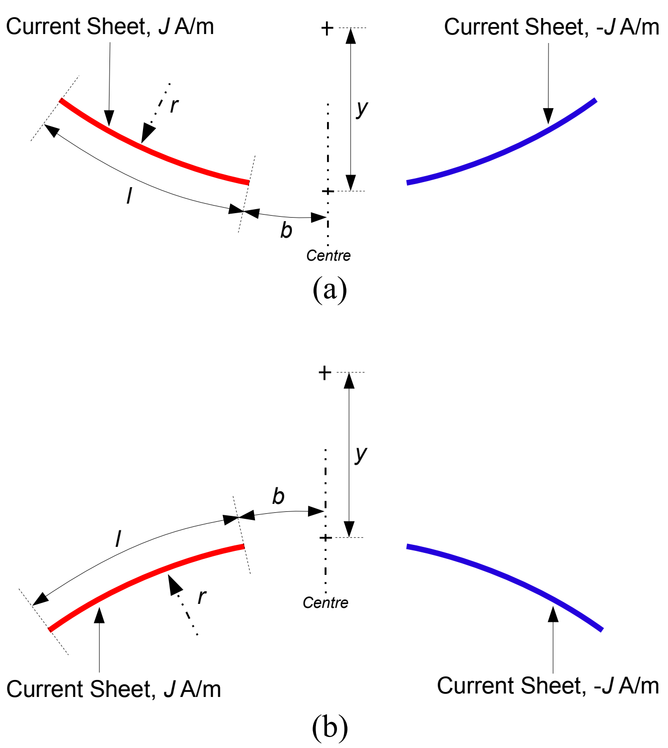


Fig 3.9 (a) Concave and (b) convex distributed current sheets, showing the field point along the ***y*** axis.

The magnetising field strength at the field point of distance ***y*** from the origin along the ***y*** axis due to these concave distributed current sheets is derived in Appendix A.6 and shown to be:

$$H = \frac{J}{2\pi(1-\frac{y}{r})} \ln\left[\frac{1+(1-\frac{y}{r})^2 - 2(1-\frac{y}{r})\cos\frac{b+l}{r}}{1+(1-\frac{y}{r})^2 - 2(1-\frac{y}{r})\cos\frac{b}{r}}\right] \qquad (3.6)$$

where ***r*** is the radius of curvature. Similarly, when the distributed planar current sheets as shown in Fig 3.2 are being curved downwards at both its limbs to become convex distributed current sheets as shown in Fig 3.9(b), the corresponding magnetising field strength at the field point of distance ***y*** from the origin along the ***y*** axis is derived in Appendix A.7 and shown to be:

$$H = \frac{J}{2\pi(1+\frac{y}{r})} \ln\left[\frac{1+(1+\frac{y}{r})^2 - 2(1+\frac{y}{r})\cos\frac{b+l}{r}}{1+(1+\frac{y}{r})^2 - 2(1+\frac{y}{r})\cos\frac{b}{r}}\right] \tag{3.7}$$

Interpreted in coil geometry equivalents, the effect of both ***l*** and ***r*** on the field penetration is investigated for the planar, concave and convex distributed coils by comparing the field plots along the ***y*** axis using Eqs 3.2, 3.6 and 3.7.

a) The effect of ***r*** is investigated by maintaining ***l*** / ***b*** = 1 and the field penetration of planar, concave and convex distributed coils along the ***y*** axis are compared in Fig 3.10 for ***r*** / ***b*** = 1.6, ***r*** / ***b*** = 2.0 and ***r*** / ***b*** = 2.4.

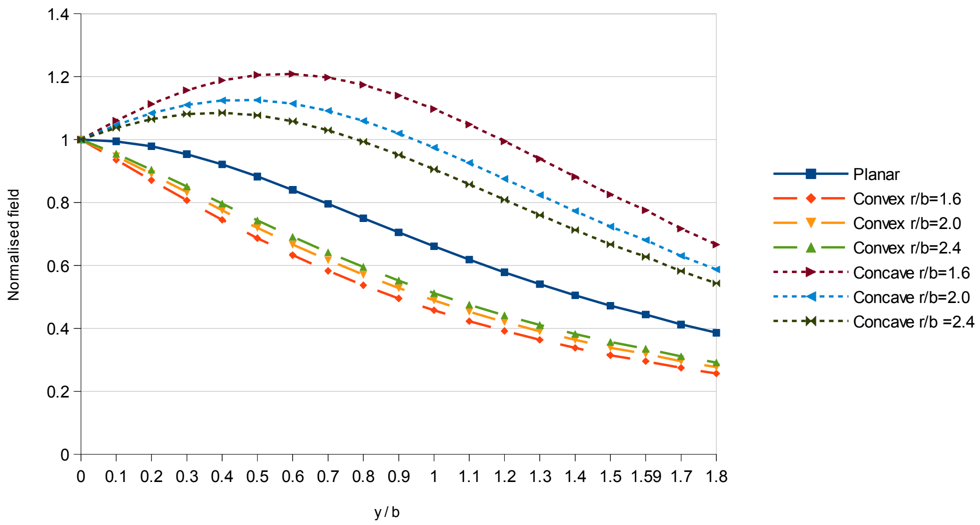


Fig 3.10 Field penetration of planar, concave and convex distributed coils for various curvatures at ***l*** / ***b*** = 1.

As expected, when the coil is curved towards the field point in the concave distributed coil, this proximity facilitates a farther field penetration. The contrary holds true for the convex distributed coil. For the same reason, reducing ***r*** increases the field penetration of the concave distributed coil and the contrary holds true for the convex distributed coil.

However, with a higher field gradient near the field point as a consequence of the Biot-Savart law, the field penetration of the concave distributed coil is more sensitive to variations of $\boldsymbol{r}$ than that of the convex distributed coil. This makes the convex distributed coil more amenable to construction variations.

b) Similarly, by maintaining $\boldsymbol{r} / \boldsymbol{b} = 2$ for the curved distributed coils, the effect of $\boldsymbol{l}$ on the field penetration is investigated. The field penetration of planar, concave and convex distributed coils for $\boldsymbol{l} / \boldsymbol{b} = 0.6$, $\boldsymbol{l} / \boldsymbol{b} = 1.0$ and $\boldsymbol{l} / \boldsymbol{b} = 1.4$ are shown in Fig 3.11.

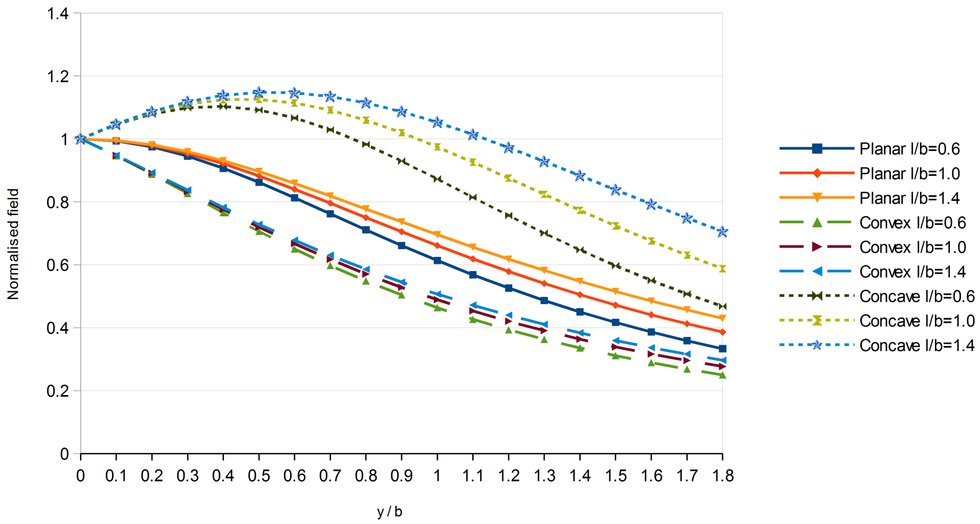


Fig 3.11 Field penetration of planar, concave and convex distributed coils for various breadths at $\boldsymbol{r} / \boldsymbol{b} = 2$ for the curved distributed coils.

The concave distributed coil again maintains its superior field penetration, but due to a higher field gradient near the field point, its field penetration is more sensitive to breadth variations. Nonetheless, increasing the breadth improves the field penetration for all 3 coil geometries.

### 3.4.2 Field Focusing of Curved Distributed Coils

Based on the earlier planar, concave and convex distributed current sheets, Fig 3.12 shows the field points for the purpose of investigating their field focusing characteristics.

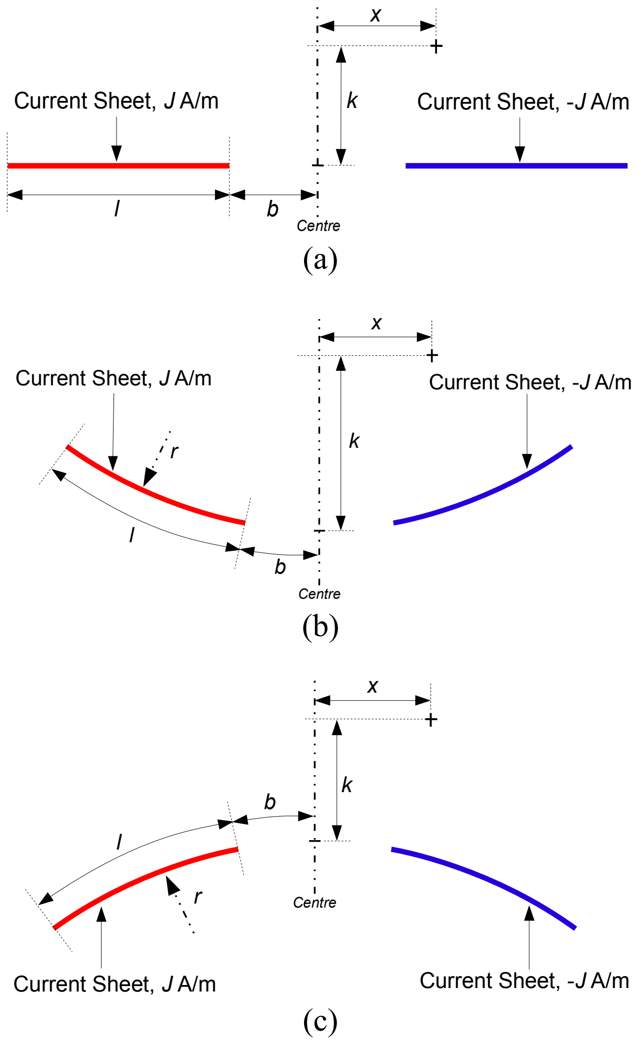


Fig 3.12 (a) Planar, (b) concave and (c) convex distributed current sheets showing the field points at distance $\boldsymbol{x}$ from the $\boldsymbol{y}$ axis and $\boldsymbol{k}$ from the $\boldsymbol{x}$ axis.

Considering the magnetising field strength at the field point of distance $\boldsymbol{x}$ from the $\boldsymbol{y}$ axis and $\boldsymbol{k}$ from the $\boldsymbol{x}$ axis, $(\boldsymbol{x},\boldsymbol{k})$, the $\boldsymbol{y}$ component of this magnetising field due to the planar distributed current sheets is derived in Appendix A.8 and shown to be:

$$H_y = \frac{J}{4\pi} \ln \left[ \frac{(k^2+(b+l-x)^2)(k^2+(b+l+x)^2)}{(k^2+(b-x)^2)(k^2+(b+x)^2)} \right] \tag{3.8}$$

Similarly, the ***y*** component of the magnetising field strength at the field point (***x***,***k***) for both concave and convex distributed current sheets is derived in Appendices A.9 & A.10 and shown to be:

$$\begin{aligned} H_y = & Kv \ln\left( \frac{r^2+d^2-2rv\cos\left(\frac{(b+l)}{r}\right)-2rx\sin\left(\frac{(b+l)}{r}\right)}{r^2+d^2-2rv\cos\frac{b}{r}-2rx\sin\frac{b}{r}} \right) \\ & + Kv \ln\left( \frac{r^2+d^2-2rv\cos\left(\frac{(b+l)}{r}\right)+2rx\sin\left(\frac{(b+l)}{r}\right)}{r^2+d^2-2rv\cos\frac{b}{r}+2rx\sin\frac{b}{r}} \right) \\ & + 2Kx\tan^{-1}\left( \frac{r^2+d^2+2rv\tan\left(\frac{(b+l)}{2r}\right)-2rx}{r^2-d^2} \right) \\ & - 2Kx\tan^{-1}\left( \frac{r^2+d^2+2rv\tan\left(\frac{b}{2r}\right)-2rx}{r^2-d^2} \right) \\ & - 2Kx\tan^{-1}\left( \frac{r^2+d^2+2rv\tan\left(\frac{(b+l)}{2r}\right)+2rx}{r^2-d^2} \right) \\ & + 2Kx\tan^{-1}\left( \frac{r^2+d^2+2rv\tan\left(\frac{b}{2r}\right)+2rx}{r^2-d^2} \right) \end{aligned} \tag{3.9}$$

where

$$K = \frac{Jr}{4\pi d^2}$$

$$v = \begin{cases} r-k & \text{for the concave distributed current sheets} \\ r+k & \text{for the convex distributed current sheets} \end{cases}$$

$$d = \sqrt{v^2+x^2}$$

By inspection of Fig 3.12, ***v*** represents the distance between the ***y*** = ***k*** line to the centre of the curvature and ***d*** represents the distance between the field point (***x***,***k***) to the centre of the curvature.

Interpreted as coil geometry equivalents, the effect of $\boldsymbol{l}$ and $\boldsymbol{r}$ on the field focusing effect is investigated for the planar, concave and convex distributed coils using Eqs 3.8 and 3.9 at various distances $\boldsymbol{k}$ from the origin by comparing the $\boldsymbol{y}$ component of the magnetising field along the $\boldsymbol{y} = \boldsymbol{k}$ line. As will be shown in the subsequent sections, 2 similar coils will be combined symmetrically along the $\boldsymbol{y} = \boldsymbol{k}$ line to form a gapped core applicator, thus cancelling the $\boldsymbol{x}$ component of the field along this line. Thus, only the $\boldsymbol{y}$ component needs to be considered. For the purpose of comparing the focusing effect, the half power beam width (HPBW) metric - defined as the width along the $\boldsymbol{y} = \boldsymbol{k}$ line where $H_y > H_y(0,\boldsymbol{k}) / \sqrt{2}$ - will be used.

(a) The effect of $\boldsymbol{r}$ is investigated by maintaining $\boldsymbol{l} / \boldsymbol{b} = 1$. Using by Eqs 3.8 and 3.9, the $\boldsymbol{y}$ component of the magnetising field strength values of planar, concave and convex distributed coils for $\boldsymbol{r} / \boldsymbol{b} = 1.6$, $\boldsymbol{r} / \boldsymbol{b} = 2.0$ and $\boldsymbol{r} / \boldsymbol{b} = 2.4$ under 3 different separation distances of $\boldsymbol{k} / \boldsymbol{b} = 0.6$, $\boldsymbol{k} / \boldsymbol{b} = 1.0$ and $\boldsymbol{k} / \boldsymbol{b} = 1.4$ from the origin are shown in Figs 3.13(a), 3.13(b) and 3.13(c) respectively.

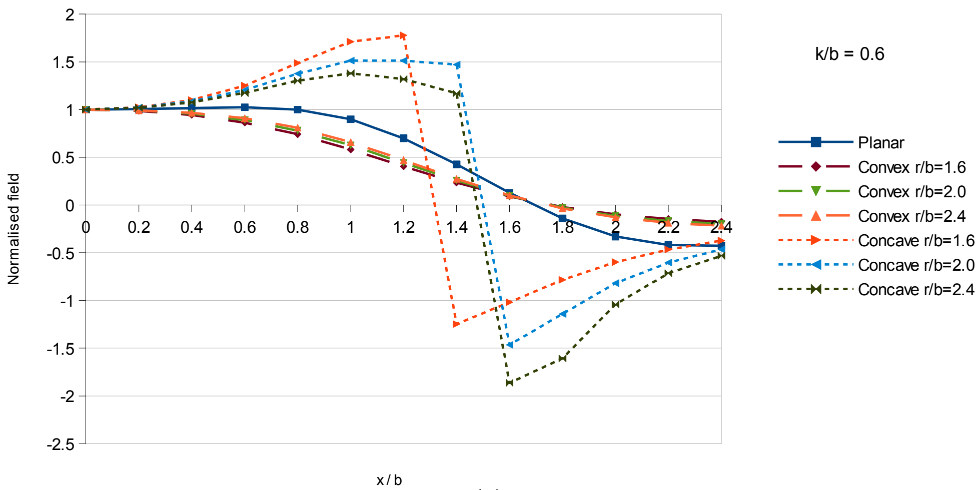


(a)

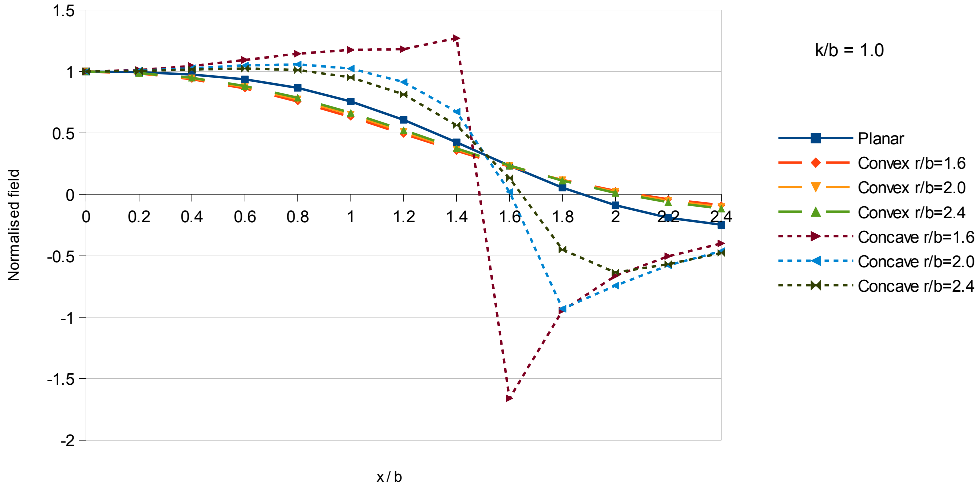


(b)

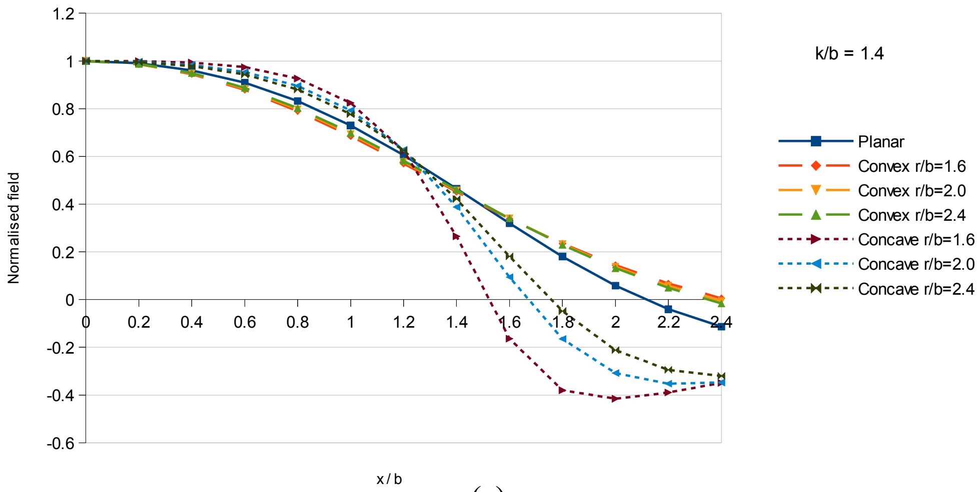


(c)

Fig 3.13 The $\boldsymbol{y}$ component of the field strength of planar, concave and convex distributed coils with $\boldsymbol{l} / \boldsymbol{b} = 1$ for various $\boldsymbol{r} / \boldsymbol{b}$ at (a) $\boldsymbol{k} / \boldsymbol{b} = 0.6$, (b) $\boldsymbol{k} / \boldsymbol{b} = 1.0$ and (c) $\boldsymbol{k} / \boldsymbol{b} = 1.4$.

Due to the geometry of the concave distributed coil, the current limbs are bent nearer towards the field point along the $\boldsymbol{y} = \boldsymbol{k}$ line and this proximity tends to sustain a higher field strength throughout the breadth along the $\boldsymbol{y} = \boldsymbol{k}$ line, hence the poorer field focusing and higher HPBW, particularly at near $\boldsymbol{k}$ and small $\boldsymbol{r}$. This proximity also renders the field along the $\boldsymbol{y} = \boldsymbol{k}$ line to be sensitive to changes in $\boldsymbol{r}$, especially near the current source. The very curvature of the concave distributed coil also limits the breadth span of the field point, especially near the origin under small $\boldsymbol{r}$ such that the line $\boldsymbol{y} = \boldsymbol{k}$ may cut through the coil limbs, causing an abrupt change of field direction as shown in Figs 3.13(a) and 3.13(b). In addition, upon crossing the null point, the higher field gradient of the concave distributed coil also renders a sharper focus effect, especially at near $\boldsymbol{k}$ and small $\boldsymbol{r}$ as shown in Figs 3.13(b) and 3.13 (c).

The contrary holds true for the convex distributed coil where the coil limbs diverge away from the field point. Although only marginally, its HPBW decreases as $\boldsymbol{r}$ decreases, contrary to that of the concave distributed coil. This insensitivity implies that $\boldsymbol{r}$ can be freely selected during the design process. Although the HPBW of the convex distributed coil is the best among the 3 coil geometries, this advantage tends to diminish as the distance from the origin increases beyond $\boldsymbol{k} / \boldsymbol{b} > 1.4$ as shown in Fig 3.13(c).

(b) Similarly, the effect of $\boldsymbol{l}$ is investigated by maintaining $\boldsymbol{r} / \boldsymbol{b} = 2$, using Eqs 3.8 and 3.9 for $\boldsymbol{l} / \boldsymbol{b} = 0.6$, $\boldsymbol{l} / \boldsymbol{b} = 1.0$ and $\boldsymbol{l} / \boldsymbol{b} = 1.4$ under 3 different separation distances of $\boldsymbol{k} / \boldsymbol{b} = 0.6$, $\boldsymbol{k} / \boldsymbol{b} = 1.0$ and $\boldsymbol{k} / \boldsymbol{b} = 1.4$ from the origin and their plots are shown in Figs 3.14(a), 3.14(b) and 3.14(c) respectively.

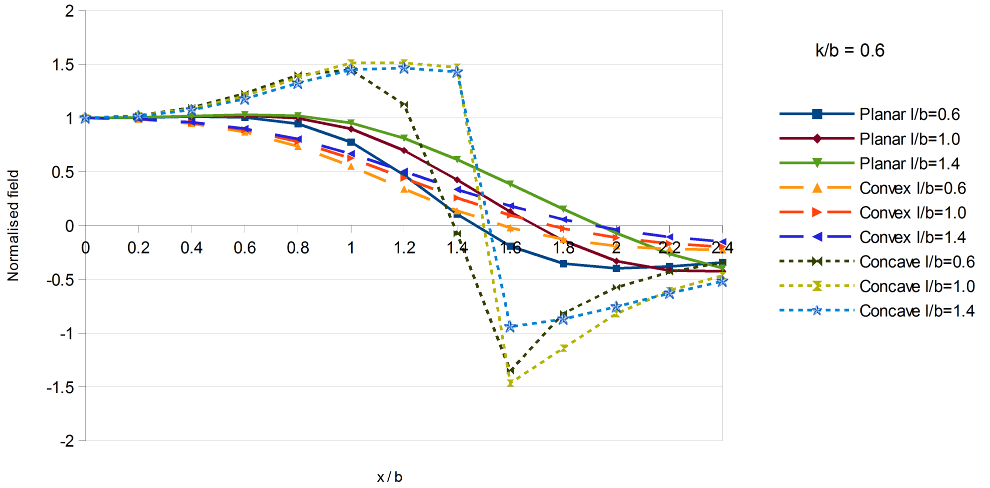


(a)

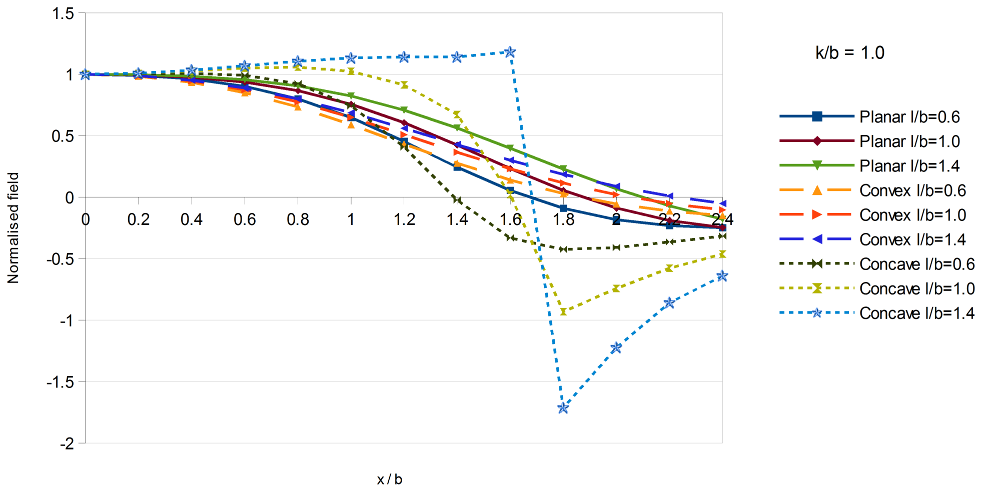


(b)

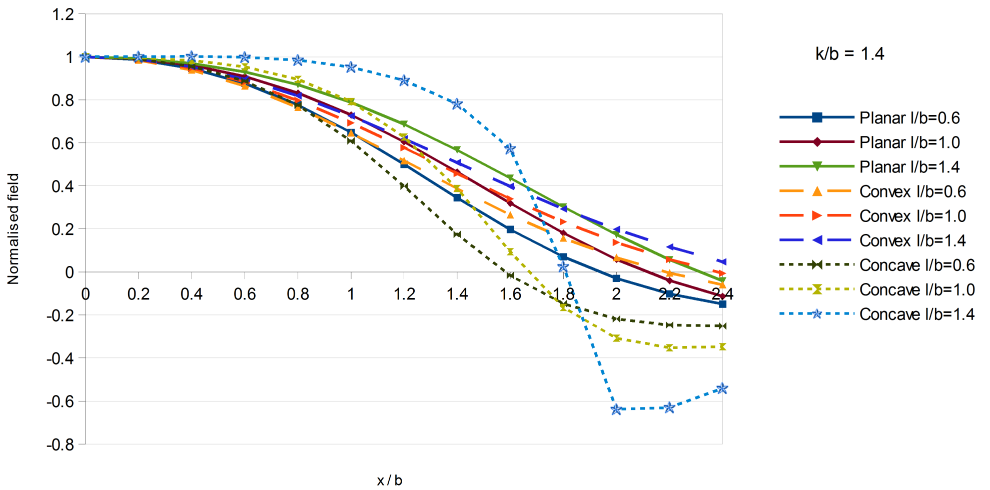


(c)

Fig 3.14 The ***y*** component of the field strength of planar, concave and convex distributed coils with ***r*** / ***b*** = 2 for various ***l*** / ***b*** at (a) ***k*** / ***b*** = 0.6, (b) ***k*** / ***b*** = 1.0, and (c) ***k*** / ***b*** = 1.4.

Although the concave distributed coil demonstrates a sharp focusing effect, its magnetising field and thus field focusing is more sensitive to changes in $\boldsymbol{l}$ due to the proximity of the current source at the field point. In contrast, the focusing effect of the convex distributed coil is less sensitive to changes in $\boldsymbol{l}$ because of the increasing separation distance between the field point and the current source as the field point extends out from the $\boldsymbol{y}$ axis. This insensitivity accords more freedom in choosing $\boldsymbol{l}$ during the design process.

All 3 distributed coils exhibit higher HPBW as the $\boldsymbol{l}$ increases. The reason for this is as $\boldsymbol{l}$ increases, the current source of the coil limbs stretches out farther from the $\boldsymbol{y}$ axis and thus, is able to sustain the field farther out from the $\boldsymbol{y}$ axis. With the lesser decay of the field strength along the $\boldsymbol{y} = \boldsymbol{k}$ line, the focusing effect also deteriorates.

Due to the geometry of the convex distributed coil, the increase in separation distance between the field point and the current source is hastened as the field point stretches out from the $\boldsymbol{y}$ axis, hence the quicker field decay along the $\boldsymbol{y} = \boldsymbol{k}$ line and its lower HPBW. However, this advantage tends to diminish beyond $\boldsymbol{k} / \boldsymbol{b} > 1.4$ as shown in Fig 3.14(c) when the distance from the field point to the origin becomes significant compared to the coil dimensions.

Overall, the choice of $\boldsymbol{r}$ is a compromise between field penetration and field focus, going in opposite directions for concave and convex distributed coils. Similarly, decreasing $\boldsymbol{l}$ reduces HPBW but this also reduces the field penetration for all 3 coil geometries. Therefore, for the purpose of expediency and balance, the ***l*** / ***b*** and ***r*** / ***b*** ratios are selected as 1.0 and 2.0 respectively in subsequent investigations.

(c) To compare the focusing effect of each coil geometry, Eqs 3.8 and 3.9 are used to plot the ***y*** component of the magnetising field at ***k*** / ***b*** = 0.6, ***k*** / ***b*** = 1.0 and ***k*** / ***b*** = 1.4 at ***l*** / **b** = 1 and ***r*** / ***b*** = 2 for the planar, concave and convex distributed coils as shown in Figs 3.15(a), 3.15(b) and 3.15(c) respectively.

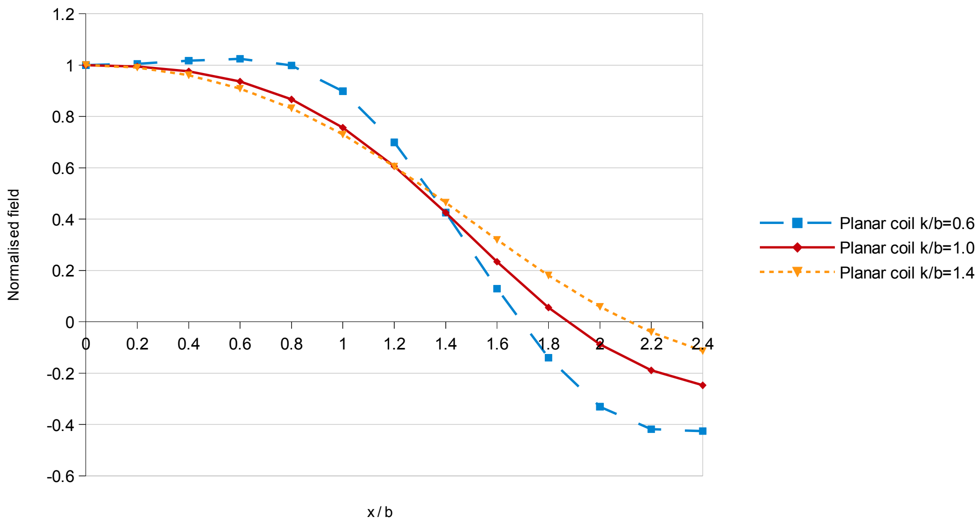


(a)

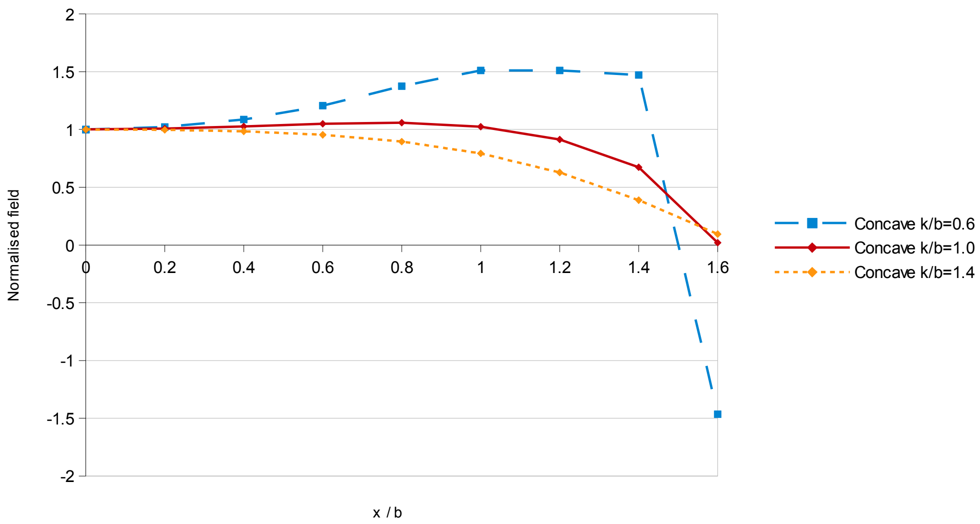


(b)

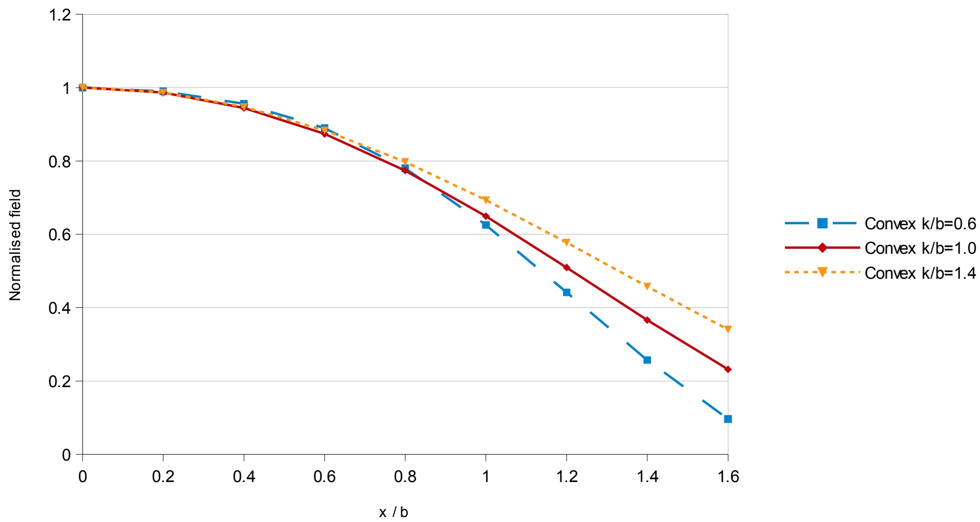


(c)

Fig 3.15 The ***y*** component of the field strength at ***r*** / ***b*** = 2, ***l*** / ***b*** = 1 at various ***k*** / ***b*** for (a) planar, (b) concave and (c) convex distributed coils.

Among the 3 coil geometries, the convex distributed coil has the most stable field focusing effect across different separation distances ***k*** from the origin, deteriorating only slightly as ***k*** increases as shown in Fig 3.15(c). On the other hand, the HPBW for both planar and concave distributed coils are broad near the origin. However, their HPBWs improve as the field point gets farther from the origin as ***k*** increases, especially that of the concave distributed coil.

For validation purpose, equivalent models with a finite current sheet thickness of 0.05***b*** were simulated with FEMM© using the block scripts described in Appendices C.2 and C.4. Based on ***r*** / ***b*** = 2 and ***l*** / ***b*** = 1, the simulated ***y*** component of both the magnetising field along the ***y*** axis and the magnetising field along the ***y*** = ***k*** = ***b*** line are compared with that calculated by Eqs 3.2 and 3.6 to 3.9 as shown in Figs 3.16(a) and 3.16(b) respectively.

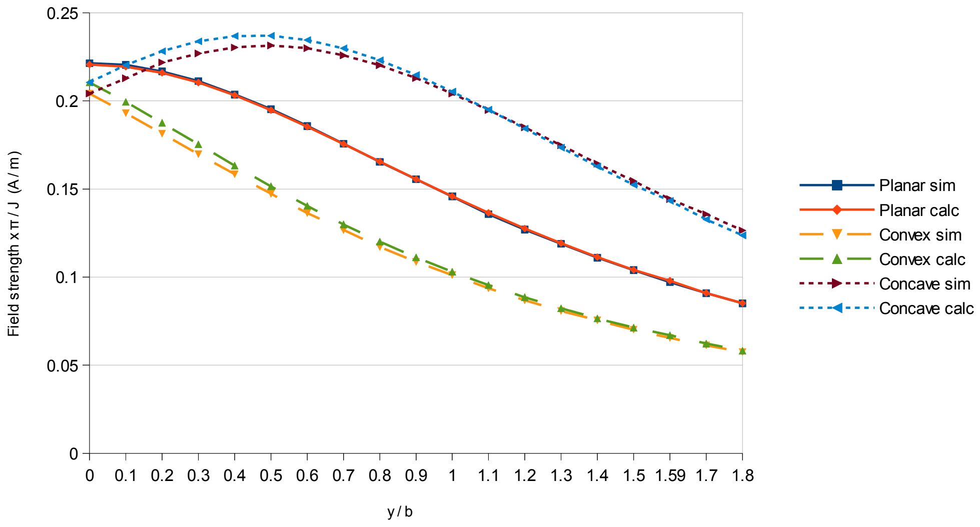


(a)

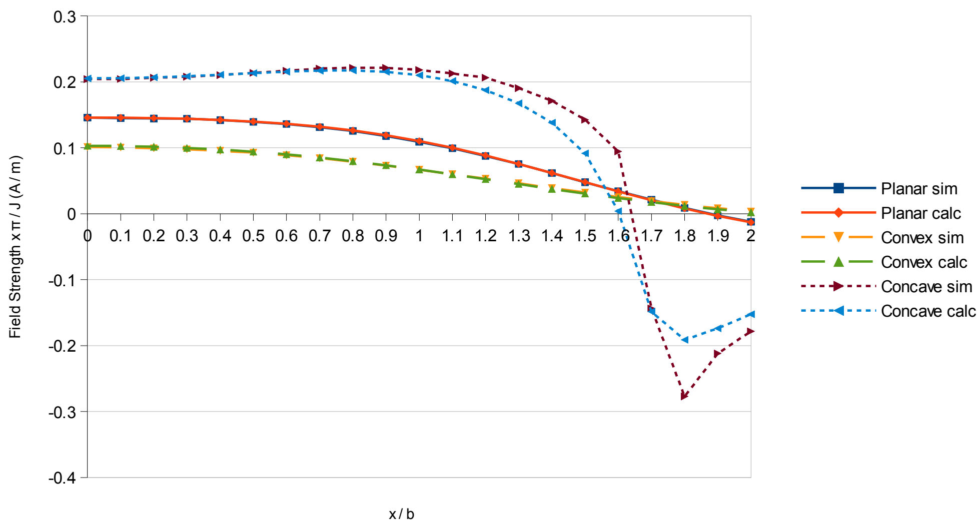


(b)

Fig 3.16 Comparison of (a) field penetration along the $\boldsymbol{y}$ axis and (b) field focusing along the $\boldsymbol{y} = \boldsymbol{k} = \boldsymbol{b}$ line between the calculated and simulated values for various current sheet geometries.

The simulated values near the current source differ slightly from the calculated values due to the finite thickness of current sheets used in the simulation models. As the field point gets farther from the current source, this thickness becomes dimensionally insignificant, hence the close agreement. Overall, the good agreement between the simulated and calculated values lends credibility to the analytical models and the conclusions drawn thus far.

### 3.5 Coil Aggregation

In order to form the gapped core applicator, 2 similar coils are positioned symmetrically such that their poles face each other, separated by a gap, 2$\boldsymbol{p}$ with the $\boldsymbol{y}$ component of their respective magnetising field reinforcing constructively in the area between the coils, identified as the target space. Since the symmetry plane in the middle between the coils is the farthest frontier in the target space from either coil, it is therefore chosen to characterise the field focusing along this plane. For the planar and convex distributed coils, this implies $\boldsymbol{k} = \boldsymbol{p}$. However, for the concave coil, $\boldsymbol{k} = \boldsymbol{p} + \boldsymbol{e}$ where $\boldsymbol{e}$ is the coil's depth. Fig 3.17 shows the 2D representation of this aggregation for planar, concave and convex distributed coils using current sheets.

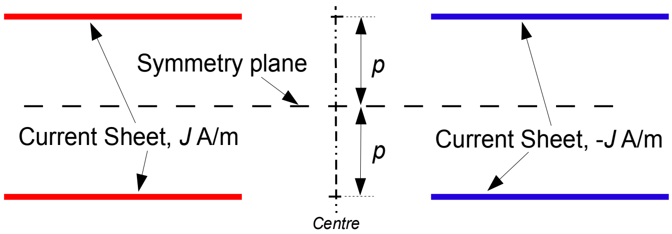


(a)

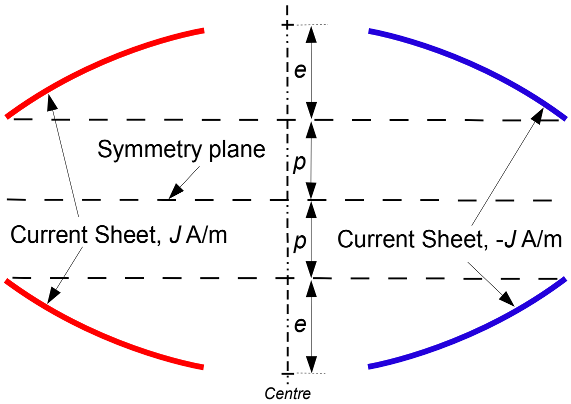


(b)

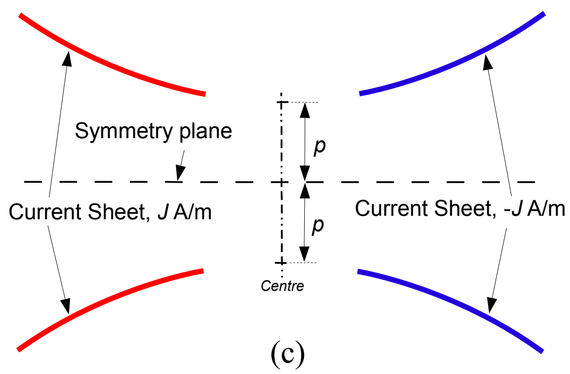


(c)

Fig 3.17 Aggregation of distributed (a) planar, (b) concave and (c) convex current sheets.

As selected earlier, the radius of curvature and breadth is characterised by ***r*** / ***b*** = 2 and ***l*** / ***b*** = 1 respectively. Based on these parameters, the concave current sheets' depth, ***e*** = 2***b*** cos(1 rad) ≈ ***b***. The magnetising field strength along the ***y*** axis of the aggregated current sheets is derived by spatially superimposing the field of the current sheets as described by Eqs 3.2, 3.6 and 3.7 according to the models shown in Fig 3.17, adjusting by ***e*** for the distributed concave current sheets. Interpreted as coil geometry representations, Fig 3.18 shows the magnetising field along the ***y*** axis at separation gaps of 2***p*** / ***b*** = 1.6, 2***p*** / ***b*** = 2.0 and 2***p*** / ***b*** = 2.4 for the planar, concave and convex distributed coil applicators, based on ***r*** / ***b*** = 2 and ***l*** / ***b*** = 1.

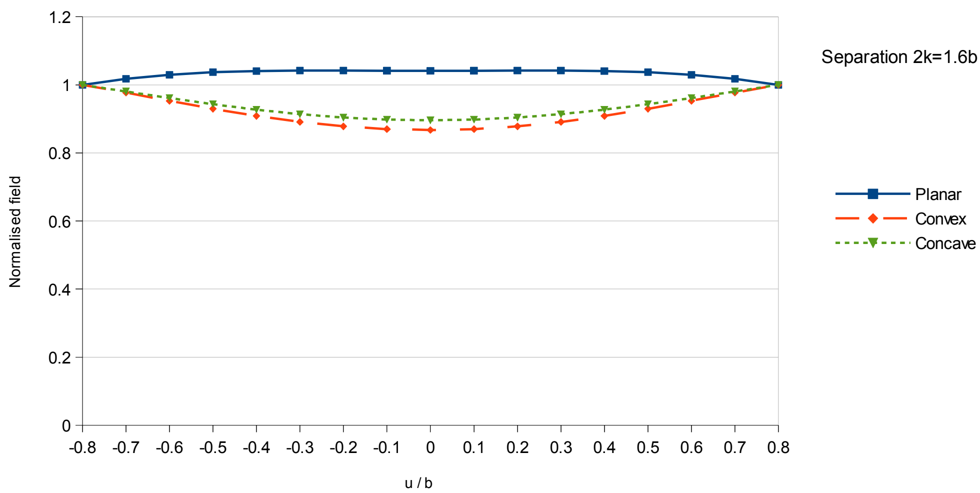


(a)

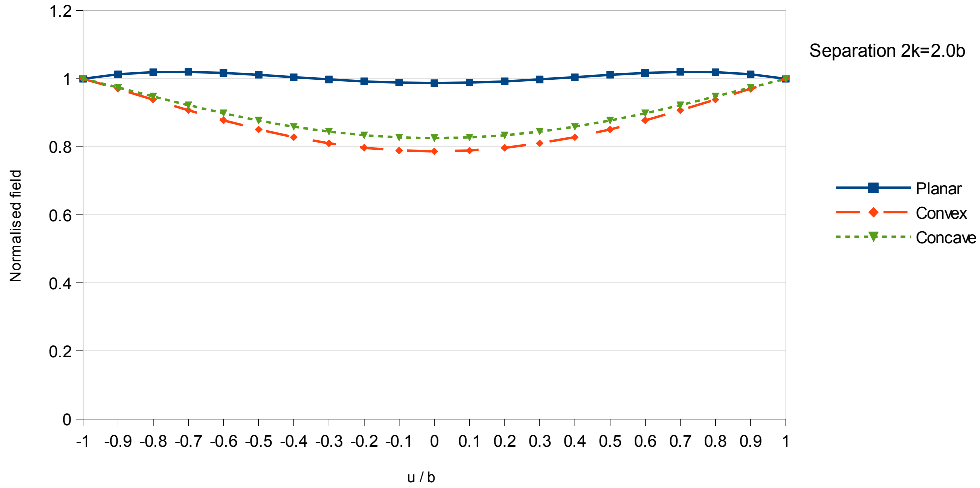


(b)

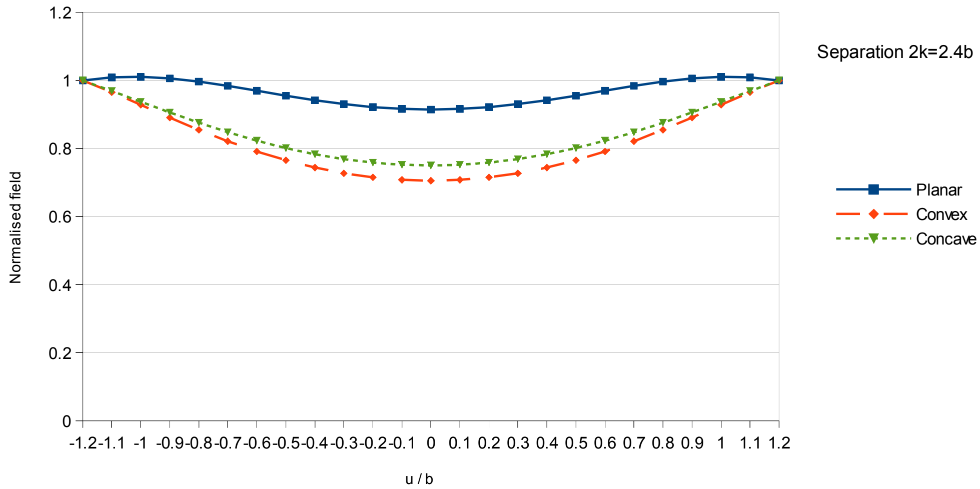


(c)

Fig 3.18 Field penetration of planar, convex and concave distributed coil applicators at the separation gap of (a) $2\boldsymbol{p} = 1.6\boldsymbol{b}$, (b) $2\boldsymbol{p} = 2.0\boldsymbol{b}$ and (c) $2\boldsymbol{p} = 2.4\boldsymbol{b}$ where $\boldsymbol{u}$ is the distance from the symmetry plane.

By inspecting Fig 3.18, the planar distributed coil applicator shows the best field penetration, followed by the concave distributed coil applicator which performs marginally better than the convex distributed coil applicator. However, all 3 coil applicator geometries suffer from field deterioration as the separation gap increases.

By spatially superimposing the values of Eqs 3.8 and 3.9 according to the models shown in Fig 3.17 while noting that $\boldsymbol{k} = \boldsymbol{p} + \boldsymbol{b}$ for the distributed concave current sheets, the magnetising field strength along the symmetry plane is derived. Due to symmetry, the $\boldsymbol{x}$ component of the magnetising field due to the current sheets will cancel out along this plane, therefore only the $\boldsymbol{y}$ component of the magnetising field needs to be considered. Interpreted as coil applicator geometry equivalents, Fig 3.19 shows the field strength along the symmetry plane for the planar, convex and concave distributed coil applicators at separation gaps of $2\boldsymbol{p} / \boldsymbol{b} = 1.6$, $2\boldsymbol{p} / \boldsymbol{b} = 2.0$ and $2\boldsymbol{p} / \boldsymbol{b} = 2.4$, based on $\boldsymbol{r} / \boldsymbol{b} = 2$ and $\boldsymbol{l} / \boldsymbol{b} = 1$.

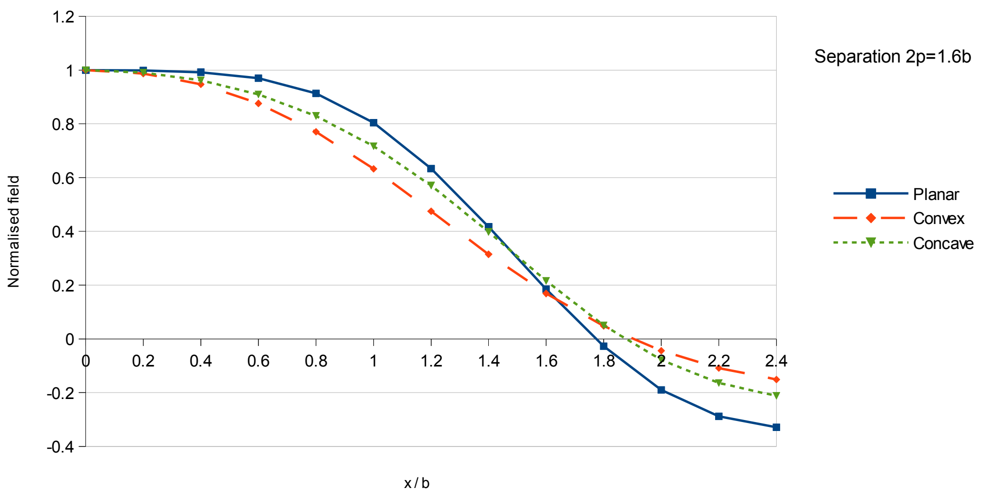


(a)

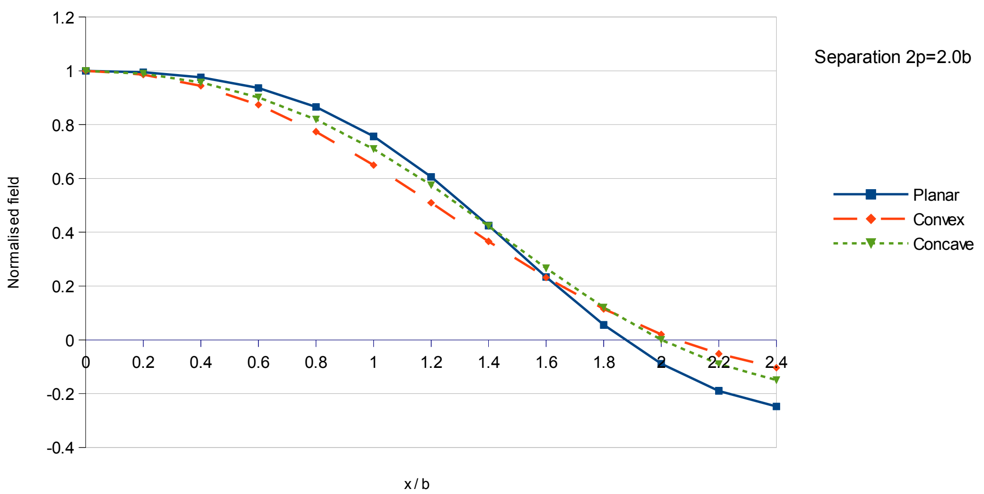


(b)

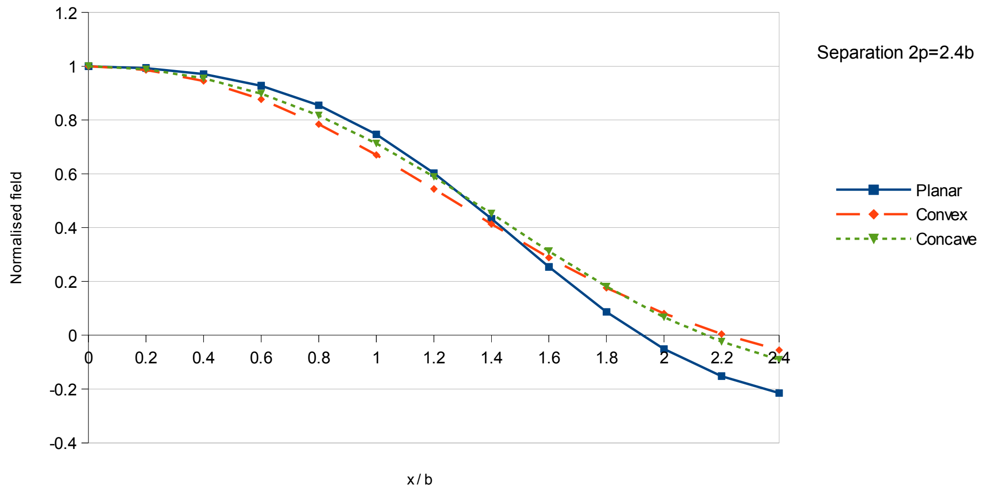


(c)

Fig 3.19 Field strength along the symmetry plane for various coil applicator geometries at separation gaps of (a) 2***p*** / ***b*** = 1.6, (b) 2***p*** / ***b*** = 2.0 and (c) 2***p*** / ***b*** = 2.4.

Fig 3.19 shows that the HPBW of the convex distributed coil applicator is consistently the smallest among the 3 coil applicator geometries for all separation gaps ***p*** under investigation, although this advantage tends to diminish as the separation gap 2***p*** / ***b*** extends beyond 2.4. For this reason, the convex distributed coil applicator is selected for subsequent investigations.

### 3.6 Performance Metric

In order to assess the field penetration and field focusing performance of the applicator, a numerical performance measurement system was developed based on the field strength at points shown in Fig 3.20 where (a) HT is the field strength at position T, denoting the pole along the ***y*** axis, (b) HC the field strength at position C, denoting the middle point between the coils along the ***y*** axis and (c) HL the field strength at position L, denoting a lateral point along the symmetry plane at distance ***b*** from point C.

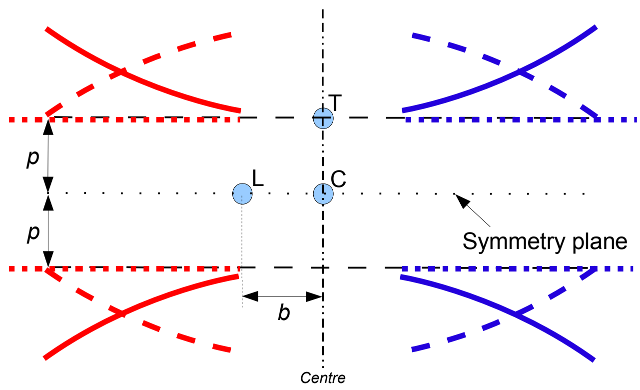


Fig 3.20 2D field points for performance evaluation.

The HT / HC ratio is a metric used to measure the degree of field penetration. A high HT / HC value implies a high field decay from the pole along the ***y*** axis and therefore, poor field penetration. On the other hand, the HC / HL ratio measures the degree of field focusing. A high HC / HL implies a high field decay from the ***y*** axis along the symmetry plane and thus, good field focusing.

The field strength at the above points, taken from the values used to plot Figs 3.18 and 3.19 are tabulated in Table 3.1 for various coil applicator geometries at separation gaps of 2***p*** / ***b*** = 1.6, 2***p*** / ***b*** = 2.0 and 2***p*** / ***b*** = 2.4, together with the accompanying ratios and HPBW. In this table, HP is the peak field strength along the ***y*** axis.

| Gap 2p | | 1.6b | | | 2.0b | | | 2.4b | | |
|---|---|---|---|---|---|---|---|---|---|---|
| Coil geometry | | Planar | Concave | Convex | Planar | Concave | Convex | Planar | Concave | Convex |
| Field ( x J / π ) | HT | 0.999 | 0.868 | 0.871 | 0.928 | 0.817 | 0.823 | 0.877 | 0.781 | 0.789 |
| | HP | 1.041 | 0.868 | 0.871 | 0.944 | 0.817 | 0.823 | 0.886 | 0.781 | 0.789 |
| | HC | 1.040 | 0.777 | 0.755 | 0.916 | 0.675 | 0.647 | 0.802 | 0.586 | 0.556 |
| | HL | 0.836 | 0.557 | 0.478 | 0.693 | 0.479 | 0.420 | 0.599 | 0.418 | 0.373 |
| Ratio | HT / HC | 0.96 | 1.12 | 1.15 | 1.01 | 1.21 | 1.27 | 1.09 | 1.33 | 1.42 |
| | HC / HL | 1.24 | 1.39 | 1.58 | 1.32 | 1.41 | 1.54 | 1.34 | 1.40 | 1.49 |
| HP BW ( x b ) | | 1.12 | 1.01 | 0.90 | 1.07 | 1.00 | 0.91 | 1.07 | 1.15 | 1.06 |

Table 3.1 2D performance metric of various coil applicator geometries at different separation gaps.

As the separation gap increases, all 3 coil applicator geometries show higher HT / HC ratios, i.e. a reduction of field penetration. At the same time, the HC / HL ratio for planar distributed coil applicator increases, implying its field focusing gets better with a farther separation gap, although this gain is marginal beyond the separation gap $2\boldsymbol{p} / \boldsymbol{b} = 2$, as evident through inspecting its HPBW. On the other hand, the concave distributed coil applicator shows its highest HC / HL as well as its lowest HPBW at the separation gap $2\boldsymbol{p} / \boldsymbol{b} = 2$, implying its field focusing is near optimum at this separation gap. Although the field focusing of the convex distributed coil applicator deteriorates with a farther separation gap, its HPBW deterioration only becomes significant beyond the separation gap $2\boldsymbol{p} / \boldsymbol{b} = 2$. Even then, the convex distributed coil applicator has the highest HC / HL ratio and the lowest HPBW among all 3 coil applicator geometries across all separation gaps $2\boldsymbol{p}$ under investigation, thus justifying the choice of the convex distributed coil applicator for further investigation.

It would appear that for the convex distributed coil applicator, the nearer the separation gap, the better is its field penetration and field focusing performance. However, in order to maximise the target space to accommodate the human body or a workpiece, it is better to stretch the separation gap until the performance deterioration becomes significant. For this reason, the separation gap is selected as $2\boldsymbol{p} = 2\boldsymbol{b}$ for subsequent investigations.

### 3.7 Concluding Remarks

The 2D analytical models, developed from the first principles and duly verified by simulation have shed light on some important properties and advantages of distributed coils over other coil geometries. By providing analytical insights, they have suggested design ideas such as coil curving. As a tool, they have proven to be useful for filtering the design parameters to the convex distributed coil applicator with $\boldsymbol{r} / \boldsymbol{b} = 2$, $\boldsymbol{l} / \boldsymbol{b} = 1$ and $2\boldsymbol{p} / \boldsymbol{b} = 2$ for subsequent 3D modelling.

# CHAPTER 4

# SIMULATION OF 3D MODELS

## 4.1 Background

The configuration of the convex distributed coil applicator with curvature $\boldsymbol{r} / \boldsymbol{b} = 2$, breadth $\boldsymbol{l} / \boldsymbol{b} = 1$ and a separation gap of $2\boldsymbol{p} / \boldsymbol{b} = 2$ will be developed into 3D models for further investigation. In the search for better applicator performance, various shapes of the convex distributed coil will be explored. The addition of components and electrical variations will also be considered. Since the primary target of this applicator is biological tissues, the effect of such tissues will be examined.

A commercially available solver, Microwave Studio® (MWS®) by CST is used to perform the 3D simulations. Throughout this chapter, the spatial unit of measurement is centimetre.

## 4.2 Performance Metric

In order to assess the performance of the 3D applicators numerically, the 2D performance metric system is expanded to cover 3D points. Considering the 3 orthogonal axes $\boldsymbol{x}$, $\boldsymbol{y}$ and $\boldsymbol{z}$ with the origin (0,0,0) assigned as C, the poles of both coils are aligned parallel to the $\boldsymbol{x}$-$\boldsymbol{z}$ plane with their centres positioned along the $\boldsymbol{y}$ axis at equal distance from point C. Therefore, C is the midpoint between the coils along the $\boldsymbol{y}$ axis and its corresponding field strength is HC. As will be shown later, the poles are located at positions (0,7.4,0) and (0,-7.4,0). Position (0,7,0) along the $\boldsymbol{y}$ axis at 0.4 cm from the centre of the pole is assigned T and its corresponding field strength is HT.

Along the ***x*** axis at 7.5 cm from point C is assigned the lateral point L at position (-7.5,0,0) with a corresponding field strength of HL. The point with the highest field strength HP along the ***y*** axis between the poles is assigned P at position (0,***a***,0). The similarities to the corresponding 2D system end here. Fig 4.1 shows the position of these points and for clarity reason, the other pole symmetrical about the ***x-z*** symmetry plane is not shown.

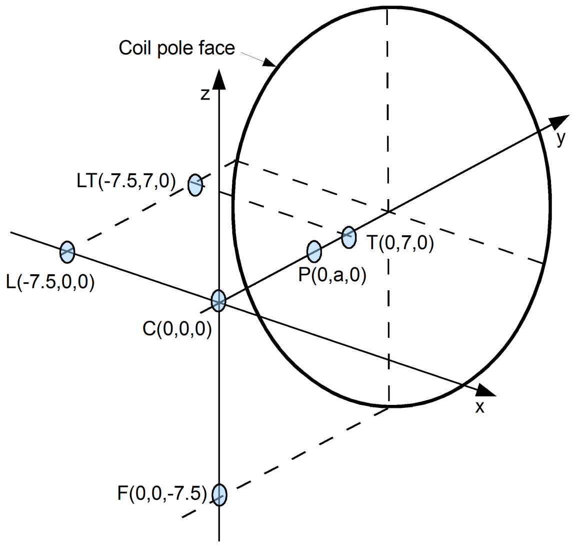


Fig 4.1 3D field points for performance evaluation.

For the 3D performance metric system, 2 additional measurement points are introduced. As will be shown later, the inner radius of the pole is 7.5 cm. Therefore, at 0.4 cm from the coil's current-carrying inner periphery at position (-7.5,7,0) is assigned point LT with a field strength of HLT. Point F at position (0,0,-7.5) is the equivalent of point L but it is along the ***z*** axis and its field strength is HF.

Similar to the 2D performance metric system, the HT / HC and HC / HL ratios are used to assess the degree of field penetration and field focusing of the applicator respectively. In the 3D performance metric system, 3 additional ratios are introduced. The ratio HLT / HC measures the extent of local field exposure near the coil's current-carrying inner periphery compared to the nominal field strength at point C. The lower the HLT / HC ratio, the more benign is the local field near the current source. To assess the degree of the peak field strength along the ***y*** axis compared to the nominal field strength at point C, the ratio HP / HC is used and as a narrower metric of field penetration, a low HP / HC ratio implies a better field penetration. Last but not least, the HC / HF ratio is a measure of field focusing, similar to the HC / HL ratio but only it is along the ***z*** axis.

### 4.3 Simulation Tool Setup Verification

A quick check was done to verify the simulation setup and output of the MWS® tool. For this purpose, a Helmholtz coil arrangement by Gyawali (2008) was referenced. This arrangement has a coil diameter of 47.5 cm and a separation gap of 47.5 cm with each coil formed by 100 turns of AWG#10 wire, carrying 4.8 $A_{rms}$ at 50 Hz. In his report, the measured magnetic flux density in the midpoint between the coils along the coil's axis is 9.2 Gs and this agrees well with both the corresponding simulation output of 9 Gs and the theoretical prediction of 9.1 Gs.

A similar simulation model of the same coil and current parameters was built, based on the simulation setup established for this project. The simulated magnetic flux density along the coil's axis is shown in Fig 4.2 and its value at the midpoint reads 9.12 Gs. Both this value and the corresponding calculated flux density of 9.09 Gs agree well with Gyawali's results within 1 %, thus establishing the credibility of the simulation setup.

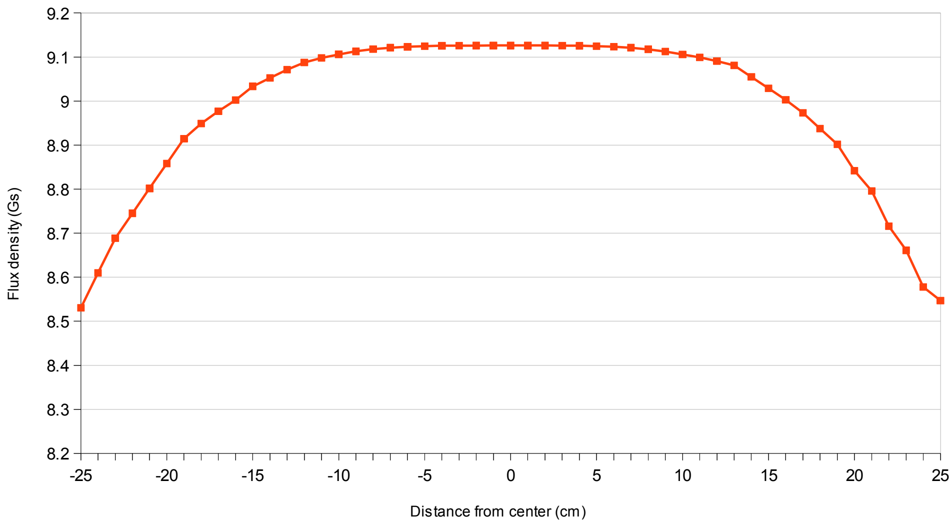


Fig 4.2 Simulated magnetic flux density of a Helmholtz coil along the coil's axis.

### 4.4 Coil Geometry Construction

In order to investigate if the convex distributed coil applicator can be tweaked for better field penetration and field focusing performance, 5 different coil geometries were considered: (a) prolate, (b) oblate, (c) sphere, (d) cone and (e) hyperboloid. In addition, the planar distributed coil applicator will also be included for comparison purpose since it is the geometry used in the state of the art MagForce® applicator.

All 3D applicator models under investigation were constructed based on the basic coil parameters as shown in Table 4.1.

| Attribute | Parameter |
|---|---|
| Coil inner radius (b) | 7.5 cm |
| Coil separation (2p) | 15 cm |
| Wire diameter | 2.6 cm |
| Number of turns | 8 |

Table 4.1 Basic parameters for 3D coil models.

Since the coil's inner radius of 7.5 cm can be expressed as 15 sin $\pi/6 = 7.5$ and $15\pi/6 = 7.85$, the coil breadth $\boldsymbol{l} = 7.85$ cm was conveniently chosen over 7.5 cm such that the coil's profile can be represented as a circular arc of radius 15 cm that spans from $\pi/6$ rad to $\pi/3$ rad. For consistency, the same coil breadth was also adopted in the construction of the planar distributed coil applicator model. However, for the purpose of simplifying the conical coil applicator model, a straight line subtending this arc was taken instead, yielding a coil breadth $\boldsymbol{l} = 15\sqrt{2}\,(\sin \pi/3 - \sin \pi/6)$ cm = 7.76 cm. In all cases, the deviation introduced is < 5 % from the nominal 7.5 cm.

The 3D coil wireframes were built using parametric equations with reference to the coordinate scheme shown in Fig 4.3. A 2D profile is built on the OQS plane at point S, tracing out the locus of the coil's wireframe as the OQS plane sweeps at an angle $\varphi$ from the $\boldsymbol{x}$-$\boldsymbol{z}$ plane for 8 revolutions, i.e. the number of turns. With $d$ and $h$ known, the coordinate of point S is thus given by $(d\cos\varphi, d\sin\varphi, h)$. The parametric equations expressed in numerical method terms are derived in Appendices B.2, B.3, B.4 and B.5 for ellipsoid & spherical, hyperboloid, conical and planar geometries respectively and their corresponding VBA scripts are listed in Appendix B.7.

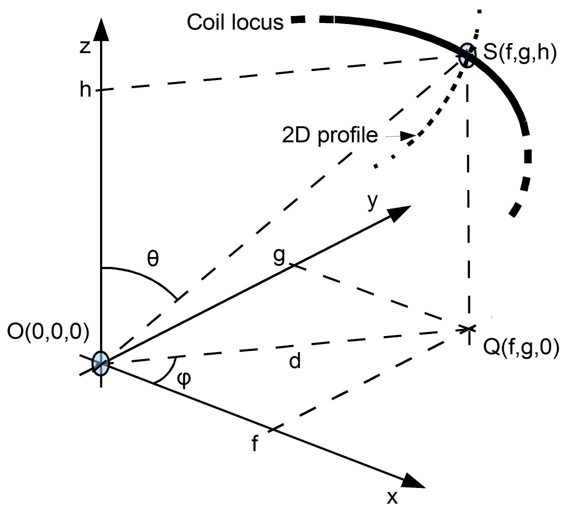


Fig 4.3 Coordinate scheme for constructing coil wireframes from parametric equations.

(a) The 3D ellipsoid construction was used to build prolate and oblate distributed coils. It uses parametric equations Eqs 4.1, 4.2 and 4.3 with Eqs 4.1 and 4.2 defining its 2D profile on the OQS plane:

$$d = B \sin\theta \tag{4.1}$$

$$h = A \cos\theta \tag{4.2}$$

where

*A* is the radius of the major axis,

*B* is the radius of the minor axis, and

$\theta$ is the angle between OS and the ***z*** axis.

The initial value of $\theta$ was set at π/6 rad. In order to maintain a constant turn pitch, it was adjusted by $\Delta\theta(\theta)$ as given in Eq 4.3 for $\Delta\varphi$ at every iteration as $\varphi$ was step-increased.

$$\Delta\theta(\theta) = \frac{l}{2\pi N} \frac{\Delta\varphi}{\sqrt{A^2 \sin^2\theta + B^2 \cos^2\theta}} \tag{4.3}$$

where $\varphi$ is the sweep angle from the ***x-z*** plane around the ***z*** axis.

With $l$ = 7.85 cm, $N$ = 8, $A$ = 30 cm and $B$ = 15 cm, the prolate distributed coil wireframe was built as the angle $\varphi$ swept from 0 to $2\pi N$ rad. Similarly, the oblate distributed coil wireframe was built as the angle $\varphi$ swept $N$ revolutions with $l$ = 7.85 cm, $N$ = 8, $A$ = 7.5 cm and $B$ = 15 cm. Figs 4.4(a) and 4.4(b) show the lateral view of the applicators assembled with prolate and oblate distributed coils respectively.

(b) In the special case of the spherical distributed coil, the major and minor axes in Eqs 4.1, 4.2 and 4.3 are equal in value to the radius of curvature $\boldsymbol{r}$, i.e. $A = B = \boldsymbol{r}$. Substituting the simplified Eq 4.3 for a constant turn pitch into Eqs 4.1 and 4.2 yields Eqs 4.4 and 4.5 respectively with the initial value of $\theta$ set at $\pi/6$ rad.

$$d = r \sin\left(\frac{l\varphi}{2\pi Nr} + \frac{\pi}{6}\right) \tag{4.4}$$

$$h = r \cos\left(\frac{l\varphi}{2\pi Nr} + \frac{\pi}{6}\right) \tag{4.5}$$

With $l$ = 7.85 cm, $N$ = 8 and $\boldsymbol{r}$ = 15 cm, the spherical distributed coil wireframe built as the angle $\varphi$ swept from 0 to $2\pi N$ rad was assembled into an applicator, the lateral view of which is shown in Fig 4.4(c).

(c) For the hyperboloid distributed coil, the hyperbola profile was built using parametric equations Eqs 4.6 and 4.7 by varying the parameter $u$ instead of angle $\theta$.

$$d = B\sqrt{1+u^2} \tag{4.6}$$

$$h = C\,u \tag{4.7}$$

where

$C$ is the elongation coefficient, and

$u$ is the nominal elevation from the $\boldsymbol{x}$-$\boldsymbol{y}$ plane

The initial value of $u$ was set at 0 and similarly, in order to maintain a constant turn pitch, $u$ was adjusted by $\Delta u(u)$ as given in Eq 4.8 for $\Delta\varphi$ at every iteration as $\varphi$ was step-increased.

$$\Delta u(u)=\frac{l\Delta\varphi}{2\pi N}\sqrt{\frac{1+u^2}{C^2+u^2(C^2+B^2)}} \tag{4.8}$$

where $\varphi$ is the sweep angle from the $\boldsymbol{x}$-$\boldsymbol{z}$ plane around the $\boldsymbol{z}$ axis.

With $l$ = 7.85 cm, $N$ = 8 and $B$ = 7.5 cm and C = 3.75 cm, the hyperboloid distributed coil wireframe was built as the angle $\varphi$ swept from 0 to $2\pi N$ rad. The lateral view of the applicator assembled with this coil is shown in Fig 4.4(d).

(d) The conical distributed coil uses a straight line profile that subtends the arc of a spherical distributed coil of radius $\boldsymbol{r}$ for $\theta \in [\pi/6,\pi/3]$ and it is given by Eqs 4.9 and 4.10 for a constant turn pitch.

$$d=b+\frac{r\varphi}{2\pi N}\left(\sin\frac{\pi}{3}-\sin\frac{\pi}{6}\right) \tag{4.9}$$

$$h=\frac{r\varphi}{2\pi N}\left(\cos\frac{\pi}{6}-\cos\frac{\pi}{3}\right) \tag{4.10}$$

With $r$ = 15 cm, $N$ = 8 and $b$ =7.5 cm, the conical distributed coil wireframe was built as the angle $\varphi$ swept from 0 to $2\pi N$ rad. The lateral view of the applicator assembled with this coil is shown in Fig 4.4(e).

(e) For comparison with the coil used in the state of the art applicator by MagForce®, a planar distributed coil with a constant turn pitch was built using the profile described by Eq 4.11 as the angle $\varphi$ swept from 0 to $2\pi N$ rad with $\boldsymbol{l}$ = 7.85 cm, $N$ = 8 and $\boldsymbol{b}$ = 7.5 cm.

$$d = b + \frac{l\varphi}{2\pi N} \tag{4.11}$$

The lateral view of the corresponding applicator is shown in Fig 4.4(f).

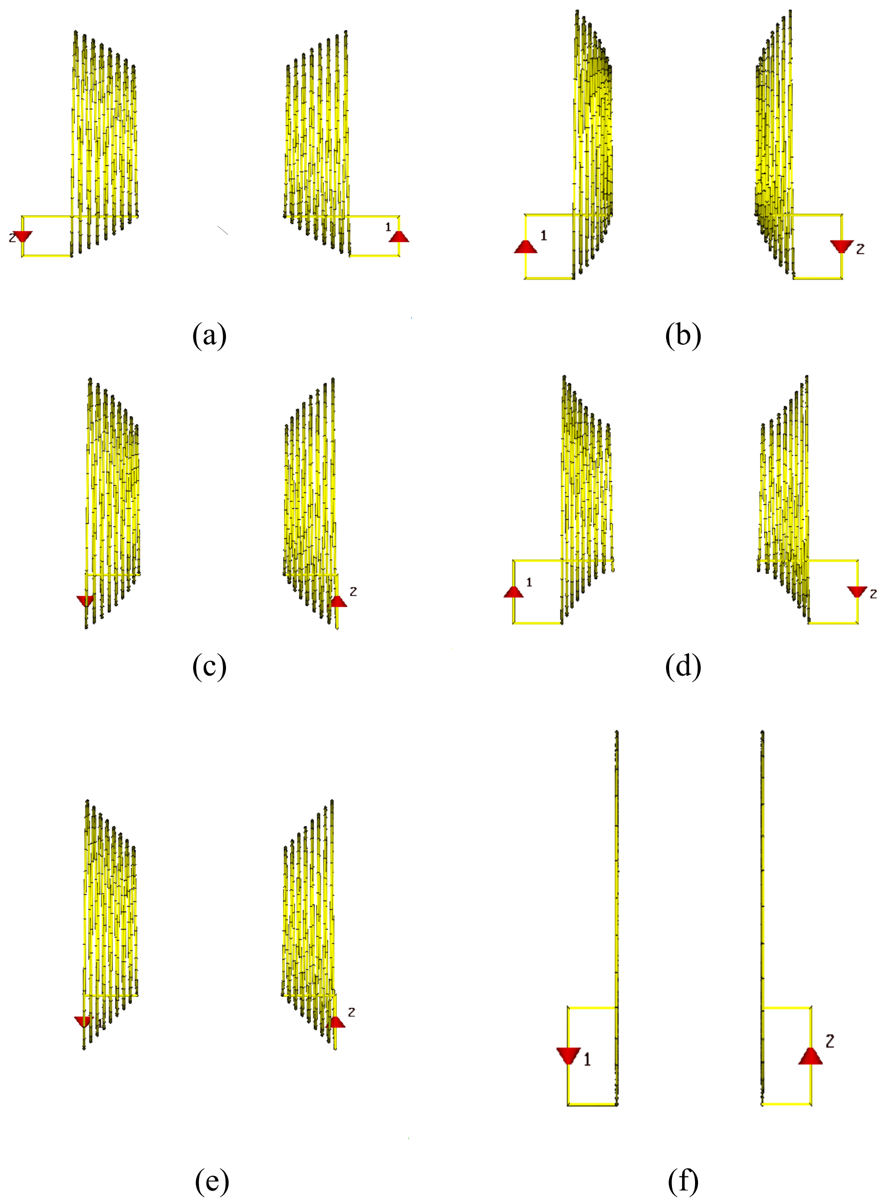

(a) (b) (c) (d) (e) (f)

Fig 4.4 Lateral view of the (a) prolate, (b) oblate, (c) spherical, (d) hyperboloid, (e) conical and (f) planar distributed coil applicators.

## 4.5 Coil Geometry Comparison

The 3D simulation models of the prolate, oblate, spherical, hyperboloid, conical and planar distributed coil applicators were then excited using a 15 $A_{pk}$ 50 kHz source such that the fields build constructively in the target space. The resultant field strength plot (a) along the coil's axis and (b) along the symmetry plane are shown in Figs 4.5 and 4.6 respectively.

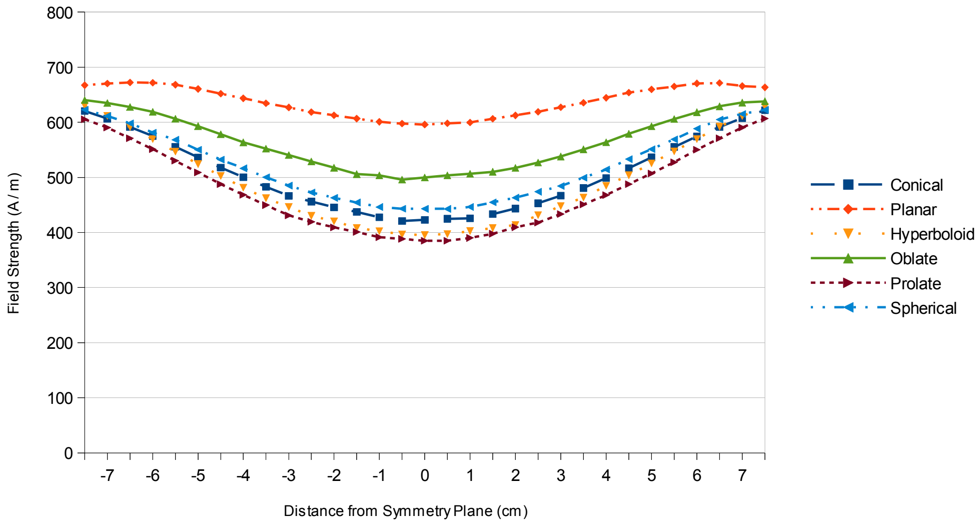


Fig 4.5 Field strength along the coil's axis of various coil applicator geometries.

Fig 4.5 shows that the planar distributed coil applicator demonstrates the best ability to sustain field strength throughout the coil's axis, indicating a good field penetration, followed by the oblate distributed coil applicator. As the separation distance between the current source and the field point along the coil's axis widens, the field penetration also deteriorates, starting with the spherical distributed coil applicator showing moderate field penetration, followed closely by the conical distributed coil applicator with the hyperboloid and prolate distributed coil applicators trailing the list.

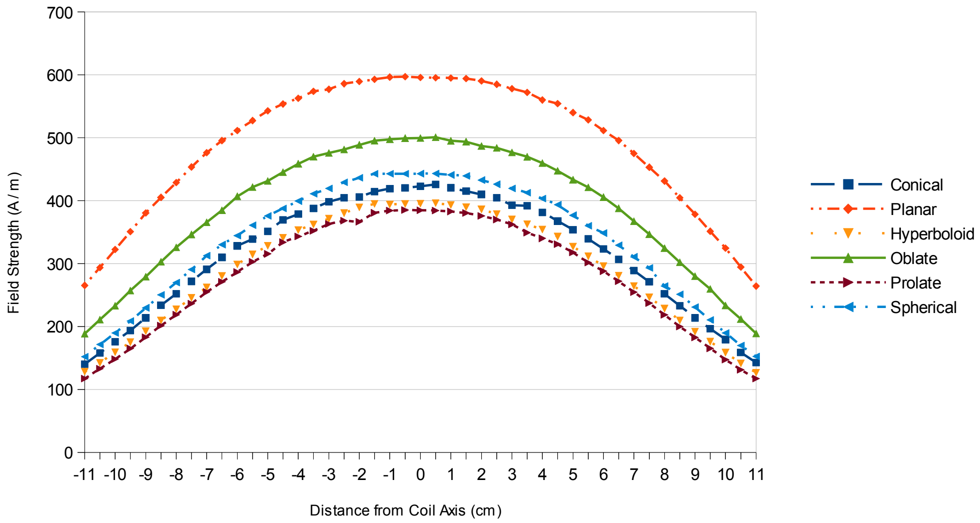


Fig 4.6 Field strength along the symmetry plane of various coil applicator geometries.

The ability of the planar and oblate distributed coil applicators to sustain magnetising field far from the pole is again demonstrated in Fig 4.6. However, the field strength plots of the planar and oblate distributed coil applicators appear to be flattened on the symmetry plane, suggesting poor field focusing. This is further confirmed by the high HPBW of these coil applicator geometries as shown in Table 4.2.

| Field | Prolate | Hyperboloid | Conical | Spherical | Oblate | Planar |
|---|---|---|---|---|---|---|
| Peak position ***a*** | 10.00 | 9.32 | 9.62 | -9.38 | -8.07 | -6.40 |
| HC(0,0,0) | 384.83 | 395.50 | 422.90 | 443.00 | 499.67969 | 595.81 |
| HT(0,7.0,0) | 590.51 | 611.07 | 607.30 | 615.16 | 635.65209 | 665.69 |
| HP(0,***a***,0) | 647.18 | 667.77 | 642.87 | 634.89 | 643.01084 | 672.98 |
| HL(-7.5,0,0) | 236.47 | 245.64 | 271.83 | 291.29 | 346.40046 | 453.59 |
| HLT(-7.5,7.0,0) | 734.05 | 720.95 | 817.25 | 832.49 | 1011.6115 | 1091.12 |
| HF(0,0,-7.5) | 236.74 | 244.27 | 272.17 | 290.73 | 337.93813 | 451.15 |
| H(1/2P) | 272.11 | 279.66 | 299.03 | 313.25 | 353.33 | 421.30 |
| HPBW | 12.94 | 13.04 | 13.44 | 13.96 | 14.64 | 16.24 |
| HC/HL | 1.63 | 1.61 | 1.56 | 1.52 | 1.44 | 1.31 |
| HC/HF | 1.63 | 1.62 | 1.55 | 1.52 | 1.48 | 1.32 |
| HP/HC | 1.68 | 1.69 | 1.52 | 1.43 | 1.29 | 1.13 |
| HLT/HC | 1.91 | 1.82 | 1.93 | 1.88 | 2.02 | 1.83 |
| HT/HC | 1.53 | 1.55 | 1.44 | 1.39 | 1.27 | 1.12 |

Note: the unit of position ***a*** & HPBW is cm and the unit of the magnetising field is A /m.

Table 4.2 Performance metric of various coil applicator geometries.

The coil geometry columns in Table 4.2 are arranged in an ascending order of HPBW, confirmed by the descending order of both HC / HL and HC / HF ratios. This deterioration of field focusing is due to the shorter separation distance between the current source and the field point along the symmetry plane when the outer periphery is bent backwards from the target space as one progresses from the prolate distributed coil applicator on the left to the planar distributed coil applicator on the right.

On the other hand, with the exception of the hyperboloid distributed coil applicator, a general counter trend can be observed in the descending order of both HT / HC and HP / HC ratios, implying the improving field penetration as one progresses from the prolate distributed coil applicator on the left to the planar distributed coil applicator on the right, consistent with the earlier observation of Fig 4.5. In the case of the hyperboloid distributed coil applicator, its comparatively poor field penetration is exacerbated by its solenoid-like current source near the pole.

Since all the 6 geometries show rather consistent levels of local field strength near the coil's inner periphery, i.e. HLT / HC within 1.8 ~ 2.0, it remains a trade-off between the field penetration and field focusing when choosing the coil applicator geometry. For reasons of simplicity and balance, the spherical distributed coil applicator was selected for further investigation. Fig 4.7 shows the field strength contour of this applicator in providing a visual interpretation of its field peaks and its focusing effect by noting the pinching in the region between the coils.

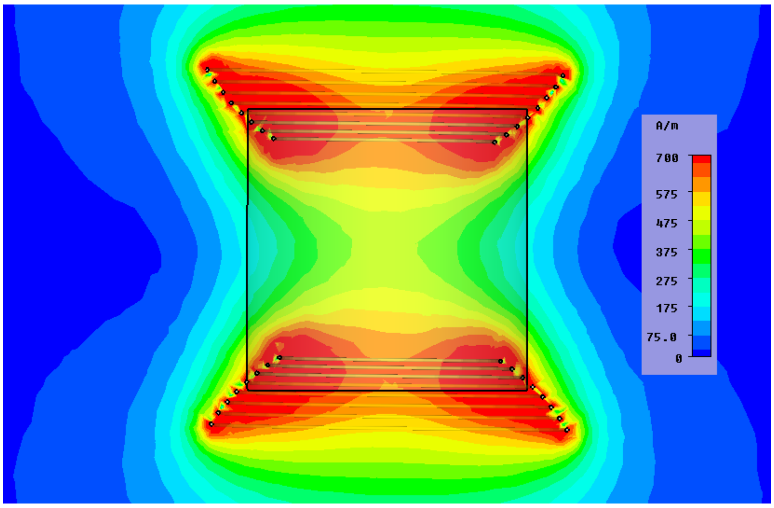


Fig 4.7 Field strength contour of the spherical distributed coil applicator, viewed on the ***x-y*** plane.

**4.6 Deflector Plates**

As shown in Table 4.2, the HT / HC and HP / HC ratios for the spherical distributed coil applicator are 1.39 and 1.43 respectively. In an attempt to reduce these ratios and thus improve the field penetration, a deflector plate is placed along the coil's axis at each pole. The deflector plate works on the principle that the eddy current induced by the incident magnetic field generates a counteracting magnetic field, thus causing a lower net magnetic field near the deflector plate. In the process, the eddy current also produces heat as a result of ohmic loss, hence the need to limit its size.

(a) The deflector plate, constructed from a copper disc of 1 mm thick was placed in front of each pole. To assess the effect of the deflector plate size on the reduction of magnetising field peaks, models of spherical distributed coil applicator with copper discs of diameter 5 mm, 10 mm and 50 mm as shown in Fig 4.8(a), 4.8(b) and 4.8(c) respectively were built. Their field strengths were then simulated, excited by a 15 $A_{pk}$ 50 kHz source such that the fields in the target space build constructively.

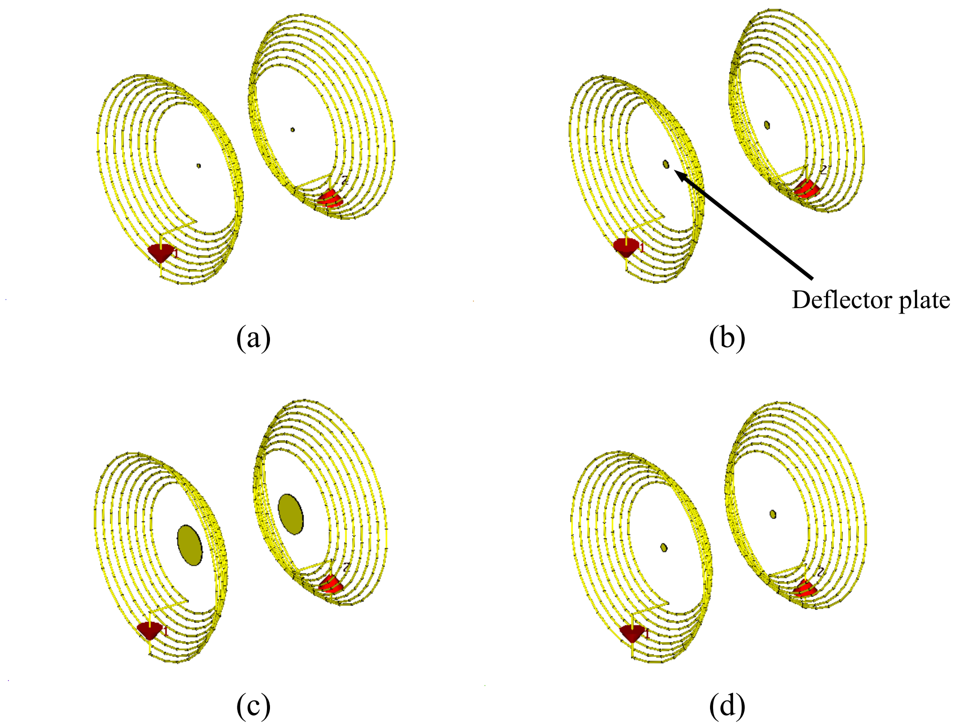


Fig 4.8 Isometric view of spherical distributed coil applicators with deflector plates of diameter (a) 5 mm, (b) 10 mm and (c) 50 mm at the poles as well as (d) 10 mm in diameter but recessed 10 mm from the pole into the coil.

The corresponding plots of the magnetising field strength along the coil's axis shown in Figs 4.9 indicate that the field peak is suppressed and the overall field strength is reduced as the deflector plate size is increased, implying a higher field penetration. The reason for this is that a larger deflector plate area induces a higher eddy current due to a higher magnetic flux which in turn produces a stronger counteracting field. This negates the incident magnetic field more and farther, hence a flatter but lower overall field strength along the coil's axis.

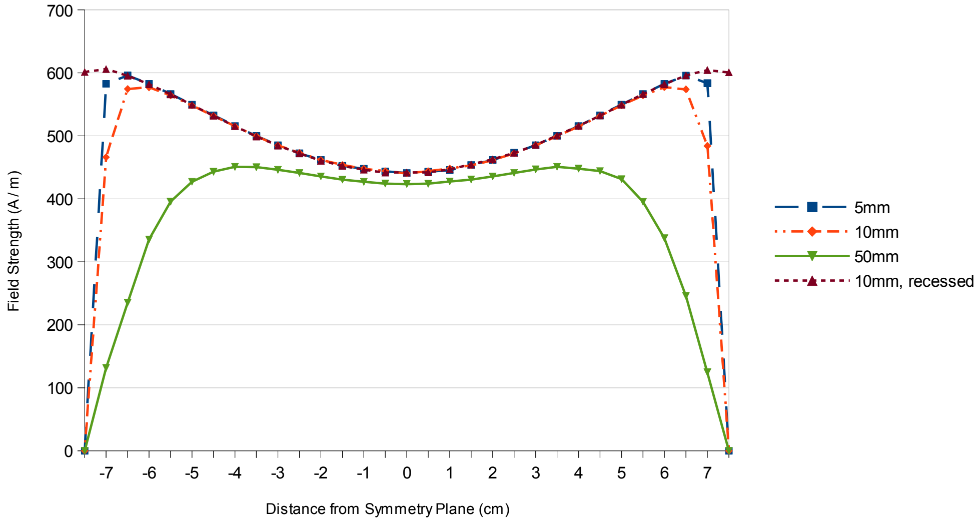


Fig 4.9 Field strength along the coil's axis of applicators with various deflector sizes and recess depths.

However, the corresponding plots of the field strength along the symmetry plane suggest that as the deflector plate increases in diameter, the field focusing deteriorates as evident from the flattened plot corresponding to the 50 mm in diameter deflector plate in Fig 4.10. By lowering the field near the coil's axis more compared to the field farther from the coil's axis, the HPBW is thus increased for the applicator with a larger deflector plate.

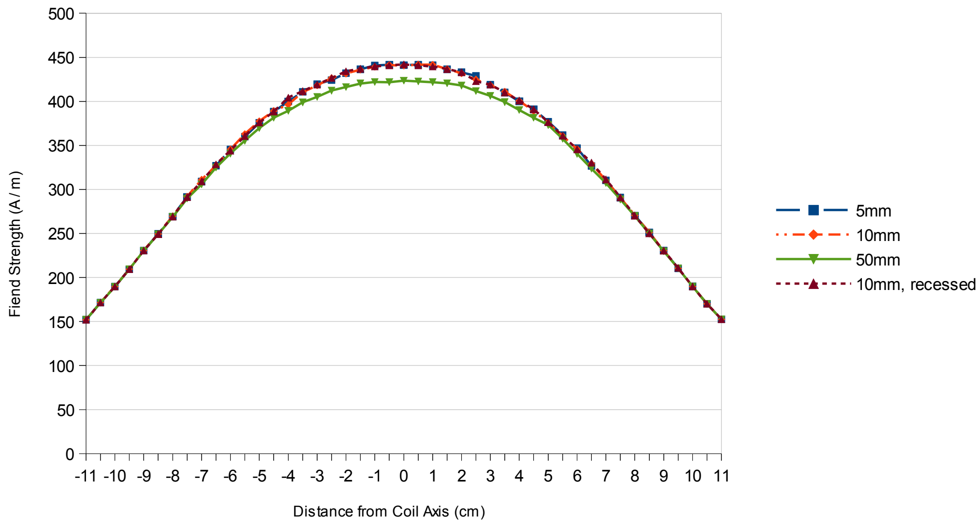


Fig 4.10 Field strength along the symmetry plane of applicators with various deflector sizes and recess depths.

(b) To explore the effect of placing the deflector inside the coil but along the coil's axis, the simulation model of a similar spherical distributed coil applicator was built but with the 1 mm thick, 10 mm in diameter deflector plates recessed 10 mm into the coils from the poles as shown in Fig 4.8(d). Similarly, this model was simulated using a 15 $A_{pk}$ 50 kHz source such that the fields in the target space build constructively.

By comparing its field strength along the coil's axis with the other applicators shown in Fig 4.9, it is apparent that recessing the deflector plates deep into the coil only relocates the field cancellation effect farther into the coil, hence the higher peak field strength and a poorer field penetration. As this eddy current effect is short-ranged (comparable to that of a small loop coil), its effect on the field focusing is negligible as shown in Fig 4.10.

By inspecting Table 4.3, the HPBW remains fairly stable just under 14 cm for applicators with smaller than 10 mm in diameter deflector plates at the poles. On the other hand, the HT / HC and HP / HC ratios have improved from 1.39 and 1.43 to 1.10 and 1.33 respectively by using the 10 mm in diameter deflector plates compared to that with no deflector plate added. In contrast, the recessed deflector plate arrangement does not yield any benefit with the higher HT / HC and HP / HC ratios as shown in Table 4.3, i.e. poor field penetration. Therefore, given its improved field penetration and a relatively stable field focusing, the spherical distributed coil applicator with a 10 mm in diameter deflector plates at its poles was chosen for further investigation.

| Field | Diameter | | | | Depth | |
|---|---|---|---|---|---|---|
| | 0mm | 5mm | 10mm | 50mm | 0mm | 10mm |
| Peak position ***a*** | -9.38 | -6.85 | 6.32 | 3.55 | 6.32 | -6.91 |
| HC(0,0,0) | 443.00 | 441.02 | 440.39 | 423.54 | 440.39 | 441.88 |
| HT(0,7.0,0) | 615.16 | 583.72 | 484.13 | 124.76 | 484.13 | 604.54 |
| HP(0,***a***,0) | 634.89 | 599.39 | 583.70 | 451.85 | 583.70 | 606.22 |
| HL(-7.5,0,0) | 291.29 | 291.57 | 291.81 | 289.81 | 291.81 | 291.28 |
| HLT(-7.5,7.0,0) | 832.49 | 864.25 | 881.63 | 874.54 | 881.63 | 868.39 |
| HF(0,0,-7.5) | 290.73 | 289.99 | 290.75 | 287.17 | 290.75 | 291.47 |
| H(1/2P) | 313.25 | 311.85 | 311.40 | 299.49 | 311.40 | 312.46 |
| HPBW | 13.96 | 13.86 | 13.98 | 14.48 | 13.98 | 13.82 |
| HC/HL | 1.52 | 1.51 | 1.51 | 1.46 | 1.51 | 1.52 |
| HC/HF | 1.52 | 1.52 | 1.51 | 1.47 | 1.51 | 1.52 |
| HP/HC | 1.43 | 1.36 | 1.33 | 1.07 | 1.33 | 1.37 |
| HLT/HC | 1.88 | 1.96 | 2.00 | 2.06 | 2.00 | 1.97 |
| HT/HC | 1.39 | 1.32 | 1.10 | 0.29 | 1.10 | 1.37 |

Note: the unit of position ***a*** & HPBW is cm and the unit of the magnetising field is A /m.

Table 4.3 Performance metric of spherical distributed coil applicators with various deflector sizes and depths.

For a visual interpretation of the deflector plates' effect on the field peaks and the focusing effect, note the null field strength region around the deflector plates in Fig 4.11.

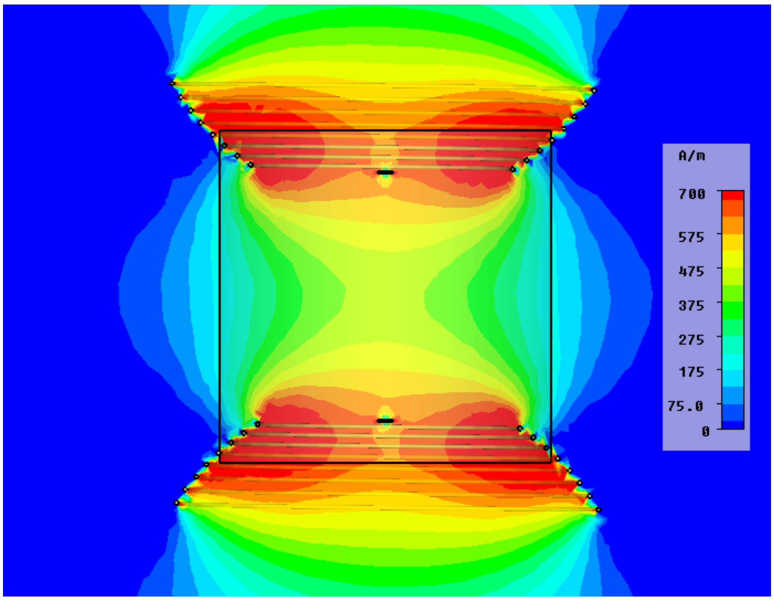


Fig 4.11 Field strength contour of the spherical distributed coil applicator with deflector plates, viewed on the ***x-y*** plane.

## 4.7 Variable Current Density

Thus far, the investigation is premised on coils with a constant turn pitch. In order to increase the current density, this turn pitch can be reduced. To effect a linearly increasing or decreasing turn pitch on a spherical distributed coil, points of a circle with varying pitch can be traced on the OQS plane by using Eqs 4.12, 4.13 and 4.14 as derived in Appendix B.6 and its VBA script is listed in Appendix B.7.

$$d = r \sin\theta \tag{4.12}$$

$$h = r \cos\theta \tag{4.13}$$

with $\theta$ varied with respect to $\varphi$ according to Eq 4.14.

$$\theta = \frac{(l - Ng_i)}{4\pi^2 rN(N-1)}\varphi^2 + \frac{(N^2 g_i - l)}{2\pi rN(N-1)}\varphi + \theta_i \tag{4.14}$$

where

$\theta_i$ is the initial angle of $\theta$, and

$g_i$ is the initial turn pitch such that if $g_i < l \,/\, N$, the turn pitch will increase with $\theta$ and if $g_i > l \,/\, N$, the turn pitch will decrease with $\theta$.

Starting out with $g_i = 0.069\boldsymbol{l}$ and $\theta_i = \pi/6$ rad with $l = 7.85$ cm, $N = 8$ and $\boldsymbol{r} = 15$ cm, a spherical distributed coil wireframe with an increasing current density from the pole towards its periphery was built as the angle $\varphi$ swept from 0 to $2\pi N$ rad and assembled into an applicator. The lateral view of this applicator is shown in Fig 4.12(a). Since this coil's terminal turn pitch is $0.181\boldsymbol{l}$, a similar process but starting out with $g_i = 0.181\boldsymbol{l}$ was used to build an applicator with a decreasing current density from the pole towards its periphery, the lateral view of which is shown in Fig 4.12(b).

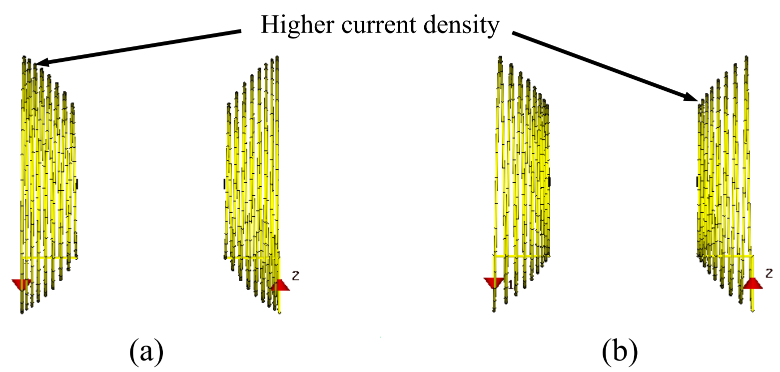


Fig 4.12 Lateral view of the applicator with (a) increasing current density and (b) decreasing current density from the pole towards its periphery.

These models were then simulated using a 15 $A_{pk}$ 50 kHz source such that the fields in the target space build constructively, resulting in the magnetising field strength plots (a) along the coil's axis and (b) along the symmetry plane shown in Figs 4.13 and 4.14 respectively.

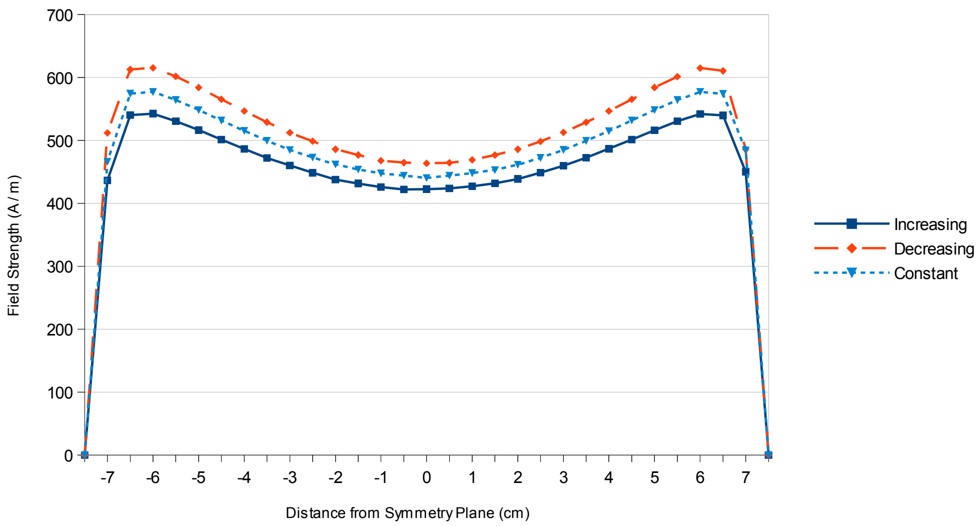


Fig 4.13 Field strength along the coil's axis for applicators of various current density distributions from the pole.

With the current source concentrating around the coil's axis for the spherical distributed coil applicator with decreasing current density from the pole, the separation distance between the current source and the field point is closer than that of a similar applicator with a uniform current density, hence the higher field strength along the coil's axis as shown in Fig 4.13. This also results in a slight reduction of field penetration as shown in Table 4.4. The contrary is true when the current density increases from the pole.

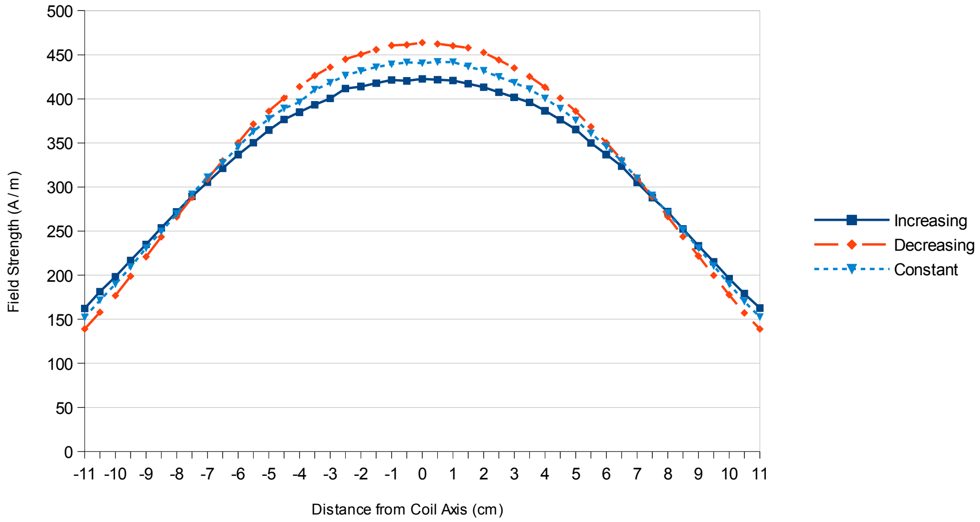


Fig 4.14 Field strength along the symmetry plane for applicators with various current density distributions from the pole.

As shown in Fig 4.14, the applicator with a decreasing current density from the pole appears to have a narrower field along the symmetry plane, evident from its smaller HPBW. The reason for this is when most of the current source is concentrated around the coil's axis, the magnetising field is also more concentrated around the coil's axis. Again, the contrary is true when the current density increases from the pole.

| Field | Current density | | |
|---|---|---|---|
| | Decreasing | Steady | Increasing |
| Peak position ***a*** | -6.32 | 6.32 | -6.33 |
| HC(0,0,0) | 463.69 | 440.39 | 422.72 |
| HT(0,7.0,0) | 485.97 | 484.13 | 450.30 |
| HP(0,***a***,0) | 623.82 | 583.70 | 548.94 |
| HL(-7.5,0,0) | 288.21 | 291.81 | 289.45 |
| HLT(-7.5,7.0,0) | 1077.73 | 881.63 | 740.87 |
| HF(0,0,-7.5) | 289.20 | 290.75 | 290.09 |
| H(1/2P) | 327.88 | 311.40 | 298.91 |
| HPBW | 13.08 | 13.98 | 14.40 |
| HC/HL | 1.61 | 1.51 | 1.46 |
| HC/HF | 1.60 | 1.51 | 1.46 |
| HP/HC | 1.35 | 1.33 | 1.30 |
| HLT/HC | 2.32 | 2.00 | 1.75 |
| HT/HC | 1.05 | 1.10 | 1.07 |

Note: the unit of position ***a*** & HPBW is cm and the unit of the magnetising field is A /m.

Table 4.4 Performance metric of spherical distributed coil applicators with decreasing, steady and increasing current density from the pole.

Comparing the performance of applicators with decreasing, steady and increasing current density from the pole in Table 4.4 further confirms the HPBW reduction advantage of the former applicator. At the same time, its field penetration is only marginally reduced, thanks to a higher eddy current on the deflector plates and thus stronger cancellation field due to the concentrated flux density along the coil's axis. However, with a higher HLT / HC, the strong magnetic field near the coils may cause excessive local eddy current heating and thus, patient discomfort. Due to this reason and also for simplicity of implementation, only the spherical distributed coil applicator with a uniform turn pitch and a pair of deflector plates at the poles will be investigated further.

### 4.8 Effect of the Target Media

At 50 kHz, the magnetic permeability of biological tissues can be taken to be the same as that of air (WHO 2007). Therefore, only the effect of electric permittivity on the resultant magnetic field will be investigated. The combined

Ampere's Law and Faraday's Law in the Maxwell's equations as expressed by Eq 4.15 shows that a material with a bulk relative permittivity $\varepsilon_r > 1$ and conductivity $\sigma$ can affect the magnetic field, $H$ due to the source electric field $E_s$ and the induced electric field $E_i$ as a function of excitation frequency.

$$\nabla \times \bar{H} = J_s - \sigma \bar{E}_i + j\omega \varepsilon_0 \varepsilon_r \bar{E}_s \tag{4.15}$$

where

$\varepsilon_0$ is the permittivity of free space,

$\omega$ is the angular frequency of the magnetising field, and

$J_s$ is the source current density.

For this reason, both kidney and thyroid are chosen for magnetising field strength comparison with that of fat and air. The kidney is chosen because it has the highest relative permittivity among the tissues in the human body while the thyroid is chosen for having tissues with the highest bulk conductivity in the human body (IFAC-CNR 2012) at 50 kHz as shown in Table 4.5. Fat is chosen for comparison as it is representative of typical tissues in the human body.

| @ 50kHz | Media | | | |
|---|---|---|---|---|
| | Air | Fat | Kidney | Thyroid |
| Relative permittivity ($\varepsilon_r$') | 1 | 172.42 | 11429 | 4023.1 |
| Conductivity ($\sigma$) / S m$^{-1}$ | 0 | 0.024246 | 0.15943 | 0.53395 |

Table 4.5 Comparison of dielectric properties of various biological tissues with that of air. (IFAC-CNR 2012)

The target space of the 3D spherical distributed coil applicator simulation model with a pair of 10 mm in diameter deflector plates at both poles is characterised by these tissues and the applicator was simulated using a 15 $A_{pk}$ 50 kHz source such that the fields build constructively. The resultant magnetising field strength plots (a) along the coil's axis and (b) along the symmetry plane as shown in Figs 4.15 and 4.16 respectively show no discernible difference for the different types of media in the target space. However, upon closer examination, the magnetic field in the kidney tissues is slightly higher and that in the thyroid tissues is slightly lower, especially around the coil's axis.

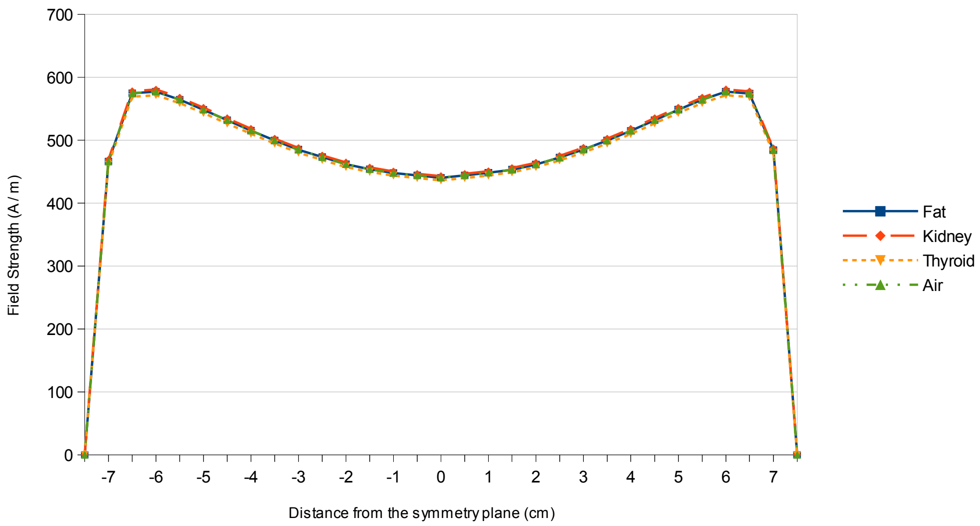


Fig 4.15 Field strength along the coil's axis of the applicator with various types of media in the target space.

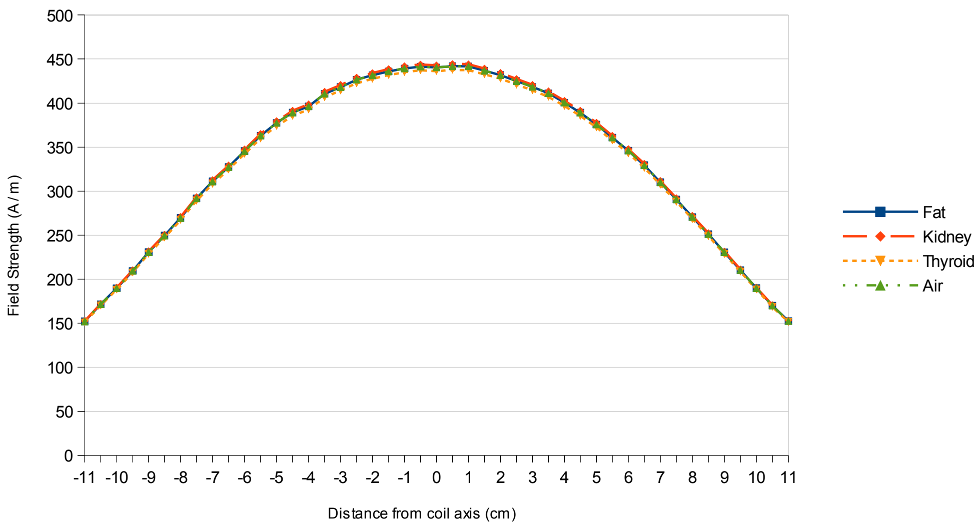


Fig 4.16 Field strength along the symmetry plane of the applicator with various types of media in the target space.

The performance metric of the applicator with various tissues in the target space as tabulated in Table 4.6 confirms there is no appreciable effect on the field penetration or field focusing performance by the biological tissues in the target space. Overall, the field strength in the kidney is enhanced by about 0.5 % and that in the thyroid is diminished by about 1 %.

Due to the kidney's high permittivity, the displacement current due to the source electric field generates a field that enhances the incident magnetising field. On the other hand, the appreciable eddy current induced in the thyroid arising from its higher conductivity generates a counter field that negates the incident magnetising field as a consequence of Lenz's law. However, at 50 kHz, these frequency dependent contributions are negligible.

Between these extremes, the fat shows little difference in magnetising field strength, field penetration and field focusing performance compared to that of air. In any case, since the difference is capped below 1 % even under the worst scenarios and typical tissues such as fat show no appreciable performance or field strength difference compared with that of air, the field strength obtained by using air as the target media is therefore representative of that in the biological target media for all practical purposes.

| Field | Media | | | |
|---|---|---|---|---|
| | Air | Kidney | Fat | Thyroid |
| Peak position ***a*** | 6.32 | 6.32 | 6.32 | 6.32 |
| HC(0,0,0) | 440.39 | 442.95 | 440.40 | 436.21 |
| HT(0,7.0,0) | 484.13 | 487.08 | 484.15 | 479.48 |
| HP(0,***a***,0) | 583.70 | 587.27 | 583.72 | 578.08 |
| HL(-7.5,0,0) | 291.81 | 293.26 | 291.82 | 289.20 |
| HLT(-7.5,7.0,0) | 881.63 | 888.98 | 881.67 | 872.97 |
| HF(0,0,-7.5) | 290.75 | 292.19 | 290.76 | 288.15 |
| H(1/2P) | 311.40 | 313.21 | 311.41 | 308.44 |
| HPBW | 13.98 | 13.88 | 13.98 | 13.98 |
| HC/HL | 1.51 | 1.51 | 1.51 | 1.51 |
| HC/HF | 1.51 | 1.52 | 1.51 | 1.51 |
| HP/HC | 1.33 | 1.33 | 1.33 | 1.33 |
| HLT/HC | 2.00 | 2.01 | 2.00 | 2.00 |
| HT/HC | 1.10 | 1.10 | 1.10 | 1.10 |

Note: the unit of position ***a*** & HPBW is cm and the unit of the magnetising field is A /m.

Table 4.6 Performance metric of the spherical distributed coil applicator with various types of media in the target space.

### 4.9 Effect of the Return Media

While the applicator can work without a closed-loop return media, the return media is a standard fixture in the state of the art applicators. The return media may reduce the magnetic path reluctance, thus leading to either a lower magnetomotive force, i.e. a lower current for the same magnetising field or a higher magnetising field for the same excitation current. In this investigation, the spherical distributed coil applicator model with a uniform turn pitch and deflector plates at the poles is used with the return media under investigation appended to this applicator. The return media is varied in (a) path length, (b) path width and (c) path permeability.

The nominal return path starts from 0.5 cm behind each pole, traversing the path shown schematically in Fig 4.17 where $L_1$ = 26 cm, $L_2$ = 15 cm & $L_3$ = 46 cm with a fillet radius of 8 cm, hence the average path length of 2 x 26 + 2 x 15 + 46 – (4 x 16 – 16π) = 114 cm and it's built with an 8 cm in diameter ferrite core of relative permeability $\mu_r$ = 2,000. The isometric view of this 3D model is shown in Fig 4.18(a).

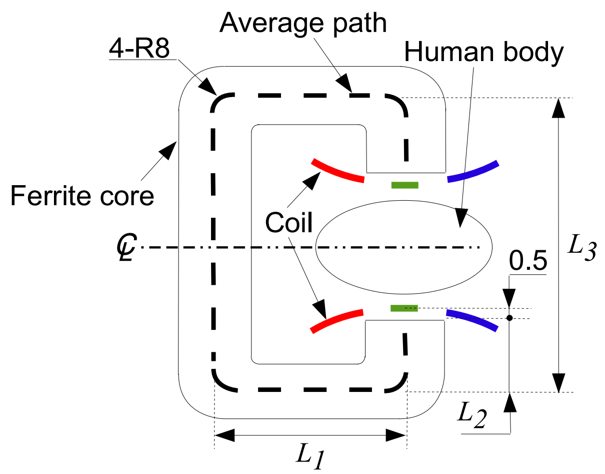


Fig 4.17 Schematic of the ferrite return media's path.

For comparison with a short return media, the nominal return path was varied such that $L_1 = 20$ cm, $L_2 = 12$ cm & $L_3 = 40$, hence the average path length of 2 x 20 + 2 x 12 + 40 – (4 x 16 – 16π) = 90 cm. The isometric view of this 3D model is shown in Fig 4.18(b).

An applicator model with a nominal but wider return path at a diameter of 14 cm as shown in Fig 4.18(c) was also built for investigating the effect of a wide return path. Last but not least, a 3D model of the applicator with a nominal return path as shown in Fig 4.16(a) but using a ferrite core with a relative permeability $\mu_r$ = 10,000 was also built for investigating the effect of a high return path permeability.

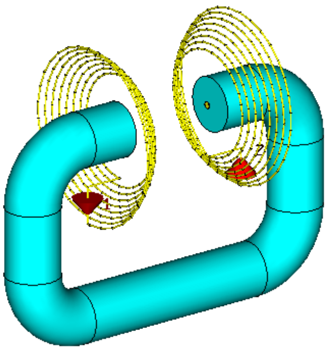

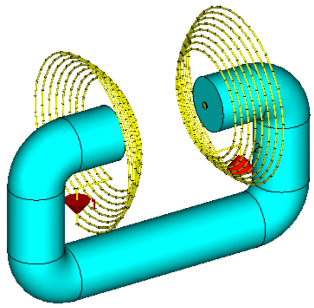

(a) (b)

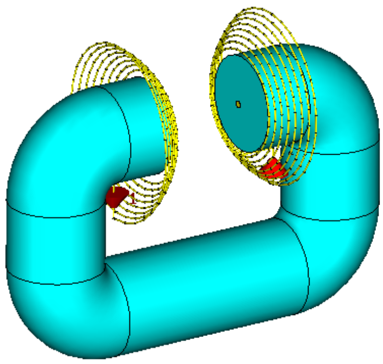

(c)

Fig 4.18 Isometric view of the spherical distributed coil applicator with 8 cm in diameter, (a) nominal 114 cm & (b) short 90 cm average path length return media and (c) 14 cm in diameter, 114 cm average path length return media.

The 3D models of the spherical distributed coil applicator with deflector plates at both poles with (a) no ferrite return path, (b) a nominal ferrite return path, (c) a short ferrite return path, (d) a wide ferrite return path and (e) a high permeability ferrite return path were simulated using a 15 $A_{pk}$ 50 kHz source such that the fields build constructively, resulting in the plots of magnetising field (a) along the coil's axis and (b) along the symmetry plane shown in Figs 4.19 and 4.20 respectively.

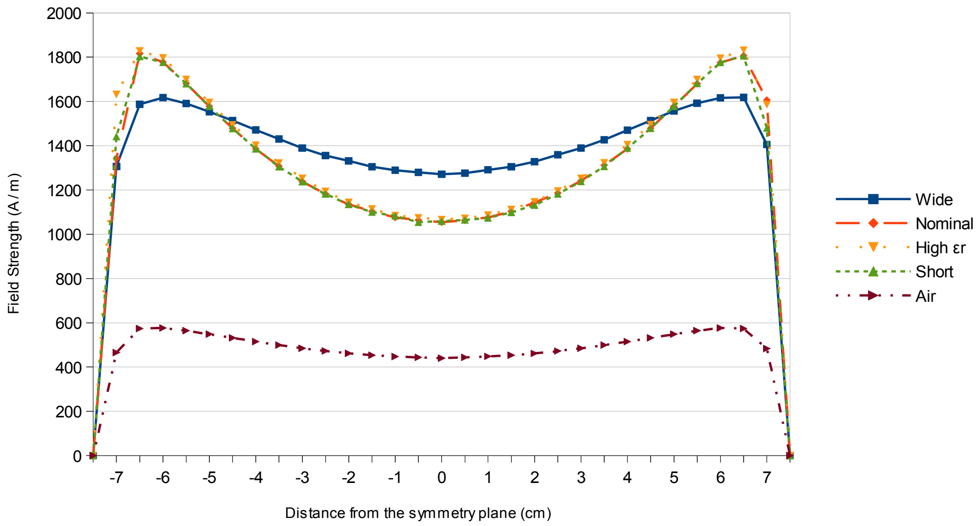


Fig 4.19 Field strength along the coil's axis for applicators with various return path and media.

With a higher permeability, the ferrite return path has a lower magnetic reluctance and thus a lower magnetomotive force drop along the return path. This leaves a higher magnetomotive force in the target space and thus, a higher magnetising field for the same excitation at the source. Since more than one half of each coil's magnetic path has been bypassed by the ferrite return path, the field increase should in principle be more than 2 times as confirmed by the ~ 2.5 to 3 times increase shown in Fig 4.19. By almost covering the pole, the wide return path also distributes the magnetic field over the pole, hence its lower field peak and farther field penetration. Save for the region near the poles, there is little field strength difference between the return paths with relative permeability $\mu_r = 2{,}000$ and $\mu_r = 10{,}000$. This is due to the reason that at $\mu_r = 2{,}000$, the ferrite return path's magnetic reluctance (2,000 times lower) is already negligible compared to that across the target space and increasing $\mu_r$ further would not reduce the total magnetic reluctance and therefore, the magnetising field in the target space appreciably. For the same reason, there is also negligible field strength difference between the nominal return path and the short return path applicators.

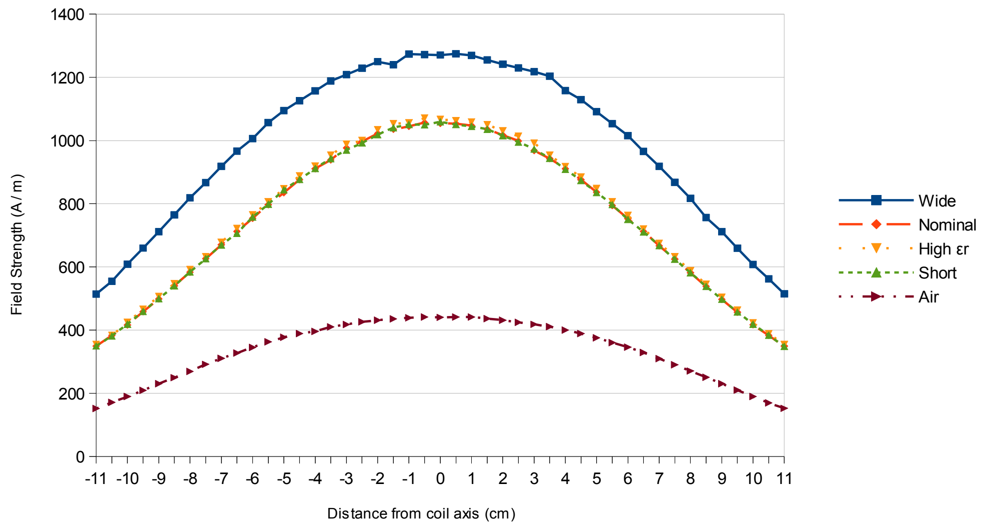


Fig 4.20 Field strength along the symmetry plane for applicators with various return path and media.

Fig 4.20 confirms again the field strength increase due to the low magnetic reluctance of the ferrite return path. For the same reason, there is also little change in field strength along the symmetry plane when the relative permeability $\mu_r$ is increased beyond 2,000 or when the return path is shortened.

| Field | | Path diameter | | Path length | | Permeability | |
|---|---|---|---|---|---|---|---|
| | Air | 8cm | 14cm | 114cm | 90cm | $\mu_r = 2000$ | $\mu_r = 10000$ |
| Peak position P | 6.32 | -6.32 | 6.47 | -6.32 | -6.31 | -6.32 | 6.30 |
| HC(0,0,0) | 440.39 | 1054.34 | 1270.79 | 1054.34 | 1059.29 | 1054.34 | 1066.90 |
| HT(0,7.0,0) | 484.13 | 1606.14 | 1405.57 | 1606.14 | 1479.26 | 1606.14 | 1585.32 |
| HP(0,***a***,0) | 583.70 | 1841.01 | 1630.72 | 1841.01 | 1828.68 | 1841.01 | 1852.43 |
| HL(-7.5,0,0) | 291.81 | 626.21 | 867.13 | 626.21 | 626.13 | 626.21 | 632.33 |
| HLT(-7.5,7.0,0) | 881.63 | 1321.28 | 2346.30 | 1321.28 | 1363.07 | 1321.28 | 1420.41 |
| HF(0,0,-7.5) | 290.75 | 625.34 | 863.52 | 625.34 | 618.48 | 625.34 | 633.79 |
| H(1/2P) | 311.40 | 745.53 | 898.59 | 745.53 | 749.03 | 745.53 | 754.41 |
| HPBW | 13.98 | 12.22 | 14.34 | 12.22 | 12.22 | 12.22 | 12.16 |
| HC/HL | 1.51 | 1.68 | 1.47 | 1.68 | 1.69 | 1.68 | 1.69 |
| HC/HF | 1.51 | 1.69 | 1.47 | 1.69 | 1.71 | 1.69 | 1.68 |
| HP/HC | 1.33 | 1.75 | 1.28 | 1.75 | 1.73 | 1.75 | 1.74 |
| HLT/HC | 2.00 | 1.25 | 1.85 | 1.25 | 1.29 | 1.25 | 1.33 |
| HT/HC | 1.10 | 1.52 | 1.11 | 1.52 | 1.40 | 1.52 | 1.49 |

Note: the unit of position ***a*** & HPBW is cm and the unit of the magnetising field is A /m.

Table 4.7 Performance metric of spherical distributed coil applicators with various return path and media.

With an 8 cm in diameter return path barely covering a quarter of the pole's area, the nominal ferrite return path has the effect of concentrating the flux around the coil's axis, much like a solenoid. Therefore, its field focusing is better than that of the air return path applicator but the contrary is true for its field penetration. However, when the ferrite return path is widened to 14 cm in diameter and almost covering the pole's area, the magnetic flux is evened out over a larger area, hence its better field penetration at a higher HPBW. Indeed, its performance is comparable to that of the air return path but at a much higher magnetising field strength.

Although not discernible from the plots, the performance metric comparing the various path lengths as listed in Table 4.7 shows that by reducing the return path length by 21 % from 114 cm to 90 cm, the field strength only increases marginally in the middle between the coils by under 0.5 %. The field strength at the deflector plates also increases, resulting in a higher cancellation field. This further suppresses the peak field but at the same time, this also increases the field strength at the fringe of the deflector plates. Fortunately, in the short ferrite return path, flux leakages at the symmetry plane near the return path also weaken its surrounding field strength. Therefore, the HPBW remains unchanged but the field penetration is improved slightly.

By using a ferrite return path with a relative permeability $\mu_r$ = 10,000, its path magnetic reluctance is reduced by 5 times comparatively. Therefore, the overall field strength is also increased, although marginally by 1 % in the middle between the coils. As before, the field strength increase at the poles results in a stronger cancellation field from the deflector plates, thereby further weakening the peak field strength, hence the slightly better field penetration. However, with much of the magnetic flux already concentrated along the coil's axis in the target space by the high $\mu_r$ material, such a marginal increase in field strength can only yield a very marginal improvement in HPBW.

In general, a ferrite return path can optionally be added to increase the field strength level of the applicator but its path diameter has to be sufficiently wide in order to maintain the trade-off between field penetration and field focusing. However, this applicator may be bulky and suffer from additional ferrite losses. Without any significant advantage in the field penetration and field focusing trade-off, this option will not be considered in subsequent investigations.

**4.10 Correlation with the 2D Analytical Model**

For the purpose of correlating the 3D simulation output with the scaled results of the 2D analytical model, the spherical distributed coil applicator with no deflector plate is used. Referring to the 2D analytical result for the convex distributed coil applicator with $\boldsymbol{l} / \boldsymbol{b} = 1$, $\boldsymbol{r} / \boldsymbol{b} = 2$ and separated by $2\boldsymbol{p} / \boldsymbol{b} = 2$ as shown in Table 3.1, the field strength in the middle between the coils is 0.647 $\boldsymbol{J}/\pi$. With $\boldsymbol{b}$ = 7.5 cm, and $\boldsymbol{J} = (8 \times 15 / \boldsymbol{l}) = 1{,}600$ A m$^{-1}$, this field strength is thus 329 A m$^{-1}$.

For scaling this field strength to that in the comparative 3D model, the 2D and 3D analytical models of the Helmholtz coil are used. The magnetic flux density in the middle of a 2D Helmholtz coil, derived in Appendix A.11 is expressed by Eq 4.16.

$$B_{2D}=\frac{8\,\mu NI}{5\,\pi d} \tag{4.16}$$

Dividing Eq 4.16 by the magnetic flux density in the middle of a 3D Helmholtz coil, expressed by Eq 4.17 (Gyawali 2008) yields the scaling ratio of the 2D to 3D midpoint field strength values as worked out in Eq 4.18.

$$B_{3D}=\left(\frac{4}{5}\right)^{\left(\frac{3}{2}\right)}\frac{uNI}{d} \tag{4.17}$$

$$\frac{B_{3D}}{B_{2D}}=\frac{H_{3D}}{H_{2D}}=\frac{\pi}{2}\left(\frac{4}{5}\right)^{\frac{1}{2}}=1.404 \tag{4.18}$$

While Eq 4.18 is strictly valid for the Helmholtz coil only, the comparable geometrical similarity between the Helmholtz coil and the spherical distributed coil applicator suggests that this ratio is likely to approximate that of the applicator. Applying this scaling ratio on the 2D midpoint field strength of 329 A $m^{-1}$ yields the corresponding 3D field strength of 1.404 (329) = 462.64 A $m^{-1}$.

By comparing this value with the corresponding 3D simulated field strength value of 443.00 A $m^{-1}$ taken from Table 4.2, the difference between these values is within 5 %. This good agreement lends additional credibility to the output of the 2D analytical models and its utility as a design tool.

## 4.11 Concluding Remarks

Expanding on the 2D concave distributed coil applicator selected earlier, 3D simulation models were developed and duly verified. Some properties and advantages of various coil shapes, current density distributions and return media paths were discovered and evaluated using a performance metric system. Deflector plates were incorporated and optimised after this opportunity for improvement was discovered during the evaluation process. The simulation output also confirms the inert nature of biological tissues on the magnetic field. Based on the performance metric, the spherical distributed coil applicator with a uniform current density & turn pitch, deflector plates and air core return was selected for prototype realisation and verification against its simulated flux density in the target space as illustrated in Fig 4.21 at the selected axes.

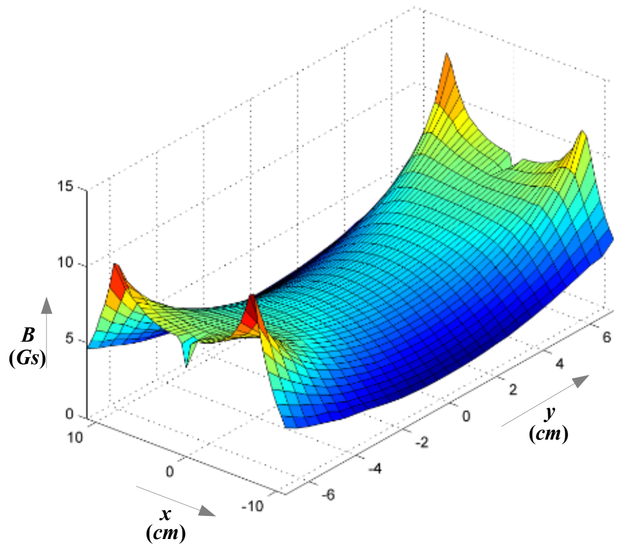


Fig 4.21 Simulated flux density in the target space of the selected applicator design.

# CHAPTER 5

# PROTOTYPE AND EXPERIMENT

## 5.1 Background

The simulation results of the 3D model of the spherical distributed coil applicator with deflector plates and a uniform turn pitch were verified against the actual measurements made on a physical prototype constructed based on the 3D model parameters. The prototype was excited by a high frequency power converter and measurements were made using a high slew-rate Hall sensor. This experiment was done at both 50 Hz and 50 kHz excitation frequencies.

## 5.2 Coil Construction

Based on the coil's construction parameters shown in Table 5.1, 2 similar prototype coils using single core enamel wires were wound on formers made from laminated corrugated papers. Corrugated paper was chosen for its inert electrical and magnetic properties at both 50 Hz and 50 kHz.

| Attribute | Parameter |
|---|---|
| Inner radius (***b***) | 7.5 cm |
| Breadth (***l***) | 7.85 cm |
| Curvature (***r***) | 15 cm |
| Wire diameter | 2.6 mm (AWG #10) |
| No of turns (***N***) | 8 |

Table 5.1 Coil's construction parameters.

A 1 mm thick copper disc of 1 cm in diameter was attached to each pole on the former, centred on the coil's axis and both the coils were assembled 15 cm apart pole-to-pole at 4 cm from a hollow wooden platform. Like the formers, hollow wood was chosen for its inert electrical and magnetic nature. A measurement table made from laminated corrugated paper and laced with measurement graph scales was placed in between the coils. Fig 5.1 shows the prototype and the measurement table.

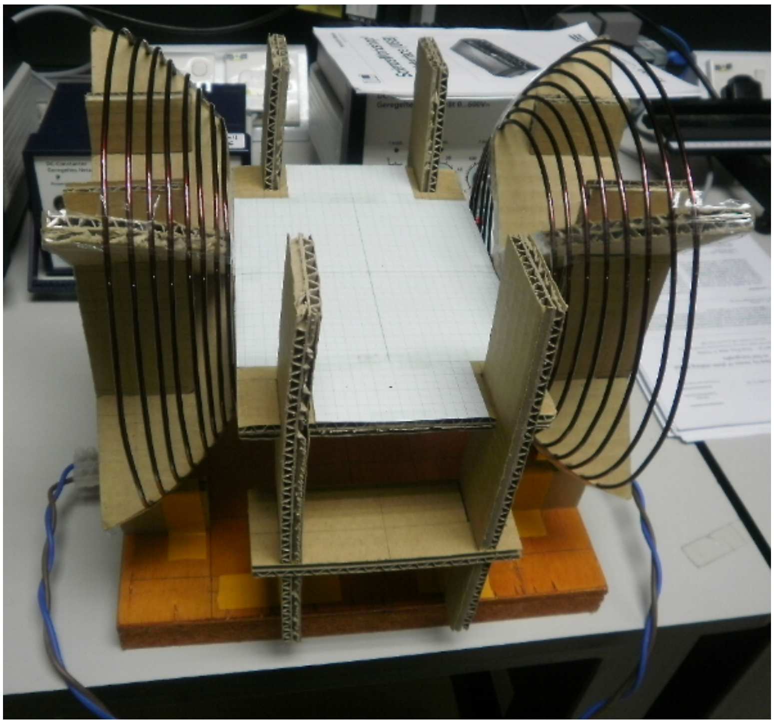

Fig 5.1 The coil applicator prototype and the measurement table.

The connections to the coils were made using a twisted pair of braided AWG#12 wires to minimise field leakages. This common applicator was used for field measurements at both 50 Hz and 50 kHz.

### 5.3 Measurement Table

Measurements were taken on the ***x-y*** plane along 4 axes: ***y*** = 0, ***y*** = 3.5, ***y*** = 7 and ***x*** = 0 as shown schematically in Fig 5.2, viewed from the top, where the origin (0,0) is in the centre between the coils along the coil's axis.

The magnetic flux density was measured at the following points along these major axes: (a) (***x***,0), ***x*** ϵ [-11,+11], (b) (***x***,3.5), ***x*** ϵ [-11,+11], and minor axes: (c) (***x***,7), ***x*** ϵ [-7,+7] and (d) (0,***y***), ***y*** ϵ [-7,+7], at intervals of 1 cm that have been marked out on the measurement table. The flux density at the $y < 0$ half plane was not measured due to the symmetry along the $x$ axis. Likewise, only the flux density on the $x$-$y$ plane was measured due to the rotational symmetry around the coil's axis. Like the applicator, the measurement table was used for field measurements at both 50 Hz and 50 kHz.

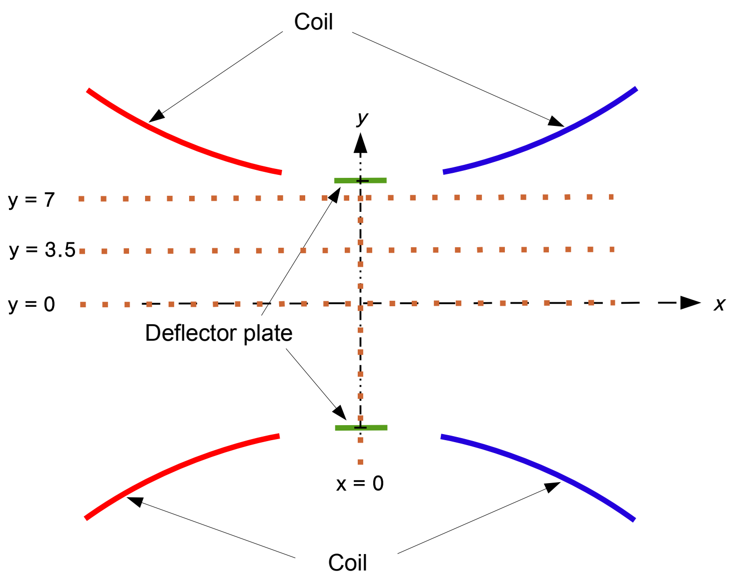


Fig 5.2 Schematic of the measurement axes on the $x$-$y$ plane, viewed from the top.

**5.4 Experiment at 50Hz**

For the 50 Hz experiment, an AC current injector was used as the current source and a commercial Hall magnetometer was used to measure the magnetic flux density. The AC current source is made of a variac with its variable output voltage fed into an EI-50 transformer rated at 750 VA with a primary to secondary turn ratio of 300 : 5 as shown in Fig 5.3. By adjusting the variac dial, the transformer's secondary output voltage was varied until the desired current of 15Arms was achieved.

Fig 5.3 AC 50 Hz current source.

The magnetic flux density measurements were taken by using a commercial Hall magnetometer capable of 0.1 Gauss resolution with a 1 kHz bandwidth. The experiment was set up by connecting the applicator, current source, magnetometer and other measuring instruments as shown schematically in Fig 5.4.

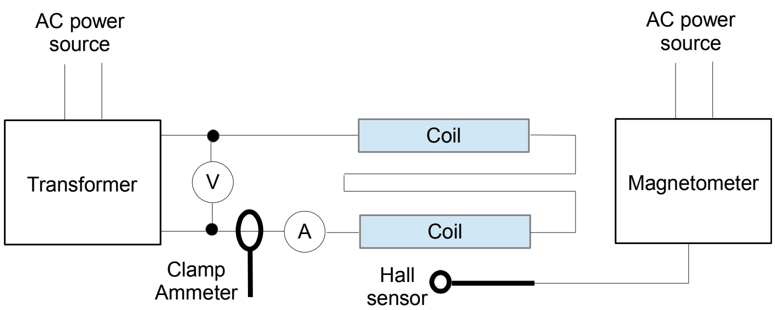


Fig 5.4 Schematic connections of the 50 Hz experiment setup.

The current was monitored by using both clamp and series ammeters as shown in Figs 5.4 and 5.5.

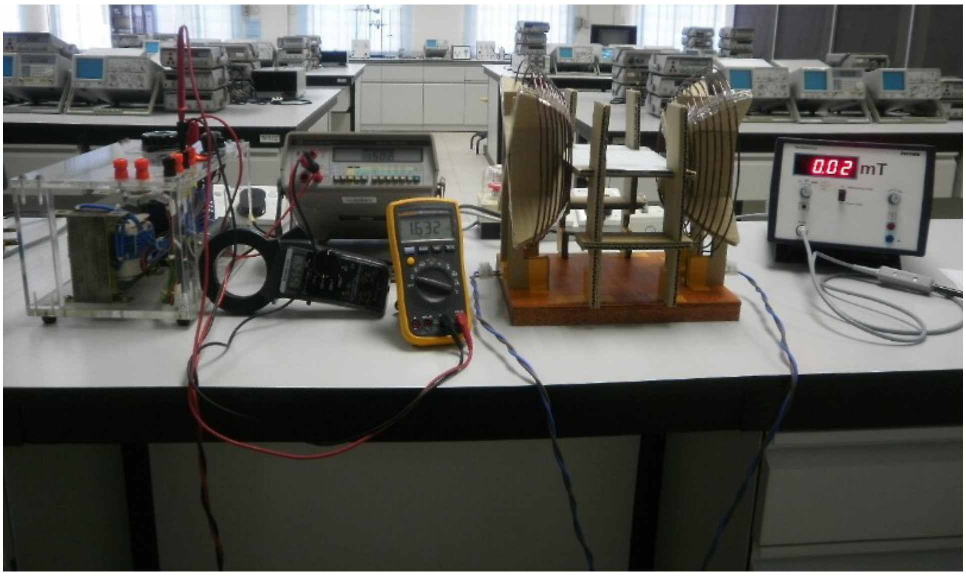


Fig 5.5 The 50 Hz experiment setup.

### 5.4.1 Measurements and Results at 50 Hz

The procedure for setting up the experiment and taking the measurements is given in Appendix D.1. The measurements of both the ***x*** and ***y*** field components at each chosen field point were taken with the Hall sensor magnetic axis parallel and anti-parallel to the ***x*** and ***y*** axes to check for measurement asymmetries due to factors such as stray field and current loops. Tables 5.2, 5.3, 5.4(a) and 5.4(b) show the flux density measurements along the major axes ***y*** = 0, ***y*** = 3.5 and minor axes ***y*** = 7 and ***x*** = 0 respectively.

| x | Measured using fluxmeter S/N: 230700221733, Date done: 13 June 2012 | | | | | | Measured using fluxmeter S/N: 360500184913, Date done: 7th June 2012 | | | | | | Simulation output | | | Error | | | |
|---|---|---|---|---|---|---|---|---|---|---|---|---|---|---|---|---|---|---|---|
| | By1+ (meas) | By1- (meas) | Bx1+ (meas) | Bx1- (meas) | Babs1+ (meas) | Babs1- (meas) | By2+ (meas) | By2- (meas) | Bx2+ (meas) | Bx2- (meas) | Babs2+ (meas) | Babs2- (meas) | By (sim) | Bx (sim) | Babs (sim) | By (mag) | Bx (mag) | Babs (mag) | Babs (%) |
| -11 | 18 | 19 | 2 | 2 | 18 | 19 | 18 | 19 | 2 | 2 | 18 | 19 | 19 | 0 | 19 | 0 | 2 | 0 | 1 |
| -10 | 22 | 23 | 2 | 2 | 22 | 23 | 23 | 23 | 2 | 2 | 23 | 23 | 24 | 0 | 24 | 1 | 2 | 1 | 4 |
| -9 | 27 | 28 | 2 | 2 | 27 | 28 | 27 | 28 | 2 | 2 | 27 | 28 | 29 | 0 | 29 | 1 | 2 | 1 | 4 |
| -8 | 32 | 33 | 2 | 2 | 32 | 33 | 32 | 33 | 2 | 3 | 32 | 33 | 34 | 0 | 34 | 1 | 2 | 1 | 3 |
| -7 | 37 | 37 | 2 | 2 | 37 | 37 | 37 | 38 | 2 | 3 | 37 | 38 | 39 | 1 | 39 | 1 | 1 | 1 | 3 |
| -6 | 41 | 41 | 2 | 2 | 41 | 41 | 41 | 42 | 2 | 3 | 41 | 42 | 44 | 1 | 44 | 2 | 1 | 1 | 3 |
| -5 | 45 | 46 | 2 | 2 | 45 | 46 | 45 | 46 | 2 | 2 | 45 | 46 | 48 | 1 | 48 | 2 | 1 | 1 | 3 |
| -4 | 48 | 49 | 2 | 2 | 48 | 49 | 48 | 49 | 2 | 2 | 48 | 49 | 50 | 1 | 50 | 1 | 1 | 1 | 2 |
| -3 | 50 | 51 | 2 | 2 | 50 | 51 | 51 | 52 | 2 | 2 | 51 | 52 | 53 | 1 | 53 | 1 | 1 | 1 | 1 |
| -2 | 52 | 53 | 3 | 2 | 52 | 53 | 53 | 53 | 2 | 2 | 53 | 53 | 54 | 0 | 54 | 1 | 2 | 1 | 2 |
| -1 | 53 | 54 | 2 | 2 | 53 | 54 | 53 | 54 | 2 | 2 | 53 | 54 | 55 | 0 | 55 | 1 | 2 | 1 | 2 |
| 0 | 54 | 54 | 2 | 2 | 54 | 54 | 55 | 55 | 2 | 2 | 55 | 55 | 55 | 0 | 55 | 0 | 2 | 0 | 1 |
| 1 | 53 | 54 | 2 | 2 | 53 | 54 | 54 | 55 | 2 | 2 | 54 | 55 | 56 | 0 | 56 | 1 | 2 | 1 | 1 |
| 2 | 53 | 53 | 2 | 2 | 53 | 53 | 53 | 54 | 2 | 2 | 53 | 54 | 54 | 0 | 54 | 0 | 2 | 0 | 1 |
| 3 | 51 | 52 | 3 | 2 | 51 | 52 | 52 | 52 | 2 | 2 | 52 | 52 | 53 | 0 | 53 | 1 | 2 | 1 | 1 |
| 4 | 50 | 50 | 2 | 2 | 50 | 50 | 49 | 50 | 2 | 2 | 49 | 50 | 50 | 1 | 50 | 0 | 1 | 0 | 1 |
| 5 | 46 | 47 | 2 | 2 | 46 | 47 | 46 | 46 | 2 | 2 | 46 | 46 | 47 | 1 | 47 | 0 | 1 | 0 | 1 |
| 6 | 42 | 42 | 2 | 2 | 42 | 42 | 43 | 43 | 2 | 2 | 43 | 43 | 44 | 1 | 44 | 1 | 1 | 1 | 1 |
| 7 | 38 | 39 | 2 | 2 | 38 | 39 | 38 | 39 | 2 | 3 | 38 | 39 | 39 | 1 | 39 | 0 | 1 | 0 | 0 |
| 8 | 33 | 34 | 2 | 2 | 33 | 34 | 33 | 34 | 2 | 3 | 33 | 34 | 34 | 1 | 34 | 0 | 1 | 0 | 0 |
| 9 | 28 | 28 | 2 | 2 | 28 | 28 | 28 | 28 | 2 | 2 | 28 | 28 | 29 | 0 | 29 | 1 | 2 | 1 | 4 |
| 10 | 23 | 23 | 2 | 2 | 23 | 23 | 23 | 23 | 2 | 2 | 23 | 23 | 24 | 0 | 24 | 1 | 2 | 1 | 4 |
| 11 | 18 | 19 | 2 | 2 | 18 | 19 | 17 | 18 | 2 | 2 | 17 | 18 | 19 | 0 | 19 | 0 | 2 | 0 | 1 |

Note: the unit of position ***x*** is cm and B is in multiples of 0.1 Gs unless otherwise specified.

Table 5.2 Flux density measurements and comparison along the $\boldsymbol{y} = 0$ major axis at 50 Hz.

| x | Measured using fluxmeter S/N: 230700221733, Date done: 13 June 2012 | | | | | | Measured using fluxmeter S/N: 360500184913, Date done: 7th June 2012 | | | | | | Simulation output | | | Error | | | |
|---|---|---|---|---|---|---|---|---|---|---|---|---|---|---|---|---|---|---|---|
| | By1+ (meas) | By1- (meas) | Bx1+ (meas) | Bx1- (meas) | Babs1+ (meas) | Babs1- (meas) | By2+ (meas) | By2- (meas) | Bx2+ (meas) | Bx2- (meas) | Babs2+ (meas) | Babs2- (meas) | By (sim) | Bx (sim) | Babs (sim) | By (mag) | Bx (mag) | Babs (mag) | Babs (%) |
| -11 | 18 | 18 | 17 | 17 | 25 | 25 | 17 | 18 | 15 | 16 | 23 | 24 | 19 | 17 | 26 | 1 | 0 | 1 | 5 |
| -10 | 24 | 23 | 19 | 20 | 31 | 30 | 24 | 25 | 18 | 19 | 30 | 31 | 27 | 20 | 33 | 2 | 0 | 2 | 6 |
| -9 | 30 | 30 | 20 | 21 | 36 | 37 | 30 | 30 | 20 | 21 | 36 | 37 | 33 | 20 | 39 | 3 | 0 | 2 | 6 |
| -8 | 37 | 37 | 20 | 21 | 42 | 43 | 38 | 38 | 20 | 19 | 43 | 42 | 41 | 20 | 46 | 3 | 0 | 3 | 6 |
| -7 | 44 | 44 | 20 | 20 | 48 | 48 | 44 | 45 | 18 | 19 | 48 | 49 | 47 | 17 | 50 | 2 | 1 | 1 | 2 |
| -6 | 49 | 49 | 18 | 18 | 52 | 52 | 49 | 50 | 15 | 15 | 51 | 52 | 52 | 14 | 54 | 2 | 1 | 2 | 4 |
| -5 | 53 | 53 | 16 | 16 | 55 | 55 | 53 | 54 | 13 | 14 | 55 | 56 | 56 | 11 | 57 | 2 | 2 | 1 | 2 |
| -4 | 56 | 56 | 13 | 14 | 57 | 58 | 56 | 57 | 8 | 9 | 57 | 58 | 59 | 8 | 59 | 2 | 0 | 2 | 3 |
| -3 | 58 | 58 | 10 | 11 | 59 | 59 | 58 | 59 | 6 | 6 | 58 | 59 | 61 | 6 | 61 | 2 | 0 | 2 | 3 |
| -2 | 59 | 59 | 8 | 8 | 60 | 60 | 60 | 60 | 5 | 4 | 60 | 60 | 62 | 4 | 62 | 2 | 0 | 2 | 3 |
| -1 | 60 | 60 | 3 | 5 | 60 | 60 | 61 | 60 | 2 | 2 | 61 | 60 | 62 | 2 | 62 | 1 | 0 | 1 | 2 |
| 0 | 61 | 61 | 2 | 3 | 61 | 61 | 62 | 61 | 2 | 3 | 62 | 61 | 63 | 0 | 63 | 1 | 2 | 1 | 1 |
| 1 | 61 | 61 | 3 | 3 | 61 | 61 | 61 | 62 | 2 | 3 | 61 | 62 | 63 | 2 | 63 | 1 | 0 | 1 | 1 |
| 2 | 60 | 61 | 3 | 3 | 60 | 61 | 60 | 61 | 3 | 4 | 60 | 61 | 62 | 4 | 63 | 1 | 0 | 1 | 2 |
| 3 | 60 | 60 | 4 | 3 | 60 | 60 | 60 | 61 | 5 | 4 | 60 | 61 | 61 | 7 | 62 | 0 | 2 | 1 | 1 |
| 4 | 59 | 59 | 5 | 4 | 59 | 59 | 58 | 59 | 6 | 7 | 58 | 59 | 60 | 10 | 61 | 1 | 3 | 1 | 2 |
| 5 | 57 | 57 | 9 | 8 | 58 | 58 | 56 | 56 | 11 | 12 | 57 | 57 | 57 | 13 | 59 | 0 | 1 | 1 | 2 |
| 6 | 53 | 53 | 11 | 10 | 54 | 54 | 52 | 52 | 14 | 15 | 54 | 54 | 53 | 16 | 55 | 0 | 1 | 1 | 2 |
| 7 | 48 | 47 | 14 | 14 | 50 | 49 | 47 | 48 | 17 | 17 | 50 | 51 | 47 | 20 | 51 | 0 | 3 | 0 | 0 |
| 8 | 40 | 41 | 16 | 18 | 43 | 45 | 40 | 40 | 20 | 21 | 45 | 45 | 40 | 21 | 45 | 0 | 0 | 0 | 1 |
| 9 | 33 | 32 | 18 | 19 | 38 | 37 | 31 | 32 | 21 | 22 | 37 | 39 | 32 | 21 | 38 | 0 | 0 | 1 | 2 |
| 10 | 24 | 23 | 20 | 19 | 31 | 30 | 24 | 24 | 20 | 19 | 31 | 31 | 24 | 20 | 31 | 0 | 0 | 0 | 0 |
| 11 | 18 | 18 | 18 | 18 | 25 | 25 | 17 | 17 | 18 | 17 | 25 | 24 | 18 | 18 | 25 | 0 | 0 | 0 | 1 |

Note: the unit of position ***x*** is cm and B is in multiples of 0.1 Gs unless otherwise specified.

Table 5.3 Flux density measurements and comparison along the ***y*** = 3.5 major axis at 50 Hz .

| x | Measured using fluxmeter S/N: 230700221733, Date done: 13 June 2012 | | | | | | Measured using fluxmeter S/N: 360500184913, Date done: 7th June 2012 | | | | | | Simulation output | | | Error | | | |
|---|---|---|---|---|---|---|---|---|---|---|---|---|---|---|---|---|---|---|---|
| | By1+ (meas) | By1- (meas) | Bx1+ (meas) | Bx1- (meas) | Babs1+ (meas) | Babs1- (meas) | By2+ (meas) | By2- (meas) | Bx2+ (meas) | Bx2- (meas) | Babs2+ (meas) | Babs2- (meas) | By (sim) | Bx (sim) | Babs (sim) | By (mag) | Bx (mag) | Babs (mag) | Babs (%) |
| -7 | 91 | 90 | 50 | 51 | 104 | 103 | 94 | 95 | 42 | 43 | 103 | 104 | 96 | 39 | 103 | 1 | 3 | 0 | 0 |
| -6 | 88 | 89 | 28 | 30 | 92 | 94 | 88 | 89 | 19 | 20 | 90 | 91 | 90 | 22 | 92 | 1 | 2 | 0 | 0 |
| -5 | 84 | 84 | 22 | 21 | 87 | 87 | 84 | 85 | 17 | 18 | 86 | 87 | 84 | 14 | 85 | 0 | 3 | 1 | 1 |
| -4 | 80 | 80 | 13 | 12 | 81 | 81 | 80 | 80 | 18 | 10 | 82 | 81 | 81 | 9 | 81 | 1 | 1 | 0 | 0 |
| -3 | 78 | 78 | 10 | 9 | 79 | 79 | 78 | 78 | 7 | 7 | 78 | 78 | 78 | 6 | 79 | 0 | 1 | 0 | 0 |
| -2 | 76 | 76 | 5 | 6 | 76 | 76 | 77 | 76 | 4 | 5 | 77 | 76 | 77 | 4 | 77 | 0 | 0 | 0 | 0 |
| -1 | 75 | 75 | 4 | 5 | 75 | 75 | 76 | 75 | 3 | 3 | 76 | 75 | 77 | 3 | 77 | 1 | 0 | 1 | 1 |
| 0 | 75 | 75 | 3 | 3 | 75 | 75 | 75 | 74 | 2 | 3 | 75 | 74 | 77 | 1 | 77 | 2 | 1 | 2 | 2 |
| 1 | 75 | 75 | 3 | 2 | 75 | 75 | 75 | 76 | 3 | 4 | 75 | 76 | 77 | 1 | 77 | 1 | 1 | 1 | 2 |
| 2 | 76 | 76 | 2 | 2 | 76 | 76 | 76 | 77 | 5 | 6 | 76 | 77 | 79 | 2 | 79 | 2 | 0 | 2 | 2 |
| 3 | 78 | 78 | 2 | 2 | 78 | 78 | 78 | 79 | 5 | 6 | 78 | 79 | 81 | 5 | 81 | 2 | 0 | 2 | 2 |
| 4 | 81 | 81 | 3 | 3 | 81 | 81 | 81 | 82 | 7 | 7 | 81 | 82 | 85 | 8 | 85 | 3 | 1 | 3 | 3 |
| 5 | 86 | 86 | 6 | 6 | 86 | 86 | 86 | 87 | 12 | 12 | 87 | 88 | 90 | 13 | 91 | 3 | 1 | 3 | 3 |
| 6 | 95 | 94 | 15 | 15 | 96 | 95 | 93 | 94 | 19 | 20 | 95 | 96 | 99 | 24 | 102 | 4 | 4 | 6 | 6 |
| 7 | 106 | 106 | 33 | 34 | 111 | 111 | 105 | 106 | 42 | 43 | 113 | 114 | 108 | 50 | 120 | 2 | 7 | 5 | 4 |

Note: the unit of position ***x*** is cm and B is in multiples of 0.1 Gs unless otherwise specified.

(a)

| y | Measured using fluxmeter S/N: 230700221733, Date done: 13 June 2012 | | | | | | Measured using fluxmeter S/N: 360500184913, Date done: 7th June 2012 | | | | | | Simulation output | | | Error | | | |
|---|---|---|---|---|---|---|---|---|---|---|---|---|---|---|---|---|---|---|---|
| | By1+ (meas) | By1- (meas) | Bx1+ (meas) | Bx1- (meas) | Babs1+ (meas) | Babs1- (meas) | By2+ (meas) | By2- (meas) | Bx2+ (meas) | Bx2- (meas) | Babs2+ (meas) | Babs2- (meas) | By (sim) | Bx (sim) | Babs (sim) | By (mag) | Bx (mag) | Babs (mag) | Babs (%) |
| -7 | 75 | 75 | 2 | 2 | 75 | 75 | 76 | 76 | 2 | 2 | 76 | 76 | 76 | 1 | 76 | 0 | 1 | 0 | 0 |
| -6 | 71 | 72 | 2 | 2 | 71 | 72 | 73 | 73 | 2 | 2 | 73 | 73 | 73 | 1 | 73 | 0 | 1 | 0 | 0 |
| -5 | 67 | 68 | 2 | 2 | 67 | 68 | 68 | 68 | 2 | 2 | 68 | 68 | 69 | 0 | 69 | 1 | 2 | 1 | 1 |
| -4 | 63 | 63 | 2 | 2 | 63 | 63 | 64 | 64 | 2 | 2 | 64 | 64 | 65 | 0 | 65 | 1 | 2 | 1 | 1 |
| -3 | 59 | 59 | 2 | 2 | 59 | 59 | 60 | 60 | 2 | 2 | 60 | 60 | 61 | 0 | 61 | 1 | 2 | 1 | 2 |
| -2 | 56 | 56 | 2 | 2 | 56 | 56 | 57 | 57 | 2 | 2 | 57 | 57 | 58 | 0 | 58 | 1 | 2 | 1 | 2 |
| -1 | 54 | 55 | 2 | 3 | 54 | 55 | 55 | 55 | 2 | 2 | 55 | 55 | 56 | 0 | 56 | 1 | 2 | 1 | 2 |
| 0 | 53 | 54 | 2 | 2 | 53 | 54 | 54 | 55 | 2 | 2 | 54 | 55 | 55 | 0 | 55 | 0 | 2 | 0 | 1 |
| 1 | 54 | 55 | 2 | 2 | 54 | 55 | 55 | 56 | 2 | 2 | 55 | 56 | 56 | 0 | 56 | 0 | 2 | 0 | 1 |
| 2 | 55 | 56 | 2 | 2 | 55 | 56 | 57 | 56 | 2 | 2 | 57 | 56 | 58 | 0 | 58 | 1 | 2 | 1 | 2 |
| 3 | 59 | 59 | 2 | 2 | 59 | 59 | 59 | 60 | 2 | 2 | 59 | 60 | 61 | 0 | 61 | 1 | 2 | 1 | 2 |
| 4 | 62 | 62 | 2 | 2 | 62 | 62 | 63 | 64 | 2 | 2 | 63 | 64 | 65 | 0 | 65 | 1 | 2 | 1 | 1 |
| 5 | 67 | 67 | 2 | 2 | 67 | 67 | 67 | 68 | 2 | 2 | 67 | 68 | 69 | 0 | 69 | 1 | 2 | 1 | 1 |
| 6 | 71 | 71 | 2 | 3 | 71 | 71 | 72 | 72 | 2 | 2 | 72 | 72 | 73 | 1 | 73 | 1 | 1 | 1 | 2 |
| 7 | 74 | 75 | 2 | 3 | 74 | 75 | 75 | 75 | 2 | 2 | 75 | 75 | 77 | 1 | 77 | 2 | 1 | 2 | 2 |

Note: the unit of position ***y*** is cm and B is in multiples of 0.1 Gs unless otherwise specified.

(b)

Table 5.4 Flux density measurements and comparison along the (a) ***y*** = 7 and (b) ***x*** = 0 minor axes at 50 Hz.

***Bn+*** and ***Bn-*** are the flux density measurements in the ***n*** axis orientation. The plus attribute in ***Bn+*** denotes the measurement being taken with the Hall sensor's magnetic axis parallel to the ***n*** axis and likewise, the minus attribute in ***Bn-*** denotes the measurement being taken with the Hall sensor's magnetic axis anti-parallel to the ***n*** axis. The magnitude of the flux density, ***Babs+*** is derived from ***By+*** and ***Bx+,*** whereas ***Babs-*** is derived from ***By-*** and ***Bx-***.

This experiment was conducted twice on different days, using different magnetometers for cross verification purpose. The measurements with the numerical notation '1' were taken using the first magnetometer and likewise for those with the numerical notation '2'.

These values were compared with the simulated magnetic flux density output for the applicator at an excitation frequency of 50 Hz to derive the consolidated magnitude error for ***Bx***, ***By*** and ***Babs*** as well as the percentage error for Babs. For visual comparison, the ***Babs***+ and ***Babs***- values are compared with the simulated flux density output as shown in Figs 5.6, 5.7, 5.8 and 5.9 along the major axes y = 0 & y = 3.5 and minor axes y = 7 & x = 0 respectively.

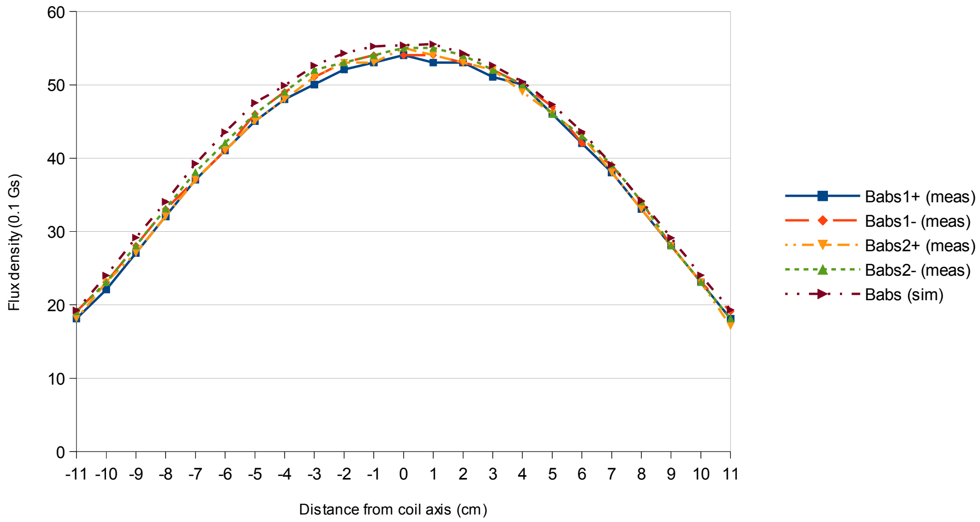


Fig 5.6 The measured ***Babs*** compared with the simulation output ***Babs*** along the major axis ***y*** = 0 at 50 Hz.

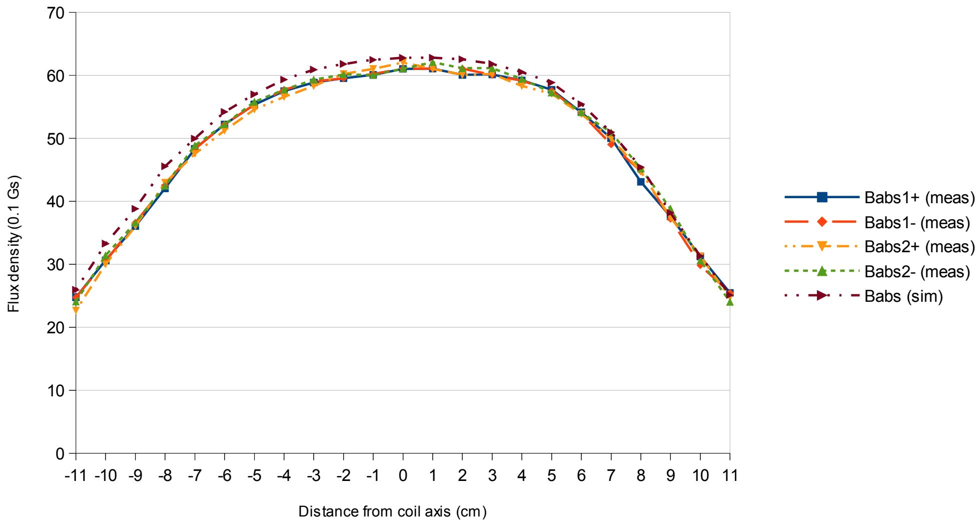


Fig 5.7 The measured ***Babs*** compared with the simulation output ***Babs*** along the major axis ***y*** = 3.5 at 50 Hz.

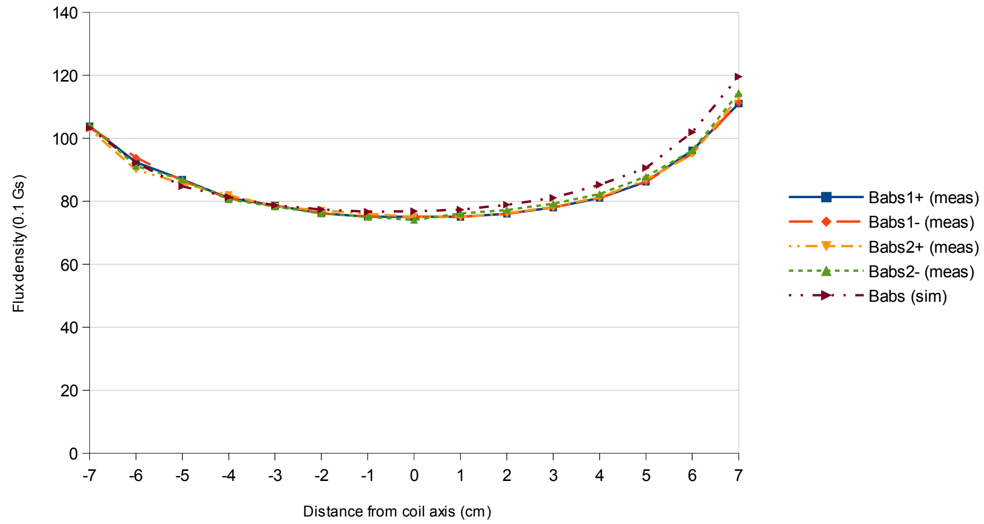


Fig 5.8 The measured ***Babs*** compared with the simulation output ***Babs*** along the minor axis y = 7 at 50 Hz.

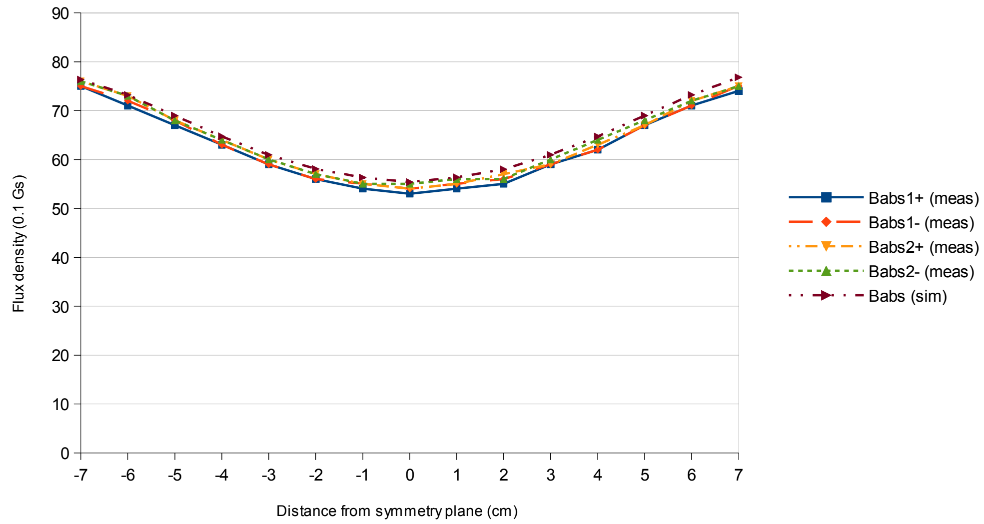


Fig 5.9 The measured ***Babs*** compared with the simulation output ***Babs*** along the minor axis x = 0 at 50 Hz.

### 5.4.2 Observations and Comparison at 50 Hz

The plots shown in Figs 5.6, 5.7, 5.8 and 5.9 show a close agreement between the measured ***Babs***+ and ***Babs***- across two different magnetometers. By inspecting Tables 5.2, 5.3 and 5.4, their corresponding magnitude error is less than 0.3 Gs, thus lending credibility to the measurements taken with either magnetometer.

These tables also show that the error between the simulation ***Babs*** output and the measured ***Babs*** is less than 0.3 Gs in magnitude and less than 5 % across all 4 measurement axes except for the outliers in the $\boldsymbol{y}$ = 3.5 and $\boldsymbol{y}$ = 7 axes around the high flux density gradient areas, particularly when the flux density is low. With a low denominator, the low flux density areas are prone to high percentage errors. In areas with a high flux density gradient (approaching 1 Gs/cm) such as those near the current source, the measurement error is very sensitive to positional or geometrical deviations.

The list of potential sources of error in the experiment includes:

1. the magnetometer zero offset error of 0.2 Gs,
2. the current source error of 0.4 A, corresponding to a 1.3 % error,
3. the rounding error of 0.05 Gs,
4. the magnetometer measurement error of 2 %, and
5. the simulation output error of 1 %, taken from the Helmholtz benchmark model in Section 4.3.

Considering the potential sources of error, the 0.3 Gs error or an under 5 % error is explicable. Therefore, the simulation output and the measured flux density for the applicator at 50 Hz show a good agreement in general.

**5.5 Experiment at 50 kHz**

To deliver a high AC current at 50 kHz, a specially designed power converter was constructed. Flux density measurements at this frequency with a fine resolution was done using a specially built magnetometer. The scheme of measurement taking is quite similar to that of the 50 Hz experiment.

### 5.5.1 Power Converter Construction

A parallel resonance circuit tuned at 50 kHz was used to excite the applicator coils. With a simulated net inductance of 35.1 μH, this translated to a resonance capacitance of 289 nF. The actual nominal tuning capacitance is 296nF, agreeing well with the simulated value within the 20 % component tolerance. The resonance capacitors are made up of 35 pieces of polypropylene capacitors as shown in Fig 5.10.

This tank circuit was coupled to a Mazzilli flyback inverter, capable of delivering up to 20Apk to the coils. Figs 5.10 and 5.11 show the prototype of this inverter and its schematic circuit diagram respectively.

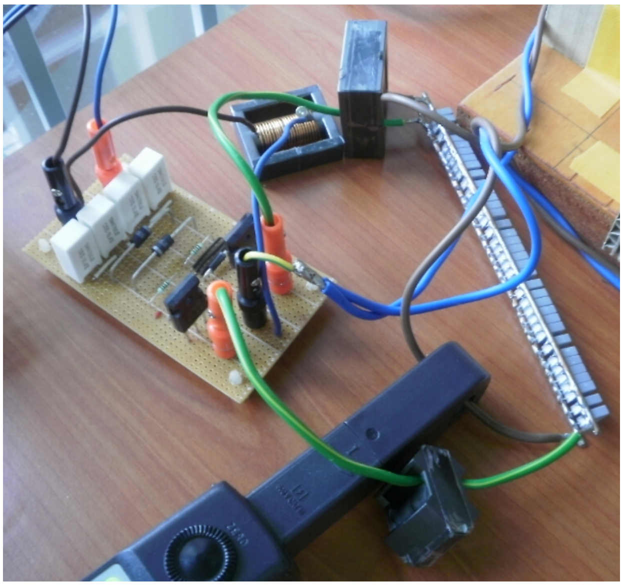

Fig 5.10 The Mazzilli inverter prototype and its resonance capacitors.

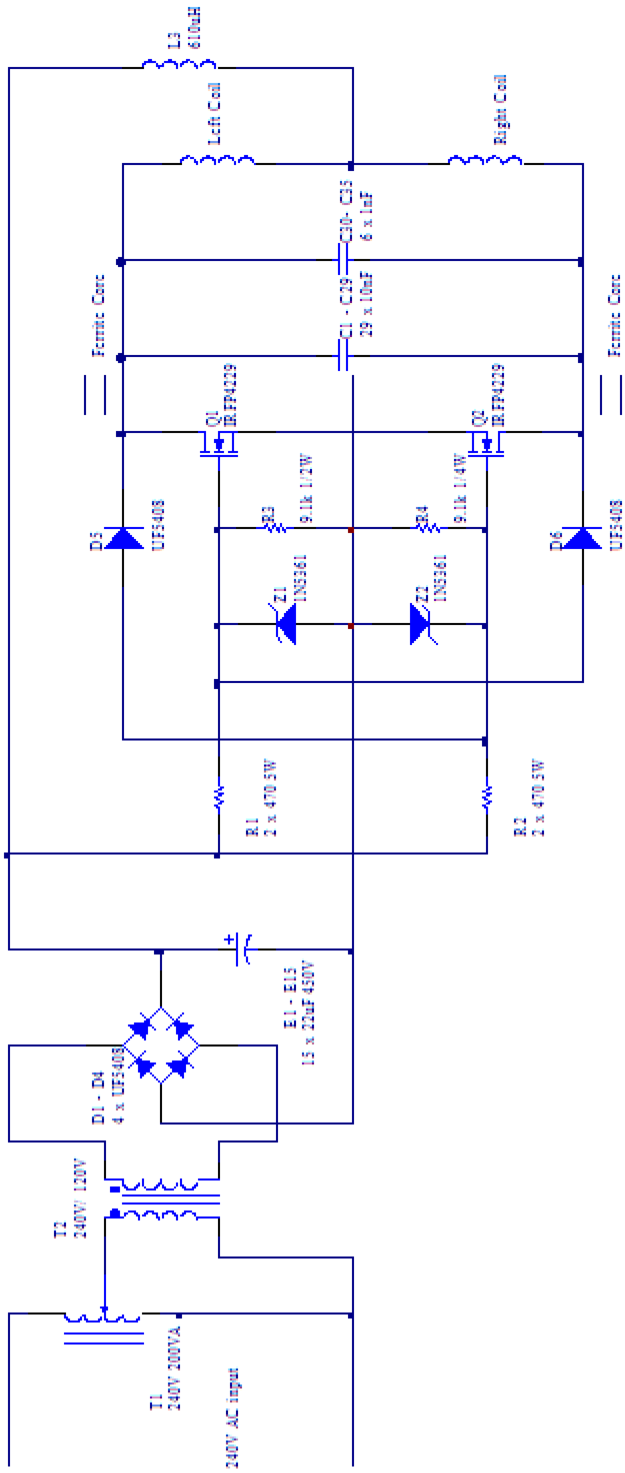


Fig 5.11 Schematic circuit diagram of the Mazzilli flyback inverter.

By adjusting the variac dial of the AC / DC converter shown in Fig 5.12, its output voltage can be varied until the desired resonance current of 15Apk is achieved as measured by a clamp current probe connected to a digital storage oscilloscope.

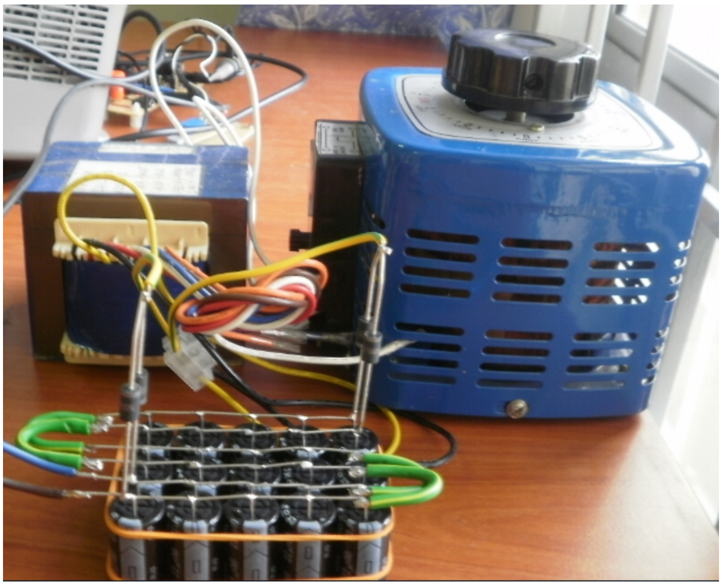

Fig 5.12 The prototype of the AC / DC converter.

### 5.5.2 Magnetometer Construction

The magnetic flux was measured using a high slew-rate Hall sensor mounted as a probe as shown in Fig 5.13. The Hall sensor was chosen because of the miniature size of its silicon die (~2 mm x 2 mm), thus offering sufficient resolution for a measurement interval of 1 cm. The connection from the probe to the signal conditioner was pair-twisted and shielded in order to minimise the error voltage induced on the cable by the magnetic field.

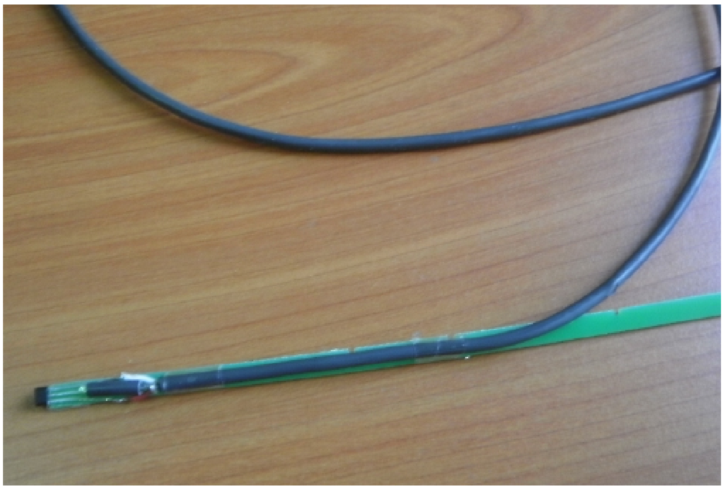

Fig 5.13 The Hall sensor probe assembly.

Due to the sensor's fast response time (~ 3 μs) and thus, its susceptibility to noise, a low noise signal conditioner as shown in Fig 5.14 was employed to process the signal before the readings were taken. Its schematic circuit diagram is shown in Fig 5.15.

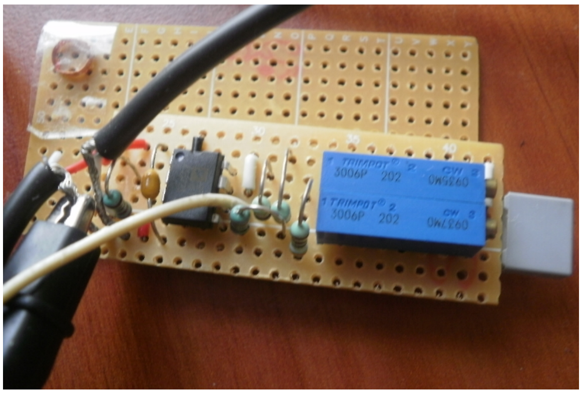

(a)

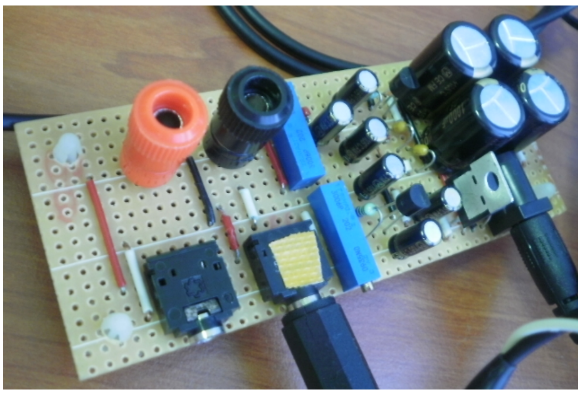

(b)

Fig 5.14 Low noise signal conditioner's (a) amplifier and (b) power supply.

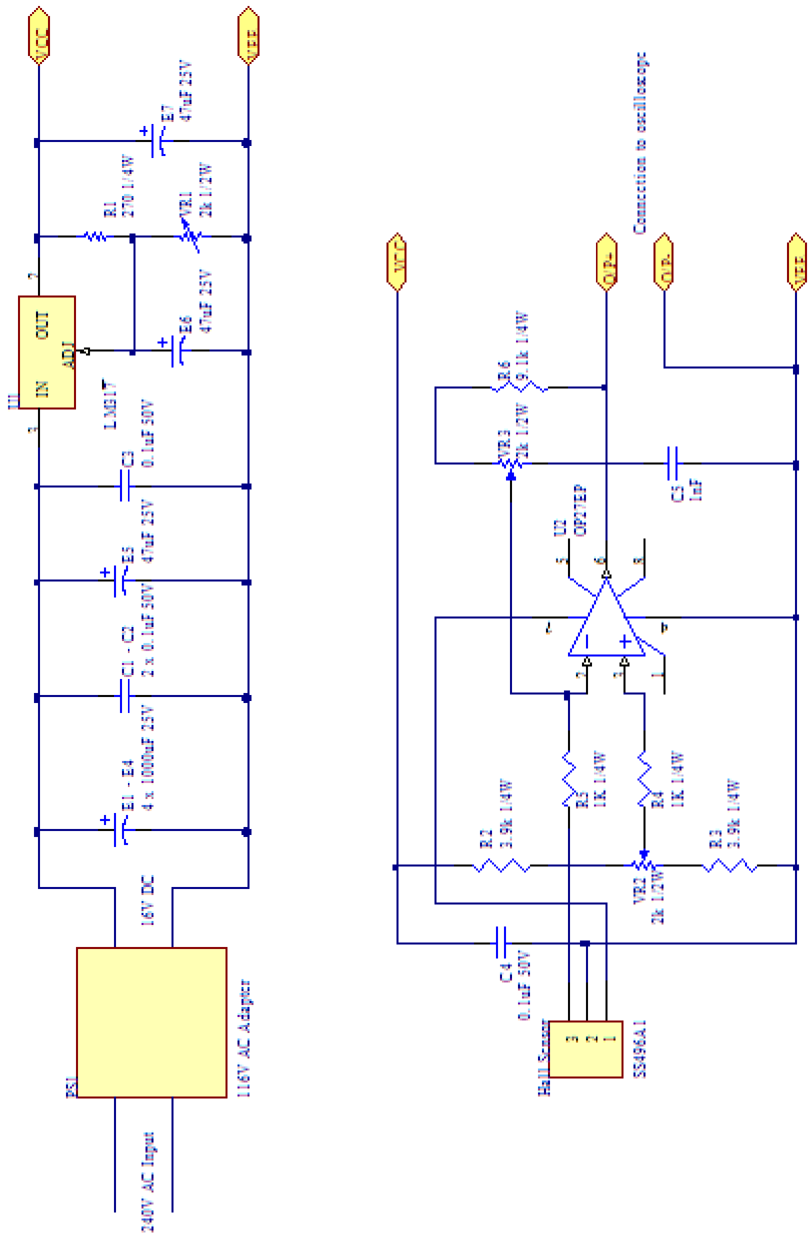


Fig 5.15 Schematic circuit diagram of the low noise signal conditioner.

The nominal gain of the low noise signal conditioner was set at a 10 x with a low pass filter tuned at a 160 kHz 3 dB roll-off frequency. Given the Hall sensor's sensitivity of 4 mV/Gauss, the output sensitivity is thus 40 mV/Gauss. Since the oscilloscope's resolution is 4 mV, the corresponding flux resolution is 0.1 Gs.  The 0.4 dB roll-off attenuation at 50kHz was subsequently compensated during the voltage to flux density conversion process.

The output signal from the signal conditioner was AC coupled into a digital storage oscilloscope for display and measurement. The output of the current probe measuring the resonance current was also coupled into the oscilloscope for monitoring purposes as shown in Fig 5.16.

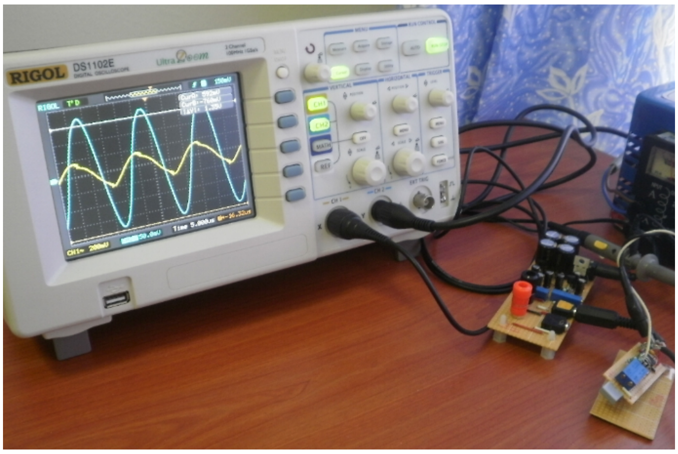


Fig 5.16 The magnetometer showing the resonance current and field strength waveforms on the digital storage oscilloscope (probe not shown).

### 5.5.3 Setup, Calibration and Measurement Results at 50 kHz

The applicator, power converter and magnetometer were connected in a setup according to the schematic diagram shown in Fig 5.17.

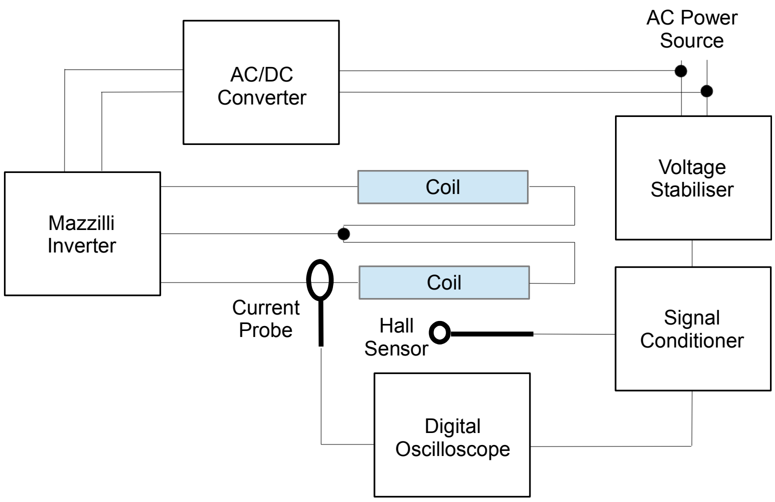


Fig 5.17 Schematic connections of the 50 kHz experiment setup.

The low noise electronics were spaced at about 1 m from the applicator to minimise magnetic field interference as shown in Fig 5.18.

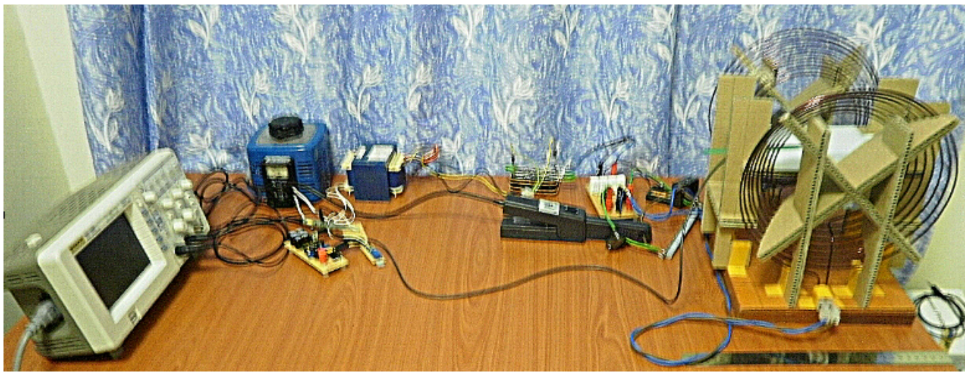

Fig 5.18 The 50 kHz experiment setup.

The low noise signal conditioner's gain was checked using the 50 Hz experiment setup. Its flux density reading at point (0,0) was found to agree with the corresponding flux density reading of 5.5 Gs as recorded in Table 5.2.

The procedure for setting up the experiment and taking the measurements is given in Appendix D.2. Similar to the 50 Hz experiment, measurements were taken along the major axes y = 0, y = 3.5 and minor axes y = 7 and x = 0 and the readings are listed in Tables 5.5, 5.6, 5.7(a) and 5.7(b) respectively.

| x | Measured values | | | | Calculated values | | | | | | Simulation output | | | Error | | | |
|---|---|---|---|---|---|---|---|---|---|---|---|---|---|---|---|---|---|
| | Vy+ (meas) | Vy- (meas) | Vx+ (meas) | Vx- (meas) | By+ (meas) | By- (meas) | Bx+ (meas) | Bx- (meas) | Babs+ (meas) | Babs- (meas) | By (sim) | Bx (sim) | Babs (sim) | By (mag) | Bx (mag) | Babs (mag) | Babs (%) |
| -11 | 78 | 74 | 2 | 2 | 20 | 19 | 1 | 1 | 20 | 19 | 19 | 0 | 19 | -1 | -1 | -1 | -4 |
| -10 | 98 | 94 | 6 | 2 | 25 | 24 | 2 | 1 | 25 | 24 | 24 | 0 | 24 | -1 | -1 | -1 | -5 |
| -9 | 118 | 110 | 6 | 6 | 30 | 28 | 2 | 2 | 30 | 28 | 29 | 0 | 29 | -1 | -1 | -1 | -4 |
| -8 | 138 | 134 | 10 | 6 | 35 | 34 | 3 | 2 | 35 | 34 | 34 | 0 | 34 | -1 | -1 | -1 | -4 |
| -7 | 158 | 150 | 10 | 2 | 40 | 38 | 3 | 1 | 40 | 38 | 39 | 1 | 39 | -1 | -1 | -1 | -3 |
| -6 | 174 | 168 | 10 | 6 | 44 | 43 | 3 | 2 | 44 | 43 | 43 | 1 | 43 | -1 | -1 | -1 | -2 |
| -5 | 190 | 186 | 10 | 4 | 48 | 47 | 3 | 1 | 48 | 47 | 47 | 1 | 47 | -1 | -1 | -1 | -2 |
| -4 | 202 | 194 | 10 | 6 | 51 | 49 | 3 | 2 | 51 | 49 | 50 | 1 | 50 | -2 | -2 | -2 | -3 |
| -3 | 210 | 202 | 10 | 6 | 53 | 51 | 3 | 2 | 54 | 51 | 53 | 1 | 53 | -1 | -1 | -1 | -2 |
| -2 | 214 | 210 | 10 | 10 | 54 | 53 | 3 | 3 | 55 | 54 | 54 | 0 | 54 | 0 | 0 | 0 | -1 |
| -1 | 218 | 214 | 10 | 10 | 56 | 54 | 3 | 3 | 56 | 55 | 55 | 0 | 55 | 0 | 0 | 0 | -1 |
| 0 | 222 | 218 | 10 | 10 | 57 | 56 | 3 | 3 | 57 | 56 | 55 | 1 | 55 | -1 | -1 | -1 | -2 |
| 1 | 218 | 210 | 10 | 10 | 56 | 53 | 3 | 3 | 56 | 54 | 55 | 0 | 55 | 0 | 0 | 0 | 0 |
| 2 | 214 | 208 | 10 | 6 | 54 | 53 | 3 | 2 | 55 | 53 | 54 | 0 | 54 | 0 | 0 | 0 | -1 |
| 3 | 210 | 200 | 10 | 6 | 53 | 51 | 3 | 2 | 54 | 51 | 53 | 1 | 53 | -1 | -1 | -1 | -2 |
| 4 | 202 | 194 | 12 | 6 | 51 | 49 | 3 | 2 | 52 | 49 | 50 | 1 | 50 | -1 | -1 | -1 | -2 |
| 5 | 190 | 182 | 8 | 2 | 48 | 46 | 2 | 1 | 48 | 46 | 47 | 1 | 47 | -1 | -1 | -1 | -3 |
| 6 | 174 | 166 | 12 | 6 | 44 | 42 | 3 | 2 | 44 | 42 | 43 | 1 | 43 | -1 | -1 | -1 | -2 |
| 7 | 158 | 148 | 12 | 6 | 40 | 38 | 3 | 2 | 40 | 38 | 39 | 1 | 39 | -1 | -1 | -1 | -4 |
| 8 | 138 | 130 | 6 | 4 | 35 | 33 | 2 | 1 | 35 | 33 | 34 | 1 | 34 | -1 | -1 | -1 | -3 |
| 9 | 118 | 106 | 10 | 2 | 30 | 27 | 3 | 1 | 30 | 27 | 29 | 0 | 29 | -1 | -1 | -1 | -4 |
| 10 | 98 | 86 | 6 | 2 | 25 | 22 | 2 | 1 | 25 | 22 | 24 | 0 | 24 | -1 | -1 | -1 | -5 |
| 11 | 78 | 70 | 6 | 2 | 20 | 18 | 2 | 1 | 20 | 18 | 19 | 0 | 19 | -1 | -1 | -1 | -4 |

Note: the unit of position ***x*** is cm, V is in multiples of mV and B is in multiples of 0.1 Gs unless otherwise specified.

Table 5.5 Flux density measurements and comparison along the $\boldsymbol{y} = 0$ major axis at 50 kHz.

| x | Measured values | | | | Calculated values | | | | | | Simulation output | | | Error | | | |
|---|---|---|---|---|---|---|---|---|---|---|---|---|---|---|---|---|---|
| | Vy+ (meas) | Vy- (meas) | Vx+ (meas) | Vx- (meas) | By+ (meas) | By- (meas) | Bx+ (meas) | Bx- (meas) | Babs+ (meas) | Babs- (meas) | By (sim) | Bx (sim) | Babs (sim) | By (mag) | Bx (mag) | Babs (mag) | Babs (%) |
| -11 | 78 | 74 | 58 | 50 | 20 | 19 | 15 | 13 | 25 | 23 | 19 | 17 | 26 | -1 | 3 | 1 | 4 |
| -10 | 102 | 102 | 62 | 58 | 26 | 26 | 16 | 15 | 30 | 30 | 26 | 20 | 33 | 1 | 4 | 3 | 8 |
| -9 | 122 | 122 | 66 | 60 | 31 | 31 | 17 | 15 | 35 | 35 | 33 | 20 | 39 | 2 | 3 | 3 | 9 |
| -8 | 156 | 154 | 62 | 62 | 40 | 39 | 16 | 16 | 43 | 42 | 41 | 20 | 45 | 1 | 4 | 3 | 6 |
| -7 | 178 | 178 | 54 | 54 | 45 | 45 | 14 | 14 | 47 | 47 | 47 | 17 | 50 | 1 | 3 | 2 | 5 |
| -6 | 202 | 202 | 38 | 38 | 51 | 51 | 10 | 10 | 52 | 52 | 52 | 15 | 54 | 1 | 5 | 2 | 3 |
| -5 | 214 | 214 | 26 | 26 | 54 | 54 | 7 | 7 | 55 | 55 | 56 | 11 | 57 | 1 | 5 | 2 | 4 |
| -4 | 222 | 226 | 18 | 18 | 57 | 58 | 5 | 5 | 57 | 58 | 59 | 8 | 59 | 1 | 4 | 2 | 3 |
| -3 | 226 | 230 | 10 | 10 | 58 | 59 | 3 | 3 | 58 | 59 | 61 | 6 | 61 | 2 | 3 | 2 | 4 |
| -2 | 230 | 234 | 10 | 10 | 59 | 60 | 3 | 3 | 59 | 60 | 62 | 4 | 62 | 2 | 1 | 2 | 4 |
| -1 | 234 | 242 | 6 | 8 | 60 | 62 | 2 | 2 | 60 | 62 | 62 | 2 | 62 | 1 | 0 | 1 | 1 |
| 0 | 234 | 250 | 2 | 2 | 60 | 64 | 1 | 1 | 60 | 64 | 63 | 0 | 63 | -1 | 0 | -1 | -1 |
| 1 | 230 | 242 | 6 | 10 | 59 | 62 | 2 | 3 | 59 | 62 | 63 | 2 | 63 | 1 | 0 | 1 | 2 |
| 2 | 226 | 234 | 10 | 10 | 58 | 60 | 3 | 3 | 58 | 60 | 62 | 4 | 63 | 3 | 2 | 3 | 5 |
| 3 | 218 | 230 | 30 | 34 | 56 | 59 | 8 | 9 | 56 | 59 | 61 | 7 | 62 | 3 | -2 | 3 | 4 |
| 4 | 214 | 226 | 42 | 42 | 54 | 58 | 11 | 11 | 56 | 59 | 60 | 10 | 61 | 2 | -1 | 2 | 3 |
| 5 | 202 | 214 | 62 | 58 | 51 | 54 | 16 | 15 | 54 | 56 | 57 | 13 | 59 | 3 | -3 | 2 | 4 |
| 6 | 182 | 190 | 78 | 70 | 46 | 48 | 20 | 18 | 50 | 52 | 53 | 16 | 55 | 4 | -3 | 4 | 7 |
| 7 | 158 | 174 | 86 | 86 | 40 | 44 | 22 | 22 | 46 | 49 | 47 | 20 | 51 | 2 | -2 | 1 | 3 |
| 8 | 130 | 142 | 90 | 94 | 33 | 36 | 23 | 24 | 40 | 43 | 40 | 21 | 45 | 4 | -2 | 2 | 4 |
| 9 | 102 | 122 | 94 | 90 | 26 | 31 | 24 | 23 | 35 | 39 | 31 | 21 | 38 | 0 | -2 | -1 | -2 |
| 10 | 78 | 91 | 86 | 86 | 20 | 23 | 22 | 22 | 30 | 32 | 24 | 20 | 31 | 0 | -2 | -1 | -3 |
| 11 | 58 | 74 | 74 | 74 | 15 | 19 | 19 | 19 | 24 | 27 | 18 | 18 | 25 | -1 | -1 | -2 | -7 |

Note: the unit of position ***x*** is cm, V is in multiples of mV and B is in multiples of 0.1 Gs unless otherwise specified.

Table 5.6 Flux density measurements and comparison along the ***y*** = 3.5 major axis at 50 kHz.

| x | Measured values | | | | Calculated values | | | | | | Simulation output | | | Error | | | |
|---|---|---|---|---|---|---|---|---|---|---|---|---|---|---|---|---|---|
| | Vy+ (meas) | Vy- (meas) | Vx+ (meas) | Vx- (meas) | By+ (meas) | By- (meas) | Bx+ (meas) | Bx- (meas) | Babs+ (meas) | Babs- (meas) | By (sim) | Bx (sim) | Babs (sim) | By (mag) | Bx (mag) | Babs (mag) | Babs (%) |
| -7 | 386 | 394 | 166 | 194 | 98 | 100 | 42 | 49 | 107 | 112 | 97 | 40 | 105 | -4 | -10 | -7 | -7 |
| -6 | 342 | 374 | 62 | 94 | 87 | 95 | 16 | 24 | 89 | 98 | 90 | 22 | 93 | -5 | -2 | -5 | -6 |
| -5 | 318 | 342 | 34 | 78 | 81 | 87 | 9 | 20 | 81 | 89 | 84 | 14 | 85 | -3 | -6 | -4 | -5 |
| -4 | 310 | 330 | 22 | 34 | 79 | 84 | 6 | 9 | 79 | 84 | 81 | 9 | 82 | -3 | 1 | -3 | -3 |
| -3 | 298 | 314 | 14 | 18 | 76 | 80 | 4 | 5 | 76 | 80 | 79 | 6 | 79 | -1 | 2 | -1 | -1 |
| -2 | 286 | 306 | 10 | 10 | 73 | 78 | 3 | 3 | 73 | 78 | 78 | 4 | 78 | 0 | 1 | 0 | 0 |
| -1 | 278 | 298 | 6 | 10 | 71 | 76 | 2 | 3 | 71 | 76 | 77 | 1 | 77 | 1 | -1 | 1 | 2 |
| 0 | 222 | 262 | 2 | 6 | 57 | 67 | 1 | 2 | 57 | 67 | 61 | 3 | 61 | -6 | 2 | -6 | -10 |
| 1 | 278 | 302 | 6 | 6 | 71 | 77 | 2 | 2 | 71 | 77 | 78 | 0 | 78 | 1 | -1 | 1 | 1 |
| 2 | 286 | 306 | 10 | 10 | 73 | 78 | 3 | 3 | 73 | 78 | 79 | 2 | 79 | 1 | 0 | 1 | 2 |
| 3 | 298 | 310 | 14 | 22 | 76 | 79 | 4 | 6 | 76 | 79 | 81 | 5 | 81 | 2 | -1 | 2 | 3 |
| 4 | 306 | 318 | 18 | 50 | 78 | 81 | 5 | 13 | 78 | 82 | 85 | 9 | 86 | 4 | -4 | 4 | 4 |
| 5 | 310 | 334 | 50 | 82 | 79 | 85 | 13 | 21 | 80 | 88 | 90 | 14 | 91 | 5 | -7 | 4 | 4 |
| 6 | 322 | 358 | 102 | 114 | 82 | 91 | 26 | 29 | 86 | 96 | 100 | 25 | 103 | 9 | -4 | 7 | 7 |
| 7 | 374 | 382 | 182 | 194 | 95 | 97 | 46 | 49 | 106 | 109 | 110 | 53 | 122 | 12 | 4 | 13 | 10 |

Note: the unit of position ***x*** is cm, V is in multiples of mV and B is in multiples of 0.1 Gs unless otherwise specified.

(a)

| y | Measured values | | | | Calculated values | | | | | | Simulation output | | | Error | | | |
|---|---|---|---|---|---|---|---|---|---|---|---|---|---|---|---|---|---|
| | Vy+ (meas) | Vy- (meas) | Vx+ (meas) | Vx- (meas) | By+ (meas) | By- (meas) | Bx+ (meas) | Bx- (meas) | Babs+ (meas) | Babs- (meas) | By (sim) | Bx (sim) | Babs (sim) | By (mag) | Bx (mag) | Babs (mag) | Babs (%) |
| -7 | 262 | 226 | 6 | 6 | 67 | 58 | 2 | 2 | 67 | 58 | 59 | 2 | 59 | -8 | 1 | -8 | -14 |
| -6 | 294 | 268 | 6 | 14 | 75 | 68 | 2 | 4 | 75 | 68 | 73 | 1 | 73 | -2 | -3 | -2 | -3 |
| -5 | 278 | 254 | 6 | 14 | 71 | 65 | 2 | 4 | 71 | 65 | 69 | 0 | 69 | -2 | -3 | -2 | -3 |
| -4 | 258 | 242 | 2 | 14 | 66 | 62 | 1 | 4 | 66 | 62 | 65 | 0 | 65 | -1 | -4 | -1 | -1 |
| -3 | 242 | 226 | 6 | 14 | 62 | 58 | 2 | 4 | 62 | 58 | 61 | 0 | 61 | -1 | -3 | -1 | -1 |
| -2 | 230 | 218 | 6 | 10 | 59 | 56 | 2 | 3 | 59 | 56 | 58 | 0 | 58 | -1 | -2 | -1 | -1 |
| -1 | 222 | 214 | 6 | 6 | 57 | 54 | 2 | 2 | 57 | 55 | 56 | 0 | 56 | 0 | -1 | 0 | 0 |
| 0 | 218 | 214 | 6 | 6 | 56 | 54 | 2 | 2 | 56 | 55 | 55 | 1 | 55 | 0 | -1 | 0 | 0 |
| 1 | 218 | 218 | 6 | 6 | 56 | 56 | 2 | 2 | 56 | 56 | 56 | 0 | 56 | 1 | -1 | 1 | 1 |
| 2 | 222 | 226 | 10 | 10 | 57 | 58 | 3 | 3 | 57 | 58 | 58 | 0 | 58 | 0 | -2 | 0 | 1 |
| 3 | 230 | 242 | 10 | 10 | 59 | 62 | 3 | 3 | 59 | 62 | 61 | 0 | 61 | -1 | -2 | -1 | -1 |
| 4 | 242 | 258 | 10 | 10 | 62 | 66 | 3 | 3 | 62 | 66 | 65 | 0 | 65 | -1 | -3 | -1 | -2 |
| 5 | 254 | 278 | 10 | 10 | 65 | 71 | 3 | 3 | 65 | 71 | 69 | 0 | 69 | -2 | -2 | -2 | -3 |
| 6 | 266 | 290 | 16 | 10 | 68 | 74 | 4 | 3 | 68 | 74 | 73 | 1 | 73 | -1 | -4 | -1 | -2 |
| 7 | 226 | 262 | 22 | 6 | 58 | 67 | 6 | 2 | 58 | 67 | 61 | 3 | 61 | -6 | -3 | -6 | -10 |

Note: the unit of position ***y*** is cm, V is in multiples of mV and B is in multiples of 0.1 Gs unless otherwise specified.

(b)

Table 5.7 Flux density measurements and comparison along the (a) y = 7 and (b) x = 0 minor axes at 50 kHz.

The variable attributes are identical to that used in the 50 Hz experiment. ***Bn+*** and ***Bn-*** are the flux density values measured in the ***n*** axis orientation with the plus attribute denoting the Hall sensor's magnetic axis being parallel to the ***n*** axis and likewise, the minus attribute denoting the anti-parallel alignment.

By comparing these values with the simulated magnetic flux density output for the applicator at an excitation frequency of 50 kHz, the consolidated magnitude error for ***Bx***, ***By*** and ***Babs*** as well as the percentage error for ***Babs*** were derived. Figs 5.19, 5.20, 5.21 and 5.22 provide a visual comparison of the ***Babs***+ and ***Babs-*** flux density measurements with the corresponding simulated flux density output along the major axes $y = 0$ & $y = 3.5$ and minor axes $y = 7$ & $x = 0$ respectively.

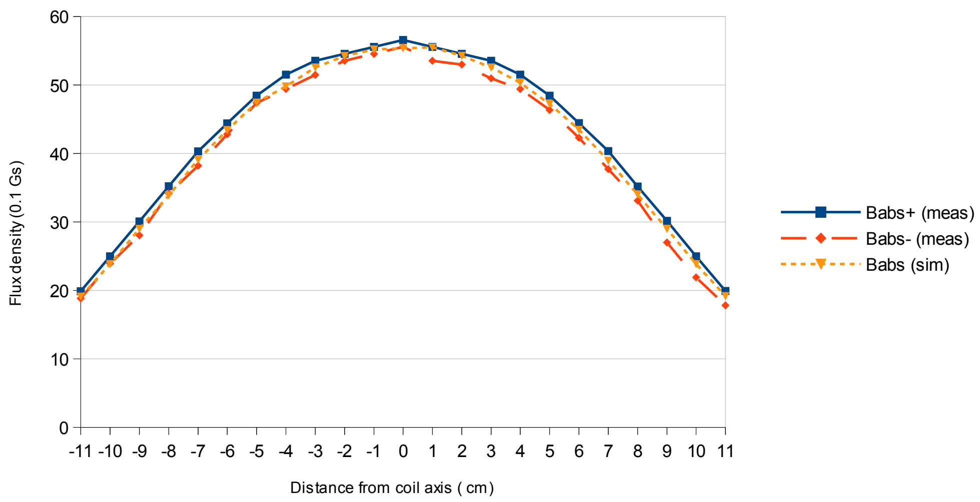


Fig 5.19 The measured ***Babs*** compared with the simulation output ***Babs*** along the major axis $y = 0$ at 50 kHz.

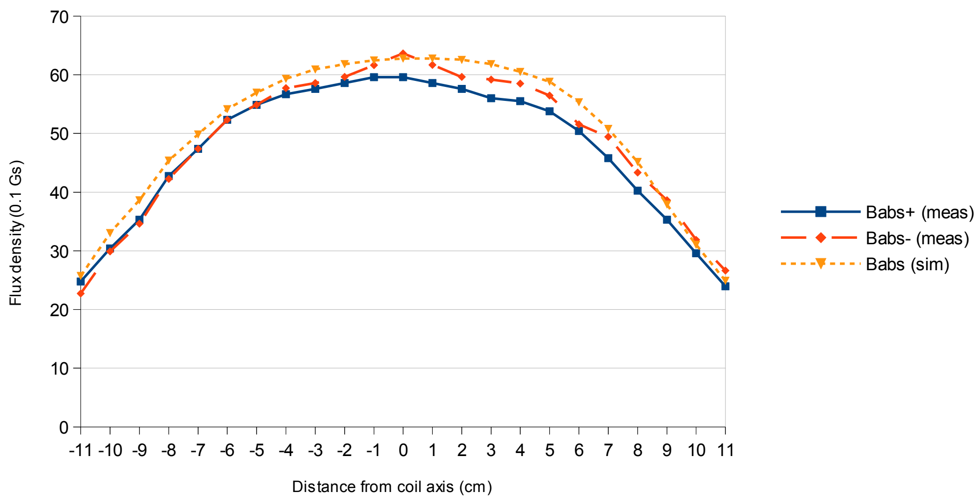


Fig 5.20 The measured ***Babs*** compared with the simulation output ***Babs*** along the major axis $y = 3.5$ at 50 kHz.

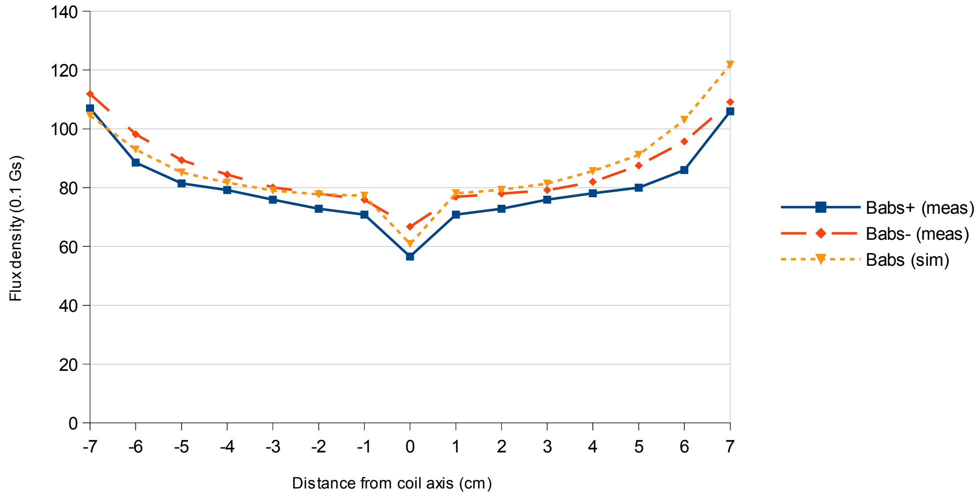


Fig 5.21 The measured ***Babs*** compared with the simulation output ***Babs*** along the minor axis ***y*** = 7 at 50 kHz.

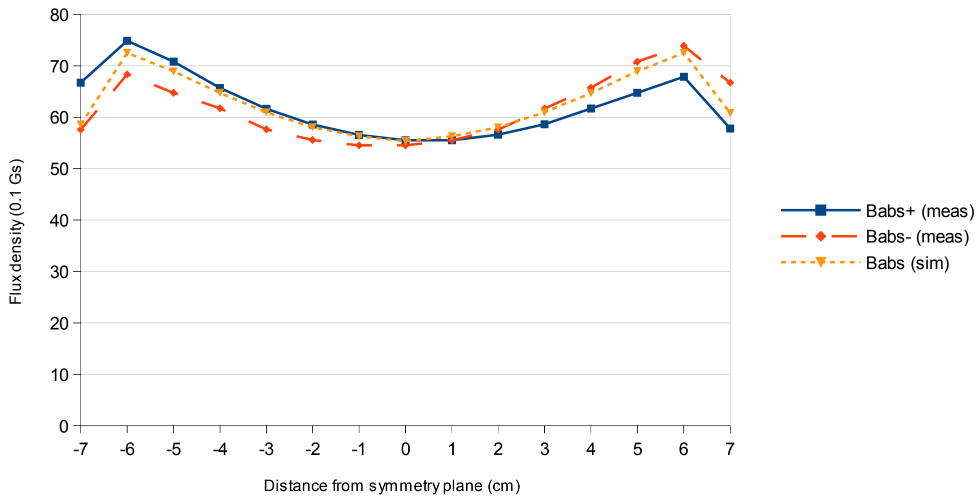


Fig 5.22 The measured ***Babs*** compared with the simulation output ***Babs*** along the minor axis ***x*** = 0 at 50 kHz.

### 5.5.4 Observations and Comparison at 50 kHz

At 50 kHz, the measurement asymmetry between ***Babs***+ and ***Babs***- is discernible from Figs 5.19, 5.20, 5.21 and 5.22. By inspecting Tables 5.5, 5.6 and 5.7, the differences are typically below 0.3 Gs but they get higher up to 0.8 Gs in field points near the current source and the deflector plates due to the higher magnetic flux density in those regions.

This high magnetic flux density can cause appreciable e.m.f. in the Hall sensor probe and thus asymmetry error. As an illustration, a 0.3 Gs error only requires a 1.2 mV e.m.f. to be induced on a single turn 3 mm in diameter loop in the probe connection positioned at the coil's axis at 50 kHz. Therefore, under a higher flux density near the pole and current source, this asymmetry error has increased to 0.5 Gs or 7 % as shown in Tables 5.7(a) and 5.7(b).

The higher error in regions close to the deflector plates along the coil's axis and near the current source is also due to its high field gradient. For example, by inspecting Fig 5.22, the field gradient near the deflector plates is above 12 Gs / cm, causing the measurement in that region to be extremely sensitive to positional deviations. In this case, only a 0.5 mm deviation in the probe position is required to cause the 10 % error shown in Table 5.7(a).

Far from the poles and current source along the symmetry plane, the typical error between the simulation output and the measured flux density is below 0.3 Gs or less than 5 %. Closer to the pole at $\boldsymbol{y}$ = 3.5, the percentage error at field points far from the coil's axis approaches 8 % as the field gradient increases but at a low field strength as shown in Table 5.6.

The list of potential sources of error in the experiment includes:

1. the current source error of 0.8 A, corresponding to a 2.6 % error,
2. the current probe error of 10 % at 50 kHz,
3. the oscilloscope's rounding error of 2mV or 0.05 Gs,
4. the oscilloscope's gain accuracy of 3 %,

5. the measurement asymmetry error of up to 0.8 Gs,

6. the positional error of up to 10 % in high field gradient regions, and

7. the simulation output error of 1 %, taken from the Helmholtz benchmark model in Section 4.3.

Considering the potential sources of error, the above error and deviations are explicable. In general, the simulation output and the measured magnetic flux density for the applicator at 50 kHz show a good agreement.

## 5.6 Comparison Between the 50 Hz and 50 kHz Excitations

Since the simulated and the measured outputs of the applicator agree well at both 50 Hz and 50 kHz excitations, the comparison between the different excitation frequencies is thus simplified to only considering the simulation output. The simulated magnetic flux density at both excitation frequencies were plotted for field points along the $\boldsymbol{y} = 0$, $\boldsymbol{y} = 3.5$, $\boldsymbol{y} = 7$ and $\boldsymbol{x} = 0$ axes as shown in Fig 5.23, 5.24, 5.25 and 5.26 respectively.

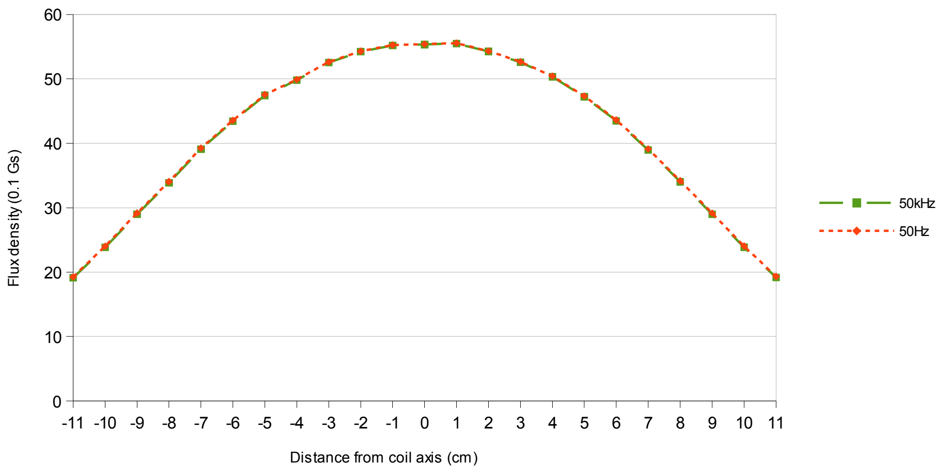


Fig 5.23 Flux density comparison between 50 Hz and 50 kHz excitations along the $\boldsymbol{y} = 0$ axis.

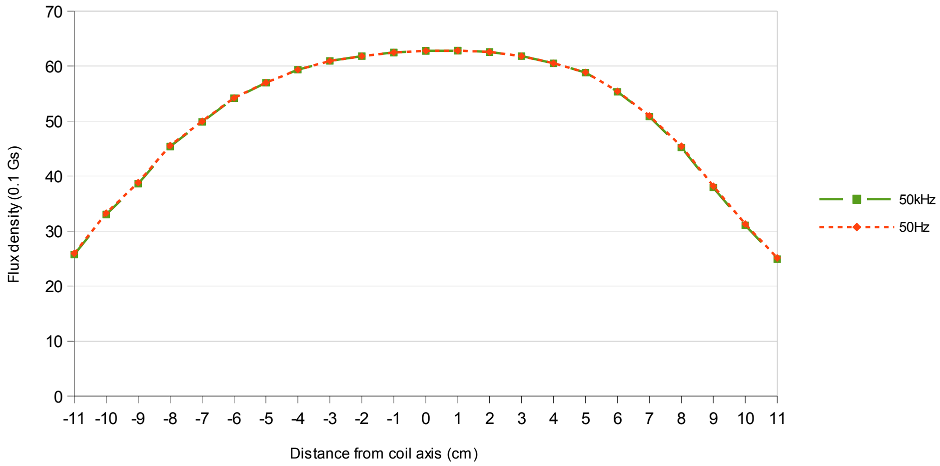


Fig 5.24 Flux density comparison between 50 Hz and 50 kHz excitations along the $\boldsymbol{y} = 3.5$ axis.

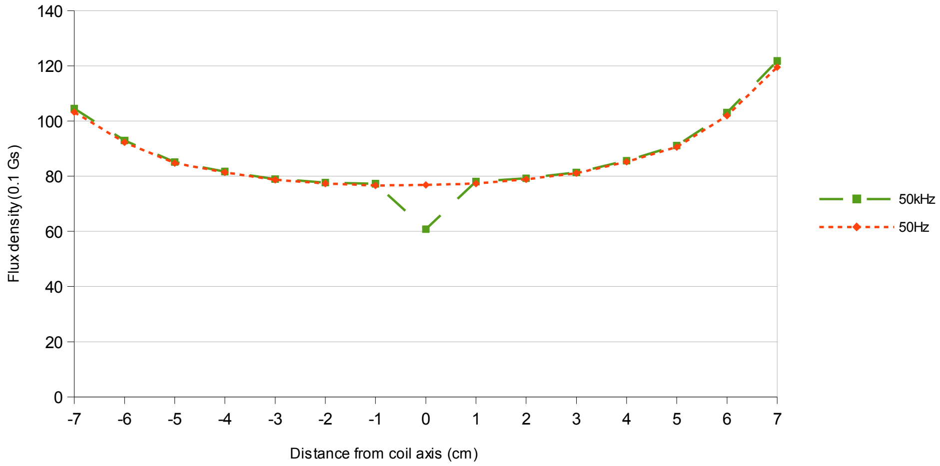


Fig 5.25 Flux density comparison between 50 Hz and 50 kHz excitations along the $\boldsymbol{y} = 7$ axis.

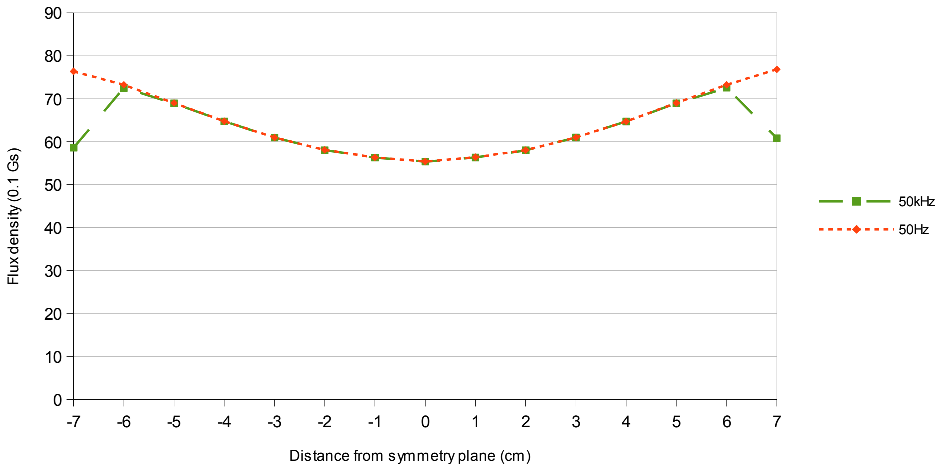


Fig 5.26 Flux density comparison between 50 Hz and 50 kHz excitations along the $\boldsymbol{x} = 0$ axis.

The flux density values at 50 Hz and 50 kHz excitation frequencies are almost identical along the 4 axes except in the regions near the deflector plates as shown in Figs 5.25 and 5.26. The reason for this is the induced eddy current at the deflector plates is proportional to the frequency of the incident magnetic field and at 50 Hz, this eddy current is negligible, thus producing an equally negligible counteracting magnetic field. At 50 kHz, this counteracting magnetic field is much stronger, hence the more pronounced null regions near the deflector plates. At higher frequencies, these null regions will grow even larger with more flux density attenuation.

## 5.7 Concluding Remarks

A physical prototype was designed and built, based on the applicator design derived from the earlier simulations and analyses. Excited by specially built power sources at 50 Hz and 50 kHz, measurements made using dedicated instrumentations show a good agreement with the simulation output values. They also show the necessity of a high frequency excitation for the deflector plates to work. With the concept proven, this design can then be scaled to live-size for comparative studies.

# CHAPTER 6

# ANALYSIS AND DISCUSSION

## 6.1 Background

The applicator was designed through a series of theoretical analyses and simulations which were duly verified experimentally. However, for comparison with the state of the art MFH®-300F applicator by MagForce AG, it has to be scaled to an equivalent life-size dimension. Therefore, the scaled applicator should have a 30 cm gap as the target space with a maximum field strength of no less than 18 kA $m^{-1}$ at the centre of the target space. By comparing the performance of this scaled applicator with that of the state of the art applicator, we can then deduce the strengths and drawbacks of this applicator and conclude its contributions to the science of applicator design. For completeness sake, the effect of the ferrite return media on the applicator's power loss will also be discussed briefly.

## 6.2 Scaling

Examining Eqs 3.7 and 3.9, the magnetising field strength is dependent on the current density, $\boldsymbol{J}$ and the linear dimensions normalised to distance $\boldsymbol{b}$ which represents the coil's inner radius. That means when the dimensions are varied, the field strength should remain the same as long as the normalised dimensions and $\boldsymbol{J}$ are maintained. Therefore, in order to double the depth of the target space, $2\boldsymbol{p}$, the coils' dimensions must also be doubled. In order to maintain the current density with the same current, the turn pitch must be maintained. Therefore, the coil turns must be doubled from 8 turns to 16 turns when the coils' size is doubled. Doing so would maintain the same magnetising field strength of 440 A $m^{-1}$ at the centre of the gap.

In order to increase the magnetising field strength, 3 specific changes need to be made: (a) interleave the coil with more wire turns, (b) stack more distributed coil windings on top of each other and (c) increase the excitation current.

Since the diameter of the wire is 2.6 mm and the initial turn pitch is 7.85 cm / 8 = 9.8 mm, the ensuing gap of 7.2 mm between the turns can be interlaced with up to 2 additional turns of wire. For illustration, Fig 6.1 shows the winding cross section in which between every 2 turns of the initial winding 'a', 2 additional turns are interlaced where windings 'b' and 'c' contribute 1 turn each. In the actual implementation, these wires are connected in series, thereby increasing the field strength by 3 times and the coil turns thus become 3 x 16 turns = 48 turns.

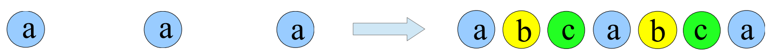


Fig 6.1 The transition from the initial winding cross section (left) to the interlaced winding cross section (right).

The prototype coil thickness of 2.6 mm is some 3.5 % of the coil's inner radius of 7.5 cm, i.e. the coil thickness is 0.035***b***. As shown in Fig 3.16 in Section 3.4, the difference in field strength between the representative distributed coils of infinitesimal thickness and that of 0.05***b*** thickness is very small. In order to maintain the coil thickness at around 0.05***b*** in this scaling exercise, 4 identical distributed coils can be stacked on top of each other, yielding a coil thickness of $0.5(1+1.5\sqrt{3})0.035b$ = 0.054***b***. Fig 6.2 shows the transition from a single layer interlaced distributed coil to a 4-layer interlaced distributed coil. This method is also employed in the MFH®-300F applicator (Feucht 2003) and doing so would increase the magnetising field strength by 4 times when the layers of coil are excited in series. The corresponding total coil turns would be increased by 4 times to 4 x 48 = 192 turns.

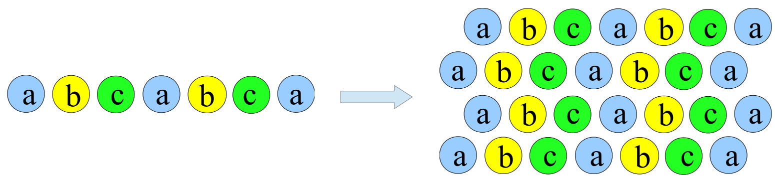


Fig 6.2 The transition from the single interlaced winding cross section (left) to the stacked interlaced winding cross section (right).

By interlacing and stacking the coils, the field strength at the centre of the gap would be increased by 12 times to 440 A $m^{-1}$ x 12 = 5,280 A $m^{-1}$. In order to achieve a maximum field strength of at least 18 kA $m^{-1}$ at the centre, the current would have to be increased by 18 / 5.28 = 3.4 times. For simplicity, the current scaling is chosen at 4 times by increasing the current from 15 $A_{pk}$ to 60 $A_{pk}$ such that the maximum field strength is increased to 21,120 A $m^{-1}$.

### 6.2.1 Losses of the Scaled Applicator

In order to minimise the copper loss, Litz wires can be used as is the case in the MFH®-300F applicator (Feucht 2003). Bartoli *et al.* (1996) has shown that in a 4-layer winding using 60-strand Litz wires, the resistance at 50 kHz is lower than that of solid wires by 35 %.

Unfortunately, doubling the size while maintaining the current density would increase the winding length by 4 times. Adding 2 interlacing windings and stacking another 3 similar winding layers on top of the initial winding layer would increase the wire length by another factor of 3 x 4 = 12 times. Therefore, the aggregate wire length increase is 12 x 4 = 48 times.

As copper loss is proportional to $(current)^2$ x length, increasing the current by 4 times alone would increase this loss by another 16 times. In total, due to the doubling of size, interlacing, stacking and increased current, having taken into account the use of Litz wires, the copper loss would be increased by a factor of 48 x 16 x 0.65 times or about 500 times.

From the simulation output, the copper loss is estimated to be 11.4 W. Therefore, the estimated power loss in the scaled applicator is thus 11.4 W x 500 = 5,700 W.

### 6.2.2 Effect of Ferrite Return Media on Losses

For the same scaled applicator, adding the ferrite return media would increase the overall magnetising field strength as shown in Section 4.9. By inspection of Table 4.7, the ferrite return media of the applicator that has a performance metric that resembles closest to that of the air core applicator is 14 cm in radius with a 112 cm average path length.

By using this ferrite return media, the magnetising field strength at the centre of the gap can be improved by 1,270 / 440 = 2.9 times. That means with this ferrite return media, the nominal current requirement of 60 $A_{pk}$ can be reduced by 2.9 times to 60 $A_{pk}$ /2.9 = 20.79 $A_{pk}$ in order to produce the same magnetising field strength. With a lower current, the copper loss is therefore only scaled by a factor of 48 x $(4 / 2.9)^2$ x 0.65 times or about 60 times, translating to an estimated copper loss of only 11.4 W x 60 = 680 W. However, in practical constructions, the joints and gaps between the ferrite blocks used to assemble the ferrite return media suffer from increased path magnetic reluctance, thus a higher current is required to achieve the same magnetising field strength and therefore, increasing the copper loss.

With an average length of 112 cm and a radius of 14 cm, the media volume is $\pi (14)^2$ x 112 = 68,964 $cm^3$. As shown in Fig 4.1, point LT is the nearest point to the ferrite media unobstructed by the deflector plates. Therefore, its magnetic flux density of ($\mu_0$ x 2,346) T, taken from Table 4.7 is assumed to be representative of that in the ferrite core. Appropriately scaled to life-size, the flux density in the ferrite core is thus estimated to be ($\mu_0$ x 2,346) T x 12 x (4 / 2.9) = 49 mT. Assuming a type F ferrite material typically used in power inductors, the hysteresis loss can be estimated by using Eq 6.1 (Huisman 2007).

$$P = k\, f^{x} B^{y} \left( a + bT + cT^2 + dT^3 + eT^4 \right) \qquad (6.1)$$

where

| | | |
|---|---|---|
| $\boldsymbol{k}$ = 3.432 x $10^{-7}$, | $\boldsymbol{x}$ = 1.72, | $\boldsymbol{y}$ = 2.66, |
| $\boldsymbol{a}$ = 1.44, | $\boldsymbol{b}$ = -0.0261, | $\boldsymbol{c}$ = 4.51 x $10^{-4}$, |
| $\boldsymbol{d}$ = 1.82 x $10^{-6}$, | $\boldsymbol{e}$ = -2.56 x $10^{-8}$ | |

and $\boldsymbol{f}$ is the excitation frequency in kHz (provided 10kHz < $\boldsymbol{f}$ < 100 kHz), $\boldsymbol{B}$ the flux density in mT, $\boldsymbol{T}$ the temperature in ºC and $\boldsymbol{P}$ the power loss density in mW / $cm^3$. At $\boldsymbol{f}$ = 50 kHz, $\boldsymbol{B}$ = 49 mT and $\boldsymbol{T}$ = 60ºC , Eq 6.1 yields $\boldsymbol{P}$ = 14 mW / $cm^3$. This translates to an estimated loss of approximately 970 W for this ferrite return media.

Adding up both the copper and ferrite losses, the total estimated power loss of an applicator with this ferrite return media is thus 970 + 680 W = 1,650 W. This figure ignores other ferrite losses such as that due to local flux peaks, flux non-uniformity and joint gaps. To illustrate the order of these losses, the coating of the toroidal ferrite alone can increase the ferrite loss by 30 % (Huisman 2007).

Comparing the above power loss figures, it would appear that the applicator with a ferrite return media is more efficient. However, with the ferrite loss underestimated, this benefit may be overstated. Indeed, Feucht (2003) in his patent claim has admitted the significant challenge to contain the ferrite loss.

### 6.3 Merit Comparison with the State of the Art

The scaled applicator is compared with the state of the art MFH®-300F applicator for the following attributes: (a) maximum magnetising field strength at the centre of the target space, (b) half power beam width, (c) gap between the poles flanking the target space, (e) size and (f) power consumption.

As mentioned in Section 1.2, the MFH®-300F applicator has a 90 % field uniformity within a 20 cm diameter. To convert this information into a comparable HPBW, an equivalent 3D simulation model that closely resembles the geometry of the MFH®-300F applicator as described in the patent was built using the planar distributed coil applicator described in Section 4.4 and a ferrite return media with an average path length of 114 cm. Since the field strength is sensitive to the radius of the return path as shown in Section 4.9, this radius was thus adjusted until the 90 % field beam width (0.9FBW) is 20 cm / 2 = 10 cm in diameter at the symmetry plane. The corresponding ferrite return path diameter was found to be 17.6 cm and its performance metric is shown in Table 6.1.

| Field | Air return path | 114 cm ferrite return path | |
|---|---|---|---|
| | Spherical coil | Spherical coil | Planar coil |
| Ferrite ***D*** | | 14 | 17.6 |
| Peak position ***a*** | 6.32 | 6.47 | 7.50 |
| HC(0,0,0) | 440.39 | 1270.79 | 1351.36 |
| HT(0,7.0,0) | 484.13 | 1405.57 | 1631.00 |
| HP(0,***a***,0) | 583.70 | 1630.72 | 1644.86 |
| HL(-7.5,0,0) | 291.81 | 867.13 | 1017.71 |
| HLT(-7.5,7.0,0) | 881.63 | 2346.30 | 2377.32 |
| HF(0,0,-7.5) | 290.75 | 863.52 | 1011.17 |
| H(1/2P) | 311.40 | 898.59 | 955.56 |
| HPBW | 13.98 | 14.34 | 16.20 |
| H(0.9P) | 396.35 | 1143.72 | 1216.22 |
| 0.9FBW | 8.42 | 8.44 | 10.00 |
| HC/HL | 1.51 | 1.47 | 1.33 |
| HC/HF | 1.51 | 1.47 | 1.34 |
| HP/HC | 1.33 | 1.28 | 1.22 |
| HLT/HC | 2.00 | 1.85 | 1.76 |
| HT/HC | 1.10 | 1.11 | 1.21 |

Note: the unit of diameter ***D***, position ***a***, 0.9FBW & HPBW is cm and the unit of the magnetising field is A /m.

Table 6.1 Comparison between the planar applicator with ferrite return media and the spherical applicator, with & without the ferrite return media.

By scaling the size of this equivalent applicator to twice, the 0.9FBW in Table 6.1 is thus increased to 20 cm, similar to that of the MFH®-300F applicator. The corresponding equivalent HPBW is approximately 33 cm.

| Attribute | Scaled applicator | MFH®-300F applicator |
|---|---|---|
| Field strength at the center | 21.12 kA / m | 18 kA / m |
| Half power beam width | 28 cm | 33 cm |
| Gap of target space | 30 cm | 30 cm |
| Est. applicator size (l x w x h) | 60 cm x 60 cm x 60 cm | 120 cm x 50cm x120 cm |
| Power consumption | 5.7 kW | 18 kW to 80 kW |

Table 6.2 Comparison between the scaled applicator and the state of the art applicator.

The comparison between the scaled applicator and the MFH®-300F applicator as tabulated in Table 6.2 shows that for a comparable magnetising field strength of above 18 kA $m^{-1}$ and a target space gap of 30 cm, the scaled applicator is (a) smaller in size, (b) consumes much less power and (c) has a narrower field beam at the centre with a comparable field penetration (HT / HC and HP / HC).

The ability of this scaled applicator to work without using a ferrite return media allows the applicator to be portable, lightweight and consequently, simpler in construction. This would ultimately lead to a more cost effective applicator compared to the MFH®-300F applicator. Additionally, this applicator may be scaled appropriately to match with specific parts of the body such as the neck and the head, thus allowing localised treatment and better control.

With a lower power consumption, the heat loss is lower and this would simplify the heat dissipation mechanism considerably. A lower power consumption also means that the scaled applicator may be readily deployed without any elaborate high power source.

Most importantly, the HPBW improvement allows the application of higher magnetising field strength for the same treatment quality of life, thus promising a higher efficacy in achieving the required hyperthermia target temperature.

## 6.4 Concluding Remarks

With the concept verified experimentally, the applicator was scaled analytically to twice the prototype's size to life-size. By using Litz wires at realistic current levels, the power consumption of this applicator was estimated to be much lower than that of the state of the art applicator, even without the use of a ferrite return media. If the ferrite return media is introduced, the estimated power consumption can be lowered further. Finally, from the comparison of performance metric between the scaled applicator and the MFH®-300F applicator, the scaled applicator has demonstrated a narrower HPBW with a comparable field penetration, implying that this smaller, more energy efficient and simpler applicator is capable of improving the treatment efficacy with a higher tolerable field strength.

# CHAPTER 7

# CONCLUSION AND RECOMMENDATION

## 7.1 Conclusion

Hyperthermia is growing in acceptance as a supplementary treatment to conventional clinical oncology. Among the different modes of hyperthermia, magnetic thermotherapy in conjunction with nanoparticles or thermo seeds shows the most promise due to its ability to target cancerous cells while leaving healthy cell relatively unscathed. However, the efficacy of the state of the art applicator is severely limited by the patient discomfort due to eddy current heating, not to mention its high energy consumption and unwieldy structure.

To overcome these drawbacks, this project has set out to design and build a prototype applicator that produces a narrower field focus but with a comparable field penetration at a reduced excitation frequency so that a higher field strength and thus more heating is possible within tolerance.

The literature review has suggested the use of loop coils, distributed planar coils and solenoids as the source of magnetic field, possibly in pairs. 2D analytical models were developed to represent these coil geometries and they revealed that the distributed planar coil has the best field penetration. From these models, the distributed planar coil has demonstrated a peculiar field focusing property, suggesting its curving into either a convex or a concave distributed coil in order to manipulate its field penetration and field focusing properties.

In order to characterise their field penetration and field focusing properties, the 2D analytical models were expanded to describe these concave and convex distributed coils. The predictions of these analytical models were verified to be in good agreement with the simulation output of the corresponding models.

These models also show that although the convex distributed coil has a marginally lower field penetration, it has the best field focusing and stability against coil dimension variations. The contrary is true for the concave distributed coil. Therefore, the choice between them is effectively a trade-off between field penetration and field focusing. From the analyses of these 2D models, the optimum coil parameters such as the coil breadth and radius of curvature were selected.

The coils were then combined in pairs to form applicators for further analyses. To aid the evaluation of these applicators, a performance metric system was developed. Through the use of this metric system, the convex distributed coil applicator with an optimum separation gap was selected.

The convex distributed coil applicator model was then expanded into 3D simulation models in various shapes such as the prolate, oblate, hyperboloid, cone and sphere. By comparing the performance metric of these models, the trade-off between field penetration and field focusing was again demonstrated. The spherical convex distributed coil applicator was chosen for its balanced performance and simplicity. In order to improve its field penetration, a metal deflector plate was added on each pole to suppress its peak field. Through the analysis of the corresponding 3D simulation output, the appropriate location and size of the deflectors were chosen.

By varying the turn pitch of the 3D convex distributed coil applicator model, thus varying its current density distribution, it was shown that concentrating more current near the coil's axis can yield higher field strength and better field focusing. However, this option was not chosen due to the higher local field exposure near the current elements and also to keep the design simple.

In order to investigate the effect of biological tissues on the field pattern, models of various biological tissues such as the kidney, thyroid and fat were incorporated into the target space of the 3D convex distributed coil applicator model. The simulation results of this model show a marginal variation of the magnetising field, thus validating the assumption that the applicator's air core field strength is similar to that in biological tissues.

Finally, the use of a ferrite return media was explored through simulations of the 3D convex distributed coil applicator model with the return media attached. As expected, the ferrite return media increases the overall field strength and also generally improves the field focusing but at the expense of poorer field penetration. However, this trade-off can be adjusted by changing the width of the return path. Changes in high media permeability and path length only affect the field strength marginally. Overall, the use of a ferrite return media may be considered if a higher field strength is required for the same current source.

In order to verify the 3D simulation setup, the 3D simulation output of a Helmholtz coil model was compared with a published simulation output and measurement of a similar Helmholtz coil. With an under 1 % deviation, the outcome of this comparison lends credibility to the simulation setup.

By comparing the field strength expression of a 3D Helmholtz coil with that of a 2D Helmholtz coil, an approximate scaling factor was derived. Using this factor, the scaled result of the 2D analytical model shows a good agreement with the 3D simulation result, lending credibility to the 2D models and analyses.

Based on the selected parameters of the 3D convex distributed coil applicator model with deflectors and a uniform current density, a physical prototype of this applicator was built. Field measurements were made in the target space at both 50 Hz and 50 kHz excitation frequencies for comparison with the corresponding simulation output. For the 50 kHz experiment, a dedicated high current frequency inverter was designed and built. Also, for measuring the magnetic flux density at 50 kHz, a dedicated Hall magnetometer was designed, built and duly calibrated.

At 50 kHz, the measurements agree with the simulation results within 5 % to 8 % while at 50 Hz, the corresponding agreement is within 5 %. Considering the sources of error and tolerance of up to 10 % in the experiments, the measurements at both 50 Hz and 50 kHz show a good agreement with the simulation output, thus validating the 3D simulation and 2D analytical models.

The measurements at 50 Hz and 50 kHz show little difference except in the regions near the deflector plates. It shows that the higher the excitation frequency, the deeper the field cancellation effect of the deflector plates.

To assess the performance of this applicator compared to that of the state of the art MFH®-300F applicator from MagForce AG, this prototype was scaled to life-size. A comparative analysis of these 2 applicators shows that the scaled applicator has a narrower field focusing and a higher efficiency at a comparable field penetration even without the use of a ferrite return media, thus meeting all the objectives of this research project.

Finally, this novel applicator permits the application of a stronger magnetic field in order to improve the treatment efficacy. With a lower heat loss, it is simpler and more cost effective. Being portable, it is also more readily adaptable to the local anatomy of the body.

### 7.2 Future Work and Recommendation

Apart from treating cancer, this applicator design can also be adapted for other medical applications such as TMS where a deep magnetic field penetration is required. It may also find potential use in industrial applications where field penetration and field focusing is required, e.g. in inductive power transfer.

It is recommended to develop a functional life-size applicator, capable of accommodating a full size human being for *in vivo* and *in vitro* studies.

## BIBLIOGRAPHY


Bahadur, D. & Giri, J. (2003) Biomaterials and Magnetism. Sadhana – Academy Proceedings in Engineering Sciences, vol. 28(parts 3 & 4), Jun/Aug 2003, pp. 639-56. Springer India.

Bartoli, M., Noferi, N., Reatti, A. & Kazimierczuk, M.K. (1996) Modelling Litz-wire Windings in High-frequency Power Inductors. 27$^{th}$ IEEE Power Electronics Specialist Conference (PESC 1996), Jun 1996, pp. 1690-96.

Bartusek, K. & Gescheidtova, E. (2005). Mapping the Induction of Magnetic Field Around an Applicator for Dermato Magnetotherapy, Using Magnetic Resonance Method. Measurement Science Review, vol. 5(2), pp. 62-66.

Chen, S., Chiang, C. & Hsieh, S. (2010). Simulating Physiological Conditions to Evaluate Nanoparticles for Magnetic Fluid Hyperthermia (MFH) Therapy Applications. Journal of Magnetism and Magnetic Material, vol. 332, pp. 247-52. Elsevier.

Di Barba, P., Dughiero, F. & Sieni, E. (2010). Magnetic field Synthesis in the Design of Inductors for Magnetic Fluid Hyperthermia. IEEE Trans. on Magnetics, vol 46(8), Aug 2010, pp. 2931-34.

Duguet, E., Hardel, L. & Vasseur, S. (2009). Cell Targeting and Magnetically Induced Hyperthermia (Ch.11). In: Thermal Nanosystems and Nanomaterials, Topics in Applied Physics, pp. 343-65. Ed. Volz, S. Springer-Verlag.

Eggers, P.E. & Ridihalgh, J.L. (2009). System Method and Apparatus For Localised Heating of Tissue. US Patent US7,567,843 B2.

Feucht, P. (2003). Magnetic field Applicator for Heating Magnetic Substances in Biological Tissue. US Patent 6,635,009 B2.

Feucht, P., Bruss, V. & Jordan, A. (2011). Alternating Magnetic Field Application Device for Heating Magnetic or Magnetisable Substances in Biological Tissue. US Patent 2011/0160515 A1.

Gleich, B. (2008). Arrangement for Influencing Magnetic Particles. US Patent 7,351,194 B2.

Gray, B.N., Jones, S.K. (2000). Targeted Hysteresis Hyperthermia as a Method for Treating Tissue. US Patent US6,149,576.

Gronemeyer, D.H.W., Busch, M., Rudiger, F. & Busch, J. (2009). Magnetic-Field Applicator. US Patent US2009/0203964 A1.

Gyawali, S.R. (2008). Helmholtz Coil Design and Characterization (Ch4) In: Design and Construction of Helmholtz Coil for Biomagnetic Studies on Soybean, MS Thesis, University of Missouri - Columbia, pp. 38-55.

Hager, E.D. (2006). Locoregional Hyperthermia (Ch.12). In: Hyperthermia in Cancer Treatment: A Primer, pp. 167–82. Ed. Baronzio, G.F. & Hager, E.D. Landes Bioscience & Springer Science.

Hanak, P., Vrba, K. & Koton, J. (2006), Method of Magnetic Field Generation for Use in Dermal Magnetotherapy. Proceedings of the International Conference on Networking, International Conference on Systems and International Conference on Mobile Communication and Learning Technologies (ICNICONSMCL 2006), Apr 2006, pp. 193-97.

Handy, E.S., Ivkov, R., Ellis-Busby, D., Foreman & A., Braunhut. (2006). Thermotherapy via Targeted Delivery of Nanoscale Magnetic Particles. US Patent US7,074,175 B2.

Hergt, R., Andra, W., d'Ambly, C.G., Hilger, I., Kaiser, W.A., Richter, U. & Schmidt, H. (1998). Physical Limits of Hyperthermia Using Magnetite Fine Particles. IEEE Trans. on Magnetics, vol 34(5), Sep 1998, pp. 3745-54.

Hergt, R., Hiergeist, R., Hilger, I., Kaiser, W.A., Lapatnikov, Y., Margel, S. & Richter, U. (2004). Maghemite Nanoparticles with Very High AC-losses for Application in RF-Magnetic Hyperthermia. Journal of Magnetism and Magnetic Materials, vol. 270, pp. 345-57. Elsevier.

Hergt, R. & Dutz, S. (2007). Magnetic Particle Hyperthermia – Biophysical Limitations of a Visionary. Journal of Magnetism and Magnetic Materials, vol. 311, pp. 187-92. Elsevier.

Ho, S.L., Niu, S. & Fu, W.N. (2012a) Design and Analysis of Novel Focused Hyperthermia Devices. IEEE Trans. on Magnetics, vol. 48(11), pp. 3254-57.

Ho, S.L., Jian, L., Gong, W. & Fu, W.N. (2012b). Design and Analysis of a Novel Targeted Magnetic Fluid Hyperthermia System for Tumor Treatment. IEEE Trans. on Magnetics, vol. 48(11), pp. 3262-65.

Huang, C., Lin, X., Yang, Y. (2009). Application of Magnetic Circuit and Multiple-coils Array in Induction Heating for Improving Localized Hyperthermia. World Academy of Science, Engineering and Technology, vol 58, pp. 724-27.

Huang, C., Lin, X., Lo, W. (2010). Design and Construction of a Hyperthermia System with Improved Interaction of Magnetic Induction-Heating. 32nd Annual International Conference of the IEEE EMBS, Sep 2010, pp. 3229-32.

Huisman, D. (2007) New Power Ferrite for Low Losses at High Frequency. Power Electronics Europe, issue 3, Apr 2007, pp. 19-21.

IFAC-CNR (Italian National Research Council) (2012). Calculation of the Dielectric Properties of Body Tissues in the Frequency Range 10 Hz – 100GHz. URL: http://niremf.ifac.cnr.it/tissprop/htmlclie/htmlclie.htm

Johannsen, M., Gneveckow, U., Taymoorian, K., Cho, C.C., Thiesen, B., Scholz, R.,Waldofner, N., Loening, S.A., Wust, P. & Jordan, A. (2007). Thermal Therapy of Prostate Cancer Using Magnetic Nanoparticles. European Urology, vol. 31(6), pp. 660-67.

Jojo, M., Murakami, A., Sato, F., Matsuki, M. & Sato, T. (2001). Considerations of Handy Excitation Apparatus for the Inductive Hyperthermia. IEEE Trans. on Magnetics, vol. 37(4), Jul 2001, pp. 2944-46.

Jordan, A., Maier-Hauff, K., Wust, P. & Johanssen, M. (2006). Nanoparticles for Thermotherapy (Ch.8). In: Nanomaterials for Cancer Therapy, pp. 242–58. Ed. Kumar, C.S.S.R. Wiley-VCH Verlag.

Kong, W.B. (2009). The Design of Magnetic Nanoparticle Induction Heating Coil and Simulation of the Magnetic Effect of Focusing. MSc Thesis, National Cheng Kung University, Taiwan. URL: http://etdncku.lib.ncku.edu.tw/ETD-db/ETD-search/view_etd?URN=etd-0728109-112545

Kotsuka, Y., Watanabe, M., Hosoi, M., Isono, I & Izumi, M. (2000). Development of Inductive Regional Heating System for Breast Hyperthermia. IEEE Trans. on Microwave Theory and Techniques, vol 48(11), Nov 2000, pp. 1807-14.

MagForce (2008). *Geschäftsberich* (Annual Report) 2007. MagForce AG.

MagForce (2009). *Thermotherapie mit magnetischen Nanopartikeln Nano-Krebs®-Therapiepp. Methode und klinische Entwicklung einer neuen Option in der Krebstherapie.* Clinical studies information slides. MagForce AG. Downloaded from MagForce's website.

Miers, Y., Hernandez, A.V. & Salas, L.L. (2002). Magnetic Induction Heating System for Local Hyperthermia Research. Proceedings of the Second Joint EMBS/BMES Conference, Oct 2002, pp. 1744-45.

Mishelevich, D. & Schneider, M. (2009). Focusing Magnetics Fields with Attractor Magnets and Concentrator Devices. WIPO Patent Appl. WO2009/033144 A2.

Mornet, S., Vasseur, S., Grasset, F., Duguet, E. (2004). Magnetic Nanoparticle Design for Medical Diagnosis and Therapy. Journal of Materials Chemistry, vol 14, 2004, pp. 2161-75.

Plewako, J., Krawczyk, A. & Grochowicz, B. (2003) Electromagnetic Hyperthermia – Foundations and Computer Modelling. ISEF 2003 11$^{th}$ International Symposium on Electromagnetic Fields in Electrical Engineering, Sep 2003, pp. 337-43.

Pollert, E., Veverka, P., Veverka, M., Kaman, O., Zaveta, K., Vasseur, S., Epherre, R., Goglio, G. & Duguet, E. (2009). Search of New Core Materials for Magnetic Fluid Hyperthermia: Preliminary Chemical and Physical Issues. Prog. in Solid State Chem., pp. 1-14. Elsevier.

Rand, R.W., Snow, H.D., Elliott, D.G. & Haskins, G.M. (1983). Induction Heating Apparatus for Use in Causing Necrosis in Neoplasm. US Patent 4,392,040.

Rand, R.W. (1991). Inductive Heating Process for Use in Causing Necrosis of Neoplasms at Selective Frequencies. US Patent 4,983159.

Sievert, C., Tucker, R.D. & Loening, S. (1993). Local Application Tumor Treatment Apparatus. US Patent US5,197,940.

Storm, F.K., Elliott, R.S., Harrison, W.H. & Morton, D.L. (1982). Clinical RF Hyperthermia by Magnetic-Loop Induction: A New Approach to Human Cancer Therapy. IEEE Trans. on Microwave Theory and Techniques, vol 30(8), Aug 1982, pp. 1149-58.

Szasz, A., Szasz, O. & Szasz, N. (2006). Physical Background and Technical Realizations of Hyperthermia (Ch.3). In: Hyperthermia in Cancer Treatment: A Primer, pp. 27–57. Ed. Baronzio, G.F. & Hager, E.D. Landes Bioscience & Springer Science.

Tai, C.C. & Chen, C.C. (2008) The Design of a Half-bridge Series-resonant Type Heating System for Magnetic Nanoparticle Thermotherapy. 23rd Progress in Electromagnetics Research Symposium Proceedings (PIERS 2008), Mar 2008, pp. 610-14.

Talebinejad, M., Musallam, S. & Marble, A.E. (2011). A Transcranial Magnetic Stimulation Coil Using Rectangular Braided Litz Wire. IEEE International Workshop on Medical Measurements and Applications Proceedings (MeMeA 2011), May 2011, pp. 280-83.

Trahms, L. (2009). Biomedical Applications of Magnetic Nanoparticles. Lect. Notes Phys., vol .763, pp. 327-58. Springer-Verlag.

Tsuyama, T. Katayama, Y., Hyodo, A., Hayami, T., Ueno, S. & Iramina, K. (2009). Effects of Coil Parameters on the Stimulated Area by Transcranial Magnetic Stimulation. IEEE Trans. on Magnetics, vol 45(10), Oct 2009, pp. 4845-48.

WHO (World Health Organisation) (2007). Electric and Magnetic Fields inside the Body (Ch.3). In: Extremely Low Frequency Fields, Environmental Health Criteria Monograph 238, pp. 73-96. WHO.

Wust, P., Henkel, T., Sehouli, J., Bohmer, J.R.D., Kahmann, F., Felix, R. & Jordan, A. (2006). Magnetic Nanoparticles for Interstitial Thermotherapy – Feasibility, Tolerance and Achieved Temperatures. International Journal of Hyperthermia, vol. 22(8), pp. 673-85. Informa.

Xu, R. Yu, H., Zhang, Y., Ma, M., Chen, Z., Wang, C., Teng, G., Ma, J., Sun, Z. & Gu, N. (2009). Three-dimensional Model for Determining Inhomogeneous Thermal Dosage in a Liver Tumor During Arterial Embolization Hyperthermia Incorporating Magnetic Nanoparticles. IEEE Trans. on Magnetics., vol. 45(8), Aug 2009, pp. 3085-91.

Zechbauer, U. (2007). Zeroing in on Cancer. Picture of the Future, Spring 2007, pp. 62-65. Siemens AG.

# APPENDIX A

## A.1 Derivation of particular integrals

In this section, the non-common integrals used in this appendix are derived. The integral ***I*** is included for completeness sake as it is used in deriving integrals ***J*** and ***K***.

(a) $$I=\int\frac{dx}{x^2+a^2}$$

$$=\int\frac{dx}{x^2-(ia)^2}$$

$$=\frac{1}{2ia}\int\frac{-(x+ia)}{(x-ia)}\frac{[-(x+ia)+(x-ia)]\,dx}{(x+ia)^2}$$

Let $t=\frac{-(x-ia)}{(x+ia)}$ => $\frac{dt}{dx}=\frac{-(x+ia)+(x-ia)}{(x+ia)^2}$

=> $$I=\frac{1}{2ia}\int\frac{1}{t}\frac{dt}{dx}dx=\frac{1}{2ia}\ln[\frac{-(x-ia)}{(x+ia)}]=\frac{k}{a}$$

where $e^{2ik}=-\frac{(x-ia)}{(x+ia)}$

but $e^{2ik}+1=e^{ik}(e^{ik}+e^{-ik})=-\frac{(x-ia)}{(x+ia)}+\frac{(x+ia)}{(x+ia)}=\frac{2ia}{(x+ia)}$ and

$$e^{2ik}-1=e^{ik}(e^{ik}-e^{-ik})=-\frac{(x-ia)}{(x+ia)}-\frac{(x+ia)}{(x+ia)}=\frac{-2x}{(x+ia)}$$

=> $$\frac{e^{ik}-e^{-ik}}{e^{ik}+e^{-ik}}=\frac{ix}{a} \Rightarrow \frac{[\frac{e^{ik}-e^{-ik}}{2i}]}{[\frac{e^{ik}+e^{-ik}}{2}]}=\frac{x}{a} \Rightarrow \frac{\sin k}{\cos k}=\tan k=\frac{x}{a}$$

=> $$I=\frac{1}{a}\tan^{-1}\frac{x}{a}+u \qquad \text{(A1.1)}$$

where ***u*** is a constant.

(b) $$J=\int\frac{d\theta}{a+b\sin\theta+c\cos\theta}$$

$$=\int \frac{d\theta}{a(\sin^2\frac{\theta}{2}+\cos^2\frac{\theta}{2})+2b\sin\frac{\theta}{2}\cos\frac{\theta}{2}+c(\cos^2\frac{\theta}{2}-\sin^2\frac{\theta}{2})}$$

$$=\int \frac{sec^2\frac{\theta}{2}d\theta}{(a-c)\tan^2\frac{\theta}{2}+(a+c)+2b\tan\frac{\theta}{2}}$$

$$=\int \frac{(a-c)sec^2\frac{\theta}{2}d\theta}{(a-c)^2\tan^2\frac{\theta}{2}+(a+c)(a-c)+2b(a-c)\tan\frac{\theta}{2}}$$

$$=\int \frac{(a-c)sec^2\frac{\theta}{2}d\theta}{[(a-c)\tan^2\frac{\theta}{2}+b]^2+[a^2-b^2-c^2]}$$

Let $u=(a-c)\tan\frac{\theta}{2}+b$ => $du=\frac{1}{2}(a-c)sec^2\frac{\theta}{2}d\theta$

=> $$J=\int \frac{2du}{u^2+[a^2-b^2-c^2]}$$

$$=\frac{2}{\sqrt{a^2-b^2-c^2}}\tan^{-1}[\frac{(a-c)\tan\frac{\theta}{2}+b}{\sqrt{a^2-b^2-c^2}}]+v \qquad \text{(A1.2)}$$

by using identity ***I*** of Eq A1.1 where ***v*** is a constant, provided $a^2 - b^2 - c^2 > 0$.

(c) $$K=\int \frac{\sin\theta\, d\theta}{a+b\sin\theta+c\cos\theta}$$

$$=\frac{1}{b^2+c^2}\int \frac{(-bc\cos\theta+c^2\sin\theta+ab+bc\cos\theta+b^2\sin\theta)d\theta}{a+b\sin\theta+c\cos\theta}$$

$$-\frac{1}{b^2+c^2}\int \frac{ab}{a+b\sin\theta+c\cos\theta}$$

$$=\frac{1}{b^2+c^2}\int [\frac{-c(b\cos\theta-c\sin\theta)}{a+b\sin\theta+c\cos\theta}+\frac{b(a+b\sin\theta+c\cos\theta)}{a+b\sin\theta+c\cos\theta}]d\theta$$

$$-\frac{1}{b^2+c^2}\int \frac{ab}{a+b\sin\theta+c\cos\theta}$$

Let $q=a+b\sin\theta+c\cos\theta$ => $\frac{dq}{d\theta}=b\cos\theta-c\sin\theta$

=> $$K=\frac{-c}{b^2+c^2}\int\frac{dq}{q}+\int\frac{b\,d\theta}{b^2+c^2}$$

$$-\frac{ab}{b^2+c^2}\int\frac{1}{a+b\sin\theta+c\cos\theta}$$

By using identity ***J*** of Eq A1.2,

$$K=\frac{-c}{b^2+c^2}\ln[a+b\sin\theta+c\cos\theta]+\frac{b\theta}{b^2+c^2}$$

$$-\frac{2ab}{(b^2+c^2)\sqrt{a^2-b^2-c^2}}\tan^{-1}\left[\frac{(a-c)\tan\frac{\theta}{2}+b}{\sqrt{a^2-b^2-c^2}}\right]+w \qquad \text{(A1.3)}$$

where ***w*** is a constant, provided $a^2-b^2-c^2>0$.

## A.2 2D solenoid field penetration

To represent a 2D solenoid, consider the cross section of 2 parallel identical current sheets of breadth ***l*** and infinite depth, separated by a distance of 2***b*** with each limb carrying current density ***J*** of opposing polarity respectively where a positive ***J*** denotes the current leaving the page as shown in Fig A2.1.

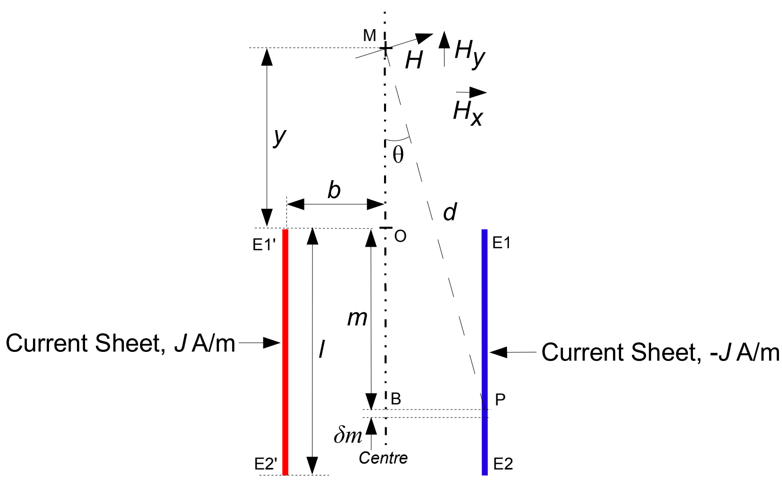


Fig A2.1 Field point along the axis of the parallel current sheets.

Take a point, M at distance ***y*** from the origin, O. Considering the geometry of points O, M, B and P in Fig A2.1,

$$d^2 = b^2 + (y+m)^2 \tag{A2.1}$$

$$\sin\theta = \frac{b}{d} \tag{A2.2}$$

The ***y*** component of the magnetising field strength, $\boldsymbol{\delta H_y}$ at point M due to the current element $\boldsymbol{\delta m}$ of infinite depth at point P is given by

$$\delta H_y = \frac{J\,\delta m \sin\theta}{2\pi d} \tag{A2.3}$$

Substituting Eqs A2.1 and A2.2 into Eq A2.3 and using identity ***I*** of Eq A1.1 yields

$$\delta H_y = \frac{J\,b\,\delta m}{2\pi(b^2 + (y+m)^2)}$$

The corresponding ***x*** component, $\boldsymbol{H_x}$ is not considered because by symmetry, its field will cancel out.

=> $$H = 2\int dH_y = \int_0^l \frac{J\,b\,dm}{\pi(b^2+(y+m)^2)}$$

$$= \frac{J}{\pi}\tan^{-1}\frac{y+m}{b}\Big|_0^l$$

$$= \frac{J}{\pi}[\tan^{-1}\frac{y+l}{b} - \tan^{-1}\frac{y}{b}] \tag{A2.4}$$

### A.3 2D distributed planar coil field penetration

To represent a 2D distributed planar coil, consider the cross section of 2 identical current sheets of breadth ***l*** and infinite depth, separated by a distance of 2***b*** with each limb carrying current density ***J*** of opposing polarity respectively where a positive ***J*** denotes the current leaving the page as shown in Fig A3.1.

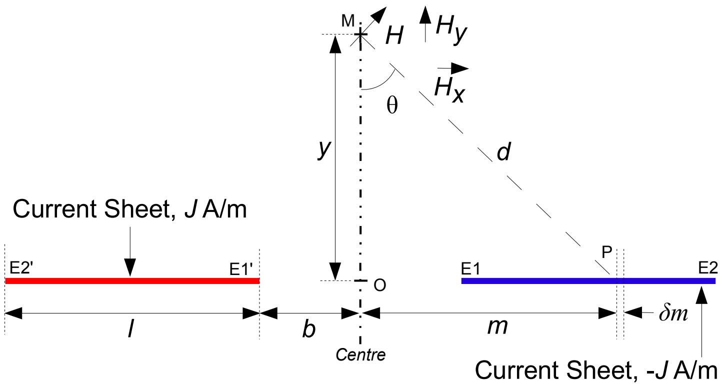


Fig A3.1 Field point along the axis of the distributed planar current sheets.

Take a point, M at distance $y$ from the origin, O. Considering the geometry of points O, M and P in Fig A3.1,

$$d^2 = y^2 + m^2 \quad \text{(A3.1)}$$

$$\sin\theta = \frac{m}{d} \quad \text{(A3.2)}$$

The $y$ component of the magnetising field strength, $\boldsymbol{\delta H_y}$ at point M due to the current element $\boldsymbol{\delta m}$ of infinite depth at point P is given by

$$\delta H_y = \frac{J\,\delta m \sin\theta}{2\pi d} \quad \text{(A3.3)}$$

Substituting Eqs A3.1 and A3.2 into Eq A3.3 yields

$$\delta H_y = \frac{J\,m\,\delta m}{2\pi(y^2+m^2)}$$

The corresponding $x$ component, $\boldsymbol{H_x}$ is not considered because by symmetry, its field will cancel out.

$$=> \qquad H = 2\int dH_y = \int_b^{l+b} \frac{J\,m\,dm}{\pi(y^2+m^2)}$$

$$= \frac{J}{2\pi}\ln(y^2+m^2)|_b^{l+b}$$

$$= \frac{J}{2\pi}\ln[\frac{y^2+(l+b)^2}{y^2+b^2}] \quad \text{(A3.4)}$$

### A.4 2D loop coil field penetration

To represent a 2D loop coil, consider the cross section of 2 current paths, C1 and C2 of infinite depth, separated by a distance of 2***b*** with each path carrying current ***I*** of opposing polarity respectively where a positive ***I*** denotes the current leaving the page as shown in Fig A4.1.

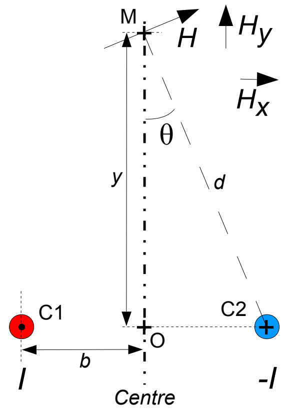


Fig A4.1 Field point along the axis of 2 current paths.

Take a point, M at distance ***y*** from the origin, O. Considering the geometry of points O, C2 and M in Fig A4.1,

$$d^2 = y^2 + b^2 \quad \text{(A4.1)}$$

$$\sin\theta = \frac{b}{d} \quad \text{(A4.2)}$$

The ***y*** component of the magnetising field strength, $\boldsymbol{\delta H_y}$ at point M due to the current path C2 of infinite depth is given by

$$H_y = \frac{I\sin\theta}{2\pi d} \quad \text{(A4.3)}$$

The corresponding ***x*** component, $\boldsymbol{H_x}$ is not considered because by symmetry, its field will cancel out. Therefore, substituting Eqs A4.1 and A4.2 into Eq A4.3 yields

$$H = 2\frac{Ib}{2\pi(y^2+b^2)}$$

For an equivalent comparison, ***I*** can be expressed as ***Jl.***

=> $$H=\frac{J}{\pi}\frac{lb}{(y^2+b^2)}$$ (A4.4)

### A.5 Zero crossing on 2D distributed planar coil

To represent a 2D distributed planar coil, consider the cross section of 2 identical current sheets of breadth ***l*** and infinite depth, separated by a distance of 2***b*** with each limb carrying a current density ***J*** of opposing polarity respectively where a positive ***J*** denotes the current leaving the page as shown in Fig A5.1.

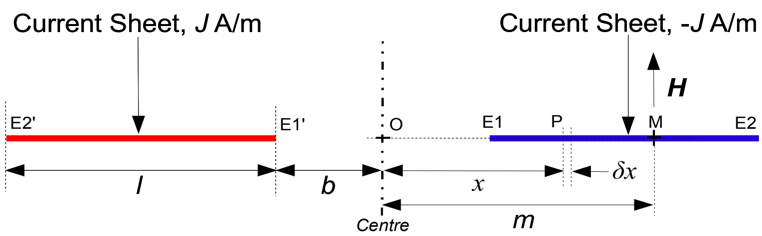


Fig A5.1 Field point **on** the distributed planar current sheets.

At point P on the current sheet at a distance ***x*** from the centre point O, the incremental current flowing through the element ***δx*** is given by ***J δx***. By Ampere's law, the magnetising field, ***H*** at point M in the direction shown in Fig A5.1 due to the current element of infinite depth at point P is given by

$$\delta H=\frac{J\,\delta x}{2\pi(x-m)}$$ (A5.1)

$$H=\int dH=\frac{J}{2\pi}\int_{x_1}^{x_2}\frac{dx}{(x-m)}$$

$$=\frac{J}{2\pi}\ln(x-m)\Big|_{x_1}^{x_2}\quad \forall\, x>m\,,\, x_2>x_1 \quad \text{, or}$$

$$=\frac{J}{2\pi}\ln(m-x)\Big|_{x_1}^{x_2}\quad \forall\, x<m\,,\, x_2>x_1$$

Taking the sum of all ***δx*** elements for segments M-E2, E1-M and E2'-E1' as shown in Fig A5.1 yields the magnetising field as expressed by Eqs A5.2, A5.3 and A5.4 respectively.

$$H_{M-E2}=\frac{J}{2\pi}\ln(x-m)\Big|_{m+\varepsilon}^{(l+b)} \quad \text{(A5.2)}$$

$$H_{E1-M}=\frac{J}{2\pi}\ln(m-x)\Big|_{b}^{m-\varepsilon} \quad \text{(A5.3)}$$

$$H_{E2'-E1'}=\frac{-J}{2\pi}\ln(m-x)\Big|_{-(l+b)}^{-b} \quad \text{(A5.4)}$$

where ε is the error as m ± ε approaches m, i.e. ε approaches 0 in limit. Summing up the magnetising field values in Eqs A5.2, A5.3 and A5.4, the aggregate magnetising field is given by Eq A5.5.

$$H=\frac{J}{2\pi}\ln(x-m)\Big|_{m+\varepsilon}^{(l+b)}$$

$$+\frac{J}{2\pi}\ln(m-x)\Big|_{b}^{m-\varepsilon}$$

$$+\frac{-J}{2\pi}\ln(m-x)\Big|_{-(l+b)}^{-b}$$

$$=\frac{J}{2\pi}(\ln(l+b-m)-\ln(m+\varepsilon-m))$$

$$+\frac{J}{2\pi}(\ln(m-(m-\varepsilon))-\ln(m-b))$$

$$-\frac{J}{2\pi}(\ln(m+b)-\ln(m+l+b))$$

=> $$H=\frac{J}{2\pi}\ln\left[\frac{((l+b)-m)((l+b)+m)}{(m-b)(m+b)}\right] \quad \text{(A5.5)}$$

The magnetising field, ***H*** in Eq A5.5 crosses a null point at $x = m_0$ as given by Eq 5.6.

$$((l+b)-m_0)((l+b)+m_0)=(m_0-b)(m_0+b) \quad \text{, or}$$

$$m_0=\sqrt{\frac{b^2+(b+l)^2}{2}} \quad \text{(A5.6)}$$

## A.6 2D distributed concave coil's field penetration

To represent a 2D distributed concave coil, consider the cross section of 2 identical current sheets of breadth ***l*** and infinite depth, curved at a curvature radius of ***r***, separated by a distance of 2***b*** with each limb carrying a current density ***J*** of opposing polarity respectively where a positive ***J*** denotes the current leaving the page as shown in Fig A6.1.

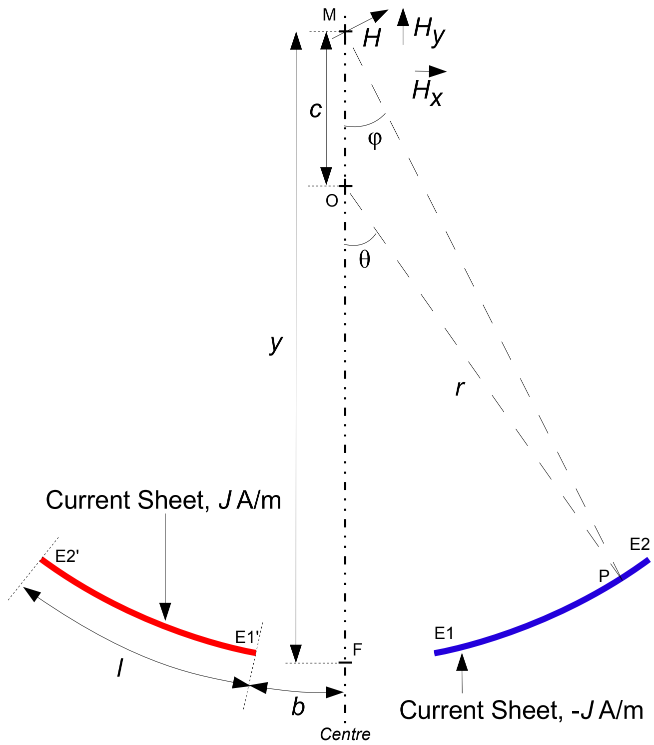


Fig A6.1 Field point along the axis of the distributed concave current sheets.

Take a point, M at a distance ***c*** from the centre of the curvature, O. Considering the geometry of points O, M and P in Fig A6.1,

$$r\cos\theta + c = d\cos\varphi \tag{A6.1}$$

$$r\sin\theta = d\sin\varphi \tag{A6.2}$$

$$d^2 = r^2\sin^2\theta + (r\cos\theta + c)^2$$

$$= r^2 + 2rc\cos\theta + c^2 \tag{A6.3}$$

The ***y*** component of the magnetising field strength, $\boldsymbol{\delta H_y}$ at point M due to the current element $\boldsymbol{r\,\delta\theta}$ of infinite depth at point P is given by

$$\delta H_y = \frac{J\,r\,\delta\theta\sin\varphi}{2\pi d} \qquad \text{(A6.4)}$$

Substituting Eqs A6.2 and A6.3 into Eq A6.4 yields

$$\delta H_y = \frac{J\,r^2\sin\theta\,\delta\theta}{2\pi d^2}$$

The corresponding $\boldsymbol{x}$ component, $\boldsymbol{H_x}$ is not considered because by symmetry, its field will cancel out.

$$=> \qquad H = 2\int dH_y = \int_{\theta_1}^{\theta_2} \frac{J\,r^2\sin\theta\,d\theta}{\pi d^2}$$

$$= \int_{\theta_1}^{\theta_2} \frac{J\,r(2rc)\sin\theta\,d\theta}{2c\pi(r^2+2rc\cos\theta+c^2)}$$

$$= \frac{-J\,r}{2c\pi}\ln(r^2+2rc\cos\theta+c^2)\Big|_{\theta_1}^{\theta_2}$$

$$= \frac{-J}{2\pi(\frac{c}{r})}\ln\left(1+\frac{2c}{r}\cos\theta+\left(\frac{c}{r}\right)^2\right)\Big|_{\theta_1}^{\theta_2}$$

But from Fig A6.1, $\boldsymbol{y} = \boldsymbol{r} + \boldsymbol{c}$, $\boldsymbol{\theta_1} = \boldsymbol{b}$ / $\mathbf{r}$ and $\boldsymbol{\theta_2} = (\boldsymbol{b} + \boldsymbol{l})$ / $\boldsymbol{r}$ where $\boldsymbol{\theta_1}$ and $\boldsymbol{\theta_2}$ span endpoints $E_1$ and $E_2$ respectively.

$$=> \qquad H = \frac{J}{2\pi(1-\frac{y}{r})}\ln\left[\frac{1+(1-\frac{y}{r})^2-2(1-\frac{y}{r})\cos\theta_2}{1+(1-\frac{y}{r})^2-2(1-\frac{y}{r})\cos\theta_1}\right]$$

$$= \frac{J}{2\pi(1-\frac{y}{r})}\ln\left[\frac{1+(1-\frac{y}{r})^2-2(1-\frac{y}{r})\cos\frac{b+l}{r}}{1+(1-\frac{y}{r})^2-2(1-\frac{y}{r})\cos\frac{b}{r}}\right] \qquad \text{(A6.5)}$$

## A.7 2D distributed convex coil's field penetration

To represent a 2D distributed convex coil, consider the cross section of 2 identical current sheets of breadth $\boldsymbol{l}$ and infinite depth, curved at a curvature radius of $\boldsymbol{r}$, separated by a distance of $2\boldsymbol{b}$ with each limb carrying a current density $\boldsymbol{J}$ of opposing polarity respectively where a positive $\boldsymbol{J}$ denotes the current leaving the page as shown in Fig A7.1.

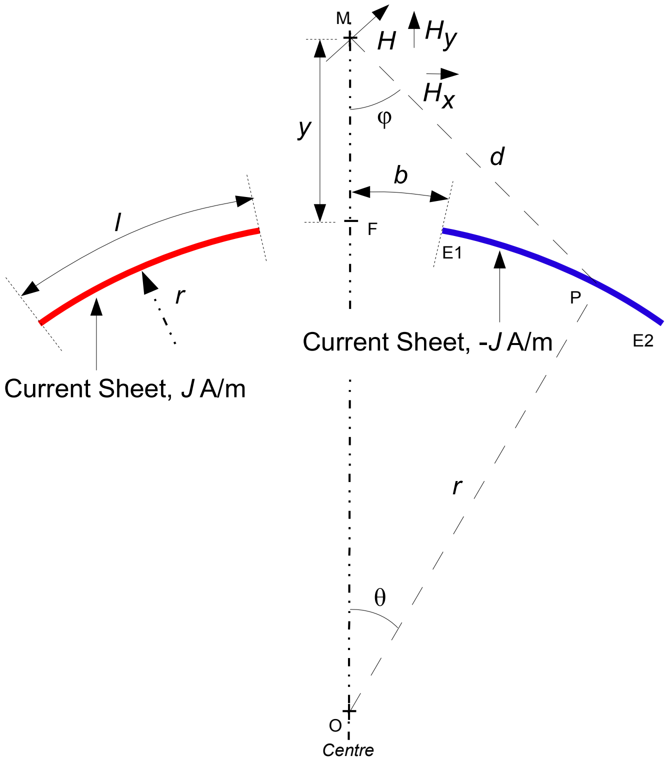


Fig A7.1 Field point along the axis of the distributed convex current sheets.

Take a point, M at a distance $\boldsymbol{y}$ from the pole centre, F. Considering the geometry of points O, M and P in Fig A7.1,

$$r\cos\theta + d\cos\varphi = r + y \tag{A7.1}$$

$$r\sin\theta = d\sin\varphi \tag{A7.2}$$

$$d^2 = r^2\sin^2\theta + (r + y - r\cos\theta)^2$$

$$= r^2 + (r+y)^2 - 2r(r+y)\cos\theta \tag{A7.3}$$

The $\boldsymbol{y}$ component of the magnetising field strength, $\boldsymbol{\delta H_y}$ at point M due to the current element $\boldsymbol{r\,\delta\theta}$ of infinite depth at point P is given by

$$\delta H_y = \frac{J\,r\,\delta\theta\sin\varphi}{2\pi d} \tag{A7.4}$$

Substituting Eqs A7.2 and A7.3 into Eq A7.4 yields

$$\delta H_y = \frac{J r^2 \sin\theta\, \delta\theta}{2\pi d^2}$$

The corresponding ***x*** component, ***$H_x$*** is not considered because by symmetry, its field will cancel out.

$$=> \qquad H = 2\int dH_y = \int_{\theta_1}^{\theta_2} \frac{J r^2 \sin\theta\, d\theta}{\pi d^2}$$

$$= \int_{\theta_1}^{\theta_2} \frac{J r [2r(r+y)] \sin\theta\, d\theta}{2(r+y)\pi(r^2+(r+y)^2-2r(r+y)\cos\theta)}$$

$$= \frac{J r}{2\pi(r+y)} \ln(r^2+(r+y)^2-2r(r+y)\cos\theta)\Big|_{\theta_1}^{\theta_2}$$

But from Fig A7.1, ***$\theta_1$*** = ***b*** / **r** and ***$\theta_2$*** = (***b*** + ***l***) / ***r*** where ***$\theta_1$*** and ***$\theta_2$*** span endpoints $E_1$ and $E_2$ respectively.

$$=> \qquad H = \frac{J}{2\pi(1+\frac{y}{r})} \ln\left[\frac{1+(1+\frac{y}{r})^2-2(1+\frac{y}{r})\cos\theta_2}{1+(1+\frac{y}{r})^2-2(1+\frac{y}{r})\cos\theta_1}\right]$$

$$= \frac{J}{2\pi(1+\frac{y}{r})} \ln\left[\frac{1+(1+\frac{y}{r})^2-2(1+\frac{y}{r})\cos\frac{b+l}{r}}{1+(1+\frac{y}{r})^2-2(1+\frac{y}{r})\cos\frac{b}{r}}\right] \qquad \text{(A7.5)}$$

### A.8 2D distributed planar coil's field focusing

To represent a 2D distributed planar coil, consider the cross section of 2 identical current sheets of breadth ***l*** and infinite depth, separated by a distance of 2***b*** with each limb carrying a current density ***J*** of opposing polarity respectively where a positive ***J*** denotes the current leaving the page as shown in Fig A8.1.

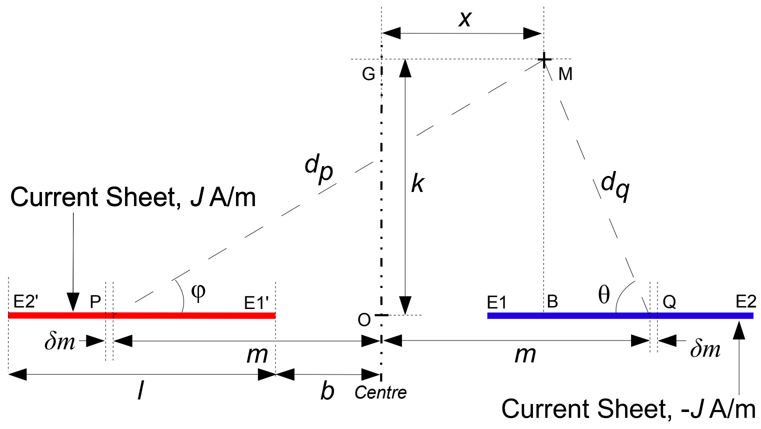


Fig A8.1 Field point along the GM plane of the distributed planar current sheets.

Take a point, M at a distance ***x*** from the OG axis along the GM plane, displaced by a distance ***k*** from the origin, O. Considering the geometry of points B, M and P in Fig A8.1,

$$d_p^2 = k^2 + (m+x)^2 \tag{A8.1}$$

$$\cos\varphi = \frac{(m+x)}{d_p} \tag{A8.2}$$

Similarly, considering the geometry of points B, M and Q,

$$d_q^2 = k^2 + (m-x)^2 \tag{A8.3}$$

$$\cos\theta = \frac{(m-x)}{d_q} \tag{A8.4}$$

Fig A8.2 shows the expanded view of the magnetising field components at point M due to the symmetrical current elements at points P and Q.

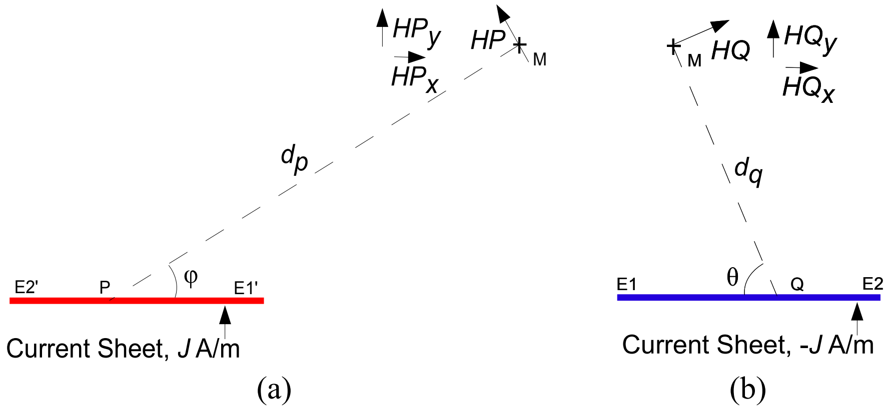


Fig A8.2 Magnetising field at point M due to current elements at points (a) P and (b) Q of the distributed planar current sheets.

The ***y*** component of the magnetising field strength, $\boldsymbol{\delta HP_y}$ at point M due to the symmetrical current elements $\boldsymbol{J\ \delta m}$ of infinite depth at points P and Q are given by Eqs A8.5 and A8.6.

$$\delta HP_y = \frac{J\ \delta m \cos\varphi}{2\pi\, d_p} \tag{A8.5}$$

$$\delta HQ_y = \frac{J\ \delta m \cos\theta}{2\pi\, d_q} \tag{A8.6}$$

The corresponding ***x*** components, $\boldsymbol{HP_x}$ and $\boldsymbol{HQ_x}$ are not considered because when the coils are aggregated symmetrically along the GM plane, they will be cancelled out by the corresponding $\boldsymbol{HP_x}$ and $\boldsymbol{HQ_x}$ of the other coil. Substituting Eqs A8.1 and A8.2 into Eq A8.5 yields

$$\delta HP_y = \frac{J(m+x)\delta m}{2\pi\left(k^2+(m+x)^2\right)} \tag{A8.7}$$

Similarly, substituting Eqs A8.3 and A8.4 into Eq A8.6 yields

$$\delta HQ_y = \frac{J(m-x)\delta m}{2\pi\left(k^2+(m-x)^2\right)} \tag{A8.8}$$

Summing A8.7 and A8.8 yields the net $\boldsymbol{H_y}$ at point M as expressed by Eq A8.9.

$$H_y = \int dHP_y + \int dHQ_y$$

$$=\frac{J}{2\pi}\int_{b}^{l+b}\frac{(m+x)dm}{k^2+(m+x)^2}+\frac{J}{2\pi}\int_{b}^{l+b}\frac{(m-x)dm}{k^2+(m-x)^2}$$

$$=\frac{J}{4\pi}\ln[k^2+(m+x)^2]|_b^{l+b}+\frac{J}{4\pi}\ln[k^2+(n-x)^2]|_b^{l+b}$$

$$=\frac{J}{4\pi}\ln\frac{(k^2+(b+l+x)^2)(k^2+(b+l-x)^2)}{(k^2+(b+x)^2)(k^2+(b-x)^2)} \qquad \text{(A8.9)}$$

### A.9 2D distributed concave coil's field focusing

To represent a 2D distributed concave coil, consider the cross section of 2 identical current sheets of breadth ***l*** and infinite depth, curved at a curvature radius of ***r***, separated by a distance of 2***b*** with each limb carrying a current density ***J*** of opposing polarity respectively where a positive ***J*** denotes the current leaving the page as shown in Fig A9.1.

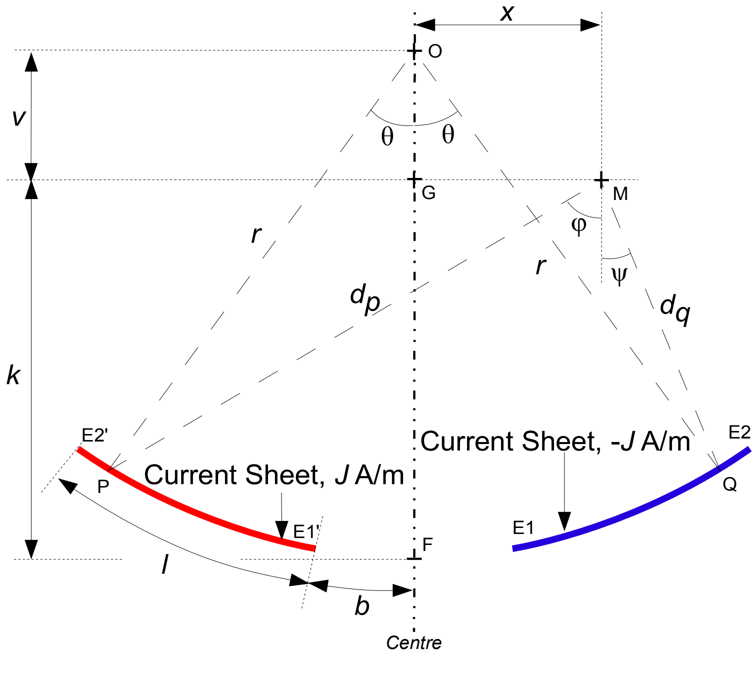


Fig A9.1 Field point along the GM plane of the distributed concave current sheets.

Figs A9.2 shows the expanded view of the magnetising field components at point M due to the symmetrical current elements at points P and Q.

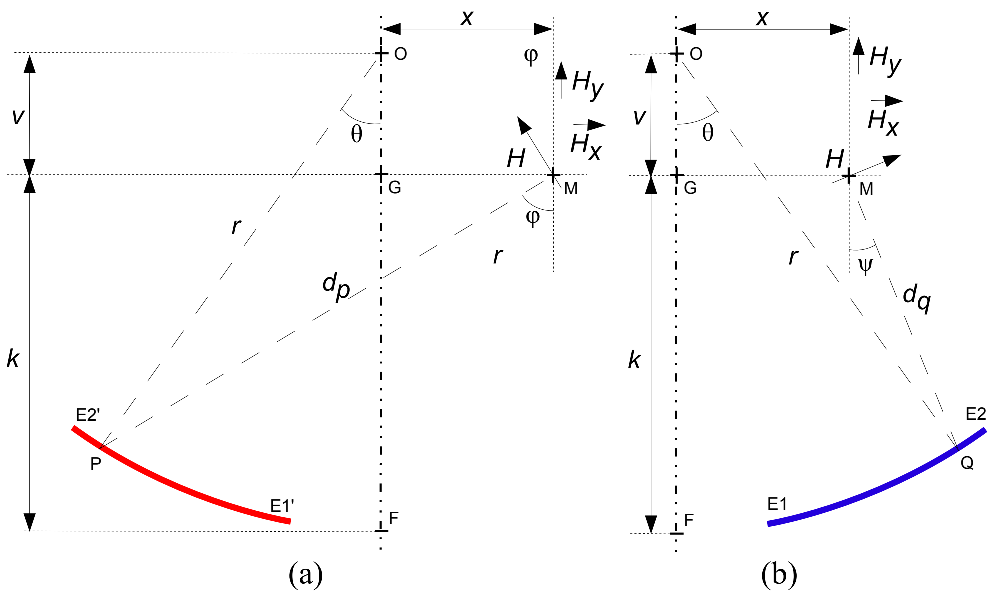


Fig A9.2 Magnetising field at point M due to the current elements at points (a) P and (b) Q of the distributed concave current sheets.

Take a point, M at a distance $\boldsymbol{x}$ from the OG axis along the GM plane, displaced by a distance $\boldsymbol{v}$ from the centre of curvature, O or $\boldsymbol{k}$ from the pole, F. Considering the geometry of points O, M and P in Fig A9.2(a),

$$d_p \cos\varphi = r\cos\theta - v$$

$$d_p \sin\varphi = r\sin\theta + x \qquad \text{(A9.1)}$$

$$d_p^{\,2} = (r\cos\theta - v)^2 + (r\sin\theta + x)^2$$

$$= r^2 + (x^2 + v^2) + 2r(x\sin\theta - v\cos\theta) \qquad \text{(A9.2)}$$

Similarly, considering the geometry of points O, M and Q in Fig A9.2(b),

$$d_q \cos\psi = r\cos\theta - v$$

$$d_q \sin\psi = r\sin\theta - x \qquad \text{(A9.3)}$$

$$d_q^{\,2} = (r\cos\theta - v)^2 + (r\sin\theta - x)^2$$

$$= r^2 + (x^2 + v^2) - 2r(v\cos\theta + x\sin\theta) \qquad \text{(A9.4)}$$

The $\boldsymbol{y}$ component of the magnetising field strength, $\boldsymbol{\delta HP_y}$ at point M due to the symmetrical current elements $\boldsymbol{J\,\delta\theta}$ of infinite depth at points P and Q are given by Eqs A9.5 and A9.6.

$$\delta HP_y = \frac{J\, r\delta\theta \sin\varphi}{2\pi d_p} \tag{A9.5}$$

$$\delta HQ_y = \frac{J\, r\delta\theta \sin\psi}{2\pi d_q} \tag{A9.6}$$

The corresponding ***x*** components, $\boldsymbol{HP_x}$ and $\boldsymbol{HQ_x}$ are not considered because when the coils are aggregated symmetrically along the GM plane, they will be cancelled out by the corresponding $\boldsymbol{HP_x}$ and $\boldsymbol{HQ_x}$ from the other coil. Substituting Eqs A9.1 and A9.2 into Eq A9.5 yields

$$\delta HP_y = \frac{J}{2\pi}\frac{r(r\sin\theta + x)\delta\theta}{r^2+(x^2+v^2)+2r(x\sin\theta - v\cos\theta)} \tag{A9.7}$$

Similarly, by substituting Eqs A9.3 and A9.4 into Eq A9.6 yields

$$\delta HQ_y = \frac{J}{2\pi}\frac{r(r\sin\theta - x)\delta\theta}{r^2+(x^2+v^2)-2r(v\cos\theta + x\sin\theta)} \tag{A9.8}$$

Summing A9.7 and A9.8 yields the net $\boldsymbol{H_y}$ at point M as expressed by Eq A9.9.

$$\begin{aligned}
H_y &= \int dHP_y + \int dHQ_y \\
&= \frac{Jr}{2\pi}\int_{\theta_1}^{\theta_2}\frac{(r\sin\theta + x)d\theta}{r^2+(x^2+v^2)+2r(x\sin\theta - v\cos\theta)} \\
&\quad + \frac{Jr}{2\pi}\int_{\theta_1}^{\theta_2}\frac{(r\sin\theta - x)d\theta}{r^2+(x^2+v^2)-2r(v\cos\theta + x\sin\theta)} \\
&= \frac{Jr^2}{2\pi}\int_{\theta_1}^{\theta_2}\frac{\sin\theta\, d\theta}{r^2+(x^2+v^2)+2r(x\sin\theta - v\cos\theta)} \\
&\quad + \frac{Jrx}{2\pi}\int_{\theta_1}^{\theta_2}\frac{d\theta}{r^2+(x^2+v^2)+2r(x\sin\theta - v\cos\theta)} \\
&\quad + \frac{Jr^2}{2\pi}\int_{\theta_1}^{\theta_2}\frac{\sin\theta\, d\theta}{r^2+(x^2+v^2)-2r(v\cos\theta + x\sin\theta)} \\
&\quad - \frac{Jrx}{2\pi}\int_{\theta_1}^{\theta_2}\frac{d\theta}{r^2+(x^2+v^2)-2r(v\cos\theta + x\sin\theta)}
\end{aligned} \tag{A9.9}$$

By using Eqs A1.2 and A1.3 as shown in Section A.1 and substituting the identity $(r^2+x^2+v^2)^2-4r^2v^2-4r^2x^2=(r^2-x^2-v^2)^2$ into Eq A9.9 yields Eq A9.10.

$$H_y=\frac{J}{4\pi(x^2+v^2)}(rv\ln[(r^2+x^2+v^2)-2rv\cos\theta+2rx\sin\theta]+rx\theta)|_{\theta_1}^{\theta_2}$$

$$-\frac{2J((r^2+x^2+v^2)rx)}{4\pi(x^2+v^2)(r^2-x^2-v^2)}\tan^{-1}[\frac{(r^2+x^2+v^2+2rv)\tan\frac{\theta}{2}+2rx}{(r^2-x^2-v^2)}]|_{\theta_1}^{\theta_2}$$

$$+\frac{4J((x^2+v^2)rx)}{4\pi(x^2+v^2)(r^2-x^2-v^2)}\tan^{-1}[\frac{(r^2+x^2+v^2+2rv)\tan\frac{\theta}{2}+2rx}{(r^2-x^2-v^2)}]|_{\theta_1}^{\theta_2}$$

$$+\frac{J}{4\pi(x^2+v^2)}(rv\ln[(r^2+x^2+v^2)-2rv\cos\theta-2rx\sin\theta]-rx\theta)|_{\theta_1}^{\theta_2}$$

$$+\frac{2J((r^2+x^2+v^2)rx)}{4\pi(x^2+v^2)(r^2-x^2-v^2)}\tan^{-1}[\frac{(r^2+x^2+v^2+2rv)\tan\frac{\theta}{2}-2rx}{(r^2-x^2-v^2)}]|_{\theta_1}^{\theta_2}$$

$$-\frac{4J((x^2+v^2)rx)}{4\pi(x^2+v^2)(r^2-x^2-v^2)}\tan^{-1}[\frac{(r^2+x^2+v^2+2rv)\tan\frac{\theta}{2}-2rx}{(r^2-x^2-v^2)}]|_{\theta_1}^{\theta_2}$$

$$H_y=\frac{Jrv}{4\pi(x^2+v^2)}\ln[\frac{(r^2+x^2+v^2)-2rv\cos\theta_2+2rx\sin\theta_2}{(r^2+x^2+v^2)-2rv\cos\theta_1+2rx\sin\theta_1}]$$

$$-\frac{2Jrx}{4\pi(x^2+v^2)}\tan^{-1}[\frac{(r^2+x^2+v^2+2rv)\tan\frac{\theta_2}{2}+2rx}{(r^2-x^2-v^2)}]$$

$$+\frac{2Jrx}{4\pi(x^2+v^2)}\tan^{-1}[\frac{(r^2+x^2+v^2+2rv)\tan\frac{\theta_1}{2}+2rx}{(r^2-x^2-v^2)}]$$

$$+\frac{Jrv}{4\pi(x^2+v^2)}\ln[\frac{(r^2+x^2+v^2)-2rv\cos\theta_2-2rx\sin\theta_2}{(r^2+x^2+v^2)-2rv\cos\theta_1-2rx\sin\theta_1}]$$

$$+\frac{2Jrx}{4\pi(x^2+v^2)}\tan^{-1}[\frac{(r^2+x^2+v^2+2rv)\tan\frac{\theta_2}{2}-2rx}{(r^2-x^2-v^2)}]$$

$$-\frac{2Jrx}{4\pi(x^2+v^2)}\tan^{-1}[\frac{(r^2+x^2+v^2+2rv)\tan\frac{\theta_1}{2}-2rx}{(r^2-x^2-v^2)}] \quad \text{(A9.10)}$$

But from Fig A9.1, $\boldsymbol{v} = \boldsymbol{r} - \boldsymbol{k}$, $\boldsymbol{\theta_1} = \boldsymbol{b} / \mathbf{r}$ and $\boldsymbol{\theta_2} = (\boldsymbol{b} + \boldsymbol{l}) / \boldsymbol{r}$ where $\boldsymbol{\theta_1}$ and $\boldsymbol{\theta_2}$ span endpoints $E_1$ and $E_2$ respectively. Simplifying Eq A9.10 yields

$$\begin{aligned}
H_y = &Kv\ln(\frac{r^2+d^2-2rv\cos(\frac{(b+l)}{r})-2rx\sin(\frac{(b+l)}{r})}{r^2+d^2-2rv\cos\frac{b}{r}-2rx\sin\frac{b}{r}}) \\
&+Kv\ln(\frac{r^2+d^2-2rv\cos(\frac{(b+l)}{r})+2rx\sin(\frac{(b+l)}{r})}{r^2+d^2-2rv\cos\frac{b}{r}+2rx\sin\frac{b}{r}}) \\
&+2Kx\tan^{-1}(\frac{r^2+d^2+2rv\tan(\frac{(b+l)}{2r})-2rx}{r^2-d^2}) \\
&-2Kx\tan^{-1}(\frac{r^2+d^2+2rv\tan(\frac{b}{2r})-2rx}{r^2-d^2}) \\
&-2Kx\tan^{-1}(\frac{r^2+d^2+2rv\tan(\frac{(b+l)}{2r})+2rx}{r^2-d^2}) \\
&+2Kx\tan^{-1}(\frac{r^2+d^2+2rv\tan(\frac{b}{2r})+2rx}{r^2-d^2}) \quad \text{(A9.11)}
\end{aligned}$$

where

$$K=\frac{Jr}{4\pi d^2}$$

$$v=r-k$$

$$d=\sqrt{v^2+x^2}=\sqrt{y^2+x^2}$$

## A.10 2D distributed convex coil's field focusing

To represent a 2D distributed convex coil, consider the cross section of 2 identical current sheets of breadth ***l*** and infinite depth, curved at a curvature radius of ***r***, separated by a distance of 2***b*** with each limb carrying a current density ***J*** of opposing polarity respectively where a positive ***J*** denotes the current leaving the page as shown in Fig A10.1.

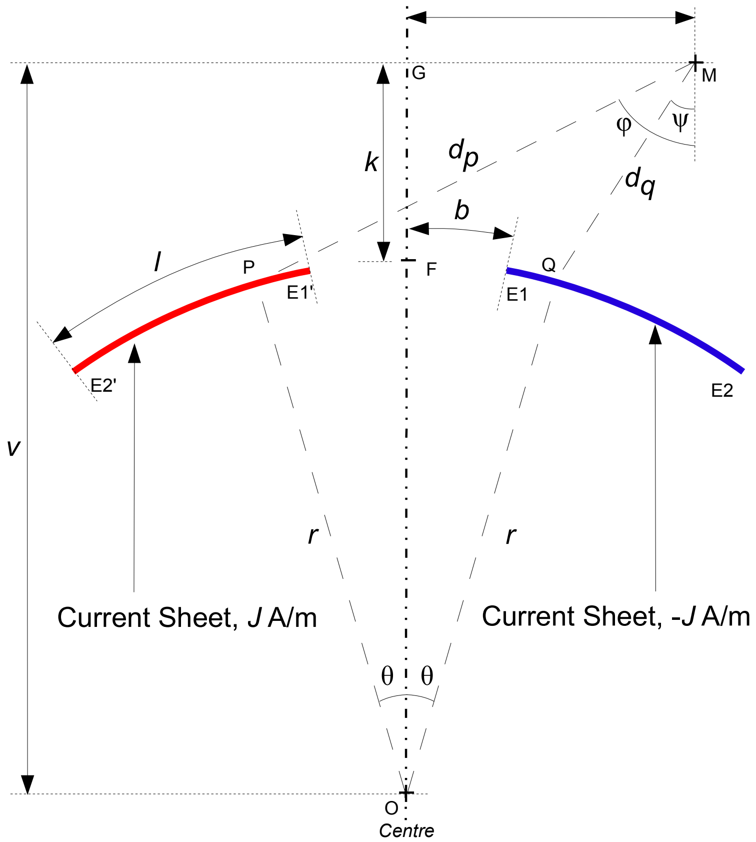


Fig A10.1 Field point along the GM plane of the distributed convex current sheets.

Figs A10.2 shows the expanded view of the magnetising field components at point M due to the symmetrical current elements at points P and Q.

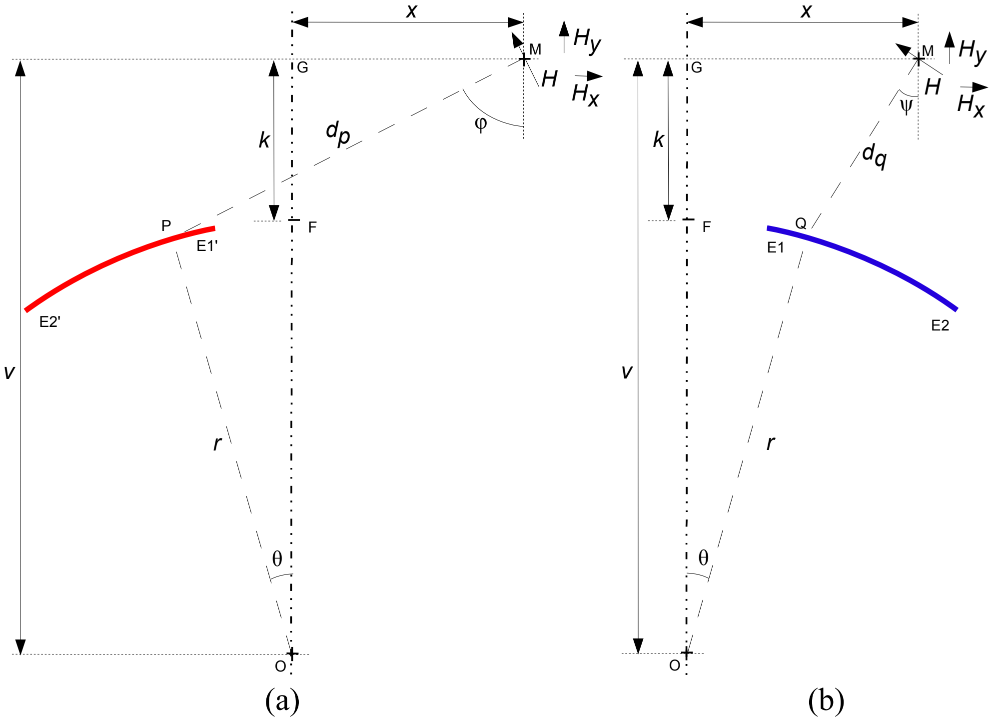


Fig A10.2 Magnetising field at point M due to the current elements at points (a) P and (b) Q of the distributed convex current sheets.

Take a point, M at a distance ***x*** from the OG axis along the GM plane, displaced by a distance ***v*** from the centre of curvature, O or ***k*** from the pole, F. Considering the geometry of points O, M and P in Fig A10.2(a),

$$d_p \cos\varphi = -r\cos\theta + v$$

$$d_p \sin\varphi = r\sin\theta + x \qquad \text{(A10.1)}$$

$$d_p^2 = (-r\cos\theta + v)^2 + (r\sin\theta + x)^2$$

$$= r^2 + (x^2 + v^2) + 2r(-v\cos\theta + x\sin\theta) \qquad \text{(A10.2)}$$

Similarly, considering the geometry of points O, M and Q in Fig A10.2(b),

$$d_q \cos\psi = -r\cos\theta + v$$

$$d_q \sin\psi = -r\sin\theta + x \qquad \text{(A10.3)}$$

$$d_q^2 = (-r\cos\theta + v)^2 + (-r\sin\theta + x)^2$$

$$= r^2 + (x^2 + v^2) - 2r(v\cos\theta + x\sin\theta) \qquad \text{(A10.4)}$$

The $\boldsymbol{y}$ component of the magnetising field strength, $\boldsymbol{\delta HP_y}$ at point M due to the symmetrical current elements $\boldsymbol{J\,\delta\theta}$ of infinite depth at points P and Q are given by Eqs A10.5 and A10.6.

$$\delta HP_y = \frac{J\, r\delta\theta \sin\varphi}{2\pi d_p} \qquad \text{(A10.5)}$$

$$\delta HQ_y = \frac{J\, r\delta\theta \sin\psi}{2\pi d_q} \qquad \text{(A10.6)}$$

The corresponding $\boldsymbol{x}$ components, $\boldsymbol{HP_x}$ and $\boldsymbol{HQ_x}$ are not considered because when the coils are aggregated symmetrically along the GM plane, they will be cancelled out by the corresponding $\boldsymbol{HP_x}$ and $\boldsymbol{HQ_x}$ from the other coil. Substituting Eqs A10.1 and A10.2 into Eq A10.5 yields

$$\delta HP_y = \frac{J}{2\pi}\frac{r(r\sin\theta + x)\delta\theta}{r^2 + (x^2 + v^2) + 2r(-v\cos\theta + x\sin\theta)} \qquad \text{(A10.7)}$$

Similarly, by substituting Eqs A10.3 and A10.4 into Eq A10.6 yields

$$\delta HQ_y = \frac{J}{2\pi}\frac{r(-r\sin\theta + x)\delta\theta}{r^2 + (x^2 + v^2) - 2r(v\cos\theta + x\sin\theta)} \qquad \text{(A10.8)}$$

Summing A10.7 and A10.8 yields the net $\boldsymbol{H_y}$ at point M as expressed by Eq A10.9.

$$\begin{aligned}
H_y &= \int dHP_y + \int dHQ_y \\
&= \frac{Jr}{2\pi}\int_{\theta_1}^{\theta_2}\frac{(r\sin\theta + x)\,d\theta}{r^2 + (x^2 + v^2) + 2r(-v\cos\theta + x\sin\theta)} \\
&\quad + \frac{Jr}{2\pi}\int_{\theta_1}^{\theta_2}\frac{(-r\sin\theta + x)\,d\theta}{r^2 + (x^2 + v^2) - 2r(v\cos\theta + x\sin\theta)} \\
&= \frac{Jr^2}{2\pi}\int_{\theta_1}^{\theta_2}\frac{\sin\theta\, d\theta}{r^2 + (x^2 + v^2) + 2r(-v\cos\theta + x\sin\theta)} \\
&\quad + \frac{Jrx}{2\pi}\int_{\theta_1}^{\theta_2}\frac{d\theta}{r^2 + (x^2 + v^2) + 2r(-v\cos\theta + x\sin\theta)} \\
&\quad - \frac{Jr^2}{2\pi}\int_{\theta_1}^{\theta_2}\frac{\sin\theta\, d\theta}{r^2 + (x^2 + v^2) - 2r(v\cos\theta + x\sin\theta)}
\end{aligned}$$

$$+\frac{Jrx}{2\pi}\int_{\theta_1}^{\theta_2}\frac{d\theta}{r^2+(x^2+v^2)-2r(v\cos\theta+x\sin\theta)} \qquad \text{(A10.9)}$$

By using Eqs A1.2 and A1.3 as shown in Section A.1 and substituting the identity $(r^2+x^2+v^2)^2-4r^2v^2-4r^2x^2=(r^2-x^2-v^2)^2$ into Eq A10.9 yields Eq A10.10.

$$H_y=\frac{J}{4\pi(x^2+v^2)}(rv\ln[(r^2+x^2+v^2)-2rv\cos\theta+2rx\sin\theta]+rx\theta)|_{\theta_1}^{\theta_2}$$

$$-\frac{2J((r^2+x^2+v^2)rx)}{4\pi(x^2+v^2)(r^2-x^2-v^2)}\tan^{-1}[\frac{(r^2+x^2+v^2+2rv)\tan\frac{\theta}{2}+2rx}{(r^2-x^2-v^2)}]|_{\theta_1}^{\theta_2}$$

$$+\frac{4J((x^2+v^2)rx)}{4\pi(x^2+v^2)(r^2-x^2-v^2)}\tan^{-1}[\frac{(r^2+x^2+v^2+2rv)\tan\frac{\theta}{2}+2rx}{(r^2-x^2-v^2)}]|_{\theta_1}^{\theta_2}$$

$$+\frac{J}{4\pi(x^2+v^2)}(rv\ln[(r^2+x^2+v^2)-2rv\cos\theta-2rx\sin\theta]-rx\theta)|_{\theta_1}^{\theta_2}$$

$$+\frac{2J((r^2+x^2+v^2)rx)}{4\pi(x^2+v^2)(r^2-x^2-v^2)}\tan^{-1}[\frac{(r^2+x^2+v^2+2rv)\tan\frac{\theta}{2}-2rx}{(r^2-x^2-v^2)}]|_{\theta_1}^{\theta_2}$$

$$-\frac{4J((x^2+v^2)rx)}{4\pi(x^2+v^2)(r^2-x^2-v^2)}\tan^{-1}[\frac{(r^2+x^2+v^2+2rv)\tan\frac{\theta}{2}-2rx}{(r^2-x^2-v^2)}]|_{\theta_1}^{\theta_2}$$

$$H_y=\frac{Jrv}{4\pi(x^2+v^2)}\ln[\frac{(r^2+x^2+v^2)-2rv\cos\theta_2+2rx\sin\theta_2}{(r^2+x^2+v^2)-2rv\cos\theta_1+2rx\sin\theta_1}]$$

$$-\frac{2Jrx}{4\pi(x^2+v^2)}\tan^{-1}[\frac{(r^2+x^2+v^2+2rv)\tan\frac{\theta_2}{2}+2rx}{(r^2-x^2-v^2)}]$$

$$+\frac{2Jrx}{4\pi(x^2+v^2)}\tan^{-1}[\frac{(r^2+x^2+v^2+2rv)\tan\frac{\theta_1}{2}+2rx}{(r^2-x^2-v^2)}]$$

$$+\frac{Jrv}{4\pi(x^2+v^2)}\ln[\frac{(r^2+x^2+v^2)-2rv\cos\theta_2-2rx\sin\theta_2}{(r^2+x^2+v^2)-2rv\cos\theta_1-2rx\sin\theta_1}]$$

$$+\frac{2Jrx}{4\pi(x^2+v^2)}\tan^{-1}[\frac{(r^2+x^2+v^2-2rv)\tan\frac{\theta_2}{2}-2rx}{(r^2-x^2-v^2)}]$$

$$-\frac{2Jrx}{4\pi(x^2+v^2)}\tan^{-1}[\frac{(r^2+x^2+v^2-2rv)\tan\frac{\theta_1}{2}-2rx}{(r^2-x^2-v^2)}] \quad \text{(A10.10)}$$

But from Fig A10.1, $\boldsymbol{\theta_1} = \boldsymbol{b} / \mathbf{r}$ and $\boldsymbol{\theta_2} = (\boldsymbol{b} + \boldsymbol{l}) / \boldsymbol{r}$ where $\boldsymbol{\theta_1}$ and $\boldsymbol{\theta_2}$ span endpoints $E_1$ and $E_2$ respectively. Simplifying Eq A10.10 yields

$$H_y = Kv\ln(\frac{r^2+d^2-2rv\cos(\frac{(b+l)}{r})-2rx\sin(\frac{(b+l)}{r})}{r^2+d^2-2rv\cos\frac{b}{r}-2rx\sin\frac{b}{r}})$$

$$+Kv\ln(\frac{r^2+d^2-2rv\cos(\frac{(b+l)}{r})+2rx\sin(\frac{(b+l)}{r})}{r^2+d^2-2rv\cos\frac{b}{r}+2rx\sin\frac{b}{r}})$$

$$+2Kx\tan^{-1}(\frac{r^2+d^2+2rv\tan(\frac{(b+l)}{2r})-2rx}{r^2-d^2})$$

$$-2Kx\tan^{-1}(\frac{r^2+d^2+2rv\tan(\frac{b}{2r})-2rx}{r^2-d^2})$$

$$-2Kx\tan^{-1}(\frac{r^2+d^2+2rv\tan(\frac{(b+l)}{2r})+2rx}{r^2-d^2})$$

$$+2Kx\tan^{-1}(\frac{r^2+d^2+2rv\tan(\frac{b}{2r})+2rx}{r^2-d^2}) \quad \text{(A10.11)}$$

where

$$K=\frac{Jr}{4\pi d^2}$$

$$v=r+k$$

$$d=\sqrt{v^2+x^2}=\sqrt{y^2+x^2}$$

### A.11 2D Helmholtz coil field strength

To represent a 2D Helmholtz coil, consider the cross section of 4 current paths C1, C2, C3 and C4 of infinite length and infinitesimal diameter arranged as a Helmholtz coil of radius ***d*** with a centre O as shown in Fig A11.1 such that the current in all paths are identical in magnitude with the positive current leaving the page in paths C2 and C4 and otherwise for the negative current in paths C1 and C3.

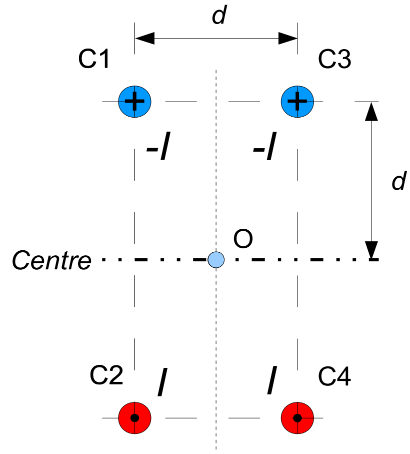


Fig A11.1 Layout of the 2D Helmholtz coil.

Fig A11.2 shows the details of the current path C1, carrying current ***-I***.

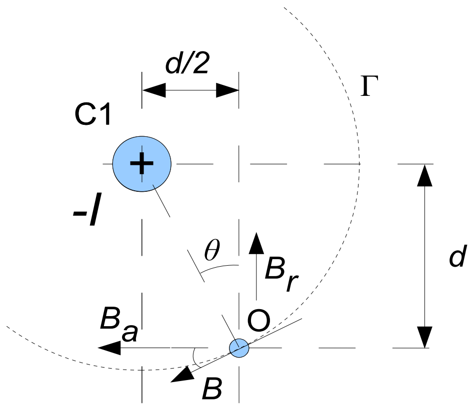


Fig A11.2 Field point of the current path C1.

By symmetry, the field is uniform along a circular path, **Γ** which intersects point O and the direction of the field is tangential to the circular path. From Ampere's Law,

$$\oint_{\Gamma} B.dl = \mu I$$

=> $$2\pi B \sqrt{\left(\frac{d}{2}\right)^2 + d^2} = \mu I$$

=> $$B = \frac{\mu I}{\pi d \sqrt{5}} \tag{A11.1}$$

Similar analyses for current paths C2, C3 and C4 yield the same expression as Eq A11.1. The ***B*** vector of each current path is further resolved into its radial component, $\boldsymbol{B_r}$ and axial component, $\boldsymbol{B_a}$. By symmetry, the radial flux density $\boldsymbol{B_r}$ due to current paths C1 and C2 will cancel out and similarly for current paths C3 and C4. On the other hand, the axial flux density $\boldsymbol{B_a}$ due to all 4 current paths will add up. $\boldsymbol{B_a}$ is expressed by Eq A11.2.

$$B_a = B\cos\theta$$

$$= \frac{\mu I \cos\theta}{\pi d \sqrt{5}} \tag{A11.2}$$

but from Fig A11.2,

$$\cos\theta = \frac{2}{\sqrt{5}}$$

Therefore the total flux density at point O, $\boldsymbol{B_t}$ is given by

$$B_t = \frac{\mu I}{\pi d \sqrt{5}} \times \frac{2}{\sqrt{5}} \times 4$$

$$= \frac{8\mu I}{5\pi d} \tag{A11.3}$$

## APPENDIX B

### B.1 Parametric model coordinate system

For the purpose of building 3D coil models symmetrical around the ***z*** axis as shown in Fig B1.1, the wireframe of the coil is constructed. To do this, the 2D profile of the model is first defined on the OQS plane. As the locus of this 2D profile is traced out either by varying the angle $\boldsymbol{\theta}$ or by some other parameter, the OQS plane also sweeps around the ***z*** axis as the angle $\boldsymbol{\varphi}$ increases from 0 to $2\pi N$, where $N$ is the number of sweep turns.

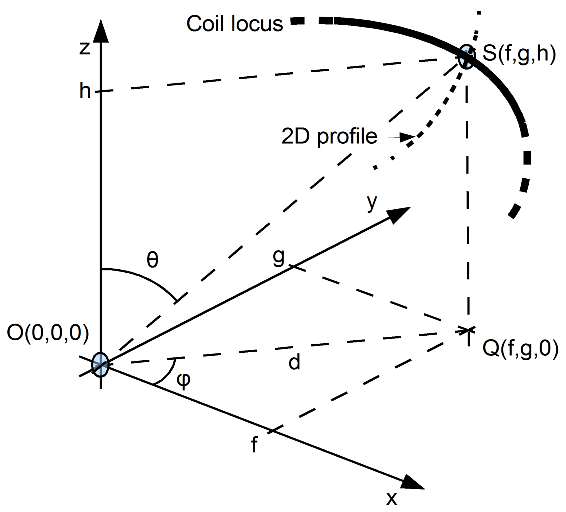


Fig B1.1 Coordinate scheme for constructing coil wireframes from parametric equations.

### B.2 3D Ellipsoid and spherical parametric construction model

Fig B2.1 shows a 2D ellipse profile AMB. This profile is symmetrical around the ***y*** axis with a major axis radius of OA, ***A*** and a minor axis radius of OB, ***B***.

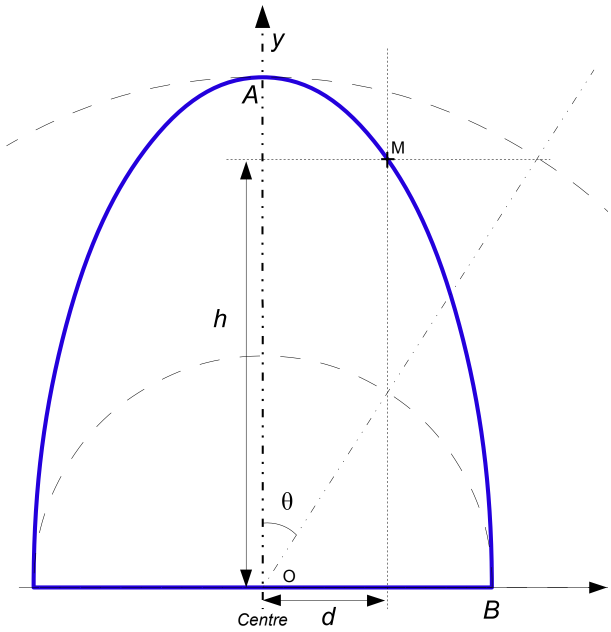


Fig B2.1 General ellipsoid parametric profile.

Parametrically, the profile of point M as shown in Fig B2.1 can be expressed by Eqs B2.1 and B2.2.

$$d = B\sin\theta \tag{B2.1}$$

$$h = A\cos\theta \tag{B2.2}$$

Taking the differential of Eqs B2.1 and B2.2 yields

$$\Delta d = B\cos\theta\,\Delta\theta$$

$$\Delta h = -A\sin\theta\,\Delta\theta$$

The differential length $\boldsymbol{\Delta s}$ can therefore be expressed as

$$\Delta s^2 = \Delta d^2 + \Delta h^2$$

$$\Rightarrow \qquad \Delta s = \sqrt{(A^2\sin^2\theta + B^2\cos^2\theta)}\,\Delta\theta \tag{B2.3}$$

Assuming a constant turn pitch over the breath ***l***,

$$\Delta s = \frac{l\,\Delta\varphi}{2\pi N} \tag{B2.4}$$

Equating Eqs B2.4 and B2.3 yields

$$\Delta\theta(\theta) = \frac{l}{2\pi N}\frac{\Delta\varphi}{\sqrt{(A^2\sin^2\theta + B^2\cos^2\theta)}} \tag{B2.5}$$

Starting from an initial value, the angle $\boldsymbol{\theta}$ can be continuously adjusted by $\boldsymbol{\Delta\theta}$ as the angle $\boldsymbol{\varphi}$ increases progressively from 0 to $2\pi N$ in steps of $\boldsymbol{\Delta\varphi}$ with the resultant $\boldsymbol{\theta}$ being used in Eqs B2.1 and B2.2 to construct the 2D profile on the OQS plane at the corresponding sweep angle $\boldsymbol{\varphi}$.

Eq B2.5 holds true for both prolate and oblate profiles where $\boldsymbol{A} > \boldsymbol{B}$ for the prolate profile and $\boldsymbol{B} > \boldsymbol{A}$ for the oblate profile. For the spherical profile where $\boldsymbol{A} = \boldsymbol{B} = \boldsymbol{r}$, the radius of curvature, Eq B2.5 can be reduced to

$$\Delta\theta = \frac{l\Delta\varphi}{2\pi Nr}$$

Integrating all the $\boldsymbol{\Delta\theta}$ and $\boldsymbol{\Delta\varphi}$ elements with the initial $\boldsymbol{\varphi} = 0$ and $\boldsymbol{\theta_i}$ = the initial $\boldsymbol{\theta}$,

$$\theta = \frac{l\varphi}{2\pi Nr} + \theta_i \qquad \text{(B2.6)}$$

**B.3 3D Hyperboloid parametric construction model**

Fig B3.1 shows a 2D hyperboloid profile EMB. This profile is symmetrical around the $\boldsymbol{y}$ axis with a minor axis radius of OB, $\boldsymbol{B}$.

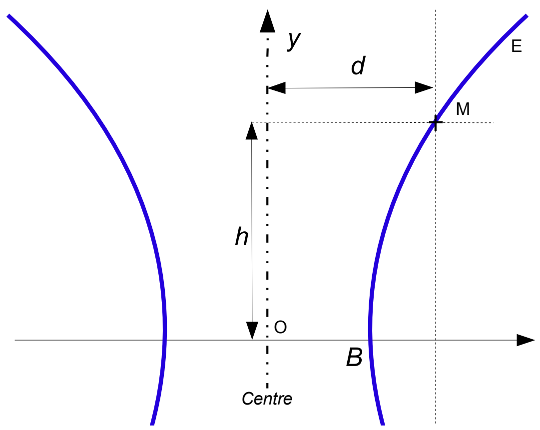


Fig B3.1 General hyperboloid parametric profile.

Parametrically, the profile of point M can be expressed by Eqs B3.1 and B3.2.

$$d = B\sqrt{1+u^2} \tag{B3.1}$$

$$h = C\,u \tag{B3.2}$$

Taking the differential of Eqs B3.1 and B3.2 yields

$$\Delta d = \frac{B\,u}{\sqrt{1+u^2}}\Delta u$$

$$\Delta h = C\,\Delta u$$

The differential length ***Δs*** can therefore be expressed as

$$\Delta s^2 = \Delta d^2 + \Delta h^2$$

$$\Rightarrow \qquad \Delta s = \sqrt{\frac{C^2 + u^2\left(C^2 + B^2\right)}{1+u^2}}\,\Delta u \tag{B3.3}$$

Assuming a constant turn pitch over the breath $\boldsymbol{l}$,

$$\Delta s = \frac{l\,\Delta\varphi}{2\pi N} \tag{B3.4}$$

Equating Eqs B3.4 and B3.3 yields

$$\Delta u(u) = \frac{l\Delta\varphi}{2\pi N}\sqrt{\frac{1+u^2}{C^2 + u^2\left(C^2 + B^2\right)}} \tag{B3.5}$$

Starting from an initial value, the value $\boldsymbol{u}$ can be continuously adjusted by $\boldsymbol{\Delta u}$ as the angle $\boldsymbol{\varphi}$ increases progressively from 0 to $2\pi N$ rad in steps of $\boldsymbol{\Delta\varphi}$ with the resultant $\boldsymbol{u}$ being used in Eqs B3.1 and B3.2 to construct the 2D profile on the OQS plane at the corresponding sweep angle $\boldsymbol{\varphi}$.

**B.4 3D Conical parametric construction model**

Fig B4.1 shows a 2D conical profile E1'ME2'. This profile is symmetrical around the $\boldsymbol{y}$ axis, formed by a straight line subtending the arc E1-E2 (and E1'-E2') of curvature radius $\boldsymbol{r}$ with an origin at O.

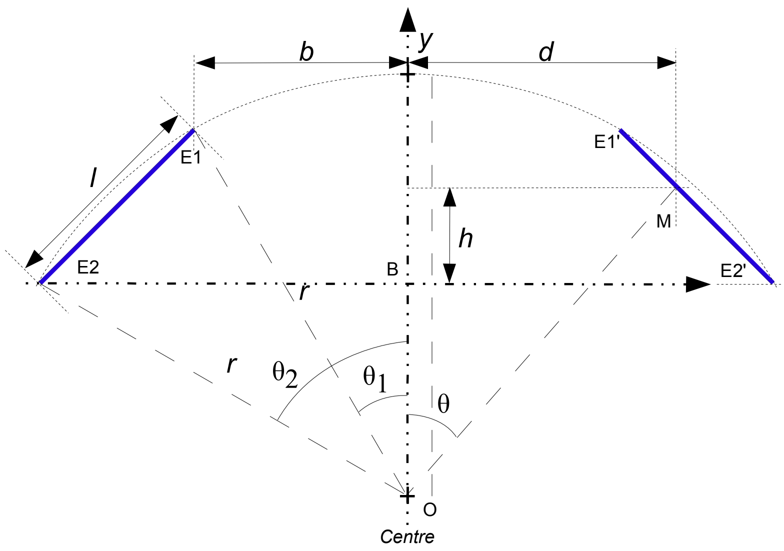


Fig B4.1 General conical parametric profile.

The height and width of line E1-E2 projected on the datums O-B and E2-B-E2' can be expressed as ***r*** (cos $\theta_1$ - cos $\theta_2$) and r (sin $\theta_2$ - sin $\theta_1$) respectively. Assuming a constant turn pitch over the breath ***l***, the parametric profile of point M as shown in Fig B4.1 is given by Eqs B4.1 and B4.2.

$$d = b + \frac{r\varphi}{2\pi N}(\sin\theta_2 - \sin\theta_1) \tag{B4.1}$$

$$h = \frac{r\varphi}{2\pi N}(\cos\theta_1 - \cos\theta_2) \tag{B4.2}$$

Therefore, with the initial and terminal $\theta$ pre-determined, the 2D profile on the OQS plane can be constructed as $\varphi$ is swept from 0 to $2\pi N$.

### B.5 3D Planar parametric construction model

Fig B5.1 shows a 2D planar profile E1ME2. This profile rests on the ***x*** axis, extending from $E_1$ to $E_2$ symmetrical around the ***y*** axis.

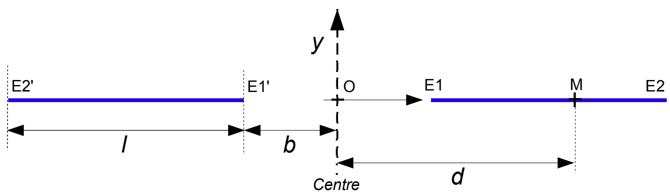


Fig B5.1 General planar parametric profile.

Assuming a constant turn pitch over the breath ***l***, the parametric profile of point M is given by Eq B5.1.

$$d = b + \frac{l\varphi}{2\pi N} \tag{B5.1}$$

Therefore, with ***h*** = 0, the 2D profile on the OQS plane can be constructed as ***φ*** is swept from 0 to 2π*N*.

### B.6 3D variable turn pitch spherical parametric construction model

Considering a 2D spherical profile with a curvature radius of ***r*** and coil breadth ***l***, the incremental span, ***δs*** due to an incremental angle, ***δθ*** is shown in Fig B6.1.

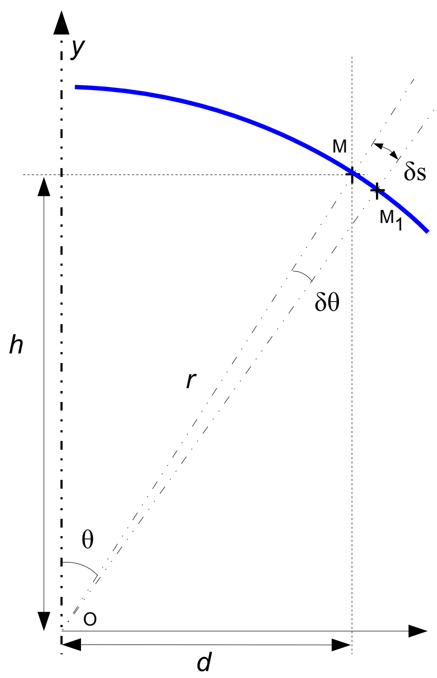


Fig B6.1 General spherical span element.

Parametrically, the profile of point M can be expressed by Eqs B6.1 and B6.2.

$$d = r\sin\theta \tag{B6.1}$$

$$h = r\cos\theta \tag{B6.2}$$

The span between points M and $M_1$ as shown in Fig B6.1, ***δs*** = ***r δθ*** is fixed for a constant incremental sweep, $\boldsymbol{\delta\varphi}$ in a uniform turn pitch spherical coil. However, for a linearly changing turn pitch, the relationship between $\boldsymbol{\theta}$ and $\boldsymbol{\varphi}$ is no longer proportional but instead, it can be modelled as a quadratic equation as shown in Eq B6.3.

$$\frac{d\theta}{d\varphi} = 2u\varphi + v$$

$$\Rightarrow \qquad \theta = u\varphi^2 + v\varphi + w \qquad \text{(B6.3)}$$

where $\boldsymbol{u}$, $\boldsymbol{v}$ and $\boldsymbol{w}$ are arbitrary coefficients. Using Eq B6.3, $\boldsymbol{\theta_i}$, the initial $\boldsymbol{\theta}$ and $\boldsymbol{\theta_f}$, the final $\boldsymbol{\theta}$ can be expressed at $\boldsymbol{\varphi} = 0$ and $\boldsymbol{\varphi} = 2\pi N$ as

$$\theta_i = w \qquad \text{(B6.4)}$$

$$\theta_f = u(2\pi \mathrm{N})^2 + v(2\pi \mathrm{N}) + w \qquad \text{(B6.5)}$$

Substituting Eqs B6.4 and B6.5 into the expressions of the spherical coil's inner radius, $\boldsymbol{b}$ and breadth, $\boldsymbol{l}$ yields Eqs B6.6 and B6.7.

$$b = r\theta_i = rw \qquad \text{(B6.6)}$$

$$l = r(\theta_f - \theta_i)$$

$$\Rightarrow \qquad l = r[u(2\pi \mathrm{N})^2 + v(2\pi \mathrm{N})] \qquad \text{(B6.7)}$$

Given the initial turn pitch, $g_i = r(\theta_1 - \theta_i)$ where $\boldsymbol{\theta_1}$ is the angle $\boldsymbol{\theta}$ after the initial turn,

$$g_i = r[u(2\pi)^2 + v(2\pi)] \qquad \text{(B6.8)}$$

Subtracting Eq B6.7 from N x Eq B6.8 yields

$$u = \frac{l - Ng_i}{4\pi^2 rN(N-1)} \qquad \text{(B6.9)}$$

Substituting Eq B6.9 into Eq B6.8 yields

$$v = \frac{N^2 g_i - l}{2\pi rN(N-1)} \qquad \text{(B6.10)}$$

Therefore, from Eqs B6.4, B6.9 and B6.10, Eq B6.3 can be expressed by Eq B6.11.

$$\theta = \frac{(l - Ng_i)}{4\pi^2 rN(N-1)}\varphi^2 + \frac{(N^2 g_i - l)}{2\pi rN(N-1)}\varphi + \theta_i \qquad \text{(B6.11)}$$

By examining Eq B6.9, setting $\boldsymbol{g_i} < \boldsymbol{l} / \boldsymbol{N}$ yields $\boldsymbol{u} > 0$, i.e. an increasing turn pitch as $\boldsymbol{\varphi}$ increases from 0 to $2\pi N$. Conversely, $\boldsymbol{g_i} > \boldsymbol{l} / \boldsymbol{N}$ yields $\boldsymbol{u} < 0$, i.e. a decreasing turn pitch as $\boldsymbol{\varphi}$ increases from 0 to $2\pi N$. At the critical initial turn pitch $\boldsymbol{g_i} = \boldsymbol{l} / \boldsymbol{N}$, the turn pitch remains constant throughout the $\boldsymbol{\varphi}$ sweep.

Therefore, with the initial $\boldsymbol{g_i}$ pre-determined, the 2D profile on the OQS plane can be constructed as $\boldsymbol{\varphi}$ is swept from 0 to $2\pi N$.

## B.7 Coil wireframe VBA scripts

### (a) Prolate coil

```
Dim Init_Ang As Double, End_Ang As Double, Maj_Rad As Double
Dim Min_Rad As Double, Space_Turn_Ang As Double
Dim Ang As Double, Rot_Rad as Double, Rot_Height As Double
Dim Turn_Ang As Double, Ecc_Ang As Double, Ecc_Chg As Double
Maj_Rad = 30
Min_Rad = 15
Init_Ang = 30*Pi/180
End_Ang = 60*Pi/180
Turn_Ang = 8*2*Pi
Space_Turn_Ang = (End_Ang - Init_Ang)*Min_Rad/Turn_Ang
Ecc_Ang = Init_Ang
For Ang = 0  To  Turn_Ang  STEP  0.2
    Rot_Rad = Min_Rad*Sin(Ecc_Ang)
    Rot_Height = Maj_Rad*(1-Cos(Ecc_Ang))
      .Point Rot_Rad*Sin(Ang) , Rot_Rad*Cos(Ang) , Rot_Height
    Ecc_Chg = 0.2*Space_Turn_Ang/Sqr((Maj_Rad*Sin(Ecc_Ang))^2+
    (Min_Rad*Cos(Ecc_Ang))^2)
    Ecc_Ang = Ecc_Ang +  Ecc_Chg
Next Ang
```

**(b) Oblate coil**

```
Dim Init_Ang As Double, End_Ang As Double, Maj_Rad As Double
Dim Min_Rad As Double, Space_Turn_Ang As Double
Dim Ang As Double, Rot_Rad as Double, Rot_Height As Double
Dim Turn_Ang As Double, Ecc_Ang As Double, Ecc_Chg As Double
Maj_Rad = 7.5
Min_Rad = 15
Init_Ang = 30*Pi/180
End_Ang = 60*Pi/180
Turn_Ang = 8*2*Pi
Space_Turn_Ang = (End_Ang - Init_Ang)*Min_Rad/Turn_Ang
Ecc_Ang = Init_Ang
For Ang = 0  To  Turn_Ang  STEP  0.2
     Rot_Rad = Min_Rad*Sin(Ecc_Ang)
     Rot_Height = Maj_Rad*(1-Cos(Ecc_Ang))
        .Point Rot_Rad*Sin(Ang) , Rot_Rad*Cos(Ang) , Rot_Height
     Ecc_Chg = 0.2*Space_Turn_Ang/Sqr((Maj_Rad*Sin(Ecc_Ang))^2+
     (Min_Rad*Cos(Ecc_Ang))^2)
     Ecc_Ang = Ecc_Ang +  Ecc_Chg
Next Ang
```

**(c) Spherical coil**

```
Dim Init_Ang As Double, End_Ang As Double, Rad As Double
Dim Ang As Double, Rot_Rad as Double, Step_Ang As Double
Dim Turn_Ang As Double, Step_Height As Double, Rot_Height As Double
Init_Ang = 30*Pi/180
End_Ang = 60*Pi/180
Rad = 15
Turn_Ang = 8*2*Pi
Step_Ang = Rad*(Cos(End_Ang) - Cos(Init_Ang))/Turn_Ang
Step_Height = Rad*(Sin(End_Ang) - Sin(Init_Ang))/Turn_Ang
For Ang = 0  To  Turn_Ang  STEP  0.2
            Rot_Rad = Rad*Cos(Ang/Turn_Ang*(End_Ang - Init_Ang) +
            Init_Ang)
            Rot_Height = Rad*Sin(Ang/Turn_Ang*(End_Ang - Init_Ang) +
            Init_Ang)
        .Point Rot_Rad*Sin(Ang) , Rot_Rad*Cos(Ang) , Rot_Height
Next Ang
```

**(d) Hyperboloid coil**

```
Dim Init_Ang As Double, End_Ang As Double, Maj_Rad As Double
Dim Min_Rad As Double, Space_Turn_Ang As Double
Dim Ang As Double, Rot_Rad as Double, Rot_Height As Double
Dim Turn_Ang As Double, Ecc_Ang As Double, Ecc_Chg As Double
Maj_Rad = 7.5
```

```
Min_Rad = 3.75
Init_Ang = 30*Pi/180
End_Ang = 60*Pi/180
Turn_Ang = 8*2*Pi
Space_Turn_Ang = (End_Ang - Init_Ang)*2*Maj_Rad/Turn_Ang
Ecc_Ang = 0
For Ang = 0  To  Turn_Ang  STEP  0.2
     Rot_Rad = Maj_Rad*Sqr(1 + Ecc_Ang^2)
     Rot_Height = Min_Rad*Ecc_Ang
        .Point Rot_Rad*Sin(Ang) , Rot_Rad*Cos(Ang) , Rot_Height
     Ecc_Chg = 0.2*Space_Turn_Ang/Sqr((Min_Rad^2 +
     Ecc_Ang^2*(Min_Rad^2 + Maj_Rad^2))/(1 + Ecc_Ang^2))
     Ecc_Ang = Ecc_Ang +  Ecc_Chg
Next Ang
```

**(e) Conical coil**

```
Dim Init_Ang As Double, End_Ang As Double, Rad As Double
Dim Ang As Double, Rot_Rad as Double, Step_Ang As Double
Dim Turn_Ang As Double, Step_Height As Double, Rot_Height As Double
Init_Ang = 30*Pi/180
End_Ang = 60*Pi/180
Rad = 15
Turn_Ang = 8*2*Pi
Step_Ang = Rad*(Cos(End_Ang) - Cos(Init_Ang))/Turn_Ang
Step_Height = Rad*(Sin(End_Ang) - Sin(Init_Ang))/Turn_Ang
For Ang = 0  To  Turn_Ang  STEP  0.2
            Rot_Rad = Ang*Step_Ang + Rad*Cos(Init_Ang)
        .Point Rot_Rad*Sin(Ang) , Rot_Rad*Cos(Ang) , Rad*Sin(Init_Ang) +
        Step_Height*Ang
Next Ang
```

**(f) Planar coil**

```
Dim Init_Ang As Double, End_Ang As Double, Inner_Rad As Double
Dim Ang As Double, Rot_Rad as Double, Step_Ang As Double, Gap As
Double
Dim Turn_Ang As Double, Step_Height As Double, Rot_Height As Double
Init_Ang = 30*Pi/180
End_Ang = 60*Pi/180
Inner_Rad = 7.5
Gap = 0.981747704
Turn_Ang = 8*2*Pi
Step_Ang = Gap/(2*Pi)
For Ang = 0  To  Turn_Ang  STEP  0.2
            Rot_Rad = Inner_Rad + Ang*Step_Ang
        .Point Rot_Rad*Sin(Ang) , Rot_Rad*Cos(Ang) , 0
Next Ang
```

**(g) Outwards increasing current density spherical coil**

```
Dim Init_Ang As Double, End_Ang As Double, Rad As Double
Dim Ang As Double, Rot_Rad as Double, Turn_Ang As Double
Dim Rot_Ang As Double, Rot_Height As Double
Dim Coeff1 As Double, Coeff2 As Double
Init_Ang = 30*Pi/180
End_Ang = 60*Pi/180
Turn_Ang = 8*2*Pi
Rad = 15
Coeff1 = 0.000106103295394597
Coeff2 = 0.005083
For Ang = 0  To  Turn_Ang  STEP  0.2
        Rot_Ang = Ang^2*Coeff1 + Ang*Coeff2 + Init_Ang
        Rot_Rad = Rad*Cos(Rot_Ang)
        Rot_Height = Rad*Sin(Rot_Ang)
    .Point Rot_Rad*Sin(Ang) , Rot_Rad*Cos(Ang) , Rot_Height
Next Ang
```

**(h) Outwards decreasing current density spherical coil**

```
Dim Init_Ang As Double, End_Ang As Double, Rad As Double
Dim Ang As Double, Rot_Rad as Double, Turn_Ang As Double
Dim Rot_Ang As Double, Rot_Height As Double
Dim Coeff1 As Double, Coeff2 As Double
Init_Ang = 30*Pi/180
End_Ang = 60*Pi/180
Turn_Ang = 8*2*Pi
Rad = 15
Coeff1 = -0.000106103295394597
Coeff2 = 0.01575
For Ang = 0  To  Turn_Ang  STEP  0.2
        Rot_Ang = Ang^2*Coeff1 + Ang*Coeff2 + Init_Ang
        Rot_Rad = Rad*Cos(Rot_Ang)
        Rot_Height = Rad*Sin(Rot_Ang)
    .Point Rot_Rad*Sin(Ang) , Rot_Rad*Cos(Ang) , Rot_Height
Next Ang
```

# APPENDIX C

## C.1 2D FEMM listing of parallel current sheets

```
[NumPoints] = 11
0     0     0     0
0.97499999999999998    -0.025000000000000001   0     0
-0.97499999999999998   -0.025000000000000001   0     0
6     0     0     0
-6    0     0     0
1.0250000000000001     -0.025000000000000001   0     0
-1.0250000000000001    -0.025000000000000001   0     0
-0.97499999999999998   1.0249999999999999      0     0
-1.0250000000000001    1.0249999999999999      0     0
0.97499999999999998    1.0249999999999999      0     0
1.0250000000000001     1.0249999999999999      0     0
[NumSegments] = 8
8     7     -1    0     0     0
7     2     -1    0     0     0
2     6     -1    0     0     0
6     8     -1    0     0     0
1     9     -1    0     0     0
9     10    -1    0     0     0
10    5     -1    0     0     0
5     1     -1    0     0     0
[NumArcSegments] = 2
3     4     180   5     1     0     0
4     3     180   5     1     0     0
[NumHoles] = 0
[NumBlockLabels] = 3
-4.3700000000000001    1.1100000000000001      2
      0.050000000000000003   0     0     0     1     0
-1.0050000000000001    0.51000000000000001     1
      0.050000000000000003   1     0     0     -1    0
0.995 0.5   1     0.050000000000000003   1     0     0     1
      0
```

## C.2 2D FEMM listing of distributed planar current sheets

```
[NumPoints] = 11
0     -0.025000000000000001   0     0
0.97499999999999998    -0.025000000000000001   0     0
2.0249999999999999     -0.025000000000000001   0     0
-0.97499999999999998   -0.025000000000000001   0     0
-2.0249999999999999    -0.025000000000000001   0     0
0.97499999999999998    0.025000000000000001    0     0
2.0249999999999999     0.025000000000000001    0     0
-0.97499999999999998   0.025000000000000001    0     0
-2.0249999999999999    0.025000000000000001    0     0
6     0     0     0
-6    0     0     0
[NumSegments] = 8
8     4     -1    0     0     0
7     3     -1    0     0     0
3     4     -1    0     0     0
8     7     -1    0     0     0
1     5     -1    0     0     0
```

```
5     6     -1    0     0     0
6     2     -1    0     0     0
2     1     -1    0     0     0
[NumArcSegments] = 2
9     10    180   5     1     0     0
10    9     180   5     1     0     0
[NumHoles] = 0
[NumBlockLabels] = 3
-1.55 0.0049999999999999975  1     0.050000000000000003   1
      0     0     -1    0
1.48  -0.0050000000000000001  1     0.050000000000000003   1
      0     0     1     0
-4.3700000000000001    1.1100000000000001      2
      0.050000000000000003   0     0     0     1     0
```

## C.3 2D FEMM listing of parallel current paths

```
[NumPoints] = 11
0     0     0     0
0.97499999999999998    -0.025000000000000001   0     0
-0.97499999999999998   -0.025000000000000001   0     0
6     0     0     0
-6    0     0     0
1.0250000000000001     -0.025000000000000001   0     0
-1.0250000000000001    -0.025000000000000001   0     0
-0.97499999999999998   0.025000000000000001    0     0
-1.0250000000000001    0.025000000000000001    0     0
0.97499999999999998    0.025000000000000001    0     0
1.0250000000000001     0.025000000000000001    0     0
[NumSegments] = 8
2     6     -1    0     0     0
5     1     -1    0     0     0
6     8     -1    0     0     0
7     8     -1    0     0     0
7     2     -1    0     0     0
9     1     -1    0     0     0
9     10    -1    0     0     0
10    5     -1    0     0     0
[NumArcSegments] = 2
3     4     180   5     1     0     0
4     3     180   5     1     0     0
[NumHoles] = 0
[NumBlockLabels] = 3
-4.3700000000000001    1.1100000000000001      2
      0.050000000000000003   0     0     0     1     0
-1.0050000000000001    -0.0050000000000000001  1
      0.050000000000000003   1     0     0     -1    0
0.995 0.0049999999999999975  1     0.050000000000000003   1
      0     0     1     0
```

## C.4 2D FEMM listing of distributed concave and convex current sheets

```
[NumPoints] = 15
6     0     0     0
-6    0     0     0
0     -1    0     0
1.6880605242113349     0.97477969850409552     0     0
1.7307962336850395     0.94882475416242706     0     0
```

```
-1.6880605242113349     0.97477969850409552     0     0
-1.7307962336850395     0.94882475416242706     0     0
0.96604340717764403     0.2773900222486203      0     0
0.99050020229606539     0.2337796430650414      0     0
-0.96604340717764403    0.2773900222486203      0     0
-0.99050020229606539    0.2337796430650414      0     0
1.6993350117076478      0.99357786292998851     0     0
1.7423561512445502      0.96809882148517801     0     0
-1.6993350117076478     0.99357786292998851     0     0
-1.7423561512445502     0.96809882148517801     0     0
[NumSegments] = 4
7     8     -1    0     0     0
9     10    -1    0     0     0
11    12    -1    0     0     0
13    14    -1    0     0     0
[NumArcSegments] = 10
0     1     180   5     1     0     0
1     0     180   5     1     0     0
14    6     0.63591299954530223     5     0     0     0
6     10    29.444371244822886      5     0     0     0
13    5     0.63591299954529912     5     0     0     0
5     9     29.4443712448229  5     0     0     0
8     4     29.444371244822882      5     0     0     0
4     12    0.63591299954529878     5     0     0     0
7     3     29.4443712448229  5     0     0     0
3     11    0.63591299954530534     5     0     0     0
[NumHoles] = 0
[NumBlockLabels] = 3
-4.3700000000000001     1.1100000000000001      2
      0.050000000000000003    0     0     0     1     0
-1.3899999999999999     0.56299999999999994     1     -1    1
      0     0     -1    0
1.4139999999999999      0.57999999999999996     1     -1    1
      0     0     1     0
```

# APPENDIX D

## D.1 50 Hz experiment procedure

### D.1.1 Setup

Fig D1.1 shows the schematic of the coil layout and the measurement axes used in the experiment.

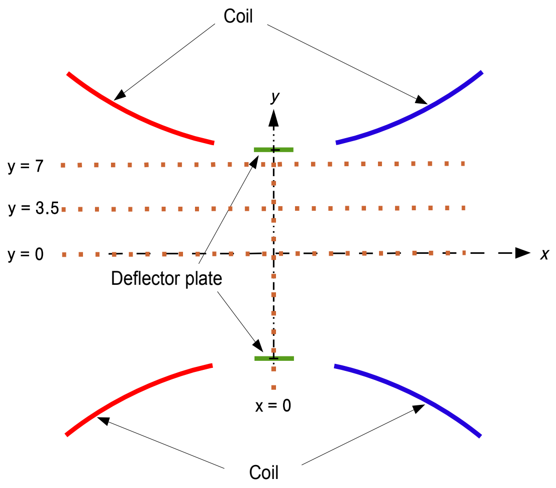


Fig D1.1 Schematic diagram of the coil layout and the measurement axes.

The coil current was measured and monitored using both:

a) bench ammeter: Goodwill GDM-8034 (S/N:CE140125)
b) current tester: Kyoritsu 2413F (S/N:W0068008)

The power source voltage was monitored using:

a) handheld voltmeter: Fluke 17B (S/N:91660726)

The magnetic flux was measured using:

a) fluxmeter: PHYWE 13610.93 (S/N:360500184913)
b) fluxmeter: PHYWE 13610.93 (S/N:230700221733)
c) Hall sensor: PHYWE 13610.02 (S/N: 90700217128)

Fig D1.2 shows the schematic connection diagram of the setup.

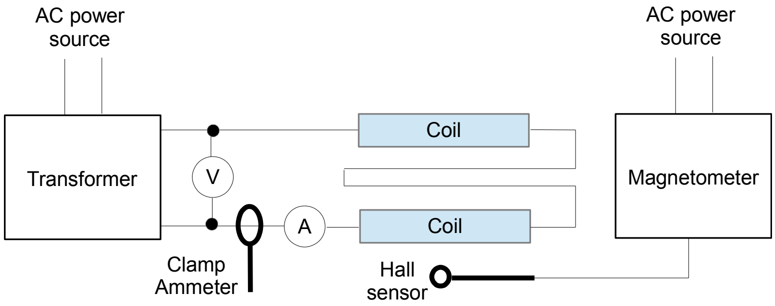


Fig D1.2 Schematic connection diagram of the 50 Hz experiment setup.

**D1.2 Procedure**

a) Set the scale full scale dial at the fluxmeter to 20 mT.

b) Allow at least 3 seconds for the fluxmeter to auto-zero to around 0, with the shield on. Note the offset reading.

c) Make sure the current reading of both meters are within 14.8 to 15.2 $A_{rms}$ (± 1.3 % drift error) by adjusting the variac dial.

d) Remove the sensor shield and position the Hall sensor vertically on the measurement table at the appropriate x and y position.

e) Direct the sensor's face at 4 directions towards the +$\boldsymbol{y}$, -$\boldsymbol{y}$, +$\boldsymbol{x}$ and -$\boldsymbol{x}$ axes for each location.

f) Wait for 3 secs for the sensor to stabilise before taking the reading for each direction in units of 0.1 Gs.

g) Do the above along the 4 axes shown in Fig D1.1.

i) coil's axis - along $\boldsymbol{x}$ = 0 cm for -7 cm ≤ $\boldsymbol{y}$ ≤ 7 cm
ii) centre line - along $\boldsymbol{y}$ = 0 cm for -11 cm ≤ $\boldsymbol{x}$ ≤ 11 cm
iii) between the centre line and the pole - along $\boldsymbol{y}$ = 3.5 cm for -11 cm ≤ $\boldsymbol{x}$ ≤ 11cm
iv) top line near the pole - along $\boldsymbol{y}$ = 7 cm for -7 cm ≤ $\boldsymbol{x}$ ≤ 7 cm

h) Repeat the above with another fluxmeter.

**D.2 50 kHz experiment procedure**

**D2.1 Setup**

The schematic of the coil layout and the measurement axes used in the experiment is shown in Fig D1.1.

The coil current was measured and monitored using:

a) oscilloscope: Rigol Digital Oscilloscope DS1102E
   (S/N:DS1EB120500409)
b) current tester: Tektronix AC/DC Current Probe A622
   (S/N:01JJ27068DV)

The signal conditioner null offset should be adjusted to cancel out the Hall sensor offset and the gain should be adjusted to provide a sensitivity of 40mV/Gauss. The magnetic flux density readings can be derived from the signal conditioner output voltage measurements at the oscilloscope.

The prototype, power source and measurement system are integrated as shown schematically in Fig D2.1.

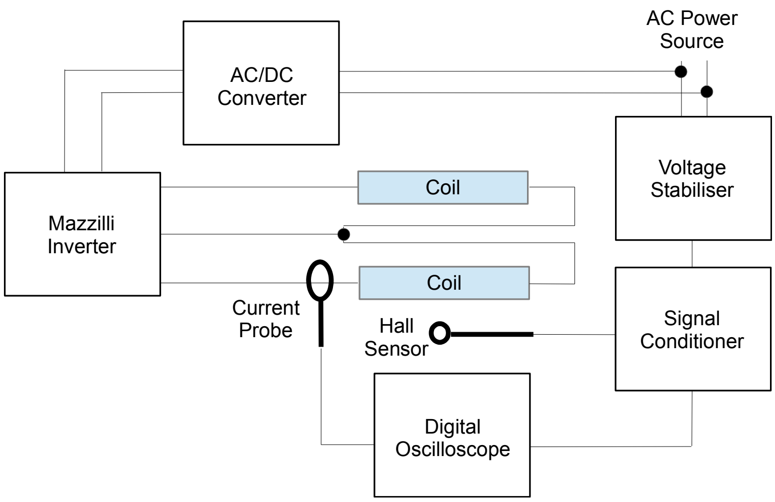


Fig D2.1 Schematic connection diagram of the 50 kHz experiment setup.

**D2.2 Procedure**

a) Turn on the power to the magnetic field measurement system.

b) Set the oscilloscope operating parameters as follow:

i) channel 1: connected to the output of the signal conditioner
ii) channel 2 : connected to the current probe
iii) trigger source: channel 2
iv) trigger level: 148 mV, i.e. 14.8 A @ 10 mV / A current probe gain

v) scale: channel 1 @ 100 mV / div, channel 2 @ 50 mV/div, time @ 1 μs / div
vi) coupling: channel 1 @ AC, 10 x gain, channel 2 @ DC, 1 x gain
vii) data acquisition mode: average 64 x

c) Turn on the power at the current probe, zero the reading before clamping on the coil feed wire and set its gain to 10 mV / A.

d) Starting from zero position, switch on the power to the AC / DC power converter and turn the variac dial until the coil current is 15 Apk.

***Make sure the peak value of channel 2 is between 148 mV and 156 mV at all times (to ensure the drift error is < 2.6 %).***

e) Position the Hall sensor vertically on the measurement table at the appropriate measurement location.

f) ***Allow the channel 1 waveform to stabilise for ~ 10 secs before taking any reading.***

g) Adjust a cursor to track the peak crest value of channel 1 (after a fixed delay from the trigger point) to avoid the switching ring waves.

h) Direct the sensor's face at 4 directions towards the +***y***, -***y***, +***x*** and -***x*** axes for each location.

***Adjust the tracking cursor after each change of orientation and allow ~ 10 secs for the waveform to stabilise before taking the reading for each direction.***

i) Do the above along the 4 axes shown in Fig D1.1.

i) coil's axis - along $x$ = 0 cm for -7 cm $\leq y \leq$ 7 cm
ii) centre line - along $y$ = 0 cm for -11 cm $\leq x \leq$ 11 cm
iii) middle line between the centre line and the pole - along $y$ = 3.5 cm for -11 cm $\leq x \leq$ 11 cm
iv) top line near the pole - along $y$ = 7 cm for -7 cm $\leq x \leq$ 7 cm